

# Calculation of patterns of solar radiation within urban geometries

A thesis submitted to the University of Manchester for the degree of Doctor  
of Philosophy in Earth Atmospheric and Environmental Sciences in the Faculty  
of Engineering and Physical Sciences

2015

Roberto Carrasco-Hernandez

School of Earth, Atmospheric and Environmental Sciences

## Contents

ABSTRACT	10
Declaration	11
Copyright statement	11
Acknowledgements	12
Chapter 1	13
1.1 Introduction	14
1.2 Aim	15
1.3 Objectives	15
1.3 Rationale/Justification	16
1.4 Research Proposal	20
References	25
Chapter 2 Theoretical Framework	29
2.1 The solar electromagnetic spectrum	30
2.2 Atmospheric radiative transfer	32
2.2.1 Attenuation of the solar direct beam	33
2.2.2 Spectral radiative transfer in the atmosphere	35
2.2.3 Spectral absorption by atmospheric gas species: ozone	36
2.2.4 Diffuse radiation from the upper-hemispheric view of the sky	38
2.2.5 Diffuse radiation in the ultraviolet ranges	40
2.2.6 Vertical Structure of the atmosphere	43
2.2.7 Radiative transfer software	44
2.2.8 The anisotropic distribution of diffuse radiation	47
2.3 Units of solar radiation	49
2.4 Studies of solar irradiance in urban canyons	51
2.4.1 Empirical studies of solar radiation in urban canyons	53
2.4.2 Theoretical models of solar radiation in urban canyons	54
2.4.3 Descriptions of urban geometries	55
Summary of Chapter 2	59
References	59
Chapter 3 Materials and Methods	63
3.1 General method for calculating canyon irradiance	64
3.2 Materials: Software tools	67
3.2.1 Google Street View	67
3.2.2 The Hugin software for panoramic reconstructions	68
3.2.3 The RayMan Model Software	69
3.2.4 SMARTS	79
3.3 Materials: Instrumentation for solar radiation measurements	80
3.3.1 Radiance measurements	81
3.3.2 Irradiance measurements	82
3.3.3 Broadband measurements: Pyranometers	83
3.3.4 Spectroradiometry	85
3.3.5 Fisheye lenses and whole-sky cameras	93
Summary of Chapter 3	97
References	98

Chapter 4	100	
Abstract .....		101
Abbreviations and Nomenclature.....		102
4.1 Introduction.....		102
4.2 Materials and Methods.....		105
4.2.1 Software tools.....		105
4.2.2 Street-level Total-shortwave Irradiance Measurements.....		108
4.2.3 Street-level Modelling.....		109
4.3 Results.....		110
4.3.1 Panorama Reconstructions from the Nokia E5 Set of Rectilinear Images.....		110
4.3.2 Panorama Reconstruction from Google Street View Images.....		112
4.3.3 Street-level Total-shortwave Irradiances.....		112
4.3.4 Combined Model.....		116
4.4 Discussion .....		120
4.4.1 Reconstructed vs. Control Fisheye Hemispheric Images. ....		120
4.4.2 Panorama reconstruction from Google snapshots .....		121
4.4.3 Street-level total-shortwave irradiances .....		122
4.5 Conclusions.....		124
Acknowledgements.....		126
References.....		126
Chapter 5	129	
Abstract .....		130
5.1 Introduction.....		130
5.1.1 Identification of urban panoramic components.....		132
5.1.2 Parametric Classification.....		133
5.1.3 Non parametric image classification .....		135
5.2 Methods.....		137
5.2.1 MAXENT image classification .....		137
5.2.2 A simple non-parametric supervised classification algorithm .....		139
5.2.3 Description of the non-parametric algorithm .....		140
5.3 Results.....		142
5.3.1 Supervised classification of a street photograph to identify urban components. .....		142
5.3.2 Results for the non-parametric classification of “sky” pixels .....		142
5.4 Discussion .....		144
5.4.1 Non-parametric classification.....		146
5.4.2 Further strategies to improve the classification.....		146
5.5 Conclusion .....		150
References.....		150
Chapter 6	152	
Abstract .....		153
6.1 Introduction.....		154
6.1.1 The diffuse-to-global spectral ratio (DGR) .....		156
6.2 Methods.....		157

6.2.1 Global spectral irradiance in urban canyons .....	157
6.2.2 Modelling the spectral DGR.....	159
6.2.3 Model Validations .....	164
6.3 Results.....	167
6.3.1 Modelling the DGR under a full sky-view .....	167
6.4 Discussion .....	173
6.5 Conclusions .....	178
Acknowledgements .....	180
References .....	180
Supplementary information for the article .....	183
Chapter 7	190
Abstract .....	191
7.1. Introduction.....	191
7.2 Block I. Digital processing of whole-sky RGB maps.....	194
7.2.1 Non-linear response to light intensity. ....	196
7.2.2 Saturation and the misrepresentation of the direct beam (Removal of saturated pixels) .....	197
7.2.3 The spectral Diffuse-minus-Circumsolar irradiance ( $D - C_{\lambda}$ ).....	198
7.3 Block II. Extrapolated UV whole-sky maps .....	201
7.3.1 Extrapolation of a hypothetical UV sky distribution.....	201
7.3.2 Extrapolation of globally-normalized RGB signatures towards the ultraviolet .....	203
7.3.3 Extrapolated UV sky-map from RGB information. ....	205
7.4 Block III. Calculations of street canyon spectral irradiance using $SVF_w$ .....	207
7.4.1 General methods for the calculation of street canyon spectral irradiance.....	207
7.4.2 Simulated canyons.....	209
7.4.3 Weighted SVF ( $SVF_w$ ) .....	211
7.4.4 Circumsolar SVF ( $SVF_C$ ) .....	212
7.4.5 Modelling relative canyon irradiance.....	212
7.5 Discussions.....	214
7.6 Conclusion .....	218
References.....	219
Chapter 8 General Discussion and Main conclusion	221
8.1 Introduction.....	222
8.2 Total-shortwave irradiance in urban canyons .....	224
8.3 Spectral irradiance in urban canyons .....	231
8.4 Corrections for global measurements under cloudy skies .....	234
8.5 Including the anisotropy of the diffuse component .....	236
Main Conclusion .....	238
References.....	239
Appendix I Published Version of Chapter 4	242
Appendix II Published Version of Chapter 6	252

## Figures

- Figure 1-1 Set of photographs associated to a single location in the city of Manchester, taken from Google Street View™ at [www.maps.google.com](http://www.maps.google.com). The set fully covers the upper-hemispheric view. The heading of each column indicates the direction of the camera (north, west, south, east) and each row indicates the tilt angle of the camera (0°, 45°, 90°). .....22
- Figure 2-1 Polar coordinate representation of the Rayleigh phase function for a molecule located at the origin. The two arrows represent the directions of incoming and outgoing radiation. The probability of scattering in a certain angle ( $\theta$ ) is proportional to the length between the origin and the pseudo-elliptical peripheral line. Extracted from Morcrette (2002). .....39
- Figure 2-2 Diagrams describe the changes in phase function with increasing particle size. Particle size is indicated by circles of increasing size from left to right. Arrows represent the direction of scattered light. The length of each arrow represents the probability of scattering occurring in each direction. Modified from Nave (2012). Mie scattering is relatively independent of wavelength; this is explained by the fact that, within larger particles, repeated events of reflection and refraction occur at numerous interfaces (Björn, 2007). In Mie-scattered radiation, the “blue” dominance of Rayleigh scattering becomes increasingly “white” with increasing particle size (Flammer et al., 2013). The types of particles that promote Mie scattering are larger particles such as aerosols, smoke, or dust. These particles are more abundant in the troposphere, and it is in this layer where most of the Mie scattering occurs. A consequence of this are the whitish colours observed in the sky, for example in hazy/polluted conditions. ....39
- Figure 2-3 Example of a polar azimuthal projection of a hemisphere (fisheye projection); Parallels (circles) and meridians (straight lines) of a hemisphere, are represented in this plane projection. Source: RayMan Model software v 1.2. ....57
- Figure 2-4 Equidistant polar projections of the upper-hemispheric sky-view; Left panel: full-sky view. Right panel: obstructed view (arbitrary obstruction). Both images include an overlaid grid of azimuth and elevation angles, along with an example solar path across the sky. Source: RayMan Model software v 1.2. ....57
- Figure 3-1 Diagrammatic representation of the general method for calculating total-shortwave and spectral irradiances, at any given canyon within the Google Street View coverage. 65
- Figure 3-2 Comparison of calculated total-shortwave global irradiance (grey dotted lines) versus measured irradiance as measured by a pyranometer (black lines). Measurements were obtained with a CM5 Pyranometer installed at the Pariser Building roof; University of Manchester. ....72
- Figure 3-3 Proportional errors for 8 days (same as those in Table 3-2), showing relative discrepancies between modelled and measured global irradiance throughout the day. Sunrise and sunset times are marked with grey dotted lines. ....73
- Figure 3-4 Selected examples from Figure 3-3, showing modelling discrepancies for distinguishable clear-sky periods. The time range (x-axis) has also been selected to show clear-sky periods mainly. ....74
- Figure 3-5 Absolute error (in  $\text{Wm}^{-2}$ ) of the modelled total-shortwave global irradiances for April 8 2011. Sunrise and sunset times are marked with grey dotted lines. ....75
- Figure 3-6 Modelled (grey-dotted line) versus measured (black line) total-shortwave irradiance under broken-cloud sky conditions. ....77
- Figure 3-7 Shows the differences between the equidistant (left panels) and orthographic (right panels) projections, of a hemisphere in front of an observing lens. The upper panels show

- diagrams of the geometries of equidistant and orthographic projections. The lower panels show example photographs of the same scene taken with the corresponding equidistant and orthographic fisheye lens. Adapted from Oshita (1999).....93
- Figure 3-8 Test fisheye image taken with the Sumlung model: SL-FE12 magnetic mini fisheye lens attached to a Nokia E5 camera. The 6 marks on the wall had known elevation angles with respect to the camera lens. The distance from each mark to the centre of the image (length of black arrows) represents the zenith angle of the marks ( $1 - \text{elevation angle}$ ). Arrow lengths were measured and normalized to 1. This distance is proportional to the R parameter in equations 3.2 and 3.3.....96
- Figure 3-9 The black line shows the comparison between the measured projected position (Y-axis) against the known elevation angle ( $E$ , X-axis) of the marks in Figure 3-7. The grey-dotted line shows the same relationship from an ideal orthographic projection (i.e.  $\sin(E)$ ). .....97
- Figure 4-1 Screenshots of the Hugin interface. Twenty-five independent images covering the full view from the Dover Street canyon in a hemispheric view (a) and plan view (b). (c) Shows the continuous hemispheric image of the view from the canyon, also projected onto a plane (d). ..... 111
- Figure 4-2 Orthographic and equidistant reconstructed hemispheric views versus a control fisheye image with corresponding SVF specified below each image.(a)Orthographic reconstructed projection, (b) equidistant reconstructed projection, and, (c) control fisheye image taken with the SLFE12 mini fisheye lens. Pictures were taken at the Dover Street canyon, University of Manchester. .... 111
- Figure 4-3 Reconstruction of Dover Street urban canyon from Google Street View database. Left and middle panels: Hugin interface screen showing the relative positioning of rectilinear images. Right panel: resulting orthographic projection. .... 112
- Figure 4-4 (a) Dover Street canyon equidistantly projected and oriented northwards with the corresponding solar path (times in UTC) for 3 April 2013. (b) Enlarged south-southeast section of the canyon showing the relevant parts of the sun path the sections where it is obstructed by buildings. This enlarged section includes the irradiance time series later shown in Figures 4-5a and 4-5b..... 113
- Figure 4-5 Showing the clear-sky modelled differences between obstructed (Dover Street canyon) and full sky (Whitworth Observatory) views on 3 (a) and 4 (b) April 2013, notice how the times of building obstructions of direct sunlight correspond to those measured in Figure 4-6)..... 114
- Figure 4-6 Showing the measurements and the observed differences between obstructed (Dover Street canyon) and full sky (Whitworth Observatory) views, on 3 April (a) and 4 April (b) 2013. .... 115
- Figure 4-7 Comparison between modelled (dashed grey line) and measurements (black line) of global total-shortwave irradiances, conducted on 3 April (a) and 4 April (b) 2013, at the Dover Street Canyon, University of Manchester. The models have been constructed using Eq. 1 for a combined model which used full-sky view measurements and an idealised ratio of canyon to full sky irradiances. .... 117
- Figure 4-8 Goodness of fit of the model described by Eq.1 for the data from both 3 and 4 April 2013 together. (a) shows the scatter plot of measured against modelled data considering all points. (b) shows the scatterplot after removing the identified time offsets. Both panels include a linear fit and the corresponding  $R^2$  values..... 119
- Figure 4-9Hugin interface screen. Left-hand side: shows the overall  $45^\circ$  rotation made from Google snapshots. Right-hand side: The panorama was then orthographically re-projected in order to simulate the perspective of the Dover Street canyon from the opposite side of the road. .... 122

- Figure 5-1 Left panel: RGB colour photograph of an urban canyon. Right panel: Scatter plot of digital pixel values in the RGB bands, for pixels identified as “clear-sky”. “Clear-sky” pixel values correspond to five arbitrarily chosen pixels, from the blue-sky sections in the left panel. RGB bands in the x-axis (right panel) have been put in inverse order (BGR) as proportional to the electromagnetic wavelength ranges they represent. .... 134
- Figure 5-2 Digital pixel values in the RGB bands, for three arbitrarily chosen pixels identified as “cloud”. Cloud-pixels were manually chosen from the Left panel on Figure 5-1. RGB bands in the x-axis (right panel) have been put in inverse order (BGR) as proportional to the electromagnetic wavelength ranges they represent. .... 136
- Figure 5-3 Original Image from Google Street View. .... 138
- Figure 5-4 Blue, Green and Red Bands (in that order) extracted from the original image. .. 138
- Figure 5-5 Training points assigned manually to represent each urban panoramic component: trees, road surfaces, sky, walls and windows. Each point was associated to its corresponding class in an ArcGIS spreadsheet file. .... 139
- Figure 5-6 Right: RGB fisheye projection of an urban canyon to be classified. Left panel: Image layer where a sample of “sky” pixels have been assigned with a white colour (digital value of circa 255). Right panel: The training set image was manually created, using the MyPaint software, as an independent layer drawn on top of the original image. .... 140
- Figure 5-7 Showing the classification of image 5.3, pixels are classified according to their highest probability of membership to an urban component: Grey: road surfaces Green: tree. Light Blue: sky; Dark Blue: windows; Yellow: wall ..... 142
- Figure 5-8 Frequency distribution histograms of the RGB bands obtained from the training set of “Sky” pixels shown in Figure 5-6. A. Red Band, B. Green Band, C. Blue Band. 143
- Figure 5-9 shows the classification of sky pixels in the image using the non-parametric algorithm presented in this text..... 144
- Figure 5-10 shows for each pixel the highest probability of membership to any class (Sky, Concrete, Bricks, Trees or Windows). Black pixels show very low probabilities of belonging to any of these classes..... 145
- Figure 5-11 Graphically shows the convolution matrix operation. In the Octave language the “conv2” command will return a 2D convolution between two matrices. The second matrix of the comma-separated list is defined as the sliding kernel. .... 147
- Figure 5-12 Left classified image as shown in Figure 5-9. Right: showing the results of a series of 20 nested convolution operations performed on the classified image (Figure 5-9), using a 5x5 kernel for calculating a neighbourhood average. .... 148
- Figure 6-1 DGRs calculated for different solar zenith angles (SZA) for a standard mid-latitude urban atmosphere using the SMARTS radiative transfer algorithm. Ozone (0.31 atm-cm) and aerosol (0.1 AOT<sub>500nm</sub>) atmospheric contents corresponded to those measured on 7 June 2013..... 157
- Figure 6-2 Orthographic fisheye images of four sky-views: Full, SVF = 0.99,  $S_{bin} = 1$ : Full sky-view with no simulated obstructions. C1, SVF = 0.54,  $S_{bin} = 1$ : Simulated Canyon obstructing the circumsolar region. C2, SVF = 0.41,  $S_{bin} = 1$ : Simulated Canyon obstructing the sky opposite to the sun. C3, SVF = 0.42,  $S_{bin} = 0$ : Simulated Canyon obstructing the solar disc and the circumsolar region. The sky view factor (SVF) was calculated using the RayMan software. .... 167
- Figure 6-3 Modelled curves of spectral DGRs for different SZAs, using Equations (6.3.10) (Panel a) and (6.4) (Panel b). Note that Panel B has a limit of solar zenith angles of < 90°; this is because the use of a tangent function (see Eq. 6.4). .... 168

- Figure 6-4 Proportional errors at different SZAs of spectral DGRs using equations (3.10) (Panel a) and (4) (Panel b), when compared against the SMARTS outputs for the same local atmospheric conditions (ozone 0.31 atm-cm and 0.1 AOT<sub>500nm</sub>)..... 169
- Figure 6-5 Results of the sensitivity analyses show errors found when comparing the SMARTS-calculated DGR ratios against equation (3.10) (Panels a and b) and equation (4) (Panels c and d). Panels a and c show the proportional errors found at different aerosol levels (AOT<sub>500nm</sub>), with constant ozone of 0.3 atm-cm. Panels b and d show the proportional error found at different ozone levels (O<sub>3</sub>) with constant AOT<sub>500nm</sub> at 0.1. All variations were modelled with a constant SZA of 32°..... 170
- Figure 6-6 Measurements of relative canyon spectral irradiances. Relative canyon irradiances are the ratio of canyon/full sky measured irradiances, for the three simulated canyons (C1, C2 and C3). ..... 171
- Figure 6-7 Model validations for the three simulated canyons (C1 to C3). Relative irradiances calculated with equations (6.3.10) and (6.4) irradiances (black lines), all relative to full sky-view. Panel C1: Canyon 1 (blocking circumsolar region). Panel C2: Canyon 2 (blocking the sky opposite to the sun), Panel C3: Canyon 3 (blocking the solar disc and circumsolar region). ..... 172
- Figure 6-8 Proportional errors of both proposed models, when comparing measured versus modelled relative canyon irradiance values. Panel C1: Canyon C1 (blocking circumsolar region). Panel C2: Canyon C2 (blocking the sky opposite to the sun). Panel C3: Canyon C3 (blocking the solar disc and circumsolar region). ..... 172
- Figure 7-1 Original RGB images obtained with a Nokia E5 digital camera, equipped with a Sumlung SL-FE12 magnetic mini-fisheye lens. Each channel approximately represents the angular distribution of peak sensitivity wavelengths: 460, 530 and 600 nm, as indicated. Digital pixel values, ranging from 0 to 255, have been reclassified in ten classes, at equal intervals across the range (This reclassification will not be used in any of the calculations, and it is only intended for illustrative purposes). ..... 195
- Figure 7-2 Inverse average response of 171 cameras obtained from the EMoR database (Empirical Model of Response). (Grossberg and Nayar, 2003) ..... 196
- Figure 7-3 Example comparison between the original “red” channel image (left panel) against the corresponding response corrected image, after applying Eq. 7.1 to all pixels (right panel). The same process was repeated for the “green” and “blue” images..... 197
- Figure 7-4 Showing the response-corrected Red image after the saturated pixels have been reclassified as “zero”. The same process was repeated for the “Green” and “Blue” images. .... 198
- Figure 7-5 Left panel: Raw spectral signature of small solid angle pointing at a clear sky). Right panel: Globally-normalized radiance i.e. The quotient of sky radiance projected onto a flat horizontal surface, to measured global irradiance. Sky radiance from a 2° field of view, with angular position: 180 ° azimuth and 30 ° zenith. Measurements were taken with a calibrated 2 channel Ocean Optics S2000 spectrophotometer, under clear sky conditions..... 202
- Figure 7-6 Globally-normalized spectral signature of different angular positions in the hemispheric sky view, modelled with LibRadTran (black filled ticks) for 6 UV and visible wavelengths (310, 355, 400, 460,530 and 700 nm); compared against a linear extrapolation (Eq. 7.6.2) from the same modelled wavelengths (white outlined ticks). Left panel shows radiances from angular positions towards the solar azimuth at zenith angles ranging from 0 to 20°. Right panel shows angular positions at zenith angles ranging from 30 to 80 ° towards the solar azimuth. .... 204
- Figure 7-7 Globally-normalized sky-maps for three UV wavelengths (310, 355 and 400nm), compared against the globally-normalized values in the blue channel (460nm). (For



illustrative purposes, all pixel values have been reclassified into twenty classes, and rescaled with respect to the maximum pixel value at the 310 nm sky-map).....	206
Figure 7-8 Orthographic fisheye photographs for three sky views. Full-sky view with no simulated obstructions. C1: Simulated Canyon obstructing a section of the the circumsolar region. C2: Simulated Canyon obstructing the anti-solar region. The sky view factor (SVF) was calculated using the RayMan software.....	210
Figure 7-9 Example showing the overlapping of simulated canyon C1. The same process was repeated for each RGB+UV sky-map. As well as for each simulated canyon .....	211
Figure 7-10 Modelled vs. Measured relative global spectral canyon irradiances, for six different wavelengths (310, 355, 400, 460, 530 and 600nm) within two simulated canyons C1 and C2. Relative irradiance values were obtained as the quotient between obstructed and full views. ....	213
Figure 8-1 Sampling transect along Oxford Road, Manchester, UK. The transect is comprised of 15 sequential Google Street View locations covering 118.24 m along Oxford Road. Panoramas of the upper-hemispheric sky-view were obtained for each locations.....	226
Figure 8-2 Variations of SVF and accumulated irradiance (E-sum), for 15 (Site Number ID 0-15) sites, along a transect of 118.24 metres on Oxford Road, Manchester UK. ....	230

## ABSTRACT

The University of Manchester

Roberto Carrasco-Hernandez. PhD in Earth Atmospheric and Environmental Sciences.

Calculation of patterns of solar radiation within urban geometries.

30 May 2015

The present work proposes methods to calculate street-level exposures to solar radiation. The methods comprise a combination of different software algorithms, online databases and real-time standard measurements of solar radiation. Firstly, the use of the free access image database “Google Street View” to reconstruct urban geometries is illustrated. Google Street View represents an enormous source of information readily available for its general use in the field of urban atmospheric studies. With the aid of existing software packages, it was possible to reconstruct urban geometries as projected fisheye images of the canyon upper-hemispheric view, and to model total-shortwave solar irradiance within an urban canyon. The models allowed the calculation of relative street-canyon irradiance as a fraction of that received under a full-sky view, depending on the visibility of the solar disc and the reduced sky view factor. The combined use of the ideal models with real-time data allows for the calculation of street-canyon irradiance under any cloud conditions. Validation of these techniques was obtained by comparing the calculations against *in situ* measurements of irradiance from a local street canyon.

The existing software, however, does not allow the calculation of spectral irradiance, required for inferring, for example, the biological effects of solar radiation. The use of spectral radiative transfer software was explored to provide spectral irradiance, but commonly available models do not include the effects of horizon obstructions. The approach presented here followed the same general guidelines used to calculate total-shortwave irradiance. The spectral models required a spectral partitioning of global irradiance into direct and diffuse components, allowing the independent analysis of horizon obstruction effects on these components at each wavelength. To partition global irradiance, two equations were developed for the calculation of the diffuse-to-global irradiance ratio (DGR) under cloudless conditions: one based on simplified radiative transfer theory, and an empirical fit for local conditions. Afterwards, the effects of horizon obstructions were evaluated in combination with real-time measurements of unobstructed global spectral irradiance. A set of simulated obstructions were used to validate the models. Finally, it was observed that neglecting the anisotropic distribution of the diffuse component of solar radiation in these simple models could produce large uncertainties in some situations. A practical solution for including the anisotropy of diffuse radiation was proposed, requiring images from an unobstructed digital sky camera.

The combination of tools described here will allow calculation of total and spectral global irradiance upon a flat horizontal surface whatever the local field of view. This is possible at any geographical location were the urban geometries can be described, either by manually obtaining digital photographs, or through the Google Street View database, and where there is a reasonably local standard measurement of radiation.

## **Declaration**

No portion of the work referred to in the thesis has been submitted in support of an application for another degree or qualification of this or any other university or other institute of learning;

## **Copyright statement**

i. The author of this thesis (including any appendices and/or schedules to this thesis) owns certain copyright or related rights in it (the “Copyright”) and he has given The University of Manchester certain rights to use such Copyright, including for administrative purposes.

ii. Copies of this thesis, either in full or in extracts and whether in hard or electronic copy, may be made only in accordance with the Copyright, Designs and Patents Act 1988 (as amended) and regulations issued under it or, where appropriate, in accordance with licensing agreements which the University has from time to time. This page must form part of any such copies made.

iii. The ownership of certain Copyright, patents, designs, trademarks and other intellectual property (the “Intellectual Property”) and any reproductions of copyright works in the thesis, for example graphs and tables (“Reproductions”), which may be described in this thesis, may not be owned by the author and may be owned by third parties. Such Intellectual Property and Reproductions cannot and must not be made available for use without the prior written permission of the owner(s) of the relevant Intellectual Property and/or Reproductions.

iv. Further information on the conditions under which disclosure, publication and commercialisation of this thesis, the Copyright and any Intellectual Property and/or Reproductions described in it may take place is available in the University IP Policy (see <http://documents.manchester.ac.uk/DocuInfo.aspx?DocID=487>), in any relevant Thesis

restriction declarations deposited in the University Library, The University Library's regulations (see <http://www.manchester.ac.uk/library/aboutus/regulations>) and in The University's policy on Presentation of Theses.

### **Acknowledgements**

This work was generously funded by the Mexican Council for Science and Technology (CONACyT) (grant reference: 214428). The company "Google" is acknowledged as the proprietor of all images extracted from the Google Street View database.

Sincere thanks to:

My supervisors, Prof Ann Webb and Dr Andrew Smedley, for all the hard work and useful lessons.

Dr Richard Kift and the staff of the Whitworth Observatory, University of Manchester for their kind help and technical support.

...All my friends and family

## **Chapter 1**

This introductory chapter will provide a general overview of the thesis, with aims and specific objectives, as well as a general rationale for the study.

## 1.1 Introduction

The present work addresses the modelling of solar radiation in urban environments, based on standard meteorological radiation measurements and through the use of free-access software tools. Solar radiation studies find many applications in different fields ranging from meteorological studies (Oleson, 2012; Levitin, 2014), photovoltaic generation (Jakubiec and Reinhart, 2013; Kardakos et al., 2014) and human health issues due to exposure (O'Hagan et al., 2002; Webb, 2006; Rhodes et al., 2010; Farrar et al., 2013). New radiometric technologies allow the delivery of real-time solar radiation data (Carlos et al., 2014; Hooke et al., 2014; Smedley et al., 2014). However, since the majority of meteorological products describing solar radiation refers to measurements taken under a full-sky view (i.e. with no horizon obstructions), there exists a general absence of realistic representations of the street-level urban environment in solar radiation studies. Yet, the increasing body of Geographic Information Systems (GIS) technologies and web applications offers novel opportunities for the creation of high resolution geographic models for urban studies. Unfortunately, the most common methods for describing solar radiation in urban geometries require either expensive 3D mapping of cities (Jakubiec and Reinhart, 2013; Chow et al., 2014; Rode et al., 2014), or user-made photographic descriptions of single locations (i.e. canyon “fisheye” images) (Fröhlich and Matzarakis, 2013; Krüger et al., 2013), which are not cost effective. In this work we propose an inexpensive method for reconstructing the 3D urban structures of large cities. The proposed method uses Google Street View images, in combination with free access software packages, to determine the sky view factor and the geometry of horizon obstructions of a specific location, thus allowing us to model relative patterns of solar radiation at street-level. These relative calculations may then be combined with routine observatory measurements (e.g. rooftop measurements with an unobstructed horizon), to

obtain absolute irradiance values for a street canyon. These methods for modelling street canyon radiation are explored and validated for both broadband and spectral irradiance.

The primary methods were designed to be as simple as possible, requiring the minimum of input data, that being easily obtained. More advanced assessments of street-level irradiance could be obtained by accounting for the surface properties in the canyon and also the anisotropy of diffuse radiation. These methods require additional computational effort and/or input data, but simple accessible approaches to these problems were explored.

The general method proposed in this work simplifies the modelling of solar radiation patterns in street canyons worldwide, without the need of digital city 3D models, and using freely available tools. Further potential improvements to the methods are also analysed, such as the use of artificial image-learning algorithms to automatically distinguish between panorama components (e.g. sky, building walls, vegetation) that may affect street canyon irradiance. Additionally, the relevance of the anisotropy of diffuse irradiance (under a cloudless sky) was assessed using sky camera images.

## **1.2 Aim**

To develop a low-cost method that allows the calculation of street-level solar irradiance at any point within a city with Google Street View coverage.

## **1.3 Objectives**

1. To develop a method for the reconstruction of urban geometries from the free-access Google Street View image database.
2. To use the reconstructed urban canyon panoramas to approximate the canyon total-shortwave irradiance on the basis of full-sky view (rooftop) observatory measurements.
3. To extend the models for the calculation of urban canyon spectral irradiance approximated from reconstructed panoramas and full-sky view spectral measurements.

4. To improve the performance of the spectral models through the approximation of the anisotropic sky distribution of diffuse irradiance, by using a cost-effective mobile phone sky camera.

### **1.3 Rationale/Justification**

The interactions between solar radiation, human health and the urban environment represent a historic field of research in the atmospheric sciences. During the last decades of the 19<sup>th</sup> Century, some severe statements about the risks of living in major cities were being expressed by academics. Hough in 1873 wrote: “...*the human race would become extinct in one or two centuries if we all lived in large cities*” (in Donaldson, 1875). Hough was acknowledging the fact that, during that time, there was a higher rate of deaths than births in the city of London.

Of particular interest was the interaction between sunlight and health, which had been discussed since the preceding century. In 1784, Mead wrote one of the earliest scientific pieces discussing the relationship between the Sun and human disease (Mead and Stack, 1748). One interesting feature of such text is the recognition of how important is the study of geometry and the relative positions of the Sun and the Earth to explain certain human conditions; besides its influence on air temperature and humidity. Mead recognized that “*the Sun and the Moon ...must at certain times make some alterations in animal bodies*”. Since, at the time, little was known about electromagnetic radiation or molecular biology, Mead mostly attributed the effects of the Sun to Newton’s gravitational forces upon body fluids. It is interesting, nonetheless, that some awareness of a direct influence of the sun upon human health existed in the early history of science.

The relationship between rickets, sunlight and vitamin D was unknown until the last decades of the 19<sup>th</sup> Century. During the preceding two centuries, rickets was treated with snail liquor (Weick, 1967) and little was known of the preventive action of sunlight or



sources of vitamin D (e.g. cod liver oil). In the 19<sup>th</sup> Century, however, some authors started acknowledging a possible relationship between rickets and poor exposure to sunlight. Rickets was of considerable importance at that time, given that between 11% and 31% of children presented the disease in medical clinics in different important cities, such as Dresden, Berlin, Prague and Manchester (Wirt, 1893). Palm (1888) wrote about his conclusions on a possible connection between sunlight exposure and the prevalence of rickets, after observing the difference between rickets occurrence in England and Japan: rickets was more common in the former country where sunlight exposure was definitely scarcer. Palm wrote: “*Our murky skies, our smoke-laden city atmosphere, our high houses and narrow streets, helping to exclude the struggling rays of the sun, are the direct opposites of the conditions prevailing in The Land of the Rising Sun*”. Later discoveries allowed the establishment of the link between rickets and the English urban landscape.

An accidental observation by Ritter in 1901 (in Rosenheim and Webster, 1925) led to the discovery of vitamin D production from cholesterol. However, it was not until 1925 that Rosenheim and Webster reported the substance acquired properties of an anti-rachitic agent after being exposed to UV radiation from mercury lamps. By the final decades of the 20<sup>th</sup> Century the relationship between UV radiation and vitamin D synthesis became well established and new technologies allowed detailed descriptions of the photochemistry of vitamin D (Webb and Holick, 1988; Webb et al., 1989). During the 20<sup>th</sup> Century, the development of electromagnetic wave physics and molecular biology brought to light the intricate relationships between sunlight and health.

In modern photobiology, the Sun is considered for its radiative properties, which can directly affect living organisms at the molecular level. By the second half of the 20<sup>th</sup> Century, the mechanism of DNA damage through the formation of thymine dimers became well known (Setlow et al., 1963), and the consequent role of UV radiation in skin cancers was

firmly established. The World Health Organisation declared ultraviolet radiation a complete carcinogen (El Ghissassi et al., 2009). In general, modern research provides robust evidence to explain the many effects of solar radiation in biological systems and human health.

Biological systems are strongly reactive to ultraviolet radiation, due to the large amounts of energy it contains. On one hand, human cells benefit from the exposure to UV radiation by using it as a source of photochemical energy to metabolize cholesterol into vitamin D. Two major forms of vitamin D are well characterized as well as their metabolic pathways: vitamin D<sub>2</sub> (ergocalciferol) and vitamin D<sub>3</sub> (cholecalciferol). Vitamin D<sub>2</sub> results when ergosterol, or pro-vitamin D<sub>2</sub> (a yeast sterol), is irradiated with UV. Vitamin D<sub>3</sub>, a sterol that is naturally present in human skin cells, results from the irradiation of 7-dehydrocholesterol (provitamin D<sub>3</sub>) (Webb and Holick, 1988). On the other hand, however, skin cells continuously exposed to UV radiation have increased chances of random mutation in DNA sequences. A specific region of the ultraviolet spectrum named UV-B (290 – 315 nm) includes the wavelengths responsible for photocarcinogenesis, but also for converting 7-dehydrocholesterol into pre-vitamin D<sub>3</sub> (Wolpowitz and Gilchrest, 2006). Hence, the synthesis of vitamin D cannot be disconnected from skin photo-damage and carcinogenesis.

Since the 20<sup>th</sup> Century, researchers have drawn attention to a spatial trend in cancer occurrence associated to geographic latitude and have also addressed a possible relationship with exposure to solar radiation. Apperly (1941) evaluated two different types of cancer separately, being, internal cancers and skin cancers. Apperly found opposite tendencies of these two types of cancer mortality in relation with latitude. While skin cancers were more common in lower latitudes, internal cancers became more frequent at higher latitudes. The reduced intensity of UV solar radiation at higher latitudes has also been regarded as a potential factor explaining these geographic patterns of cancer incidence. The geographic patterns of internal cancers reported by Apperly and others (e.g. Garland et al., 1990; Garland

et al., 2006) have raised the question whether optimal UV exposure, and vitamin D synthesis, may have a protective effect against internal cancers. This topic is a matter of intense debate in certain academic circles (Grant and Boucher 2009; Reddy and Gilchrest 2010) due to conflicting laboratory observations and a lack of clear functional mechanisms that unequivocally explain the role of vitamin D in preventing cancer (Tuohimaa et al., 2007). In this regard, some molecular studies on breast cancer by Zinser et al. (2011) suggest a molecular link between vitamin D and breast cancer: “...*the vitamin D receptor is expressed in mammary epithelial cells, suggesting that vitamin D may directly influence sensitivity of the gland to transformation*”. Moreover, Giovannucci (2005) mentions that vitamin D receptors in different types of cells inhibit carcinogenic behaviours of cells such as proliferation, invasiveness, angiogenesis and metastatic potential. Although further studies are needed, these observations suggest a mechanism that links exposure to UV radiation, vitamin D production and protection against some internal cancers.

Apart from human exposure, other matters of interest in public health may also be affected by atmospheric ultraviolet radiation, for example, the survival rate of airborne infectious pathogens that could also be affected by UV radiation. If we consider that microorganisms subjected to UV exposure will suffer from similar DNA damage as human skin cells, then these organisms will potentially decay under natural sunlight (McCambridge and McMeekin, 1981; Shaffer and Lighthart, 1997; Tong and Lighthart, 1998). Thus, certain doses of UV radiation in the troposphere could potentially reduce the prevalence of some airborne infectious diseases. Additionally, it has been suggested that human beings exposed to large doses of this kind of radiation could be subject to depression of the immune system (Selgrade et al., 1997; Halliday et al., 2012; Vaid et al., 2013). The contrasting positive and negative effects of exposure to solar radiation make it a controversial and complex topic (Webb et al., 2011). While continuing to explore the health benefits and risks of solar

radiation, it is also important to understand the exposures typical in the locations where humans are most frequently found (i.e. the street-level in major cities around the world). Measurements and models of solar radiation in the urban environment are therefore a useful meteorological product for public health authorities.

The creation of city maps showing the highly variable solar exposure patterns in the urban landscape can be considered a relevant meteorological product. Although latitude is the major determinant of the maximum exposure, building obstructions may play an important role, especially at densely built areas. Unfortunately, most modern meteorological indices of solar exposure are obtained from observatory measurements (i.e. usually taken under unobstructed full sky-view) and do not represent realistic patterns of human exposure, since the average person is exposed to solar radiation within street canyons (i.e. under an obstructed view of the sky). The present thesis aims to provide a way to reconstruct urban canyon irradiance, to create more realistic descriptions of the street-level radiative environment. Such descriptions may find useful applications in meteorological and human exposure studies.

#### **1.4 Research Proposal**

In the urban landscape, buildings are the main cause of sky-view obstructions. The most obvious effect of buildings is the shading that prevents direct sunlight from reaching the ground at particular times of the day, accompanied by an obstruction of the sky view (decrementing the total incoming sky radiation). The urban atmosphere is also characterised by wide spatial variations at local scales, attributable to the varying panoramas in architecture. The description of building geometries in the street is therefore a main problem in meteorological urban studies.

Hitherto, digital elevation models (DEMs) of cities are a common way for assessing the shading effect of buildings and mapping the solar radiation reaching urban canyons (Gal et al., 2007; Gal et al., 2009; Kastendeuch, 2013). However, DEMs usually provide low

resolution descriptions of the urban geometries, they demand large amounts of computer power and there exists a limited availability of city DEM reconstructions. A secondary method for describing urban geometries is by manually taking fisheye photographs with specialised 180° lenses (Chapman and Thornes, 2004; Chapman et al., 2007). Unfortunately, with this method, extensive amounts of field work would be required to cover large areas within major cities.

An alternative way of finding precise urban geometries for many cities is the Street View™ web tool of Google Maps™. The Google Street View database represents an enormous collection of photographs at ground level in major cities covering most of Australia, Asia, Europe, North America, and Central America (Anguelov et al., 2010). These grids exhaustively describe the slight spatial changes in the landscape around the camera. The information provided may be of great use in the specific field of solar radiation studies, since panoramas cover the full hemispheric view of the sky at each specific location. The image database therefore satisfies the requirements for modelling sky radiation upon a surface at the base of the hemispheric view (i.e. the position of the camera).

Google Street View has found many applications in natural and social sciences (Frome et al., 2009; Zamir and Shah, 2010; Mazerolle and Blaney, 2011). Yet, this image database has apparently been overlooked within the atmospheric sciences. In the reviewed literature, no research works were found that used the Google Street View image database for atmospheric or solar radiation studies. In this thesis, a method is proposed that uses these images to reconstruct street-level geometries and the corresponding incident solar radiation; this will provide a great advantage for users that do not have access to expensive DEM models of a city.

For cities with Google Street View coverage, every individual street location is linked to photographs of its surroundings facing north, east, south, and west and also facing towards the horizon and the zenith. An example location is shown in Figure 1-7, a set of independent photographs was obtained, covering the full upper-hemispheric view of a street canyon in Manchester, UK.



Figure 1-1 Set of photographs associated to a single location in the city of Manchester, taken from Google Street View at [www.maps.google.com](http://www.maps.google.com). The set fully covers the upper-hemispheric view. The heading of each column indicates the direction of the camera (north, west, south, east) and each row indicates the tilt angle of the camera (0°, 45°, 90°).

However, individual images may duplicate the panoramic information. For this reason the independent rectilinear images must be merged together to form a coherent picture of the hemisphere around the point of interest (e.g. a 180° fisheye image). Software tools such as Hugin (d'Angelo, 2007; German et al., 2007) are specifically designed for the geometrically correct creation of panoramic images from several independent rectilinear images. In the following chapters, tools and methods will be described that allow the reconstruction of fisheye polar representations of urban canyons from rectilinear photographs. Obstructions represented in the view will obstruct parts of the sky and sections of the solar path throughout

a specific day of the year. It is therefore necessary to identify the areas in the photographs that correspond to visible sky or which correspond to obstructions. Once the panoramas have been classified in sky and buildings, the solar path can be superimposed on the reconstructed hemispheric view by using the RayMan Model software (Matzarakis et al., 2010). The RayMan software also allows for the calculation of the canyon's total short-wave irradiance throughout the day, under cloudless conditions.

However, in order to include the effects of clouds, the initial methods for calculating street canyon irradiances have been on the basis of total-shortwave real-time measurements under broken-cloud conditions; as measured by a pyranometer located (under a full-sky view) at the Whitworth Observatory, University of Manchester. It is assumed that street canyon irradiance is a fraction of the observatory (full-sky) measurement, as a function of the visibility of the solar disc and the fraction of visible sky. Further extensions to the calculations include spectral irradiance calculations within a canyon, as a fraction of full-sky spectral measurements obtained from a diode-array spectrometer.

It can be argued, however, that describing a single perspective (i.e. that of the exact position of the camera) is rather limited for urban and human exposure studies. For example, people walking on either side of the street will have different perspectives of the sky. Yet, the position of a Google Street View panorama (at the centre of the road) could be advantageous, since it can be considered an approximation to the average canyon perspective. In this regard, an average sky view may be ideal for representing and modelling the whole variety of perspectives in a single canyon. In Chapter 4 it is described how a software tool (Hugin) partially allows the simulation of different perspectives within the same canyon by rotating the hemispheric panorama. Another disadvantage of fisheye photographs is that large sets of images would be required to represent the highly varying sky-views across an entire city. Before the existence of the Google Street View database, the gathering of images would have

been an enormous task for individual researchers. However, since the Google Street View images are taken by standardized cars driving along streets, a new panoramic view is available every few meters (at variable spacing, usually 7 – 8 m). The standard height (2.5 m from ground level) and position of Google Street View images may be an asset when trying to compare two or more sequential perspectives. While accepting that both the SVF and the resulting irradiance will change with exact position in the canyon, especially if the canyon is non-uniform along its length, a single position was selected for developing the methodology. Although the general methods described here are for analysing one point location, the same procedures can be easily repeated for adjacent locations (i.e. sequential perspectives); an example of this will be given in Chapter 8.

The next chapter (Chapter 2) contains a general introduction to basic concepts in solar radiation and radiometry. Chapter 3, for materials and methods, describes the software tools used to create the models, as well as the radiometric devices used for model validations. The subsequent chapters (4 to 7) contain specific methods, results and discussions for particular problems/aspects of the modelling process. Each of these chapters is presented as a stand-alone journal article. In Chapter 4, the reconstruction of urban geometries from Google Street View is presented in the format of an article published in the *Energy and Buildings Journal*. This chapter also presents the use of free access software to project Google screenshots into a “fisheye” panoramic view of the canyon geometries. Chapter 5 presents an implementation of image-learning algorithms to automatically identify panoramic components in the Google Street View images. However, this technique, and the complexity it represents, was not carried through to the broad-scale applications that follow. Projected fisheye images of real and simulated urban canyons were then used to calculate broadband (Chapter 4) and spectral solar irradiance reaching the urban canyon (Chapter 6, published in *Theoretical and Applied Climatology*). Finally, further improvements to the clear-sky spectral radiation models may



be made when considering the anisotropic distribution of diffuse irradiance; these methods are described in Chapter 7. To illustrate the potential use of Google Street View to model the varying urban landscape a small example is given (in Chapter 8), that shows a spatial sequence of Street View perspectives and their corresponding irradiance calculations along a street in the city of Manchester. Chapter 8 finally provides a general discussion of the findings of this research and makes some suggestions on future developments.

The general method proposed in this work allowed for the calculation of street-level broadband and spectral irradiance on the basis of panoramic projections of street canyons and routine solar measurements (the latter taken at the Centre for Atmospheric Sciences in the University of Manchester, UK). These techniques can be easily reproduced in other locations with minimum software and hardware requirements. The main advantage of developing this tool will be the possibility of creating urban atmospheric models for any city in the world with Google Street View coverage.

## References

- Anguelov, D., Dulong, C., Filip, D., Frueh, C., Lafon, S., Lyon, R., and Weaver, J. (2010). Google street view: Capturing the world at street level. *Computer*, (6), 32-38.
- Apperly, F. L. (1941). The relation of solar radiation to cancer mortality in North America. *Cancer Research*, 1(3), 191-195.
- Carlos, B., Alvaro, D. B., Freddy, K., Eduardo, P., Gianfranco, P., and Franco, S. (2014). GEULMóvil-real-time ultraviolet radiation index mobile network. In *Instrumentation and Measurement Technology Conference (I2MTC) Proceedings, 2014 IEEE International* (pp. 557-560). IEEE.
- Chapman, L., and Thornes, J. E. (2004). Real-time sky-view factor calculation and approximation. *Journal of Atmospheric and Oceanic Technology*, 21(5), 730-741.
- Chapman, L., Thornes, J. E., Muller, J. P., and McMuldloch, S. (2007). Potential applications of thermal fisheye imagery in urban environments. *Geoscience and Remote Sensing Letters, IEEE*, 4(1), 56-59.
- Chow, A., Fung, A. S., and Li, S. (2014). GIS modeling of solar neighborhood potential at a fine spatiotemporal resolution. *Buildings*, 4(2), 195-206.
- d'Angelo P. (2007) Radiometric alignment and vignetting calibration.
- Donaldson, F. (1875). Public Health Care and General Physical Conditions Relating to Hygiene: Influence of City Life and Occupations in Developing Pulmonary Consumption. *Public health papers and reports*, 2, 95.

- El Ghissassi, F., Baan, R., Straif, K., Grosse, Y., Secretan, B., Bouvard, V., and Coglianò, V. (2009). A review of human carcinogens—part D: radiation. *The lancet oncology*, 10(8), 751-752.
- Farrar, M. D., Webb, A. R., Kift, R., Durkin, M. T., Allan, D., Herbert, A., and Rhodes, L. E. (2013). Efficacy of a dose range of simulated sunlight exposures in raising vitamin D status in South Asian adults: implications for targeted guidance on sun exposure. *The American journal of clinical nutrition*, 97(6), 1210-1216.
- Fröhlich, D., and Matzarakis, A. (2013). Modeling of changes in thermal bioclimate: examples based on urban spaces in Freiburg, Germany. *Theoretical and applied climatology*, 111(3-4), 547-558.
- Frome, A., Cheung, G., Abdulkader, A., Zennaro, M., Wu, B., Bissacco, A., and Vincent, L. (2009, September). Large-scale privacy protection in google street view. In *Computer Vision, 2009 IEEE 12th International Conference on* (pp. 2373-2380). IEEE.
- Gal, T., Lindberg, F., and Unger, J. (2009). Computing continuous sky view factors using 3D urban raster and vector databases: comparison and application to urban climate. *Theoretical and applied climatology*, 95(1-2), 111-123.
- Gal, T., Rzepa, M., Gromek, B., and Unger, J. (2007). Comparison between sky view factor values computed by two different methods in an urban environment. *Acta Climatologica et Chorologica*, 40(41), 17-26.
- Garland, C. F., Garland, F. C., Gorham, E. D., Lipkin, M., Newmark, H., Mohr, S. B., and Holick, M. F. (2006). The role of vitamin D in cancer prevention. *American Journal of Public Health*, 96(2), 252.
- Garland, F. C., Garland, C. F., Gorham, E. D., and Young, J. F. (1990). Geographic variation in breast cancer mortality in the United States: a hypothesis involving exposure to solar radiation. *Preventive medicine*, 19(6), 614-622.
- German, D. M., d'Angelo, P., Gross, M., and Postle, B. (2007, June). New methods to project panoramas for practical and aesthetic purposes. In *Proceedings of the Third Eurographics conference on Computational Aesthetics in Graphics, Visualization and Imaging* (pp. 15-22). Eurographics Association.
- Giovannucci, E. (2005). The epidemiology of vitamin D and cancer incidence and mortality: a review (United States). *Cancer Causes and Control*, 16(2), 83-95.
- Grant, W. B., and Boucher, B. J. (2009). Current impediments to acceptance of the ultraviolet-B-vitamin D-cancer hypothesis. *Anticancer research*, 29(9), 3597-3604.
- Halliday, G. M., Damian, D. L., Rana, S., and Byrne, S. N. (2012). The suppressive effects of ultraviolet radiation on immunity in the skin and internal organs: implications for autoimmunity. *Journal of dermatological science*, 66(3), 176-182.
- Hooke, R., Pearson, A., and O'Hagan, J. (2014). Autonomous Portable Solar Ultraviolet Spectroradiometer (APSUS)—a New CCD Spectrometer System for Localized, Real-Time Solar Ultraviolet (280–400 nm) Radiation Measurement. *Photochemistry and photobiology*, 90(4), 903-910.
- Jakubiec, J. A., and Reinhart, C. F. (2013). A method for predicting city-wide electricity gains from photovoltaic panels based on LiDAR and GIS data combined with hourly Daysim simulations. *Solar Energy*, 93, 127-143.
- Kardakos, E. G., Alexiadis, M. C., Vagropoulos, S. I., Simoglou, C. K., Biskas, P. N., and Bakirtzis, A. G. (2013, September). Application of time series and artificial neural network models in short-term forecasting of PV power generation. In *Power Engineering Conference (UPEC), 2013 48th International Universities'* (pp. 1-6). IEEE.
- Kastendeuch, P. P. (2013). A method to estimate sky view factors from digital elevation models. *International Journal of Climatology*, 33(6), 1574-1578.

- Krüger, E., Drach, P., Emmanuel, R., and Corbella, O. (2013). Urban heat island and differences in outdoor comfort levels in Glasgow, UK. *Theoretical and applied climatology*, 112(1-2), 127-141.
- Levitin, Y. (2014). Urban Scale Meteorological and Air Quality Forecast for the Biggest Israeli Cities Jerusalem, Tel Aviv and Haifa: WRF-Chem Model Simulation. In *Air Pollution Modeling and its Application XXII* (pp. 693-701). Springer Netherlands.
- Matzarakis, A., Rutz, F., and Mayer, H. (2010). Modelling radiation fluxes in simple and complex environments: basics of the RayMan model. *International Journal of Biometeorology*, 54(2), 131-139.
- Mazerolle, D., and Blaney, S. (2011). Google Street View: A New Online Tool with Potential Application to Roadside Invasive Species Detection and Monitoring. *Plant Invasions*, 77.
- McCambridge, J., and McMeekin, T. A. (1981). Effect of solar radiation and predacious microorganisms on survival of fecal and other bacteria. *Applied and environmental microbiology*, 41(5), 1083-1087.
- Mead, R. (1748). *A treatise concerning the influence of the sun and moon upon human bodies, and the diseases thereby produced*. Printed for J. Brindley, bookseller.
- O'Hagan, J. B., Driscoll, C. M. H., and Pearson, A. J. (2002). Occupational exposure to optical radiation in the context of a possible EU proposal for a directive on optical radiation. National Radiological Protection Board (United Kingdom).
- Oleson, K. (2012). Contrasts between urban and rural climate in CCSM4 CMIP5 climate change scenarios. *Journal of Climate*, 25(5), 1390-1412.
- Palm, T. A. (1888). Etiology of Rickets. *British medical journal*, 2(1457), 1247.
- Reddy, K. K., and Gilchrist, B. A. (2010). What Is All This Commotion about Vitamin D?. *Journal of Investigative Dermatology*, 130(2), 321-326.
- Rhodes, L. E., Webb, A. R., Fraser, H. I., Kift, R., Durkin, M. T., Allan, D., and Berry, J. L. (2010). Recommended Summer Sunlight Exposure Levels Can Produce Sufficient ( $\geq 20$  ng ml<sup>-1</sup>) but Not the Proposed Optimal ( $\geq 32$  ng ml<sup>-1</sup>) 25 (OH) D Levels at UK Latitudes. *Journal of Investigative Dermatology*, 130(5), 1411-1418.
- Rode, P., Keim, C., Robazza, G., Viejo, P., and Schofield, J. (2013). Cities and energy: urban morphology and residential heat-energy demand. *Environment and Planning B: Planning and Design*, 40(1), 138-162.
- Rosenheim O., and Webster T.A. (1925). Rickets and cholesterol. *The Lancet* 205:1025–1026.
- Selgrade, M. K., Repacholi, M. H., and Koren, H. S. (1997). Ultraviolet radiation-induced immune modulation: potential consequences for infectious, allergic, and autoimmune disease. *Environmental health perspectives*, 105(3), 332.
- Setlow, R. B., Swenson, P. A., and Carrier, W. L. (1963). Thymine dimers and inhibition of DNA synthesis by ultraviolet irradiation of cells. *Science*, 142(3598), 1464-1466.
- Shaffer, B. T., and Lighthart, B. (1997). Survey of culturable airborne bacteria at four diverse locations in Oregon: urban, rural, forest, and coastal. *Microbial Ecology*, 34(3), 167-177.
- Smedley A. R. D., Kift R. C., and Webb A. R. (2014). Application of a dual-channel solid state spectrometer to measure spectral surface radiation and atmospheric constituents. Thematic Network for Ultraviolet Measurements. UVnet workshop 2014. <http://metrology.hut.fi/uvnet/>.
- Tong, Y., and Lighthart, B. (1998). Effect of simulated solar radiation on mixed outdoor atmospheric bacterial populations. *FEMS microbiology ecology*, 26(4), 311-316.
- Tuohimaa, P., Pukkala, E., Scélo, G., Olsen, J. H., Brewster, D. H., Hemminki, K., and Brennan, P. (2007). Does solar exposure, as indicated by the non-melanoma skin cancers, protect from solid cancers: vitamin D as a possible explanation. *European Journal of Cancer*, 43(11), 1701-1712.

- Vaid, M., Prasad, R., Singh, T., Elmets, C. A., Xu, H., and Katiyar, S. K. (2013). Silymarin inhibits ultraviolet radiation-induced immune suppression through DNA repair-dependent activation of dendritic cells and stimulation of effector T cells. *Biochemical pharmacology*, 85(8), 1066-1076.
- Webb, A. R. (2006). Considerations for lighting in the built environment: Non-visual effects of light. *Energy and Buildings*, 38(7), 721-727.
- Webb, A. R., DeCosta, B. R., and Holick, M. F. (1989). Sunlight Regulates the Cutaneous Production of Vitamin D<sub>3</sub> by Causing Its Photodegradation\*. *The Journal of Clinical Endocrinology and Metabolism*, 68(5), 882-887.
- Webb, A. R., and Holick, M. F. (1988). The role of sunlight in the cutaneous production of vitamin D<sub>3</sub>. *Annual review of nutrition*, 8(1), 375-399.
- Webb, A. R., Kift, R., Berry, J. L., and Rhodes, L. E. (2011). The vitamin D debate: translating controlled experiments into reality for human sun exposure times. *Photochemistry and photobiology*, 87(3), 741-745.
- Weick, M. T. (1967). A history of rickets in the United States. *The American journal of clinical nutrition*, 20(11), 1234-1241.
- Wirt, W. E. (1893). Rickets, and the treatment of its resulting deformities. *Journal of the American Medical Association*, 20(1), 13-16.
- Wolpowitz, D., and Gilchrist, B. A. (2006). The vitamin D questions: how much do you need and how should you get it?. *Journal of the American Academy of Dermatology*, 54(2), 301-317.
- Zamir, A. R., and Shah, M. (2010). Accurate image localization based on google maps street view. In *Computer Vision—ECCV 2010* (pp. 255-268). Springer Berlin Heidelberg.
- Zinser, G. M., Narvaez, C. J., and Welsh, J. (2011). The Vitamin D Signaling Pathway in Mammary Gland and Breast Cancer. In *Vitamin D and Cancer* (pp. 279-293). Springer New York.

## **Chapter 2**

### **Theoretical Framework**

This chapter describes basic concepts in solar radiation theory and radiometry that will be used throughout the thesis.

## 2.1 The solar electromagnetic spectrum

The continuous vibration of atoms in any substance leads to emission of energy in a form known as electromagnetic radiation. As a consequence, any substance with a temperature above absolute zero will radiate energy as its atoms or molecules agitate. The emitted electromagnetic radiation exhibits dual behaviour, both as a wave and as discrete particles (photons) (Siegel 2001; Bohren and Clothiaux 2006; Seeds and Backman 2009). In most circumstances electromagnetic radiation can be considered a wave, but some phenomena can only be explained by assuming a particle-like nature. The small amount of high energy (short wavelength) radiation from the Sun, for example, can only be explained by Planck's theory of quantized waves (Siegel 2001; Turro et al., 2009).

Electromagnetic radiation may be characterized by its frequency, which is directly proportional to the amount of energy that it contains. This in accordance with Planck's theory, which postulates that

$$E = \frac{h}{2\pi} \nu,$$

where  $E$  is energy (in Joules, J);  $\nu$  is the wave frequency ( $\text{s}^{-1}$ ) and  $h$  is Planck's constant ( $\approx 1.054 \times 10^{-34}$  Js) (Turro et al., 2009). Alternatively, electromagnetic radiation can be characterized by its wavelength which is inversely proportional to the frequency of the wave and to the energy it contains.

However, not all objects radiate electromagnetic waves/photons in the same way. The energy emitted (as electromagnetic radiation) by an ideal blackbody is comprised of a spectrum (i.e. a continuum of different wavelengths, each one with a specific intensity) with a distinctive shape that follows Planck's blackbody curve. The peak of this curve shifts to shorter wavelengths as the temperature ( $T$ ) of the body increases, and the total energy emitted is a function of  $T^4$  (Stefan's Law).

Stars can reach extraordinarily high temperatures, with our Sun being the greatest source of electromagnetic radiation reaching the surface of the Earth. The spectral intensity of radiation received from the Sun at the top of our atmosphere closely follows that of an ideal blackbody radiator at 5600 K (Ryer 1998). Discrepancies are explained by the fact that the solar photosphere contains materials at different temperatures, which results in slight deviations from an ideally homogeneous blackbody radiator (Celarier and Hollandsworth 2003). Also, absorption by elements in the outer atmosphere of the sun gives the distinctive spectral lines observed.

The energy contained in a beam of propagating electromagnetic radiation may interact with matter encountered on its path, resulting in the increase of the energetic state of matter (e.g. the excitation of bio-molecular systems) (Starr et al., 2012). Phenomena such as heating, vision and photosynthesis are examples of relevant interactions between electromagnetic radiation and matter. Other important interactions include the mutagenic effects of electromagnetic radiation on DNA sequences and other biomolecules or the photoelectric effect. In the photoelectric effect, a photon is absorbed by an atom and an electron is released (Hobbie and Roth, 2007). This phenomenon makes possible the electronic measurement of light using a photodiode (Gupta, 2012).

Because of these interactions, the radiation emitted by the Sun is a major source of direct energy for terrestrial systems, including natural meteorological and biological systems, but also the human-made landscapes. At the wider scale, heat and temperature differences are the fundamental forces producing general air movement and water cycling around the planet. Hence, the main effect of overall solar radiation on the planet is the creation of climatic patterns of continents and oceans, by the non-homogeneous heating of the Earth's surface.

At smaller scales, different regions of the solar electromagnetic spectrum have effects of their own on specific systems. For example, visible light (wavelength: 400 – 700 nm) provides the energy required for the photosynthesis of glucose in plants and algae, consequently allowing the development of food chains and complex ecosystems. Also, human beings and our technologies are systems that interact with solar radiation: examples range from human vision to photovoltaic generation or domestic water heating systems.

The present work focused on shortwave solar radiation, in the UV – visible regions of the solar electromagnetic spectrum received at ground level (with wavelengths between 280 – 700 nm). This region of shortwave radiation includes the peak intensities of solar radiation emitted by the Sun. This energy is used by natural and technological systems. However, it must be acknowledged that the actual amounts of radiant energy received at the planet's surface are further affected by the atmosphere.

## **2.2 Atmospheric radiative transfer**

The general theory of radiative transfer describes electromagnetic radiation propagating through a medium and its interactions with molecules and other particles encountered on its path (e.g. aerosols). Whenever a photon encounters a particle in the medium, the photon may be absorbed or absorbed and re-emitted (at the same wavelength) in a direction different to the propagation of the original beam (i.e. scattering) (Björn, 2007). Such interactions (absorption and scattering) result in attenuated intensities of the original beam in the direction of propagation and also act as a source of radiation moving in directions other than the original beam (diffuse radiation). The following subsections (2.2.1 to 2.2.3) describe the attenuation of the solar beam when passing through the Earth's atmosphere. Then, the diffuse radiation and the effects of the atmosphere on scattered light will be described in sections 2.2.4 and 2.2.5. Afterwards, Subsections 2.2.6 and 2.2.7 describe, respectively, the vertical structure of the atmosphere and a brief introduction to software tools. Subsection 2.2.8



describes relevant aspects of the anisotropic distribution of diffuse radiation across the sky vault.

### 2.2.1 Attenuation of the solar direct beam

The sun is sufficiently distant from the Earth that it can be considered a point source, and solar radiation reaches the outside of the atmosphere as a parallel beam. On entering the atmosphere, the attenuation of the original beam is a negative exponential function of the initial intensity (at the top of the atmosphere), and the thickness and density of the medium; this, in accordance with the *Beer – Lambert Law* (Beer 1852; Lambert 1892).

The *Beer – Lambert Law* or *Extinction Law*, (see Thomas and Stamnes, 2002) results from the solution of the ordinary differential equation:

$$\frac{dE}{ds} = -\tau E_0, \quad (\text{Eq. 2.1})$$

where  $dE/ds$  represents the rate of change of irradiance ( $E$  in  $\text{Wm}^{-2}$ ) of an initial irradiance ( $E_0$ ) crossing an infinitesimal distance ( $ds$ ) in a medium with optical depth ( $\tau$ ). The optical depth is a dimensionless quantity that may be defined as the integral throughout the path length ( $s$ ), of either the mass extinction coefficient, times the mass density, or the extinction cross section, times the particle density.

The mass extinction coefficient ( $k_m$ , in  $\text{m}^2 \cdot \text{kg}^{-1}$ ) (Eq. 2.1.1) is defined as the extinction of intensity ( $I$ ) per mass volume density unit ( $\rho$ , in  $\text{kg} \cdot \text{m}^{-3}$ ), crossing a volume of air ( $v$ ), with an infinitesimal path length ( $ds$ )

$$k_m = \frac{dI_v}{I_v \rho ds}. \quad (\text{Eq. 2.1.1})$$

On the other hand, the extinction cross section ( $k_n$ , in  $\text{m}^2 \cdot \text{kg}^{-1}$ ) (Eq. 2.1.2) is the extinction per particle volume density unit ( $n$ , in  $\text{m}^{-3}$ ) of the presented molecule, in  $ds$ .

$$k_n = \frac{dI_v}{I_v n ds}. \quad (\text{Eq. 2.1.2})$$

The extinction cross section has also been interpreted as the effective area of the presented molecule (Molina and Molina, 1986). Extinction coefficients are usually determined with laboratory measurements of specific gases under standard conditions (e.g. Molina and Molina, 1986).

The Earth's atmosphere will act as a fluid medium affecting the incoming radiation from the sun. At the top of the atmosphere, the initial intensity is known as the solar constant; and has total irradiance values of 1366 to 1368  $\text{Wm}^{-2}$  approximately. The term "constant" is of course arguable (Drusch and Crewell, 2005) because of the slight variations observed along the orbit of the Earth around the Sun and with the fluctuating activity of the Sun itself. Still, the term solar constant will be used in this work, since other terms proposed (e.g. "total solar irradiance" in Thomas and Stamnes, 2002) may become ambiguous and can be easily confused with other concepts used in this work for ground-level measurements (total-e.g. shortwave irradiance). The solar constant represents an integrated value of all the different wavelengths emitted by the Sun. Therefore, it describes the instantaneous radiant energy received at the top of our atmosphere on a surface perpendicular to the solar beam. After entering the atmosphere, radiation will undergo complex processes of absorption and scattering before reaching an observer at ground level.

In the Earth's atmosphere, the path length  $s$  may be calculated as the air mass factor ( $M$ ), which is a function of the solar zenith angle (SZA) (Eq.2.2).

$$M = \sqrt{\left\{\left(\frac{r}{\cos z}\right)^2 + 2r + 1\right\}} - \frac{r}{\cos z}, \quad (\text{Eq. 2.2})$$

where  $r = \frac{\text{Radius of the Earth}}{\text{Height of the Atmosphere}} \approx 708$ ; and  $Z$  is the SZA.

In Eq. 2.2 the air mass factor was calculated considering a spherical atmosphere, according to Schoenberg (1922).

The air mass factor is directly proportional to the SZA: When the sun is near the local zenith ( $SZA = 0^\circ$ ) the air mass is at minimum and it equals 1. As the sun moves towards the horizon ( $SZA = 90^\circ$ ) the air mass factor increases as the inverse of the cosine of the SZA. The increase in air mass results in increased probabilities of interactions between all wavelengths in the radiation beam with the atmospheric particles. Locally, as the day goes through, the SZA changes, moving from the horizon towards the zenith (during morning hours) and back again toward the horizon (during the afternoon). The minimum SZA depends on the latitude (being lower at locations near the Equator) and day of the year.

An integrated form of the Beer-Lambert law (Eq. 2.1), in the Earth's atmosphere, is therefore

$$E = E_0 \exp(-M\rho\alpha), \quad (\text{Eq. 2.3})$$

where  $M$  is the optical air mass factor (Eq. 2.2),  $\rho$  is a measure of the atmospheric density of the atmosphere and  $\alpha$  is the specific extinction coefficient of the atmosphere.

Incident radiation therefore changes with time and space (with the changing local apparent position of the Sun). Incident radiation has also variations with respect to wavelength. The spectral effects of the atmospheric interactions will be explained below in section 2.2.2.

### **2.2.2 Spectral radiative transfer in the atmosphere**

A spectral partitioning of solar radiation becomes relevant when considering the wavelength dependency of radiative transfer interactions. The spectrum emitted by the sun approximately behaves as the radiation emitted by a black body at 5600 K. This spectrum ranges from gamma rays ( $< 10^{-3}$  nm) to infrared radiation ( $> 700$  nm), but each different wavelength will be attenuated by the atmosphere in a different way. The simplest forms of attenuation are smooth functions of wavelength, for example, Rayleigh scattering which is an inverse function of the fourth power of wavelength.

Rayleigh (1871) proposed that the magnitude of light scattering was proportional to the molecular density of the gas; also, that the amount of scattered light towards the direction of incident light was twice that of the light scattered at right angles from it. Rayleigh scattering can be understood as the scattering of electromagnetic radiation passing through a gaseous medium caused by gas particles that are smaller in diameter than the wavelength of radiation (particle size  $< 1/10$  wavelength). Scattering is strongly wavelength dependent (as an inverse function of the fourth power of wavelength), meaning that shorter wavelengths are more easily scattered by gas molecules. Rayleigh scattering processes explain the blue colour of clear skies, because blue light is scattered about 10 times more than red light.

An exponential polynomial approximation to the Rayleigh scattering transmittance of the atmosphere is provided by Gueymard (1995):

$$T_R = \exp(-MP/(a_1\lambda^4 + a_2\lambda^2 + a_3 + a_4\lambda^{-2})), \quad (\text{Eq. 2.4})$$

where  $M$  is the air mass (Eq. 2.2),  $P$  is the atmospheric pressure,  $a_1 = 117.26 \mu\text{m}^{-4}$ ,  $a_2 = -1.32 \mu\text{m}^{-2}$ ,  $a_3 = 3.20 \mu\text{m}^{-4}$ ,  $a_4 = -7.68 \times 10^{-5} \mu\text{m}^2$ .

### 2.2.3 Spectral absorption by atmospheric gas species: ozone

Not all extinction processes are simple inverse functions of wavelength as Rayleigh scattering. In fact, the various gases in the atmosphere will have specific absorption spectral curves, which create complex spectral patterns of irradiance at ground level (see: Webb, 1998, p.2).

Each different atmospheric compound will have a specific spectral absorption curve. One clear example of this is the strong reduction in the UV region ( $< 400$  nm) at ground level due to the presence of ozone in the stratosphere. The spectral absorption of ozone is of special interest for this thesis, because of its attenuating properties on ultraviolet radiation.

The absorption spectrum of ozone in the ultraviolet region is well studied (Molina and Molina, 1986; Malicet et al., 1995). Its spectral absorption cross sections show a quasi-

symmetrical bell-shaped continuum at wavelengths between 200 to 350 nm, reaching a maximum absorption near 250 nm (Hartley Band). At the larger wavelengths (310 – 350 nm), the absorption spectrum is dominated by a slightly more oscillating region known as the Huggins band.

Since wavelengths shorter than 250 nm are scarce in the solar spectrum, the left tail of the bell-shaped curve may be neglected in studies of natural solar radiation. In turn, the right tail of the ozone absorption curve explains why shorter UV wavelengths are largely absent in the ground-level solar spectrum, but increase through the UVB and into the UVA region.

Attenuation of the direct solar beam due to ozone (i.e. ozone transmittance,  $T_{o\lambda}$ ) can be approximated using the *Beer – Lambert law* as:

$$T_{o\lambda} = \exp(-m_o * \tau_o), \quad (\text{Eq. 2.5})$$

where  $m_o$  is the ozone air mass as a function of the SZA and  $\tau_o$  is the ozone optical thickness, in turn expressed as:

$$\tau_o = u_{o\lambda} A_{o\lambda}.$$

The spectral optical thickness of atmospheric ozone ( $\tau_o$ ) is equal to the product of the ozone column ( $u_{o\lambda}$ ) and the spectral ozone absorption coefficients ( $A_{o\lambda}$ ). The absorption coefficients are usually obtained from standard laboratory data, which comes in the form of tables (e.g. Molina and Molina, 1986; Gueymard, 1995; Malicet et al., 1995).

Apart from ozone, other gases in the atmosphere absorb different wavelengths according to specific spectral absorption coefficients. Thus, each gas will independently affect the

overall atmospheric transmittance. The calculations shown here for ozone transmittance can be generalized for other gases, provided their specific spectral absorption curves are known.

#### **2.2.4 Diffuse radiation from the upper-hemispheric view of the sky**

Apart from the attenuation of the direct beam, light scattering in the atmosphere creates what is known as diffuse radiation, which comprises all the electromagnetic radiation scattered by the atmosphere towards an observer at ground level. Therefore, the process of radiation scattering does not only contribute to the attenuation of direct electromagnetic radiation, but also to the creation of diffuse radiation. Under cloudless conditions, Rayleigh scattering of the direct solar beam is the most important source of diffuse radiation.

However, when radiation encounters larger particles (e.g. aerosols or water droplets), other types of scattering processes occur. These alternative scattering processes differ from Rayleigh scattering in regard to the predominant change of direction and the wavelength dependency. To understand the differences between different scattering phenomena, the concept of phase functions must be explained. Phase functions describe the probability of angular changes in direction when a single scattering event occurs. Figure 2-1 graphically shows the Rayleigh phase function. In Rayleigh scattering, right angle changes in direction have approximately half the probability of occurring than forward and backscattering (i.e. scattering opposite to the direction of wave propagation).

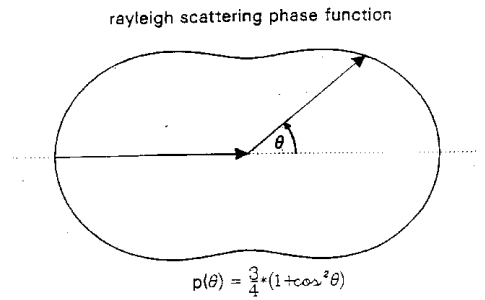


Figure 2-1 Polar coordinate representation of the Rayleigh phase function for a molecule located at the origin. The two arrows represent the directions of incoming and outgoing radiation. The probability of scattering in a certain angle ( $\theta$ ) is proportional to the length between the origin and the pseudo-elliptical peripheral line. Extracted from Morcrette (2002).

In general, whenever an electromagnetic wave encounters a particle, its direction will be changed to a certain angle according to a specific phase function that is dependent on the size of the particle.

The Mie scattering phase function describes the probability of direction changes with particles similar in size to the wavelength of radiation (Martin, 2014). Figure 2-2 illustrates the changes in phase function with particle size. Notice that Mie scattering is caused by larger particles, and is characterized by a predominant forward scattering (Thomas and Stamnes, 2002).

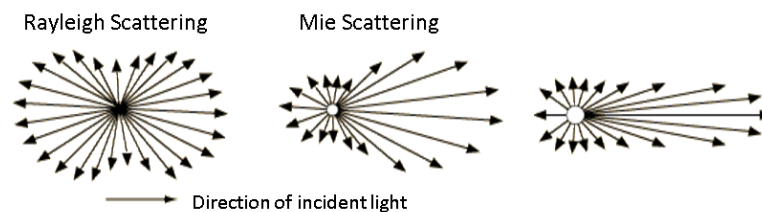


Figure 2-2 Diagrams describe the changes in phase function with increasing particle size. Particle size is indicated by circles of increasing size from left to right. Arrows represent the direction of scattered light. The length of each arrow represents the probability of scattering occurring in each direction. Modified from Nave (2012).

Mie scattering is relatively independent of wavelength; this is explained by the fact that, within larger particles, repeated events of reflection and refraction occur at numerous interfaces (Björn, 2007). In Mie-scattered radiation, the “blue” dominance of Rayleigh scattering becomes increasingly “white” with increasing particle size (Flammer et al., 2013). The types of particles that promote Mie scattering are larger particles such as aerosols, smoke, or dust. These particles are more abundant in the troposphere, and it is in this layer where most of the Mie scattering occurs. A consequence of this are the whitish colours observed in the sky, for example in hazy/polluted conditions.

In clouds, Mie scattering is also accompanied by what is known as non-selective scattering, which is produced by particles much larger than the electromagnetic radiation (Pidwirny, 2014). The characteristic white colour of a cloud is the result of Mie and non-selective scattering of the direct solar beam. Because of the intense scattering they render, clouds may have both attenuating and enhancing effects on ground-level solar radiation, depending on the properties of cloud cover and whether the sun is hidden or not (Parisi and Downs, 2004). Effects of clouds have not been included in the calculations presented here, yet, some of the methods used include the effects of clouds as obtained from real-time measurements.

The diffuse component of sky radiation is of great importance in studies of human exposure due to the large proportional amounts of UV radiation it contains. However, the behaviour of diffuse radiation in the UV range holds special features described below.

### **2.2.5 Diffuse radiation in the ultraviolet wavelengths**

The UV spectral range is mainly contained in the diffuse radiation received at ground level due to the strong Rayleigh scattering they are subject to. In the UV waveband, the diffuse component is reportedly at least 50% of the global irradiance (Grant et al., 1997). Moreover, with large solar zenith angles, virtually all UV radiation is diffuse.



Consequently, UV radiation reaching a ground observer may be strongly affected by horizon obstructions, due to the eventual obstruction of the direct solar beam and also the restricted sky-view; the latter leading to reduced amounts of received diffuse radiation. The assessment of ground-level UV radiation within obstructed sky-views therefore requires an evaluation of the visibility of both the direct beam and the fraction of obstructed/visible sky. For larger wavelengths (e.g. visible light), most of the incoming radiation at ground level comes increasingly in the direct solar beam and therefore the fraction of visible sky becomes less relevant.

Diffuse radiation in the UV-B range (roughly below 315 nm) is also susceptible to strong ozone absorption, showing patterns that may contradict the expected spectral proportions due to Rayleigh scattering alone: In a hypothetical atmosphere without ozone, UV wavelengths should be more easily scattered, therefore more abundant in the diffuse radiation. In the real atmosphere, due to ozone absorption, shorter wavelengths, in the far UV range (approximately  $< 305$  nm), tend to come at relatively lower quantities in the diffuse component (thus, at a relatively larger proportion in the direct beam); this pattern being more similar to that of longer (visible) wavelengths. To add complexity, said pattern in the diffuse UV-B is apparently dependent on the SZA: When the SZA is low ( $< 35^\circ$  approx.), short wavelengths behave as described above (being scarce in the diffuse component), but when the SZA is higher, the short wavelengths tend to come at larger relative quantities in the diffuse radiation (i.e. behaving again as expected by Rayleigh scattering). In this regard Gueymard opines: “...it appears that the depleting effect of ozone on the downward diffuse radiation does not follow Bouguer’s (Beer – Lambert) law” (Gueymard, 1995). Physical explanations of these patterns were not found in the reviewed literature, but they may be related to the optical path (air mass) of the direct beam after radiation has passed through the ozone layer. Possibly, at low SZAs (small air mass) and after having passed through the

ozone layer, the small quantities of UV-B radiation can be easily backscattered towards the absorbing ozone layer. Whereas at large SZAs (large air mass after passing through the ozone layer), the scattered radiation has greater probabilities of being directed towards the ground, instead of being backscattered to the ozone layer. Despite any possible explanation, these patterns have been empirically observed and included in state-of-the-art modelling techniques for radiative in the atmosphere (SMARTS, Gueymard, 1995). Please refer to Figure 6-1 (in Chapter 6) to see a scatter-plot showing the spectral proportions of diffuse radiation with respect to the global at different SZA.

Unlike the UV, the visible ranges of the solar spectrum (400 – 700 nm) are barely affected by ozone absorption or Rayleigh scattering. Yet, aerosols may have important scattering effects on the visible range of the solar beam. Aerosol scattering ( $T_{as\lambda}$ ) is a function of the aerosol single scattering albedo ( $W_0$ ), which, in turn, may be understood as the probability of one single particle to scatter incoming radiation (instead of absorbing it). Transmittance of the direct beam due to aerosol scattering may be calculated as:

$$T_{as\lambda} = \exp(-W_0 * A_{ot} * M), \quad (\text{Eq.2.6})$$

where  $W_0$  is the single scattering albedo,  $A_{ot}$  is the aerosol optical thickness and  $M$  is the air mass (Bird and Riordan, 1986).

Single scattering albedo  $W_0$  is a complex function of wavelength and relative humidity of the atmosphere. In the simple approach given in this thesis, an average value for shortwave radiation will be used ( $W_0 = 0.85$ ). Single scattering albedo values range from 0.6 to 0.9 in the shorter wavelengths (UV and visible).

The spectral dependency of aerosol optical thickness relies on the Ångström wavelength exponent  $\alpha$  (Masmoudi et al., 2003). It can be calculated by using Ångström's empirical expression:

$$A_{ot} = \beta \lambda^{-\alpha}, \quad (\text{Eq. 2.7})$$

where  $\lambda$  is the wavelength expressed in micrometres and  $\beta$  is the Ångström turbidity coefficient. The  $\beta$  coefficient may be measured empirically using the aerosol optical thickness at 500 nm ( $A_{ot0.5}$ ), and modified according to its definition (Gueymard, 1995):

$$\beta = \frac{A_{ot0.5}}{\ln(10)}. \quad (\text{Eq. 2.8})$$

Finally, in the works of Gueymard (1995), the constant  $\alpha$  has two different values for wavelengths greater or smaller than 0.5  $\mu\text{m}$ . However, during the course of this work, it was found that using two different values with our present calculations resulted in mismatching curves for the two sections (wavelengths greater or smaller than 0.5  $\mu\text{m}$ ). For this reason and for the specific purposes of this thesis, an average value of  $\alpha = 1.5$  was used for all wavelengths.

### 2.2.6 Vertical structure of the atmosphere

The density of the atmosphere decreases with height as a result of the exponential decrease of pressure in the upper layers of the atmosphere. The varying gas density in the atmosphere is relevant in radiative transfer since, according to Beer's Law, the attenuation of radiation through a medium depends on the concentration of absorbing/scattering species. The concentration of gas molecules and other attenuating particles in the atmosphere will decrease with height.

For practicality in describing these changes, the atmosphere above a ground-level observer is frequently characterized as a set of stratified plane-parallel layer, each one with specific physical and chemical properties. These theoretical models are often called one-dimensional models, since the vertical dimension is the only one considered for atmospheric variation. Apart from physical properties (temperature and pressure), each atmospheric layer

can also be characterised by the content of relevant atmospheric gases (water, ozone, nitrogen, carbon).

In general, radiative transfer algorithms use location and season dependent standard vertical profiles, describing the typical physical and chemical properties of each atmospheric layer for each specific time and place. In the following section (2.2.7), a brief introduction will be given to radiative transfer software and algorithms.

### **2.2.7 Radiative transfer software.**

Atmospheric radiative transfer can be calculated by using specialised software for solving radiative transfer equations. A radiative transfer equation is a mathematical expression that describes the attenuation of a monochromatic beam as a function of the transmittance properties of the atmosphere. Software for the calculation of radiative transfer equations is available, for example, LibRadTran (Mayer and Kylling, 2005) or SMARTS (Gueymard, 1995; Myers and Gueymard, 2004), representing state-of-the-art modelling techniques for the calculation of spectral irradiance. These software packages have been widely validated against measurements (Lohmann et al., 2006; Gueymard, 2008).

Although one-dimensional models are the most widespread choice for radiative transfer calculations, their main disadvantage is that they do not provide means for assessing three-dimensional sky obstructions. As pointed out by Hess and Koepke (2008), the unobstructed descriptions of radiation fail to describe the actual conditions of certain systems (e.g. solar radiation incident in street canyons).

Some advanced algorithms like MYSTIC (Mayer et al., 2010), allow Monte-Carlo tracking of independent photons, in a 3D complex atmosphere with topographic reflectors like mountains or buildings (Wagner et al., 2010; Weihs et al., 2012). Unfortunately, these algorithms have a high demand of computational power. A trade-off must therefore be considered between physical accuracy and computational performance. In this work, the

computationally-efficient one-dimensional algorithms have been favoured. Their outcomes will be combined with other techniques to evaluate the effects of horizon obstructions, by using fisheye images of urban canyons. These techniques will be thoroughly described in Chapters 3, 6 and 7.

The SMARTS algorithm has been used as a reference throughout this work for being user-friendly, free to access and comprising simplified algorithms that increase computing performance. In this section, some of its algorithms are presented to exemplify the basics of general radiative transfer models. In SMARTS, a set of parameterized transmittance functions are combined to obtain the attenuated direct beam irradiance from:

$$E(\lambda) = E_0(\lambda)Tr(\lambda)To(\lambda)Tmg(\lambda)Ttg(\lambda)Tw(\lambda)Ta(\lambda), \quad (\text{Eq. 2.9})$$

where  $E$  is the terrestrial spectral irradiance for a single wavelength ( $\lambda$ ),  $E_0$  is the extraterrestrial spectral irradiance. The factors in Eq. 2.9 are spectral transmittances for Rayleigh scattering ( $Tr$ ), ozone absorption ( $To$ ), mixed gases absorption ( $Tmg$ ), trace gases absorption ( $Ttg$ ), water absorption ( $Tw$ ), and aerosol extinction ( $Ta$ ).

Each one of the transmittances in Eq. 2.2 has the form of a parameterized exponential function, according to Table 2-1.

**Table 2-1 Transmission expressions developed for the SMARTS algorithm.  
Modified from Myers and Gueymard (2004).**

<b>Extinction Process</b>	<b>Transmittance Expression</b>
<b>Rayleigh scattering</b>	$Tr(\lambda) = \exp \{ (P/P_0) / [a_0(\lambda/\lambda_1)^4 + a_1(\lambda/\lambda_1) + a_2 + a_3(\lambda/\lambda_1)^{-2}] \}$
<b>Ozone absorption</b>	$To(\lambda) = \exp [ - m_0 u_0 A_0(\lambda) ]$
<b>Mixed gases absorption</b>	$Tmg(\lambda) = \exp [ - m_j u_j A_j(T, \lambda) ]$
<b>Trace gases absorption</b>	$Ttg_k(\lambda) = \exp [ - ( m_k u_k A_k(T, \lambda) ) ]$ .
<b>Water vapour absorption</b>	$Tw(\lambda) = \exp [ - (m_w u_w)^n B_w(u_w, \lambda) B_m(m_w, \lambda) B_p(P, \lambda) B_{mw}(m, u_w, \lambda) A(\lambda) ]$
<b>Aerosol extinction</b>	$Ta(\lambda) = \exp [ - m_a \beta_i (\lambda/\lambda_1)^{-\alpha_i} ]$

Expression parameters are;  $P$ : station pressure;  $P_0$ : standard pressure;  $T$ : temperature;  $a_i$ : fitting coefficients;  $m_x$ : optical mass correction for extinction process  $x$ ;  $u_y$ : abundance for absorber  $y$ ,  $A_z$ : absorption coefficient for absorber  $z$ ;  $B$ : water vapour band function or scaling factor;  $\alpha_i$  and  $\beta_i$ : Ångström parameters,  $i = 1$  for  $\lambda < 500$  nm,  $i = 2$  for  $\lambda \geq 500$  nm;  $\lambda_1$ : reference wavelength (1000 nm or 1  $\mu$ m)

By solving each individual transmittance equation from Table 2-1 and then solving Equation 2.9, the algorithm will return the attenuated beam for a specific atmospheric profile (specified by the user) and will also simulate its projection onto a flat horizontal surface. The same process is repeated for discrete wavelengths in a user-specified range. The spectral diffuse radiation is also calculated by SMARTS following the simplified algorithm proposed by Bird and Riordan (1986); this algorithm is based on the arithmetic complement expressions of atmospheric scattering transmittances (e.g. the arithmetic complement of the Rayleigh transmittance:  $[1 - Tr(\lambda)]$ ) and will be further described in Chapter 6.

Such simplified calculations of the diffuse component do not take into account the uneven (anisotropic) distribution of diffuse radiation across the sky vault. Under cloudless sky conditions, the intensity of the diffuse radiation changes across the sky, being greater in the

proximity of the solar disc. Representations of these anisotropic distributions are relevant, for example, in the evaluation of solar radiation loads on non-horizontal surfaces such as building walls (Steven and Unsworth, 1977; Rossini and Krenzinger, 2007) or to assess the effect of asymmetrically-oriented sky obstructions commonly found in urban canyons. The following section explains the basic concepts, measuring and modelling techniques to represent the anisotropic distribution of diffuse radiation.

### **2.2.8 The anisotropic distribution of diffuse radiation.**

According to Steven and Unsworth (1977), “...*the radiance of a point in the sky depends on its position relative to the sun and on its air mass*”. Since the direct solar beam is the initial source of all scattered radiation, most of the multi-scattering events occur near such source and the sky is, therefore, “brighter” nearer to the position of the solar disc. Additionally, the diffuse radiation also tends to increase towards the horizon of an observer at ground level, because the larger air mass contains more molecules on which scattering events may occur. To add complexity, the sky distribution of diffuse radiation is wavelength dependent because of Rayleigh scattering: Given that shorter wavelengths (e.g. UV or blue light) are strongly scattered, their distributions across the sky tend to be more isotropic than the distributions of larger wavelengths (e.g. red light or the infrared).

The angular distribution of the diffuse radiation can be modelled using LibRadTran (an example is given in Chapter 7). Also, parametric models exist that describe the sky radiation distributions (Steven and Unsworth, 1977; Hooper and Brunger, 1980; Igawa et al., 2004). Their main input variables are the position of the sun, air turbidity and a selection of zenith angles in the hemispheric sky-view. Air turbidity and gas concentrations may however become problematic as input variables for models, because they usually require specialised routine measurements. In order to simplify calculations, Steven and Unsworth (1977) proposed to use a normalized value of sky radiance measurements with respect to the

horizontal diffuse irradiance. They found that the standardized angular distributions were independent of atmospheric turbidity. In Chapter 7 a similar approach is followed for describing smooth relative values of sky radiance that are independent of atmospheric turbidity.

State-of-the-art modelling techniques are, unfortunately, time-consuming and limited to ideal conditions (i.e. cloudless skies). Measurements of the angular distributions, on the other hand, may prove to be easier and more efficient than current modelling algorithms. The most common way for measuring angular distributions has been by using direct input optics pointing towards several known angular coordinates of the sky vault. The term *sky scan* has been used to refer to this way of “sampling” the diffuse radiation to create interpolable grids (Rezaei-Ghaleh, 2003). Modern techniques of sky scanning may include automatic devices (sky-scanners) which can be programmed to repeat a sampling routine several times. However, some of these sky-scans have reported to take up to 40 minutes to complete the complete hemispheric view (Rezaei-Ghaleh, 2003). For broken-cloudy skies, such scanning times may not be convenient, considering the fast changes of sky conditions in 40 minutes. An alternative to sky-scans is the use of digital CCD *whole-sky cameras*, equipped with fisheye lenses.

The main advantage of using a fisheye whole-sky camera (or sky-camera) is that the entire hemispheric view can be captured at one single moment. In recent years, different types of cameras have been developed to analyse diffuse radiance distributions. Ranging from cameras that create monochromatic sky maps (Rossini and Krenzinger, 2007), luminance distributions with common digital RGB bands (Tohsing et al., 2013), others have specialised high dynamic ranges (fully capable of representing the intensities of the direct beam and the diffuse radiance (Stumpf et al., 2004)); or specifically designed to detect the small intensities in the UV range (Sabburg and Long, 2004). Digital colour sky-cameras can



be installed at observatories and programmed to capture whole-sky images at specific time-intervals, allowing the generation of real-time multi-band descriptions of the dynamic distribution of sky radiation throughout the day and the year. The main disadvantages of sky-cameras are, usually, their poor spectral resolution and the deformations of the fisheye lenses, when projecting a 3D hemispheric view onto a two dimensional image. Chapter 7 discusses these issues when using a low-cost digital sky-camera.

Variations of the solar radiation in direction, time and wavelength generate a variety of units—and measuring techniques—that allow descriptions for different purposes. Solar radiation units are based on the dissociation or integration of the different dimensions (i.e. space/direction, time and wavelength). Section 2.3 describes some basic units used throughout this thesis.

### **2.3 Units of solar radiation**

In this section, basic concepts and units are explained in context. Keywords are underlined to highlight the important concepts.

The concept of spectral radiance is a basic form of radiometry, from which the rest of the concepts and radiometric techniques used in this work can be constructed. Spectral radiance may be conceptualized as the amount of instantaneous optical power (Watts, W) of a single wavelength ( $\lambda$ , in nm), originated from a unit solid angle (in steradians, sr) of the upper-hemispheric view and received upon a ground-level surface unit ( $\text{m}^2$ ); the latter perpendicular to the direction of incoming radiation. Therefore the units of spectral radiance are  $\text{Wm}^{-2}\text{nm}^{-1}\text{sr}^{-1}$ .

Broadband radiance arises from integrating a range of wavelengths comprising a beam. Broadband radiance has the same spatial and temporal characteristics as described above (i.e.

instantaneous radiation coming from a solid angle upon a surface perpendicular to the direction of radiation). The units of broadband radiance are therefore  $\text{Wm}^{-2}\text{sr}^{-1}$ .

The angular coordinates of incoming radiance (either broadband or spectral) must also be defined: the zenith angle of radiation is defined as the angle formed between the zenith direction and the direction of incoming radiation, whereas the azimuth angle of radiation is defined as the angle formed between the geographic North and the horizontal direction of incoming radiation. The zenith and azimuth angles together uniquely define a position on the sky hemisphere from which the radiation originates. The magnitude of radiance varies with changing zenith and azimuth angles. Under cloudless conditions, a radiance measurement may coincide with the angular coordinates of the solar disc and will therefore become a measurement of direct solar radiance. Radiance measurements may capture, however, another solid angle of the sky-view, thus becoming a sky radiance measurement. Sky radiance values may describe for example the anti-solar region (i.e. the region opposite to the sun) or a section of the circumsolar region (i.e. any solid angle in the proximity of the solar disc). The integration over the spatial dimension (direction of incoming radiation) introduces a new concept: Irradiance represents the spatially integrated optical power received from the entire upper-hemispheric view onto a (ground) surface. The irradiated surface is usually flat and parallel to the Earth's surface at the observer's location (i.e. a horizontal plane). Irradiance may also be measured as spectral irradiance or as broadband irradiance (spectrally integrated) over a determined wavelength range, with units  $\text{Wm}^{-2}\text{nm}^{-1}$  and  $\text{Wm}^{-2}$  respectively. In this work, we will use the term total-shortwave irradiance to refer to a spectrally-integrated broadband measurement of irradiance, ranging from the UV to the near infrared from the entire upper-hemispheric view, as measured by a pyranometer (for more information on pyranometers see Chapter 3, Section 3.3.3).

Finally, the term global irradiance represents of the sum of the direct beam and diffuse irradiances. Global irradiance upon a flat horizontal surface is a standard description of solar radiation received at the ground. An independent analysis of its two components (direct and diffuse) is needed when calculating global irradiance within an obstructed sky-view (detailed descriptions of these methods are described in Chapters 4, 6 and 7). In the following section (2.5), a brief review is given of previous studies on irradiance within urban canyons.

#### **2.4 Studies of solar irradiance in urban canyons.**

The term “urban canyon” is often used in urban climatology to refer to locations at street-level surrounded by buildings. The urban canyon is a geometric abstraction that illustrates how the basic geometries regulate the access to solar radiation (Strømmandersen and Sattrup, 2011). Current methods for describing urban canyons in atmospheric models require expensive 3D mapping of cities or user-made photographic descriptions of single locations which are not cost effective, especially when there is a need for models of large cities. In recent years some interest has arisen in the use of street photographs as a basis for the creation of radiative transfer models (Coubard et al., 2011; Hämmerle et al., 2011), the advantage of such methods is the high resolution descriptions of urban geometries. The main meteorological effect of the urban canyon is the obstruction of both the direct and diffuse irradiances. The parameterization of urban geometries as affecting the sky radiation is a key step in models of the urban atmosphere.

In this regard, another useful concept is that of the sky view factor (SVF). The SVF is a dimensionless measurement of the fraction of sky that is visible at an individual geographical point. The term is rather recent, the oldest article found to mention the term was from Bergen (1971), in which the author describes the effects of topography (described as the SVF) and sky nocturnal radiation on temperature in a conifer canopy.

The extent of visible sky in a particular location is a relevant feature affecting the local weather and climate, besides affecting the incoming amounts of solar radiation. Some research works discuss the relevance of describing the SVF as a useful parameter in climatic and meteorological models for the urban environment (Hämmerle et al., 2011; Matzarakis and Matuschek, 2011; Ooka et al., 2011; Wong et al., 2011). The SVF has been recognized as a useful parameter for modelling local air temperature in urban canyons. For example, a study by Svensson (2004) reported a correlation between SVF and night-time air temperature: during day-time, a positive correlation between air temperature and SVF would be expected, due to the increased exposure to solar radiation. By contrast, night-time air temperature can be increased by the long-wave radiation losses from building walls being trapped in the canyon. In this case, smaller SVFs are related to tighter urban geometries. Yet, the relationship between urban SVF and local air-temperature is affected by other variables. Although reporting a "*strong*" correlation between these two variables ( $R^2 = 0.78$  in "*dense canyons*"), Svensson also makes reference to other studies that did not find significant correlations between air temperature and the SVF. Other parameters like air movement may have significant effect on the correlation. The same author explains that, when including "*less dense*" urban locations into the correlation analyses, the  $R^2$  values decrease from 0.78 to 0.57. Thus indicating that, for some situations, the SVF factor alone becomes a less reliable predictor of air temperatures. Still, the overall conclusion in Svensson's study is that the SVF is a potentially useful parameter, partially explaining night-time air temperature in urban canyons. As stated by Oke (1982): "*...at night, the low rates of radiative emission are largely a consequence of the reduced sky view factor inside the canyon*". Thus, SVF maps of large areas may also be useful for modelling night-time energy exchanges.

High resolution city maps of the SVF are expected to become a basic instrument for urban meteorological and climate models in the coming years (Yasumoto et al., 2011), but at

present are not available. Large spatial variations of the SVF are expected within small areas, given the small differences in the building geometry from one city block to the next. Architectonic variations will cause important alterations to sections of visible sky. These geographical models may become the basis of further urban climatic and meteorological models.

Current interest is also focused on calculating solar irradiance in an individual urban canyon, as the basic landscape unit of urban meteorological models (Oke 1988). In the following sections, previous studies are described that assess the effects of buildings on incident solar radiation in individual urban canyons. Studies have been divided into empirical observations and theoretical models.

#### **2.4.1 Empirical studies of solar radiation in urban canyons**

Field studies comprise direct measurements of solar radiation within a specific urban canyon. For example, in Podstawczynska and Pawlak (2003) UV and total solar radiation were measured in urban canyons with different orientations (north-south and east-west) and insulation regimes at different times (i.e. sunlit and shadowed walls). Measurements were compared against a meteorological station with a full-sky view. They reported not only an attenuation of total solar energy due to obstructions, but also a change in the spectral signature of shadowed periods of time (with larger relative proportions of UV radiation). These large relative amounts of UV are related to Rayleigh scattering in the atmosphere, resulting in proportionally less UV affected by the obstruction of the direct beam. An intermediate kind of study, in-between empirical observations and laboratory experiments, is exemplified by Aida (1982) that simulated urban canyons by assembling and dismantling concrete building blocks. Their experiments returned an increment in radiation absorption of 20% of an irregular structure compared against a flat surface. Some other experimental scaled models have been carried out by to assess the reflection effect of vertical metal walls (Turner

and Parisi, 2009). In chapters 6 and 7 experiments are described that used simulated obstructions to compare experimental measurements against the calculations of urban canyon spectral irradiances.

#### **2.4.2 Theoretical models of solar radiation in urban canyons**

So far, mathematical and computer-based methods for modelling the urban troposphere require large amounts of information about the urban canopy geometry that is not easy to acquire. Terjung and Louie (1973) modelled the patterns of absorbed solar radiation using a 3D digital city model which consisted in a grid system covering streets and buildings. For every cell in the system, a SVF was calculated and then related to the absorptive capacities of buildings. In Oke (1988) the main input parameters are: i) the aspect ratio (i.e. the ratio between the average height of the canyon and the canyon width), and ii) the building density (i.e. the plan or roof area of the average building and the ground area occupied by each building), finally, the compass orientation of the canyon is needed to relate to obstructions of the solar path across the sky. In another example, Kondo et al. (2001) used a model for urban configuration assuming buildings of regular or irregular size, but arranged in a regular lattice with roads running either north-south or east-west direction, within the urban canopy. However this regular configuration would be difficult to find in many cities, reducing the utility of such theoretical models. Some recent models are based on remote sensing techniques of the 3D structure of cities. LIDAR technology has been used as an airborne sensor that can measure high resolution patterns of buildings' heights (Yu et al., 2009).

A number of research works have combined GIS software, 3D city models, and solar radiation models for different purposes in urban areas. Lindberg and Grimmond (2011) describe a method to simulate radiation fluxes in urban settings. Lagouarde et al. (2010) used a city model to simulate infrared thermal radiation. Hofierka and Kanuk (2009) proposed the creation of a 3D city model, based on DEM models, for evaluating the potential photovoltaic

usage of solar energy. However, the information needed can only be obtained from original blueprints of buildings or from airborne scanners; it is therefore not readily available for most researchers or cities.

### **2.4.3 Descriptions of urban geometries**

There are two main techniques to describe and parameterize urban geometries, namely, digital elevation models (DEMs) and fisheye photographs. Both represent advantages and disadvantages of their own.

DEMs of a region or city are grid maps in which every pixel contains the height of the obstruction/building that corresponds to that location. DEMs allow the rapid mapping of calculated local irradiance for large areas. However, their main disadvantages consist of very limited availability (especially for cities due to the high costs of acquiring building height information) and low spatial resolution regarding the variability of buildings' heights. Low resolution DEMs that provide a pixel averaged height may lead to large inaccuracies, even for the calculation of mountain shading effects in large areas; as reported by Weihs et al. (2012) "*...it was found that the DEM resolution may change the altitude at some locations by up to 500 m, resulting in changes in the sky obscured by the horizon of up to 15 %*". Street canyons represented with DEMs would therefore require a very high spatial resolution to obtain accurate calculations of street irradiance.

As an alternative, fisheye photographs are polar projections of the upper-hemispheric view usually taken manually with the use of special lenses attached to digital cameras. A comparison of the performance of DEMs and fisheye photographs can be found in Hämmerle et al. (2011). Fisheye images provide an accurate representation of the urban geometry allowing more accurate calculations of the street-level solar irradiance. On the disadvantages, because fisheye photographs are usually taken manually, large amounts of field work would

be required to represent large cities. Fortunately, the Google Street View image database provides a means for accessing street-level imagery. Chapter 4 describes methods for projecting the Google images as fisheye representations of urban canyons. Additionally, fisheye images of sky obstructions were taken manually in Chapters 4, 6 and 7. The present thesis focused on the use of fisheye photographs to calculate urban canyon irradiances.

Some software applications are available, such as the RayMan model (Matzarakis et al., 2010) and SOLWEIG (Lindberg et al., 2008), that allow the description and parameterization of urban geometries and their effects on incident solar radiation.

In order to parameterize horizon obstructions, fisheye projections are divided in parallels and meridians; where the largest parallel (equator) corresponds to the  $360^\circ$  horizon line. The rest of the parallels run concentric from the horizon towards the zenith and define elevation/zenith angles. Meridians, in turn, define azimuth angles or bearing directions (e.g. north, east, south or west). Figure 2-3 illustrates the polar plane projection of a hemisphere. Concentric circumferences and straight lines represent parallels and meridians, respectively. The centre of the projection corresponds to the zenith of the hemisphere, under which is the observer.



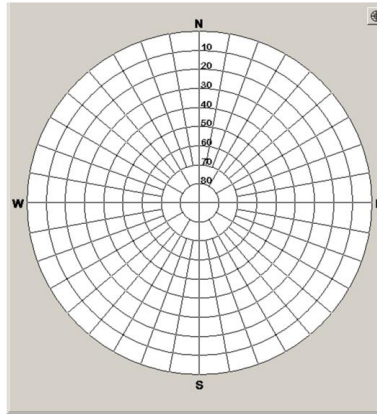


Figure 2-3 Example of a “fisheye” equidistant projection of a hemisphere (fisheye projection); Parallels (circles) and meridians (straight lines) of a hemisphere, are represented in this plane projection. Source: RayMan Model software v 1.2.

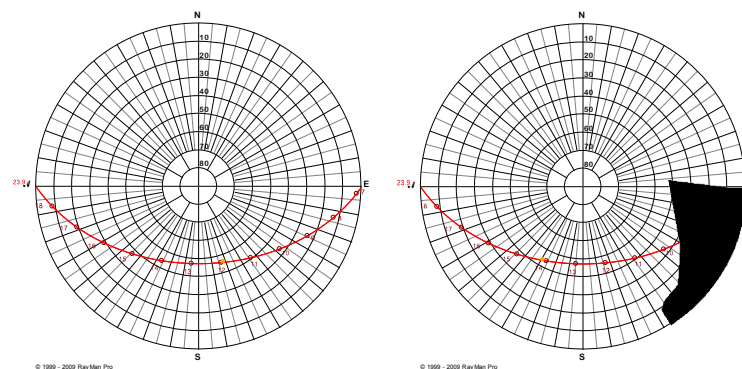


Figure 2-4 Equidistant “fisheye” projections of the upper-hemispheric sky-view and the solar path; Left panel: full-sky view. Right panel: example of an obstructed view (with an arbitrary obstruction). Both images include an overlaid grid of azimuth and elevation angles, along with an example solar path across the sky. Source: RayMan Model software v 1.2.

The total area of the polar projection in Figure 2-4 (left panel) corresponds to a SVF of 1 (full sky-view). The SVF of a street canyon (Figure 2-4, right panel) may be calculated by subtracting the area of obscured cells. However, fisheye projections introduce distortions to the actual size of objects in the image and therefore require some geometrical corrections to estimate the proportion of obstructed sky in a street canyon.

Steyn (1980) proposed a method to estimate the SVF from fisheye photographs; and this method was included in the RayMan Model software (Matzarakis et al., 2010). Steyn's method considers that in an equidistant fisheye projection solid angles will be projected onto a larger area as they approach the horizon line. The geometrical corrections consist of dividing the polar projection into several concentric annuli, each representing a set of solid angles with the same elevation. The actual SVF can be approximated by independently calculating a SVF for each annulus. Then the SVF at each annulus would be weighted as a cosine function of their zenith angle. Also notice from Figure 2-4 that, if the solar path is known for a particular location (represented by a red line), the visibility of the direct solar beam can also be evaluated for each specific urban canyon (see the obstructions exerted to the solar path on left panel in Figure 2-4). The fisheye projections from Figures 2-3 and 2-4 are useful representations of the upper-hemispheric view of the sky and any horizon obstructions. These representations will be used in this thesis for describing urban geometries and assessing the shading effect of buildings within specific urban canyons.

Moreover, fisheye projections of horizon obstructions, in combination with fisheye images of the unobstructed sky, can be used to evaluate the effects of horizon obstructions on the anisotropic diffuse radiation. Under cloudless conditions, a building blocking the bright circumsolar region (next to the direct beam) has a larger shading effect than when blocking the duller anti-solar region (opposite to the direct beam). Although an obvious statement, these effects are not always included in common models of urban canyon irradiance. For practicality, some models of urban canyon irradiance (e.g. Matzarakis et al., 2010) consider the diffuse component to be isotropic (i.e. having the same intensity from any direction in the hemispheric view). Under this assumption, the diffuse irradiance coming from any section of unobstructed sky will only be proportional to the size of the section and not to its relative position. Although this assumption may be unrealistic under cloudless skies, considering an

isotropic diffuse component results in simple and fast calculations. Some of the algorithms proposed in this work assume an isotropic diffuse component (Chapters 4 and 6) and evaluate some of the errors arising from such assumption. Still, the information on the distribution of diffuse radiation is necessary, as the anisotropy may contribute to differences between canyons of different orientations. Because of this, in Chapter 7 a method is proposed to approximate the anisotropy of diffuse radiation from whole-sky fisheye photographs, as well as its effects on the radiation incident within urban canyons.

## Summary of Chapter 2

In this chapter, basic concepts and units of solar radiation studies have been described. A general overview has also been given for modelling solar radiation at ground level and its interactions with the Earth's atmosphere. Main concepts and background studies of radiation within urban canyons have been addressed. In the following chapter (Ch. 3), general materials and methods will be presented that describe the software tools used for the modelling process, as well as the devices used for obtaining comparison measurements.

## References

- Aida, M. (1982). Urban albedo as a function of the urban structure—a model experiment. *Boundary-layer meteorology*, 23(4), 405-413.
- Beer, A. (1852). Bestimmung der Absorption des rothen Lichts in farbigen Flüssigkeiten. *Annalen der Physik und Chemie*, 86, 78-88.
- Bergen, J. D. (1972). Topographic effects apparent in nocturnal temperature profiles in a conifer canopy. *Agricultural Meteorology*, 9, 39-50.
- Bird, R. E., and Riordan, C. (1986). Simple solar spectral model for direct and diffuse irradiance on horizontal and tilted planes at the earth's surface for cloudless atmospheres. *Journal of Climate and Applied Meteorology*, 25(1), 87-97.
- Björn, L. O. (2008). *Photobiology*. Springer, Sweden.
- Bohren, C. F., and Clothiaux, E. E. (2006). *Fundamentals of atmospheric radiation: an introduction with 400 problems*. John Wiley and Sons.
- Celarié E, Hollandsworth S (2003) Radiation and the Atmosphere. In: Todaro RM (ed) *Stratospheric Ozone an Electronic Textbook*. Center for Coastal Physical Oceanography at Old Dominion University.
- Coubard, F., Brédif, M., Paparoditis, N., and Briottet, X. (2011). Reflectance estimation from urban terrestrial images: Validation of a symbolic ray-tracing method on synthetic data. *International Archives of the Photogrammetry, Remote Sensing and Spatial Information Sciences*, 38, 3..

- Drusch, M., and Crewell, S. (2005). Principles of radiative transfer. Encyclopedia of hydrological sciences.
- Flammer, J., Mozaffarieh, M., and Bebie, H. (2013). The Interaction Between Light and Matter. In Basic Sciences in Ophthalmology (pp. 21-39). Springer Berlin Heidelberg.
- Grant, R. H., Heisler, G. M., and Gao, W. (1997). Ultraviolet sky radiance distributions of translucent overcast skies. *Theoretical and Applied climatology*, 58(3-4), 129-139.
- Gueymard, C. (1995). SMARTS2: a simple model of the atmospheric radiative transfer of sunshine: algorithms and performance assessment. Cocoa, FL: Florida Solar Energy Center.
- Gueymard, C. A. (2008). Prediction and validation of cloudless shortwave solar spectra incident on horizontal, tilted, or tracking surfaces. *Solar Energy*, 82(3), 260-271.
- Gupta, S. C. (2012). Textbook on optical fiber communication and its applications. PHI Learning Pvt. Ltd.
- Hämmerle, M., Gál, T., Unger, J., and Matzarakis, A. (2011). Comparison of models calculating the sky view factor used for urban climate investigations. *Theoretical and applied climatology*, 105(3-4), 521-527.
- Hess, M., and Koepke, P. (2008). Modelling UV irradiances on arbitrarily oriented surfaces: effects of sky obstructions. *Atmospheric Chemistry and Physics*, 8(13), 3583-3591.
- Hobbie, R. K., and Roth, B. J. (2007). *Intermediate physics for medicine and biology*. Springer Science and Business Media.
- Hofierka, J., and Kaňuk, J. (2009). Assessment of photovoltaic potential in urban areas using open-source solar radiation tools. *Renewable Energy*, 34(10), 2206-2214.
- Hooper, F. C., and Brunger, A. P. (1980). A model for the angular distribution of sky radiance. *Journal of Solar Energy Engineering*, 102(3), 196-202.
- Igawa, N., Koga, Y., Matsuzawa, T., and Nakamura, H. (2004). Models of sky radiance distribution and sky luminance distribution. *Solar Energy*, 77(2), 137-157.
- Lagouarde, J. P., Hénon, A., Kurz, B., Moreau, P., Irvine, M., Voogt, J., and Mestayer, P. (2010). Modelling daytime thermal infrared directional anisotropy over Toulouse city centre. *Remote Sensing of Environment*, 114(1), 87-105.
- Lambert, J. H. (1892). *Photometria sive de mensura et gradibus luminis colorum et umbrae* (Augsburg, 1760). German translation by E. Anding (Leipzig, Verlag von Wilhelm Engelmann, 1892).
- Lindberg, F., Holmer, B., and Thorsson, S. (2008). SOLWEIG 1.0—Modelling spatial variations of 3D radiant fluxes and mean radiant temperature in complex urban settings. *International journal of biometeorology*, 52(7), 697-713.
- Lohmann, S., Schillings, C., Mayer, B., and Meyer, R. (2006). Long-term variability of solar direct and global radiation derived from ISCCP data and comparison with reanalysis data. *Solar Energy*, 80(11), 1390-1401.
- Malicet, J., Daumont, D., Charbonnier, J., Parisse, C., Chakir, A., and Brion, J. (1995). Ozone UV spectroscopy. II. Absorption cross-sections and temperature dependence. *Journal of atmospheric chemistry*, 21(3), 263-273.
- Martin, S. (2014). *An introduction to ocean remote sensing*. Cambridge University Press.
- Masmoudi, M., Chaabane, M., Medhioub, K., and Elleuch, F. (2003). Variability of aerosol optical thickness and atmospheric turbidity in Tunisia. *Atmospheric research*, 66(3), 175-188.
- Matzarakis, A., and Matuschek, O. (2011). Sky View Factor as a parameter in applied climatology—Rapid estimation by the SkyHelios Model. *Meteorologische Zeitschrift*, 20(1), 39-45.

- Matzarakis, A., Rutz, F., and Mayer, H. (2010). Modelling radiation fluxes in simple and complex environments: basics of the RayMan model. *International Journal of Biometeorology*, 54(2), 131-139.
- Mayer, B. A., and Kylling, A. (2005). Technical note: The libRadtran software package for radiative transfer calculations-description and examples of use. *Atmospheric Chemistry and Physics*, 5(7), 1855-1877.
- Mayer, B., Hoch, S. W., and Whiteman, C. D. (2010). Validating the MYSTIC three-dimensional radiative transfer model with observations from the complex topography of Arizona's Meteor Crater. *Atmospheric Chemistry and Physics*, 10(18), 8685-8696.
- Molina, L. T., and Molina, M. J. (1986). Absolute absorption cross sections of ozone in the 185-to 350-nm wavelength range. *Journal of Geophysical Research: Atmospheres* (1984–2012), 91(D13), 14501-14508.
- Morcette, J. J. (2000). Radiation Transfer, Meteorological Training Course Lecture Series. Meteorological Training Course Lecture Series, ECMWF, Reading UK.
- Myers, D. R., and Gueymard, C. A. (2004, November). Description and availability of the SMARTS spectral model for photovoltaic applications. In *Optical Science and Technology, the SPIE 49th Annual Meeting* (pp. 56-67). International Society for Optics and Photonics.
- Nave, R. (2012). Mie Scattering. Retrieved November 7, 2014, from Hyperphysics <http://hyperphysics.phy-astr.gsu.edu/hbase/atmos/blusky.html#c3>
- Oke, T. R. (1982). The energetic basis of the urban heat island. *Quarterly Journal of the Royal Meteorological Society*, 108(455), 1-24.
- Oke, T. R. (1988). Street design and urban canopy layer climate. *Energy and buildings*, 11(1), 103-113.
- Ooka, R., Sato, T., Harayama, K., Murakami, S., and Kawamoto, Y. (2011). Thermal energy balance analysis of the Tokyo Metropolitan area using a mesoscale meteorological model incorporating an urban canopy model. *Boundary-layer meteorology*, 138(1), 77-97.
- Parisi, A. V., and Downs, N. (2004). Variation of the enhanced biologically damaging solar UV due to clouds. *Photochemical and Photobiological Sciences*, 3(7), 643-647.
- Pidwirny, M. (2014). Chapter 5: Atmospheric Structure and Radiation Transfer. In *Understanding Physical Geography*. British Columbia, Canada: Our Planet Earth Publishing.
- Podstawczynska, A., and Pawlak, W. (2003, September). Daily course of ultraviolet and total solar radiation in an urban canyon—Lodz case study. In *Proceedings of the 5th International Conference on Urban Climate*, Łódź, Poland (pp. 1-5).
- Rayleigh, Lord. (1871). On the light from the sky: *Philosophical Magazine*, v. 41, p. 107; also *ibid* (1945). *Theory of sound*, 2nd ed.: New York, Dover Publications, Inc. p. 274,447.
- Rezaei-Ghaleh A (2003) *Ultraviolet Spectral Radiance Distribution under Cloudy Skies* (Doctoral dissertation). University of Manchester, UK.
- Rossini, E. G., and Krenzinger, A. (2007). Maps of sky relative radiance and luminance distributions acquired with a monochromatic CCD camera. *Solar Energy*, 81(11), 1323-1332.
- Ryer, A. (1998). *Light measurement handbook*. Massachusetts: International Light, Inc.
- Sabburg, J. M., and Long, C. N. (2004). Improved sky imaging for studies of enhanced UV irradiance. *Atmospheric Chemistry and Physics*, 4(11/12), 2543-2552.
- Schoenberg, E. (1922). *Photométrie der Gestirne* (pp. 831-986). Vieweg+ Teubner Verlag.
- Seeds, M., and Backman, D. (2009). *Astronomy: the solar system and beyond*. Cengage Learning.
- Siegel, R., and Howell, J. R. (1992). *Thermal radiation heat transfer*. National Aeronautics and Space Administration, Cleveland, OH (United States). Lewis Research Center.

- Steven, M. D., and Unsworth, M. H. (1977). Standard distributions of clear sky radiance. *Quarterly Journal of the Royal Meteorological Society*, 103(437), 457-465.
- Steyn DG (1980) The calculation of view factors from fisheye-lens photographs: Research note. *Atmosphere-Ocean* 18:254–258.
- Strømmand-Andersen, J., and Sattrup, P. A. (2011). The urban canyon and building energy use: Urban density versus daylight and passive solar gains. *Energy and Buildings*, 43(8).
- Stumpf, J., Tchou, C., Jones, A., Hawkins, T., Wenger, A., and Debevec, P. (2004, November). Direct HDR capture of the sun and sky. In *Proceedings of the 3rd international conference on Computer graphics, virtual reality, visualisation and interaction in Africa* (pp. 145-149). ACM.
- Svensson, M. K. (2004). Sky view factor analysis—implications for urban air temperature differences. *Meteorological applications*, 11(03), 201-211.
- Terjung, W. H., and LOUIE, S. S. (1973). Solar radiation and urban heat islands. *Annals of the Association of American Geographers*, 63(2), 181-207.
- Thomas, G. E., and Stamnes, K. (2002). *Radiative transfer in the atmosphere and ocean*. Cambridge University Press.
- Tohsing, K., Schrempf, M., Riechelmann, S., Schilke, H., and Seckmeyer, G. (2013). Measuring high-resolution sky luminance distributions with a CCD camera. *Applied optics*, 52(8), 1564-1573.
- Turner, J., and Parisi, A. V. (2009). Measuring the influence of UV reflection from vertical metal surfaces on humans. *Photochemical and Photobiological Sciences*, 8(1), 62-69.
- Turro, N. J., Ramamurthy, V., and Scaiano, J. C. (2009). *Principles of molecular photochemistry: an introduction*. University science books. USA
- Wagner, J. E., Angelini, F., Arola, A., Blumthaler, M., Fitzka, M., Gobbi, G. P., and Weihs, P. (2010). Comparison of surface UV irradiance in mountainous regions derived from satellite observations and model calculations with ground-based measurements. *Meteorologische Zeitschrift*, 19(5), 481-490.
- Weihs, P., Wagner, J. E., Schreier, S. F., Rieder, H. E., Angelini, F., Blumthaler, M., and Webb, A. R. (2012). The influence of the spatial resolution of topographic input data on the accuracy of 3-D UV actinic flux and irradiance calculations. *Atmospheric Chemistry and Physics*, 12(5), 2297-2312.
- Webb, A. R. (1998). *UVB instrumentation and applications*. CRC Press.
- Wong, N. H., Jusuf, S. K., Syafii, N. I., Chen, Y., Hajadi, N., Sathyanarayanan, H., and Manickavasagam, Y. V. (2011). Evaluation of the impact of the surrounding urban morphology on building energy consumption. *Solar Energy*, 85(1), 57-71.
- Yasumoto, S., Jones, A., Yano, K., and Nakaya, T. (2012). Virtual city models for assessing environmental equity of access to sunlight: a case study of Kyoto, Japan. *International Journal of Geographical Information Science*, 26(1), 1-13.
- Yu, B., Liu, H., Wu, J., and Lin, W. M. (2009). Investigating impacts of urban morphology on spatio-temporal variations of solar radiation with airborne LIDAR data and a solar flux model: a case study of downtown Houston. *International Journal of Remote Sensing*, 30(17), 4359-4385.

## **Chapter 3**

### **Materials and Methods**

General software tools and instrumentation for solar radiation measurements will be described in this chapter.

### 3.1 General method for calculating canyon irradiance

This work proposes the combination of several software tools that help in the calculation of solar irradiance at the street level. Figure 3-1 shows the general flow chart of the proposed method including the different data types used, the software tools required for their processing, and the instruments used for data gathering and model validation. A main objective was to develop methodologies that could be easily applied without any special facilities and at low cost. Therefore, all software tools run in a Windows environment and were chosen for their free availability and user-friendly interfaces.

Firstly, a set of Google Street View images must be available for the required location, covering the full upper-hemispheric view. Secondly, a 180° “fisheye” projection of the upper hemisphere is reconstructed from the set of Street View images. In the third step, images from Google Street View should be classified to discern horizon obstructions from sky. Next, the reconstructed and classified fisheye image of the canyon is used to calculate the corresponding SVF. Additionally, the path of the sun for a specific day is superimposed to assess the times of the day at which the solar disc is visible/obstructed. Finally, solar irradiance can be calculated for specific moments of the day, considering the visibility of the sun and the SVF, if the unobstructed irradiance is known. These first steps, which combine freely available images and software, with results and validations are described in more depth in Chapter 4.



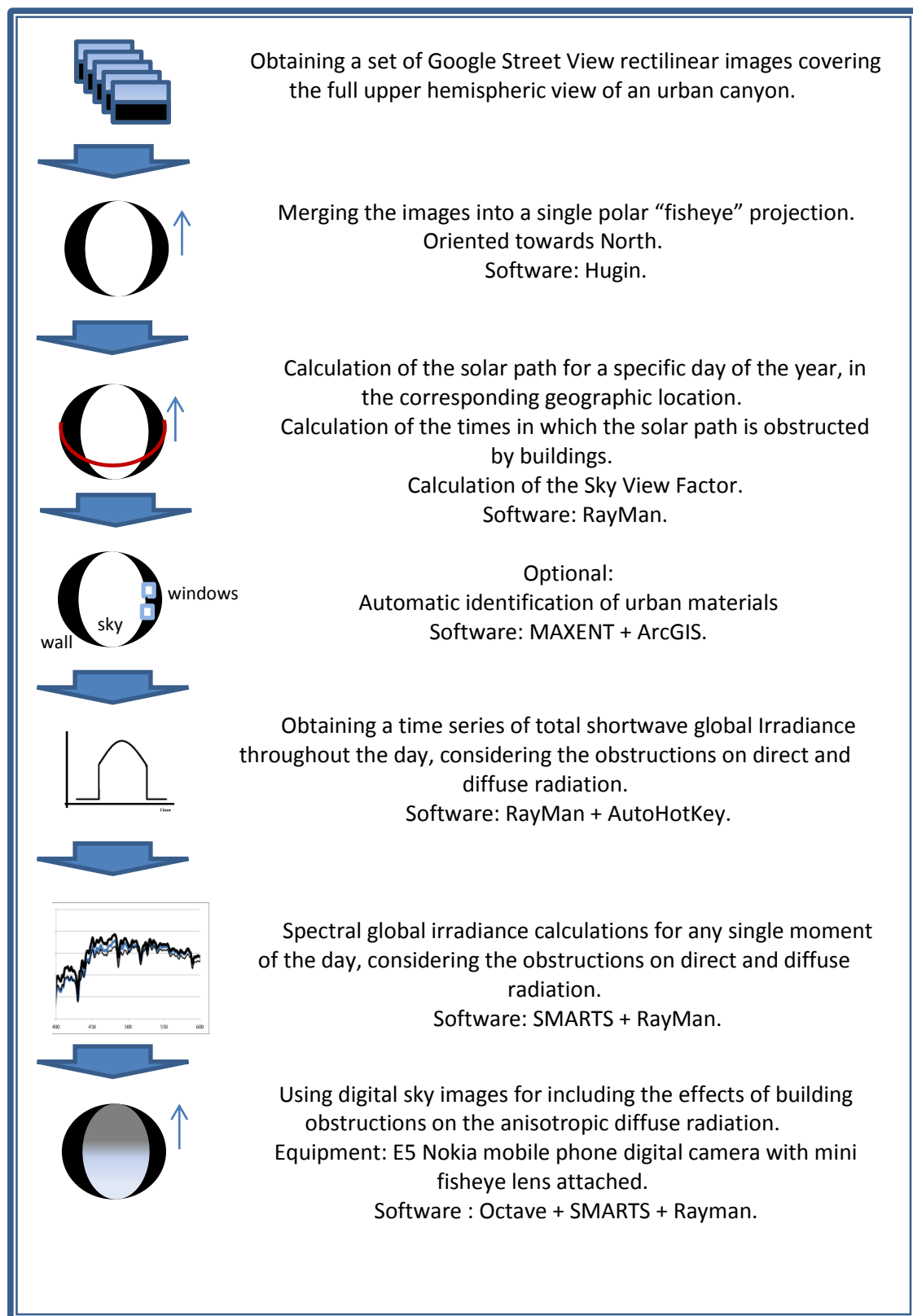


Figure 3-1 Diagrammatic representation of the general method for calculating total-shortwave and spectral irradiances, at any given urban canyon within the Google Street View coverage.

The subsequent step in the flow chart (marked as “Optional” in Figure 3-1) still requires further development, but takes advantage of colour images in the Google Street View database. This multi-band (RGB) information potentially allows the automatic identification of sky/building sections in the panoramic images. To make such process automatic will be a key step in extending these algorithms to cover large cities, through the analysis of individual street canyons. However, since these algorithms require further improvement, the identification has been performed manually elsewhere, when illustrating other steps in the software chain.

In addition, RGB information may be of use when modelling multi-reflections from diverse materials within a canyon, that may—in some situations—lead to large increases in the incoming radiation for specific periods of the day. Chapter 5 also describes a potential processing method for identifying different reflecting materials. Once again, the methods for material identification are mentioned as a potential aid for future work, but have not been included in the following steps. Nor has the reflected radiation been included into calculations, as it will require further development of the methods and more complex calculations.

The first steps of the chart would only allow calculations of total-shortwave irradiance (i.e. an integrated spectrum), but not spectral calculations. To create spectral models, a spectral irradiance measurement under a full-sky view is necessary (it can also be calculated for cloudless conditions with a radiative transfer model, such as SMARTS). Then, the SVF and the visibility of the solar disc can be evaluated using RayMan. However, the spectrally changing proportions of diffuse and direct (hence the spectrally varying effects of obstructions) cannot be assessed with RayMan. A method is therefore proposed (in Chapter 6) to calculate the spectral partitioning of global irradiance into its direct and diffuse

components. Two simplified models (based on SMARTS) are described, which calculate the spectral proportions of diffuse irradiance to global irradiance (i.e. the diffuse-to-global ratio, DGR). The final step in Fig. 3-1 refers to other small corrections associated to the anisotropic distribution of diffuse irradiance and its interactions with canyons with different orientations or SVFs (Chapter 7). The anisotropic angular distribution of diffuse irradiance is approximated from whole-sky fisheye images, using a simple algorithm written in the Octave language (equivalent to MatLab).

By following the entire flow chart in Figure 3.1, it is then possible to calculate total and spectral global irradiance under a clear (cloudless) sky within any specific urban canyon. The basic input data are a Google Street View panorama and a full sky-view measurement of global irradiance. The possibilities for calculations of canyon irradiances under all-sky conditions (provided real-time measurements are available under an unobstructed sky-view) are also considered. Empirical validations are provided for each model stage in the corresponding chapters (4, 6 and 7).

The following section (Section 3.2) describes software tools used in the modelling process. Then, Section 3.3 will describe the instruments used for obtaining empirical measurements of irradiance under full and obstructed views.

## **3.2 Materials: Software tools.**

### **3.2.1 Google Street View.**

The availability of free access geospatial information has increased substantially in the last few years. In 2007, the development of Google Street View (Anguelov et al., 2010) established an unprecedented stage for high resolution online geospatial data (Rousselet et al., 2013). Google Street View provides 360° panoramic street-level images within cities and

roads around the world. Panoramas are obtained by data-collection vehicles equipped with a system of cameras that cover a quasi-spherical view around the vehicle. The system comprises 15 cameras with CMOS as image sensors (i.e. complementary metal-oxide semiconductors) and a resolution of 5-megapixels (Anguelov et al., 2010).

Single-shot panoramas are taken every 7 – 8 m along the track of the data-collecting vehicles, resulting in a very high-resolution grid of panoramas along the streets and roads of large cities and main highways of cities in North America, Europe and Australia. This research work proposes to use these images as the basis for calculating solar global irradiance within urban canyons. Under the assumption that all Google Street View panoramas are taken at the same standard height of 2.5 meters above the ground level (Mazerolle and Blaney, 2011), the database provides a reliable standard (with constant parameters) for comparison between canyons.

Finally, Google Street View images do not only provide high resolution grids of panoramas but also high quality colour images of the landscape at each location. This kind of information provides a means of describing the urban geometries with unique levels of detail. This feature contrasts with other tools used in solar radiation studies (e.g. digital elevation models of cities).

### **3.2.2 The Hugin software for panoramic reconstructions**

The software tool Hugin (d'Angelo, 2007; German et al., 2007) was originally designed as an open source “panorama stitcher” in use by general photographers for the creation of panoramic photographs. However, the software offers certain advanced features that are of great utility for the purposes of this work. Hugin supports digital photographs in common formats (e.g. \*.jpg images). A wide variety of lenses are supported, as well as several output

projections such as the orthographic or equidistant polar projections. Further discussions of their relevance are given in the instrumentation section (Section 3.3). Finally, the software provides a comprehensive visual interface which allows for the manual positioning of photographs on a simulated upper-hemispheric view from the camera's position. Additionally, these settings can be saved so that the positioning of similar panoramas becomes a semi-automatic task. Since one of the future objectives of this work will be the automatic generation of projected urban geometries, these tools will be a useful aid towards such objectives.

The fact that images from Google are independent and rectilinear opens the possibility of reconstructing different projections (using Hugin) for different purposes. For example, the sky view of a flat horizontal surface may be reconstructed (through an orthographic projection) to simulate the view of a standard global radiometer. Alternatively, an equidistant projection may be closer to representing the view of a spherical surface, which in turn, may be used as a rough approximation of the human body (Dahlback and Moan, 1990; Matzarakis et al., 2010).

### **3.2.3 The RayMan Model Software.**

The RayMan Model 2.1 is a Windows-based software by Matzarakis et al. (2010). It is primarily designed to calculate thermal radiant fluxes and other variables related to human thermal comfort. However, the program also allows the calculation of global, direct and diffuse irradiance for a flat horizontal surface, as well as the SVF and direct sunlight obstructions for any single minute of the day, and any day of the year, given a hemispheric projection of the obstacles at a given location. Therefore, the RayMan model may also be a useful tool for general meteorological applications. Because of its recent release thorough validations of the RayMan software are still required. The following section describes

comparisons of the software's performance against total-shortwave global irradiance measurements at the Whitworth Observatory at the University of Manchester.

To calculate total-shortwave irradiance, the program requires as input data: geographic longitude and latitude, altitude, day of the year, and time of the day. The program automatically considers monthly variations of the atmospheric turbidity (higher in summer than during winter months) and monthly variations of the solar constant (higher for winter months in the Northern Hemisphere). According to Matzarakis the program calculates global irradiance ( $G_0$ ) based on the equation (Eq.3.1) by Jendritzky et al. (1990) (in Matzarakis et al., 2010).

$$G_0 = 0.84 E_0 * \cos(Z) * \exp\left(-0.27 \cdot \frac{P}{P_0} \cdot \frac{T_L}{\cos(Z)}\right), \quad (\text{Eq. 3.1})$$

where  $E_0$  is the solar constant,  $Z$  is the Zenith angle,  $\frac{P}{P_0}$  is the relative local atmospheric pressure,  $T_L$  is the Linke turbidity factor\*. The complete exponential term in Eq. 3.1 may be understood as proportional to the atmospheric transmittance.

\* The Linke turbidity factor can be defined as the number of Rayleigh atmospheres (i.e. a hypothetical atmosphere without aerosols or water vapour) needed to produce the observed attenuation of the direct beam. (López and Batlles, 2004)

The performance of the RayMan model has been tested here in calculating the global total-shortwave irradiance under a full sky-view, for the city of Manchester. In order to obtain comparison measurements, the database of the University of Manchester was browsed in search of clear days. A total of 8 clear days were found (from December 2010 to October 2011) which represent the seasonal variations of daily irradiance in the city of Manchester. The list of days and the season they represent is shown in Table 3-1.

**Table 3-1 Clear or partially clear days throughout the year used to validate modelled global irradiance.**

<b>08-Dec-10</b>	Winter
<b>08-Mar-11</b>	Early spring
<b>08-Apr-11</b>	Spring
<b>01-May-11</b>	Late spring
<b>03-Jun-11</b>	Early summer
<b>04-Jul-11</b>	Summer
<b>29-Sep-11</b>	Early autumn
<b>22-Oct-11</b>	Autumn

Tests consisted of a comparison between calculated global irradiance and those measured on the days shown in Table 3-1. The default standard conditions were chosen as atmospheric parameters in the RayMan software (Temperature: 20°C, Relative humidity: 50%). A simple macro routine written with AutoHotkey allowed the RayMan software to be run several times, incrementing by one minute on each run. This routine was performed to calculate global irradiance for every minute of the day, for all the days shown in Table 3-1; at the geographic coordinates: 53°28'N, 1°14'W. Other input parameters were the SVF of 1.0, the timezone as UTC + 0.00, and a cloud cover of 0 octas. Models have been compared against measured data as can be seen in Figure 3.2

In Figure 3-2 calculated total-shortwave global irradiance for every minute of the day is shown for 8 clear days, along with corresponding measurements taken at the Whitworth observatory, University of Manchester. Models, in general, follow the shape of the measured irradiance during each day. In the following set of plots (Figure 3-3), discrepancies between modelled and measured irradiance are plotted for the same days shown in Table 3-1. Discrepancies have been measured as the proportional error (i.e. the ratio of the difference between modelled and measured, to observed irradiance). In Figure 3-3 some large discrepancies arise from clouds blocking the direct beam while the model assumed a

cloudless sky. Proportional discrepancies are also large at sunrise and sunset although their absolute values are small.

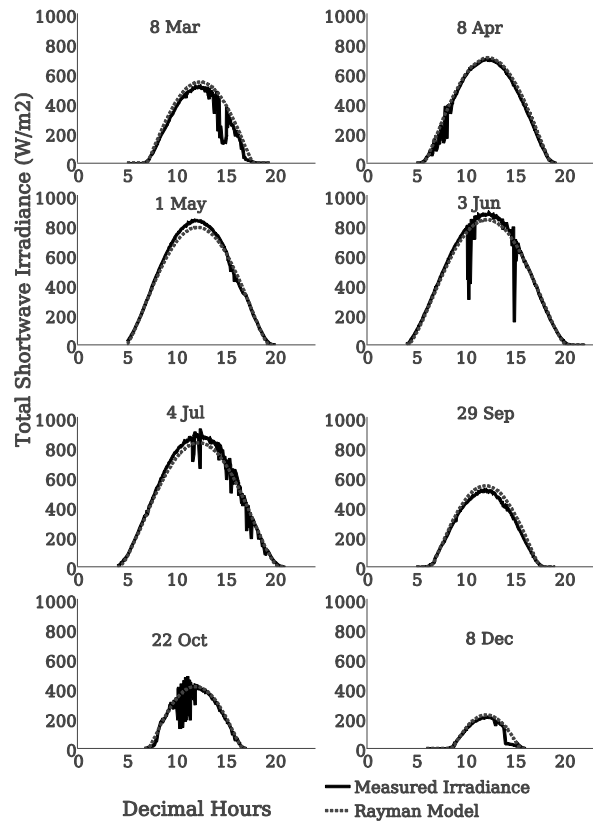


Figure 3-2 Comparison of calculated total-shortwave global irradiance (grey dotted lines) versus measured irradiance as measured by a pyranometer (black lines). Measurements were obtained with a CM5 Pyranometer installed at the Pariser Building roof, University of Manchester.



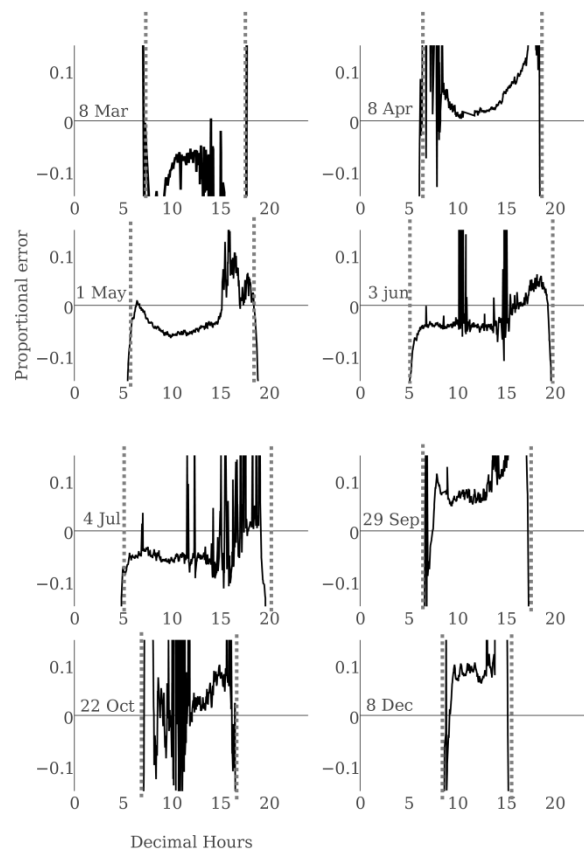


Figure 3-3 Proportional errors for 8 days (same as those in Table 3-1), showing relative discrepancies between modelled and measured global irradiance throughout the day. Sunrise and sunset times are marked with grey dotted lines.

The following figure (Fig. 3-4) shows selected examples of extended clear-sky periods of the day, from plots in Figure 3-3 in more detail. The selected plots show how the modelling error during clear-sky periods is generally below or near 0.1 (i.e. 10%).

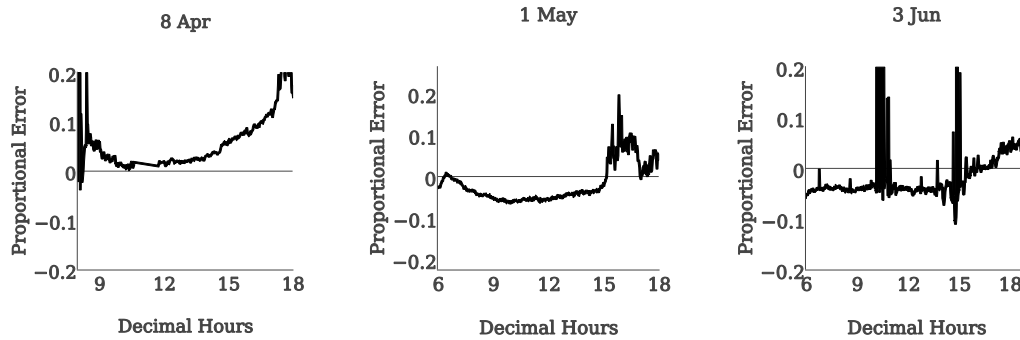


Figure 3-4 Selected examples from Figure 3-3, showing modelling discrepancies for distinguishable clear-sky periods. The time range (x-axis) also excludes the sunrise/set hours, at least for May and June.

Discrepancies (measured as proportional errors) during clear sky periods are below or near 0.1 (i.e. 10%). Thus, the RayMan calculations for total-shortwave irradiance have been considered as acceptable approximations of global irradiance in Manchester, under standard urban atmospheric conditions. In Figures 3-3 and 3-4 periods of wide fluctuations correspond to the effect of broken clouds which are not included in the calculations. Finally, errors in the daily figures may seem exaggerated towards sunrise and sunset times since proportional errors for smaller quantities can appear large even if small in absolute terms. In the following figure (Figure 3-5), an example of absolute irradiance error (in  $\text{Wm}^{-2}$ ) is given for 8 April. Notice that the absolute error is relatively flat and small throughout the day (without considering the effects of clouds), including near-sunrise/sunset times. The model used standard atmospheric inputs rather than location and time specific descriptions of the state of the atmosphere, so offsets between measurement and model (which can vary from day to day) can be a result of local conditions.

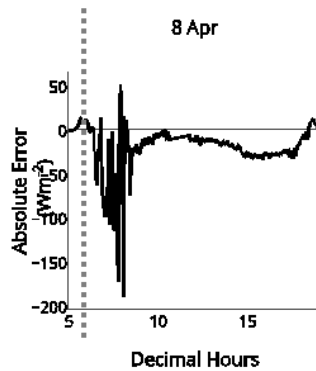


Figure 3-5 Absolute error (in  $\text{Wm}^{-2}$ ) of the modelled total-shortwave global irradiances for April 8 2011. Sunrise and sunset times are marked with grey dotted lines.

Additionally, some discrepancies at sunrise/sunset may arise from horizon obstructions, of the direct solar beam at the measuring site, rather than modelling errors. Notice in Figure 3-2 that for 8 December 2011 solar irradiance at sunset shows the typical pattern of a building obstruction.

The offset of modelled irradiances can be mainly attributed to inconsistencies between the input atmospheric parameters against the actual atmospheric conditions. Aerosol and water contents may affect total-shortwave irradiance at ground level, but the calculations shown in Figure 3-2 were performed using the default values of the RayMan software. Atmospheric turbidity, however, could be greater or smaller than the default values, thus leading to miscalculations of irradiance. Unfortunately, measurements of Linke turbidity were unavailable, but the discrepancies arising from these sources of uncertainty are within the 0.1 proportional errors (or 10%) for clear-sky periods and can be considered small.

In order to rule out measurement uncertainties when validating the model, the pyranometer outputs were cross-checked against a reference pyranometer installed at the Whitworth Observatory in Manchester. The latter is a relatively new pyranometer (installed in 2010), and its calibration is traceable to the World Radiometric Reference (WRR) at the

World Radiation Centre (WRC) in Davos, Switzerland. The irradiance measurements of both instruments agree throughout the day, with their output signals showing a constant ratio throughout the day. This fact indicates that there are no clear instrumental issues, such as temperature or solar zenith angle dependency. Further descriptions of these instruments are given in Section 3.3.3.

The RayMan model software will be used throughout this thesis, firstly to evaluate the visibility of the solar disc and the SVF, using fisheye images of specific canyons. Additionally, in Chapter 4, the RayMan model has been used to calculate street-level total-shortwave irradiances in specific urban geometries. Calculations using the RayMan model software were performed for cloudless sky conditions. Although the software allows the calculation for overcast and partially clouded skies, these tools were not used in the present work.

The goodness of fit of the RayMan model under partially cloudy conditions remains to be assessed, but in general, such parameterized models cannot account for the complex fluctuations in ground irradiance values due to clouds. Cloud movement across the sky cannot be easily predicted and may create complex patterns of reduced and enhanced irradiance values. Observed irradiance during broken-cloud skies (Figure 3-6) shows that maximum irradiance may be even larger than that expected under a clear sky.

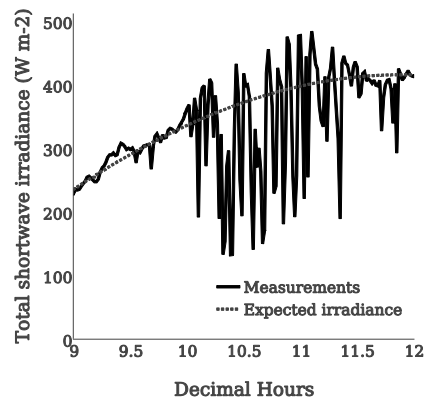


Figure 3-6 Modelled clear-sky (grey-dotted line) versus measured (black line) total-shortwave irradiance under broken-cloud sky conditions.

Enhancements of solar radiation at ground level during broken-cloud periods are well studied. A broken-cloud cover of 7 octas may enhance total irradiance up to 33% over the expected irradiance when the sun is not obstructed (Cede et al., 2002). Due to the difficulties of modelling clouds, the present work will describe a method for calculating relative canyon irradiance values as a fraction to those received under a full-sky view. If these relative fractions are combined with actual observatory measurements, then, the actual canyon irradiance may be more realistically estimated, by including the measured fluctuations due to the effect of clouds under a full sky-view.

Measuring the effect of clouds on ground irradiance is a relatively simple task, if a global radiometer is set to measure global irradiance continuously under an unobstructed view. For the purposes of this work the concept of relative canyon irradiance will be defined, as the ratio between irradiance under a partially obstructed sky view (such as a street canyon) against irradiance under a full-sky view, both taken at the same time or averaged for the same minute (Eq. 3.2).

$$\text{Relative canyon irradiance} = \frac{\text{Global irradiance under obstructed sky view}}{\text{Global irradiance under full-sky view}}. \quad (\text{Eq. 3.2})$$

The relative canyon irradiance is a dimensionless quantity that can be equally applied to either broadband or spectral irradiances. It is a function of the sky view factor and the visibility of the solar disc due to horizon obstructions in the canyon. Chapter 4 shows how this concept is modelled under cloudless skies, while Chapters 6 and 7 use this same concept for clear-sky canyon spectral irradiance.

Equation 3.2 may be extended to all sky conditions only when the direct beam is not obstructed by buildings and any fluctuations of the direct solar beam due to clouds will cancel out in Equation 3.2. When the solar disc is not obstructed, the relative canyon irradiance will remain approximately constant regardless of clouds. However, when the direct solar beam is obstructed by a building, the relative canyon irradiance may vary greatly depending on whether it is obstructed or not by clouds. Such conditions are not addressed in the body of the thesis, but are considered in Chapter 8 under examples of future developments.

All the models used in this work follow two assumptions made by the RayMan model: i) Multiple reflections within the urban canyon are neglected and ii) The diffuse component is assumed to be isotropic at all times. These assumptions have been made for simplicity of calculations. The validity of assuming an isotropic diffuse irradiance is specifically addressed in Chapters 6 and 7, whereas the potential effects of reflections from walls remained unstudied in the present work.

Finally, the RayMan model does not allow calculations of spectral irradiance. Instead, a well-validated radiative transfer model (SMARTS) has been used for that purpose, in combination with the tools provided by the RayMan software. The basics of the algorithm have already been outlined as an example of radiative transfer software in Section 2.2.8 and

will be further explained in Chapter 6. In the following section (Sec. 3.2.4), a brief summary of SMARTS is given for completeness.

### 3.2.4 SMARTS

The “Simple Model for Atmospheric Transmission of Sunshine” (SMARTS) was developed by Myers and Gueymard (2004), and has been used as a reference for terrestrial spectra by the American Society for Testing and Materials (ASTM). The model is based on parameterizations of transmittance and absorption functions for atmospheric constituents in well-defined standard atmospheres (e.g. the United States Standard Atmosphere, USSA). The SMARTS software offers 10 default reference atmospheres that consist of vertical profiles at 0,1,2,3 and 4 kilometres of temperature, pressure and concentration of the main atmospheric gases. After the user has selected a reference atmosphere and provided information about the angular position of the sun (either as azimuth and elevation angles or as geographical location and times of the day and the year), the SMARTS algorithm solves a radiative transfer equation for the different extinction processes that occur in the atmosphere.

According to the authors, the SMARTS model provides spectral irradiance values that are comparable to other well validated models like MODTRAN, but with “*far simpler inputs*”. Amongst other advantages of using SMARTS is the Microsoft Excel user interface (smarts.xls), developed by The National Renewable Energy Laboratory (NREL). The package can be downloaded at: [http://www.nrel.gov/rredc/smarts/smarts\\_files.html](http://www.nrel.gov/rredc/smarts/smarts_files.html).

One limitation of the model is that it was designed for clear sky days only. Therefore, it cannot generate data for broken clouds or overcast conditions in the sky (Kudish and Evseev, 2012). Additionally, SMARTS belongs to the family of one-dimensional models which do

not allow for horizontal variations in the atmosphere, therefore it cannot account for horizon obstructions.

In this thesis, the SMARTS algorithm was used as a reference model to validate two compressed models of the ratio of diffuse-to-global spectral irradiance (DGR) that are proposed in Chapter 6. Also, for the consideration of diffuse sky anisotropy in chapter 7 the DGR was calculated using SMARTS. The models (described in Chapter 6) include further simplifications of Rayleigh, ozone transmittance and the effective-to-standard ozone transmittance equations used by the SMARTS algorithm. The simplifications proposed in this work are described in Chapter 6 and its corresponding supplementary information document (annexed at the end of Chapter 6 in the same form as it was submitted to the *Theoretical and Applied Climatology* journal).

Thus far, the software tools used in this thesis have been described. The following section will describe the instrumentation used to measure irradiance and validate the models and also as a reference for translating relative modelled values into absolute irradiance values.

### **3.3 Materials: Instrumentation for solar radiation measurements.**

In general, radiometric devices transform radiant energy into instantaneous electrical currents or voltages, which, depending on the instrument, might be integrated over very short periods of time (< 100 ms) and then are frequently averaged in sets to return readings every minute, or every five minutes, for example. The intensity of electrical currents is recorded onto a data logging system and afterwards transformed with specific calibrating factors, to obtain radiation intensity values.

According to Webb (1998), the basic components of any radiometer are therefore: i) input optics, ii) sensors and iii) a data logging system. Input optics is the component exposed to natural radiation, with a suitable geometry specific to the radiation unit of interest. The



sensors are conducting or semi-conducting materials that transform radiant energy into electric currents. Finally, the data logging system refers to a computational system that allows the recording and the mathematical transformations of the output electrical information.

Additional pointing devices, diffusers, filters, or light diffracting systems may be used to suit the radiometric unit of interest. Some of these accessories will be described in the following sections. Different radiation concepts require different techniques for their measurement. In the following sections, specialised techniques and devices will be described for radiance (Sec. 3.3.1), irradiance (Sec. 3.3.2), broadband (Sec. 3.3.3) and spectral measurements (Sec. 3.3.4). Finally, Section 3.3.5 describes fisheye lenses for capturing whole-sky images.

### **3.3.1 Radiance measurements**

Radiance entails direct input optics with a known field of view (i.e. the extent of the solid angle from which the detector accepts radiation). Interchangeable direct input optics for radiance measurements usually come in the form of a hollow metallic tube with an aperture for light entrance on one end and a light guide (fibre optics) attached to the opposite end. The measured solid angle will be proportional to the radius of the entrance aperture of the input optics, and inversely proportional to the distance between the aperture and the sensor or light guide. Multi-reflection processes inside the hollow tube may, however, become a source of stray light, so baffles and/or optical lens systems can be used to reduce these effects. Another important aspect in radiance measurements is the directional pointing mechanism: Sky-scanners are mechanical devices that automatically rotate the direct input optics in azimuth and elevation angles. The precision required for these types of instrument must be very high if its objective is to measure direct radiance from the solar disc which subtends an angle of only about  $0.5^\circ$  at the surface: slight errors in the pointing mechanisms may result in the misalignment from the solar disc. When diffuse sky radiance is being measured, directional

precision becomes less important. In Chapter 7 an automatic sky-scanner was used to exemplify—empirically—the relationship between diffuse sky radiance from a small solid angle and a corresponding global irradiance measurement.

### 3.3.2 Irradiance measurements

Irradiance measurements, in turn, require an integrated surface exposed to a  $2\pi$  field of view. This might be achieved by using either an integrating sphere or a cosine response diffuser. The ideal flat and horizontal surface (i.e. the common reference surface for irradiance measurements) will show a varying response (output signal) to incident radiation from different elevation angles ( $\theta$ ); the response ( $s$ ) being proportional to the cosine of  $\theta$ . This ideal response is known as the cosine response:

$$s = s_0 \cos(\theta),$$

where  $s_0$  is the maximum response when  $\theta$  equals  $0^\circ$ .

However, the ideal response of a flat surface may not be completely achieved by the input optics. According to Myers (1997), imperfections in the fabrication of such devices (e.g. inhomogeneous variations in surface absorption and reflectance), will result in deviations from the theoretical response. For example, Gröbner et al. (2012) mentioned that state-of-the-art Teflon diffusers produce uncertainties in solar UV irradiance of  $\pm 2.5\%$ . They also reported a temperature dependency with marked changes of up to 3% at  $19^\circ\text{C}$ . In a similar way, the response of an ideal irradiance radiometer should be independent of the azimuth angle of radiation sources (i.e. its angular orientation with respect to North), although, irregularities in the Teflon surface may also cause different responses with changes in the rotation position of the input optics. It is therefore very important both to know any nonconformity with respect to the ideal behaviour, and also to maintain measuring devices, and their parts, in a static position.

An additional complication arises from the shape of irradiated surfaces. The concept of irradiance usually refers to radiation received upon a flat surface, but, the irradiated surface may have a different shape, for example, a spherical surface. The main difference between irradiance on these two surfaces is that the latter, as a whole, does not have a cosine response to radiation sources (Webb et al., 2002). Although spherical surfaces were not studied in this work, some models use the spherical shape as a simplification of the human body (Dahlback and Moan, 1990; Matzarakis et al., 2010) and it may be an important issue to consider in future developments of this work.

The general characteristics of radiance or irradiance measurements are applicable to both broadband and spectral measurements. The following sections describe general aspects of measuring devices for obtaining broadband (Sec. 3.3.3) and spectral (Sec. 3.3.4) data, as well as the technical details of the devices used in this work.

### **3.3.3 Broadband measurements: Pyranometers**

Pyranometers are designed to obtain integrated measurements of the total-shortwave radiation spectrum from the entire upper-hemispheric sky-view (i.e. total-shortwave global irradiance). They typically integrate a spectrum extending from 300 to 2800 nm, ideally with a constant response throughout. The thermoelectric effect is the basic functional principle of pyranometers: metallic materials generate small electrical currents, proportional to an increase in temperature due to solar irradiation (Lee, 2015). However, the sensitivity of a pyranometer is also dependent on the environment temperature. Thus, other components are needed (e.g. protective glass domes, shade plates), that permit the thermal isolation of the detector while allowing transmittance of solar energy, and protect the reference body of the instrument from direct solar radiation. A desiccator is also used to prevent dew formation on the inner side of the domes. State-of-the-art pyranometers can return instantaneous readings,

allowing for real-time descriptions of the fluctuations of total-shortwave irradiance throughout the day (including the effects of clouds).

The data returned by any radiometer will only be as reliable as its calibration. Radiometric calibration is the mathematical transformation of output current signals or voltages into units of radiation (e.g. radiance or irradiance). The most common calibration technique for pyranometers consists of inter-comparisons between instruments, with the sun as the radiation source. The World Meteorological Organization (WMO) recommends an outdoor comparison against a reference pyranometer at the same location. Standardization of pyranometers is in accordance to the ISO 9060 standard, adopted by the WMO (Kipp & Zonen, 2013). Calibration is usually relative to the World Radiometric Reference (WRR) in Davos, Switzerland.

Total-shortwave global irradiance measurements have been taken with two CM5 Kipp & Zonen pyranometers. Both pyranometers have a  $2\pi$  field of view and were levelled with respect to the horizontal to measure global irradiance from the upper-hemispheric view of the sky (as received upon a flat horizontal surface). In the literature, the total measurement uncertainty with CM5 pyranometers has been estimated as approximately 5% (Myers et al., 1989).

The first pyranometer from which data was taken is temperature stabilized with a calibration traceable to the World Radiation Centre in Davos, Switzerland. It is installed at the Whitworth Observatory, University of Manchester for routine daily measurements of total-shortwave irradiance (one measurement every 5 minutes). The Whitworth observatory is on a rooftop (approx. 45 m above ground level), with a SVF of approximately 1. Readings from this pyranometer were provided by the staff of the Whitworth Observatory as reference for full sky-view total-shortwave irradiance over the city of Manchester.

The second pyranometer is usually installed at the rooftop of the Pariser Building, University of Manchester, (< 1 km away from the Whitworth Observatory), as part of the monitoring station devices of the UV group at the Centre for Atmospheric Sciences. This second pyranometer has been cross-calibrated against the Whitworth pyranometer. The fact that no clear deviations have been observed between the two instruments (i.e. there is a constant ratio between the two outputs) suggests a general stability of both pyranometers with changing SZA and temperature. The second pyranometer was taken to a local street canyon to measure canyon irradiances, which could be compared against the Whitworth pyranometer data (more details are given in Chapter 4).

### **3.3.4 Spectroradiometry**

Unlike broadband radiometry, in spectroradiometric measurements a spectral diffraction of the input radiation is required to obtain—ideally—an independent reading for each discrete wavelength (often at intervals of 1.0 or 0.5 nm). The general process of spectroradiometry consists of collecting electromagnetic radiation by using input optics with a specific field of view, then guiding the light (with fibre optics) into a monochromator system, which, in turn, will diffract radiation into its spectral components and, finally, to measure the intensity of each separate wavelength (Webb, 1998).

The monochromator is the functional basis of any spectrometer. It comprises a diffraction grating, sometimes in combination with a set of mirrors that optimize the separation of a beam of light into its spectral components. Diffraction gratings are reflective or translucent materials with a periodic micro-structure of slits or grooves. This periodic structure produces a multi-slit interference effect on electromagnetic waves (i.e. when passing through the grating, each point of the wave front becomes a new point source).

The spatially split wavelength components are then projected onto a detector or an array of detectors. In this regard, spectrometers usually follow one of two designs: i) array spectrometers, which have a static diffraction grating and a linear array of detectors to capture a range of wavelengths at once; and ii) scanning spectrometers, which have a rotating diffraction grating and a single detector to obtain a single measurement at a time. In this work, only array spectrometers have been used because of the need for fast measurements. The main advantage of array spectrometers is that they allow full spectral measurements to be obtained in milliseconds. Still, they have some drawbacks, mainly related to low efficiency at shorter wavelengths, high levels of stray light from adjacent wavelengths (because of the usage of single, instead of double monochromators) and smaller dynamic ranges, in comparison to their scanning counterparts.

Once the diffracted spectral radiation has been measured by the sensors, the corresponding output electrical currents must be calibrated to be expressed as irradiance or radiance values. For array spectrometers, calibration techniques should be able to identify two main aspects: i) the position of each diffracted wavelength on the detector array (wavelength calibration) and ii) the radiation intensity values corresponding to the electric output of each pixel in the array (intensity calibration) (Carruthers and Dymond, 1999; Yoshizawa, 2009); described below.

i) Wavelength calibration is achieved by using a low-pressure pencil mercury lamp for UV wavelengths and a Neon pencil lamp for longer visible wavelengths. Those pixels in the detector array that return a local maximum electric output after exposure can be identified. The sub-pixel wavelength peak (i.e. a hypothetical pixel with the highest intensity) was determined for each mercury/neon peak wavelength, by using a centroid method (Eq. 3.3).

$$\bar{p} = \frac{\sum I_i p_i}{\sum I_i}, \quad (\text{Eq. 3.3})$$

where  $\bar{p}$  is the resulting centroid sub-pixel,  $I_i$  is the intensity of each pixels in the neighbourhood of a peak.  $p_i$  is the pixel number. (Personal communication by Dr. Andrew Smedley)

After the sub-pixel wavelength peaks have been determined, each pixel was assigned a corresponding wavelength through a cubic polynomial interpolation as a function of pixel number. Once each pixel is correlated to a corresponding wavelength, the output current can be translated into units of radiation.

ii) Intensity calibration consists of using a standard lamp with a known spectral intensity output. Standard lamps are usually certified by a national standards laboratory (for example, the National Institute of Standards and Technology USA (NIST) or the National Physical Laboratory, UK). Lamps are accompanied by a file of the known spectral radiation curve of their emitted spectrum. Output current values are then linearly related to their corresponding spectral irradiance values. To minimize errors when measuring the known intensity spectrum, strict laboratory conditions must be maintained, matching the conditions specified in the lamp certificate. The position and orientation of the lamp, the distance between the lamp and the input optics (0.500 m,  $\pm$  0.001 m), the input current to the lamp (8.000 amps,  $\pm$  0.01% ) and room temperature (20 °C).

Finally, the response to changes in intensity is assumed to be linear. The response of the METCON device to intensity changes was determined to be close to linear (< 1%) in an inter-comparison at the WRC, Davos (personal communication by Dr Andrew Smedley).

Global irradiance spectral measurements were taken with the METCON diode array installed at the rooftop of the Pariser Building, University of Manchester, for routine global

spectral measurements. The system (including the global input optics, fibre optics and the spectrometer) has been calibrated at the Centre for Atmospheric Sciences, and undergoes regular international inter-comparisons at the World Radiation Center in Davos, Switzerland. The METCON device is a dual-channel single-monochromator spectrometer, each with a 512 pixels array, and a wavelength range from 280 to 700 nm. The spectral resolution (full-width-half-maximum of the slit function) is approximately 2.2 nm. Spectrometers were wavelength calibrated against mercury and neon lamps; and intensity calibrated against 1000W NIST lamps. A 200W field calibration unit is used for checking the calibration during monitoring and campaigns. Field checks were conducted every few weeks, and before and after moving the instruments.

The global input optics of the METCON device consists of a Schreder Teflon diffuser. Schreder diffusers are generally considered to return good cosine responses for UV wavelengths (Manninen et al., 2006). The cosine response at four quadrants of the Schreder diffuser was assessed in the laboratory by Dr. Richard Kift. The integrated cosine error  $\langle f_2 \rangle$  has been calculated from Dr. Kift's data, following Schreder et al. (1998)

$$\langle f_2 \rangle = \int_0^{70^\circ} |f_2(\theta)| \cdot \sin(2\theta) d\theta,$$

where  $\theta$  is the zenith angle of the source, The weighting term  $\sin(2\theta)$  is equal to  $[2 \cdot \cos(\theta) \cdot \sin(\theta)]$ , and it accounts for the fact that errors at larger zenith angles are usually high, but they contribute less to global irradiance. Finally,  $f_2(\theta)$  is the cosine error.

$$f_2(\theta) = \left[ \frac{S(\theta, \varphi)}{S(\theta, \varphi) \cdot \cos(\theta)} \right] \cdot 100\%,$$

where  $S$  is the average spectral signal at  $\theta$  and  $\varphi$  zenith and azimuth angles.



The calculated  $\langle f_2 \rangle$  for four quadrants (Q1 to Q4) of the Schreder diffuser was respectively: 1.28%, 0.78%, 1.8%, and 1.7%. With these small errors it is possible to say that the global input optics has an acceptable cosine response.

The calibrated data required further processing, to account for dark current and stray light. Dark current was accounted for by measuring a datum dark current at the appropriate integration time and under temperature-stabilised conditions, which was then subtracted from each raw solar spectrum.

Additionally, a stray light correction was applied to the calibrated data. The term stray light refers to background radiation contributing to an instrument's signal. Stray light originates from internal scattering in the instrument, due to imperfections in the grating or other optical components (Brown et al., 2003). An ideal detector would return an electrical output entirely corresponding to a discrete wavelength, but in practice, the output response of detectors contains a large contribution from the central wavelength along with a sum of small contributions from adjacent wavelengths.

The method for stray light correction used at the Centre for Atmospheric Sciences at the University of Manchester follows that proposed by Kreuter and Blumthaler (2009) in which the stray-light distribution on a diode array spectrometer is characterized by using a single monochromatic (laser) source. This is a simplification of Zong et al's (2006) method that relies on a tuneable laser source, although the mathematical correction is similar. In Zong et al's method from each monochromatic light source, a data vector is obtained describing the distribution of a single wavelength ( $\lambda$ ) over the instrument's diode array (i.e. the spectral line spread function or LSF). The LSF allows the line signal response (or in-band response, IB-response) to be separated from the stray light contribution of wavelength  $\lambda$  over the array. By normalizing the signal values, and setting the IB-response to zero, the stray-light distribution

function (SDF) is obtained for wavelength  $\lambda$ . A square SDF matrix is then constructed from the concatenated set of SDF vectors, jointly describing the array distribution of all wavelengths in the spectral range. The SDF matrix therefore contains information on the proportional contributions of stray light to each pixel from all wavelengths. Finally, a recursive stray light correction matrix (SCL) is constructed as the inverse of the sum of SDF plus the identity matrix. Kreuter and Blumthaler (2009) describe an equation for obtaining a corrected vector for an array, from the SDF and SCL matrices, as follows:

Firstly, the measured spectrum vector ( $Y_{meas}$ ) should equal the sum of the IB-response vector ( $Y_{IB}$ ) and the stray light contribution vector ( $Y_{SL}$ ).

$$Y_{meas} = Y_{IB} + Y_{SL}.$$

The  $Y_{SL}$  is, in turn, computed as the matrix multiplication of the SDF matrix with the IB-response.

$$Y_{SL} = D \cdot Y_{IB},$$

where  $D$  is the SDF matrix.

Therefore,

$$Y_{meas} = Y_{IB} + D \cdot Y_{IB} = [I + D] \cdot Y_{IB},$$

where  $I$  is the identity matrix

Rearranging the equation:

$$Y_{IB} = [I + D]^{-1} \cdot Y_{meas}.$$

Given that  $[I + D]^{-1}$  was defined as the SCL matrix ( $C$ ):

$$Y_{IB} = C \cdot Y_{\text{meas}},$$

$Y_{IB}$  corresponds to the stray-light corrected signal response.

Spectral measurements shown in this work were stray-light corrected through this method, using a 408 nm laser as in Kreuter and Blumthaler's simplification (Kift et al., 2013).

The overall estimated uncertainty of the METCON spectrometer is expected to be below 5% given that standard calibrating procedures were followed i.e. standard lamps traceable to NIST were used under specified and stabilized conditions of distance to the sensor, ambient temperature and electrical current.

A final consideration to be made is the potential variation in ambient temperature. Changes in ambient temperature may also lead to changes in the performance of spectrometers (Baczynska et al., 2011). The dispersion of the gratings and the position of wavelengths in the CCD array may change due to thermal expansion. For this reason spectrometers may be either contained within a temperature stabilized environment or the output data should be temperature corrected. The METCON spectrometer operated with a PID temperature controlling system.

An additional two-channel Ocean Optics spectrometer was used during the initial experimental stages of this thesis. However, the data generated with this second spectrometer do not generally appear in this final version; except for an illustrative example of the relationship between simultaneous spectral radiance of a clear-sky section and global spectral irradiance, shown in Chapter 7. For this example, sky-radiance and global irradiance were

simultaneously measured using the two channels of the instrument. Channel A was connected to a global irradiance entrance optic, incorporating a Teflon diffuser, via 3m fibre optic. Channel B received input from a 2° field-of view radiance input optics attached to the instrument via an 8m fibre optic. The Ocean Optics spectrometer was wavelength and intensity calibrated at the Centre for Atmospheric Sciences, using similar procedures to those described for the METCON spectrometer. The main difference was that dark and stray light correction was applied using a simplified methodology whereby it was assumed that for solar UV radiation there should be no signal in the first few pixels of the array (pixels 1 to 10), corresponding to wavelengths < 290nm. Therefore any output signal from these pixels would only be due to the dark current and a contribution from stray light. It was also assumed that this was constant throughout the spectrum. Under these assumptions, the average output signal from the first pixels was subtracted from every pixel in the array before applied the intensity calibration. The Ocean Optics spectrometer also operated with a PID temperature controlling system.

In upcoming chapters (4, 6 and 7), modelled calculations of irradiances are compared against broadband and spectral measurements obtained with the instruments described here (i.e. pyranometers and spectrometers). Given the small estimated uncertainties of the instruments, the differences between modelled and measured data can be mostly attributed to simplifications and assumptions in the modelling process. Such discrepancies between measurements and calculations are discussed within the corresponding chapters (4, 6 and 7).

Global input optics used here for global broadband and spectral measurements do not provide a means for assessing the position of horizon obstructions in the upper-hemispheric view nor the anisotropic distribution of sky radiation. To describe such parameters, a fisheye

lens and a mobile phone digital camera have been used and are presented in the following section.

### 3.3.5 Fisheye lenses and whole-sky cameras.

Fisheye images of the upper-hemispheric sky view at ground level can be useful for describing canyon geometries, as will be shown in Chapter 4. In addition, whole-sky fisheye images can be used for describing the anisotropic sky distribution of diffuse irradiance.

Fisheye lenses may return different projections of the upper-hemispheric sky-view, for example, orthographic or equidistant projections. The main differences between orthographic and equidistant projections may be seen in Figure 3-7 adapted from Oshita (1999).

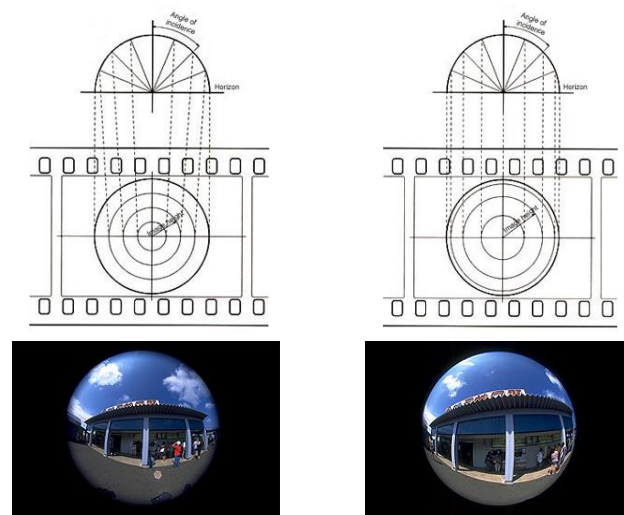


Figure 3-7 Shows the differences between the equidistant (left panels) and orthographic (right panels) projections, of a hemisphere in front of an observing lens. The upper panels show diagrams of the geometries of equidistant and orthographic projections. The lower panels show example photographs of the same scene taken with the corresponding equidistant and orthographic fisheye lens. Adapted from Oshita (1999).

In an equidistant projection, the position of any object, described as its linear distance from the centre of the projected image, is directly proportional to its relative zenith angle

position in the hemispheric view (Eq. 3.4). While in an orthographic view, the distance of an object from the centre of the image is proportional to the sine of its zenith angle in the hemispheric view (Eq. 3.5). This results in an orthographic projection showing objects “compressed” towards the horizon line of the hemisphere.

The equidistant projection is expressed as

$$R = f \cdot \theta \quad , \quad (\text{Eq. 3.4})$$

the orthographic projection as

$$R = f \cdot \sin(\theta), \quad (\text{Eq. 3.5})$$

where  $R$  is the projected linear distance of any object from the centre of the image (or image height);  $f$  is the focal length and  $\theta$  is the zenith angle; and  $\theta$  is the real zenith angle of the object in the hemispheric view.

Interestingly, orthographic projections provide a unique advantage for atmospheric studies in that they simulate the cosine response of flat horizontal surfaces, i.e. objects towards the horizon line have less contribution to the hemispheric view, than objects towards the zenith. Failure to consider these different contributions of sky regions may lead to miscalculations of irradiance or the sky view factor. Therefore, it is imperative to know the projections provided by fisheye lenses and/or the geometrical corrections that may be applied, in order to correctly represent the sky view of flat horizontal surfaces.

Since most conventional fisheye lenses provide equidistant projections, they do not simulate the cosine response of flat surfaces. Atmospheric researchers using these images must apply Steyn’s (1980) geometrical corrections to “reduce” the contribution of distorted areas towards the horizon line (this method has been described in Section 2.4.3).

On the other hand, if an orthographic lens is used, the projection resembles the cosine response of a flat horizontal surface, given that all the visual information towards the horizon has a lower contribution (compare the right and left panels in Figure 3-7). It is therefore very important to make sure the geometrical corrections are not applied automatically to orthographic fisheye images. Because of the scarcity of orthographic lenses, most of the specialised software for the calculation of SVF from fisheye images automatically applies mathematical corrections. The RayMan model is (to the extent of the author's knowledge) the only tool that provides an option to not apply the corrections, and therefore allows the use of orthographic images. These considerations will be further discussed in Chapter 4.

To obtain fisheye images, a commercial digital mobile phone camera (Nokia E5 mobile phone) was equipped with a magnetic mini-fisheye lens (Sumlung, model: SL-FE12). These magnetic fisheye lenses are inexpensive alternatives (\$19 USD approx.), that may be used to roughly represent both the canyon geometries and the whole sky anisotropic distributions of visible RGB bands. Lenses are attached by a magnetic ring to any type of mobile phone.

Fisheye lenses may perform different projections of the 3D hemisphere onto a plane (e.g. orthographic, equidistant). To identify the projection of the lens, a photograph was taken of six marks with known elevation angles with respect to the normal of the lens (see Figure 3-8). The marks were simple pieces of tape fixed unto the wall (to the left of the image in Fig. 3-8). The black arrows on Figure 3-8 indicate the distance of each object from the centre of the image, which represents the 2D projected zenith angle (i.e.  $[1 - \text{elevation angle}]$ ) of the objects in the 3D view of the fisheye lens. If the lens returned an equidistant projection, then the projected elevation angle in the objects should correspond linearly to the known 3D elevation angle of the objects (according to Eq. 3.4). If the projection of the lens is

orthographic, then the projected elevation should correspond to the sine of the known 3D elevation angle (Eq. 3.5).

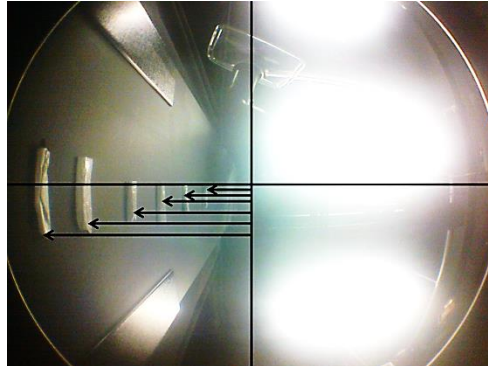


Figure 3-8 Test fisheye image taken with the SL-FE12 magnetic mini fisheye lens attached to a Nokia E5 camera. Six marks were put on a wall within the view of the fisheye lens (pointed by black arrows on the left-hand side of the image). Each mark had a known elevation angle with respect to the camera lens. The distance from each mark to the central vertical line (i.e. the length of black arrows) is proportional to the zenith angle of the marks ( $1 - \text{elevation angle}$ ).

Arrow lengths from Fig. 3-8 were measured and normalized to 1. This normalized distance is proportional to the R parameter in equations 3.4 and 3.5. Projected elevation angles (i.e.  $[1 - \text{normalized arrow length}]$ ) have been plotted against the known 3D elevation angles. The result is close to an ideal sine relationship (Fig. 3-9). Thus, the mini fish-eye lens return orthographic projections of the hemispheric view. It can be said that projected images taken with this lens approximately represent the sky view of a flat horizontal surface, without any further processing being necessary. The specific use of this information will be further explained in Chapter 4.



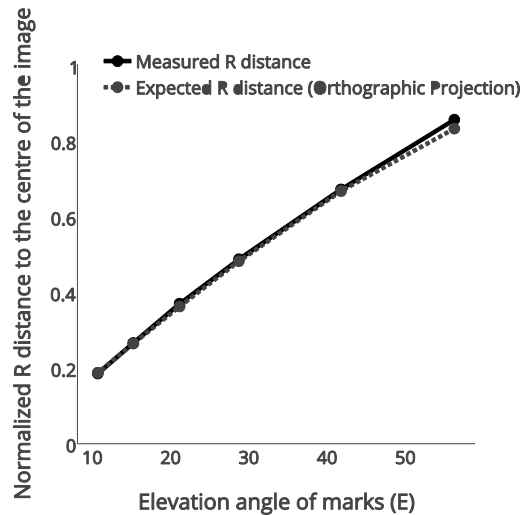


Figure 3-9 The black line shows the comparison between the measured projected position (Y-axis) against the known elevation angle ( $E$ , X-axis) of the marks in Figure 3-7. The grey-dotted line shows the same relationship from an ideal orthographic projection (i.e.  $\sin(E)$ ).

To obtain images of the sky-view of the global input optics of radiometers, the fisheye camera was manually positioned and levelled as close as possible to the input optics and pointing towards the zenith and azimuthally oriented towards the north. Images taken with a fisheye lens within a canyon can be used for describing horizon obstructions, these techniques are described in Chapter 4. Additionally, the fisheye images obtained can be used for approximating the anisotropic distribution of diffuse irradiance; this possibility is explored and further discussed in Chapter 7.

### Summary of Chapter 3

General methods, software tools and measuring devices have been described. Software tools are free to access on the internet and will allow the projection of urban geometries into fisheye images at any location with Google Street View coverage; which will facilitate the future continuation of the present work. Additionally, minimum instrumentation for solar radiation measurements (i.e. a pyranometer, a global spectrometer, a fisheye digital camera)

will allow approximating street-level global irradiances. The CM5 pyranometer was used to obtain the results presented in Chapter 4, for the calculations of street-level total-shortwave irradiance. Global spectral irradiance data from the METCON spectrometer were used in Chapters 6 and 7 to validate calculations of spectral irradiance using simulated obstructions over the sky view of the spectrometer. These experiments are described in Chapter 6.

Chapters 4 to 7 are presented as stand-alone articles, each one describing one step of the general flow chart (presented in Figure 3-1). Finally, Chapter 8 will provide a summary and a final discussion of the general findings and potential future developments.

## References

- Anguelov, D., Dulong, C., Filip, D., Frueh, C., Lafon, S., Lyon, R. and Weaver, J. (2010). Google street view: Capturing the world at street level. *Computer*, (6), 32-38.
- Baczynska, K., O'Hagan, J. B., Pearson, A. J., and Eriksen, P. (2011). Temperature Correction of UV Spectral Solar Measurements for ICEPURE Project. *Photochemistry and Photobiology*, 87, 1464–1467.
- Brown, S. W., Johnson, B. C., Feinholz, M. E., Flora, S. J., Lykke, K. R., and Clark, D. K. (2003). Stray-light correction algorithm for spectrographs. *Metrologia*, 40(1), 81.
- Carruthers, G. R., and Dymond, K. F. (1999) Ultraviolet atmospheric and space remote sensing: methods and instrumentation II(Denver CO, 22 July 1999). In SPIE proceedings series. SPIE.
- Cede, A., Blumthaler, M., Luccini, E., Piacentini, R. D., and Nuñez, L. (2002). Effects of clouds on erythemal and total irradiance as derived from data of the Argentine Network. *Geophysical research letters*, 29(24), 76-1.
- d'Angelo, P. (2007). Radiometric alignment and vignetting calibration. *Proc. Camera Calibration Methods for Computer Vision Systems*.
- Dahlback, A., and Moan, J. (1990). Annual exposures to carcinogenic radiation from the sun at different latitudes and amplification factors related to ozone depletion. The use of different geometrical representations of the skin surface receiving the ultraviolet radiation. *Photochemistry and photobiology*, 52(5), 1025-1028.
- German, D. M., d'Angelo, P., Gross, M., and Postle, B. (2007, June). New methods to project panoramas for practical and aesthetic purposes. In *Proceedings of the Third Eurographics conference on Computational Aesthetics in Graphics, Visualization and Imaging* (pp. 15-22). Eurographics Association.
- Gröbner, J., Blattner, P., Blumthaler, M. (2012) Traceability for surface spectral solar ultraviolet radiation – EMRP ENV03. The WMO Technical Conference on Meteorological and Environmental Instruments and Methods of Observation (TECO-2012). Brussels, Belgium,
- Kift, R., Smedley, A., Webb, A. R. (2013) Initial laboratory instrument characterisation and solar simulator measurements of Manchester spectrometers involved in the EMRP

- project. Thematic Network for Ultraviolet Measurements. UVnet : 27 – 28 August 2013, Davos, Switzerland.
- Kipp & Zonen. (2013) Calibration Standards. Retrieved 25 Jul 2014 from <http://www.kippzonen.com/ProductGroup/112/Calibration-Standards>.
- Kreuter, A., and Blumthaler, M. (2009). Stray light correction for solar measurements using array spectrometers. *Review of Scientific Instruments*, 80(9), 096108.
- Kudish, A. I., and Evseev, E. G. (2012). UVB irradiance and atmospheric optical depth at the Dead Sea basin, Israel: Measurements and modeling. *Renewable Energy*, 48, 344-349.
- Lee, C. (2015). The Working Principle of a Thermopile Pyranometer. Retrieved 7 April 2007 from Kipp & Zonen. [http://www.kippzonen.com/News.aspx?id=572#.VSRYeVnF\\_Cu](http://www.kippzonen.com/News.aspx?id=572#.VSRYeVnF_Cu)
- López, G., and Batlles, F. J. (2004, September). Estimate of the atmospheric turbidity from three broad-band solar radiation algorithms. A comparative study. In *Annales Geophysicae* (Vol. 22, No. 8, pp. 2657-2668). Copernicus GmbH.
- Manninen, P., Hovila, J., Seppälä, L., Kärhä, P., Ylianttila, L., and Ikonen, E. (2006). Determination of distance offsets of diffusers for accurate radiometric measurements. *Metrologia*, 43(2), S120.
- Matzarakis, A., Rutz, F., and Mayer, H. (2010). Modelling radiation fluxes in simple and complex environments: basics of the RayMan model. *International Journal of Biometeorology*, 54(2), 131-139.
- Mazerolle, D., and Blaney, S. (2011). Google Street View: A New Online Tool with Potential Application to Roadside Invasive Species Detection and Monitoring. *Plant Invasions*, 77.
- Myers, D. (1997) Radiometric instrumentation and measurements guide for photovoltaic performance testing. National Renewable Energy Laboratory, Colorado, USA
- Myers, D. R., Emery, K. A., and Stoffel, T. L. (1989). Uncertainty estimates for global solar irradiance measurements used to evaluate PV device performance. *Solar Cells*, 27(1), 455-464.
- Oshita, K. (1999) The World's First Aspherical SLR Lens and Orthographic Projection Fisheye Lens OP Fisheye-Nikkor 10mm f/5.6. *Nikkor-The Thousand and One Nights*, 6.
- Rousselet, J., Imbert, C. E., Dekri, A., Garcia, J., Goussard, F., Vincent, B., and Rossi, J. P. (2013). Assessing species distribution using Google Street View: A pilot study with the pine processionary moth. *PloS one*, 8(10), e74918.
- Schreder, J. G., Blumthaler, M., and Huber, M. (1998). Design of an input optic for solar UV-measurements. Protection against the Hazards of UVR, *Internet Photochemistry and Photobiology* (<http://www.photobiology.com/UVR98/schreder/index.htm>).
- Steyn DG (1980) The calculation of view factors from fisheye-lens photographs: Research note. *Atmosphere-Ocean* 18:254–258.
- Webb, A. R. (1998). UVB instrumentation and applications. CRC Press.
- Webb, A. R., Kift, R., Thiel, S., Bais, A. F., Blumthaler, M., Kylling, A., and Gobbi, G. P. (2002, January). Empirical approach to converting spectral UV measurements to actinic flux data. In *International Symposium on Optical Science and Technology* (pp. 104-114). International Society for Optics and Photonics.
- Yoshizawa, T. (Ed.). (2009). *Handbook of optical metrology: Principles and Applications*. CRC Press.
- Zong, Y., Brown, S. W., Johnson, B. C., Lykke, K. R., and Ohno, Y. (2006). Simple spectral stray light correction method for array spectrometers. *Applied Optics*, 45(6), 1111-1119.

## Chapter 4

This chapter is presented as the final version of an article published in the journal *Energy and Buildings*, available as the online version in 2014, and in print in 2015. Please note that the referencing style is different from that of previous chapters.

The author of this thesis (Roberto Carrasco Hernandez) is also the first author of the article. The original concept, research methods, and outcomes were developed by the first author, under the close supervision of co-authors Andrew R.D. Smedley and Ann R. Webb. The article was written by Carrasco-Hernandez, with advice and assistance from the co-authors. Some of the radiometric data was kindly provided by the staff of the Whitworth observatory, University of Manchester. Google Street View images are property of the Google Company, and their use falls within the terms of use for non-profit purposes.

The paper describes the first steps in the process of obtaining street-level irradiance, i.e. the identification of the local horizon obstructions (specified as the street-level field of view) and the calculation of this influence on the total (all wavelengths) solar radiation reaching the ground.

Appendix I, at the end of the thesis, shows the published version of this chapter as it appears in the *Energy and Buildings Journal*.

**Using urban canyon geometries obtained from Google Street View for atmospheric studies: Potential applications in the calculation of street-level total-shortwave irradiances.**

Roberto Carrasco-Hernandez<sup>\*1</sup>, Andrew R.D. Smedley<sup>1</sup>, Ann R. Webb<sup>1</sup>

<sup>1</sup>*Centre for Atmospheric Sciences, School of Earth, Atmospheric and Environmental Sciences, University of Manchester, Manchester, M13 9PL, UK.*

Corresponding Author

Name : Roberto Carrasco-Hernandez

Affiliation : University of Manchester

Address : Simon Building, Oxford Road, Manchester M13 9PL

Phone : +44 7412852056

Email : roberto.carrascohernandez@postgrad.manchester.ac.uk

**Abstract**

This paper presents an implementation of digital image processing tools, in order to reconstruct building geometries and urban sky view factors for individual street canyons around the world. By using the Google Street View image database, it is possible to reconstruct canyon fisheye images at any point where a Google panorama is available. The Hugin software allows the geometrically correct merging of independent images to create a fisheye projection, covering the upper-hemispheric view of the sky. Sky view factor calculations may then be performed by specialised software on the reconstructed fisheye image. In order to analyse the fitness of reconstructed panoramas, control images taken with a fisheye lens camera were used for comparison. The RayMan model was then used to calculate total-shortwave global irradiances from the restricted canyon view and from a full hemispheric view. Finally, total-shortwave global irradiances were measured for the same

position in the street canyon and compared against observatory measurements under a full-sky view; this to evaluate the performance and usefulness of idealised calculations. The reconstructed urban geometries returned acceptable fine-scale descriptions, and their potential utility for scientific purposes in the atmospheric sciences was demonstrated with the examples provided.

### **Keywords**

Google Street View, Street canyon irradiances, Canyon fisheye images

### **Abbreviations and Nomenclature**

**SVF** : Sky View Factor.

$E_C(t)$ : Canyon irradiance ( $\text{Wm}^{-2}$ ) at time  $t$ .

$E_F(t)$ : Actual measured irradiance ( $\text{Wm}^{-2}$ ) under a full-sky view (in our case from the Whitworth observatory measurements, University of Manchester).

$E_{IC}(t)$ : Idealised canyon irradiance ( $\text{Wm}^{-2}$ ) inside a given canyon profile under cloudless conditions calculated using the RayMan model and the canyon's SVF.

$E_{IF}(t)$ : Idealised full-sky irradiance ( $\text{Wm}^{-2}$ ) under a full-sky view and cloudless conditions.

### **4.1 Introduction**

A growing proportion of the global population lives within urban canyons, i.e. city streets surrounded by buildings [1], in which the restricted sky view reduces solar energy access. Because of the unique microclimate conditions created by the specific geometry of each canyon, urban geometries affect the energy performance of buildings and, since main outdoor activities occur at these spaces, they also play a crucial role in human thermal comfort in

streets [2, 3]. Human exposure to sunlight within urban canyons is also a relevant health issue due to the diverse biological effects of ultraviolet light [4, 5]. Some of the future aims of our study will include spectral irradiance calculations within urban canyons in order to determine urban solar UV patterns, as an aid for health studies. This paper presents the initial stages of reconstructing urban geometries for the calculation of total-shortwave irradiances.

The geometry of urban canyons, defined by the variations in height, length and spacing between buildings, has a significant effect on the energy budgets of urban areas [6]. Since the 1980s many urban meteorologists and climatologists have been using geometrical indices for describing urban canyons, particularly the Sky View Factor (SVF). According to the definition of [7] in [8], the Sky View Factor is “*the ratio of the radiation received (or emitted) by a planar surface to the radiation emitted (or received) by the entire hemispheric environment*”. However a more common way of understanding it is as the proportion of unobscured sky from the perspective of an observer. The SVF index has proven to be useful, not only for describing canyons, but also for modelling and predicting atmospheric conditions on urban micro-scales, affecting energy exchanges, temperature variations, and air movement phenomena [9-16]. The SVF has also been used to explain public health issues and create geographic models of disease risks, for example tuberculosis [17]. It also has potential applications in building and city planning e.g. daylight in buildings, heat loading and energy conservation. In addition, it can provide with the exposure to sunlight of individuals within the canyons, for realistic assessment of people’s exposure to ultraviolet radiation, for example. Given its importance, current and future research needs to focus on creating ways to model the SVF factors for large cities, without compromising the level of detail and resolution required.

In general, methods for determining SVF and solar access calculations can be divided into four groups: Geometrical Methods, Fisheye image analyses, inferences from GPS signals, and 3D models of terrain and buildings. For a short review of these methods see:[18], also[19] gave a comprehensive up-to-date list of associated literature. Hitherto, 3D modelling techniques have been most widely used to generate SVF maps and solar radiation models for cities [20-22]. However the geographic coverage of 3D models is restricted since it may compromise computational performance. Most digital models of cities will also oversimplify the complex shapes of urban canyons. Additionally, these models contain information about buildings' heights and widths, but not details about materials comprising the urban canopy. Certain features and materials like glass windows, trees or walls exert different effects on the incoming radiation (i.e. reflection, filtering and absorption) [4, 23-26]. Although it is not within the scope of this article to analyse these particular effects, the proposed methods will allow researchers to map SVFs for large cities at a very high resolution, while maintaining detailed descriptions of urban canopy shapes and colours, which in turn could be related to the underlying materials.

In this work it is proposed to use the Google Street View image database, to reconstruct fisheye images and SVFs for an individual urban canyon, at a location where a Google panorama is available. For this purpose, we used the open-source software Hugin for image merging and projection, and the RayMan software tool, originally developed for modelling mean radiant temperatures and thermal comfort[27]. The combination of these tools enables us to calculate detailed SVFs for an urban canyon, without the need to physically taking fisheye images. Furthermore, street-level total-shortwave irradiances can be modelled using the RayMan software, as a tool for the assessment of urban energy budgets and microclimate patterns.



## 4.2 Materials and Methods

### 4.2.1 Software tools

Google Street View has not often been used for scientific purposes in the atmospheric sciences. Other Google products have been proposed as platforms for sharing atmospheric data, e.g. Smith and Lakshmanan [28] proposed the usage of Google Earth, for the integration of weather data with GIS information. Dall'O [29] addresses the potential usefulness of using Google Earth satellite imagery for the assessment of energy performance of buildings. In 2011 Patel et al.[30]used Google Street View to estimate the heights of buildings in a study block by comparing them with objects of known dimensions; they used building height information to create a digital elevation model and calculate shading patterns using ArcGIS. However, it seems that the usefulness of Google Street View for urban atmospheric studies has been overlooked. Within the reviewed literature, most academic articles either discuss technical and computational issues [31-33], or focus on potential social implications and uses of Google Street View, like privacy protection [34] or neighbourhood assessment [35]. Google Street View possesses an immense collection of images, comprising 360° (spherical) panoramas of individual locations at the street level in many countries around the world. This opens up the possibility of describing the SVF wherever Google Street View is available.

Hugin is an open source software originally created by Pablo d'Angelo [36, 37]. This software allows the assemblage of independent rectilinear images into a single panorama. It also allows the user to collocate different images according to their central positions on a 3D hemisphere. Such hemisphere represents the upper-hemispheric view of the camera which is very useful for sunlight and skylight calculations.

The freely available RayMan Model 2.1 software was released in the year 2010 [27]. It calculates total-shortwave global irradiance and mean radiant temperature for any minute of

the day. Calculations can be performed at any geographical location, including urban canyons, for which the building geometry can be described using a fisheye image. The RayMan software has a graphical user interface to manually draw polygons covering the area of buildings in the projected “fisheye” hemispheric view of the canyon, simply by delimiting the boundary between sky and buildings. The result is basically a binary classification of the pixels in the fisheye image, where white pixels are considered to be sky and therefore contribute to radiation; while black “building” pixels represent obstructions to the background light, which may be direct or diffuse radiation. The proportion of white pixels is proportional to the SVF. However, the exact proportion of sky that each pixel represents will also depend on its elevation angle, which in turn depends on the planar projection used for the hemispheric view. Therefore a correction must be made to the calculations following Steyn (1980). Additionally, the RayMan software allows the generation of sun path diagrams for the analysis of sunlight duration and irradiance intensity within a canyon. Other commercial software packages like ECOTECH provide similar tools [38].

#### Study site and image details

The Dover Street urban canyon is located in the University of Manchester city campus, UK. The canyon has a northeast-southwest orientation, with medium size (5 to 7 storey) buildings at both sides. Two sets of rectilinear images were taken from different directions that cover the full upper-hemispheric view of the canyon. These sets were projected into a reconstructed fisheye view; the reconstruction was compared against a control fisheye image taken at the same location with an orthographic fisheye lens that closely represents a cosine response, i.e. that of radiation incident on a horizontal plane.

Twenty-five independent rectilinear images were taken with an E5 Nokia mobile phone camera, with a 50° horizontal field of view (HFV). The set of images covered the full

hemispheric view of the Dover Street canyon and were each associated to the 3D hemispheric coordinates of the image centre. This set is referred to as the Nokia set in the following sections.

A set of 10 Google Street View images, with a  $90^\circ$  HVF, were taken at the closest possible point to that used in the Google database. The set covered the entire hemispheric view of the Dover Street canyon. The images were also labelled according to their 3D hemispheric coordinates.

The centre of the hemispheric view of these two sets differed in horizontal position by a few meters. It also differed in vertical position by approximately 2m, since Google images are taken at approximately 2.5 meters above ground level in the centre of the carriageway [31], whereas the Nokia set were taken at 0.5m above ground to match the radiation measurements used for validation.

In order to record a control orthographic hemispheric image, a mini fisheye lens (Sumlung, model: SL-FE12) was fitted to the same E5 Nokia phone camera as used to record the rectilinear images. The mini lens consists of a detachable fisheye lens, with a small magnet to align it in front of the optics of a mobile or digital camera. The orthographic projection of the mini-fisheye lens was confirmed in the laboratory against objects of known heights with respect to the edge of the lens. Canyon control images were taken to describe the upper-hemispheric view within the canyon: The lens was positioned facing towards the zenith, and the vertical axis of the camera was oriented with the north-south axis. However, the internal CCD array of the camera is not able to capture the full upper-hemispheric view in one single take, being cropped on the north and south edges in this orientation. Therefore, a second image was taken with a  $90^\circ$  azimuthal rotation to cover the missing parts of the hemispheric view. Finally the two images were overlaid.

Two panorama reconstructions were made for the Dover Street canyon: the first one was made from the twenty five rectilinear images set taken within the canyon. The second reconstruction was made from the Google Street View images by using the Hugin software: images were positioned and projected according to their hemispheric coordinates. The fisheye projections (equidistant and orthographic) were constructed with the Hugin software for comparison with the directly measured fisheye image.

The reconstructed projections and the control image were imported into the RayMan software, in order to calculate their corresponding sky view factors using the method described by Steyn [39]. SVFs of the two reconstructions and the control images were compared.

#### **4.2.2 Street-level Total-shortwave Irradiance Measurements**

Total-shortwave irradiances were measured in a city canyon and compared against measurements under a full-sky view. On 3–4 April 2013 total-shortwave global irradiances were measured at the Dover Street urban canyon using a Kipp & Zonen CM5 pyranometer with a verified cosine response and compared against measurements of another CM5 pyranometer installed at the rooftop of the Whitworth Observatory of the University of Manchester. The Whitworth Observatory has an almost unobstructed view of the sky with an estimated SVF  $> 0.999$ . Previously, the Dover Street pyranometer had been cross-calibrated under a full-sky view with the instrument at the Whitworth Observatory, the calibration of the Whitworth pyranometer being traceable to the World Radiation Centre in Davos, Switzerland. The data logging systems for both devices were synchronised and set to Universal Coordinated Time. The distance between the measuring sites was approximately 230m, and this can be considered a sufficiently small distance such that both sites are subject to the same meteorological and cloud conditions.

### 4.2.3 Street-level Modelling

The measured irradiances for both pyranometer positions were modelled using the RayMan software which allows the calculation of the path of the sun across the sky for a particular date, time and geographical location. The software evaluates the visibility of the solar disc throughout the day, given the specific horizon obstructions of the canyon; and additionally it calculates the observable fraction of diffuse irradiance by using the calculated SVF.

The objective of this core part of the study is to evaluate the accuracy of the canyon reconstruction by comparing modelled and measured irradiances in the canyon both in terms of their absolute and relative values, and any temporal offsets.

Notice that, although the RayMan model allows the introduction of clouds in the sky, it does not assess the complex interactions of moving clouds blocking and unblocking the solar disc from the observer's perspective, for this reason the models were run assuming cloudless skies. Still, the relative patterns of canyon irradiances throughout the day are expected to be well described by idealised models, because of the dominance of direct sunlight in global irradiance: i.e. whenever the sun is visible in the canyon, irradiance values should be very similar between full sky and canyon irradiances. If intermittent decreases due to the passage of clouds occur, we anticipate both full sky and canyon irradiances to be affected in a similar manner. On the other hand, when the sun is obstructed by the canyon buildings, then the difference between canyon and full sky irradiances should be larger; in this case the effect of clouds blocking direct sunlight are not anticipated to be observable in the canyon assuming the diffuse component to be isotropic.

## 4.3 Results

### 4.3.1 Panorama Reconstructions from the Nokia E5 Set of Rectilinear Images

The Hugin software tool allowed the relative 3D positioning of the Nokia set of independent images to be specified, shown in Figure 4-1(a) as a hemispheric view and in Figure 4-1(b) as a plan view. These images are subsequently deformed to create a continuous hemispheric image (Figure 4-1c) which is then finally projected onto a plane (Figure 4-1d). All deformations produced as well as any overlapping between images are automatically calculated by Hugin, the only input information required is the relative position of each image and its horizontal field of view. Lastly the Hugin tool handles merging of the overlapping images from Figure 4-1d by edge softening; the first two images in Figure 4-2 are the result of this complete process, showing both an equidistant projection for comparison (Figure 4-2a) and an orthographic projection in Figure 4-2b. The latter projection is most relevant for instruments such as pyranometers which have a cosine response. In this case the pixel distance from the centre of the image is related to the sine of the zenith angle for the corresponding point of the sky. The orthographic projection of the SLFE12 fisheye is also confirmed by the much better agreement in the calculated SVF for the Hugin orthographic projection to that for the fisheye image.

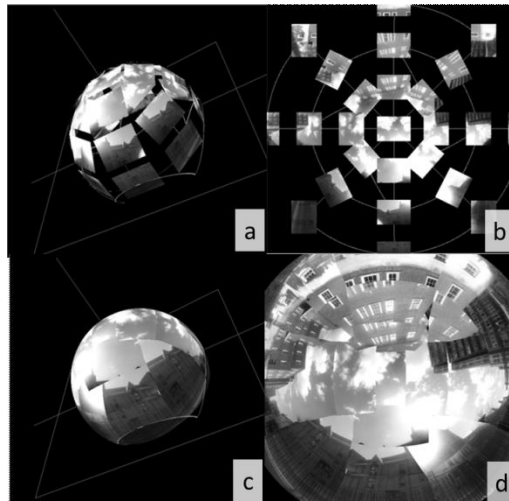


Figure 4-1 Screenshots of the Hugin interface. Twenty-five independent images covering the full view from the Dover Street canyon in a hemispheric view (a) and plan view (b). (c) Shows the continuous hemispheric image of the view from the canyon, also projected onto a plane (d).

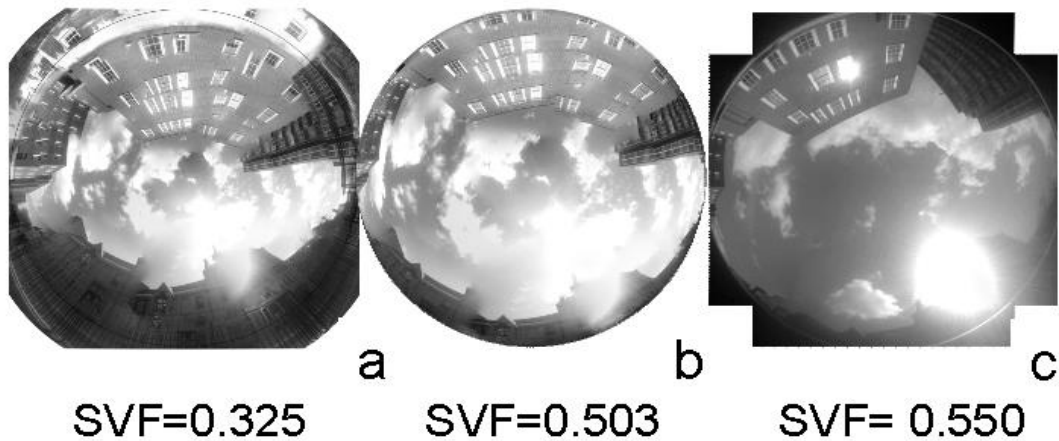


Figure 4-2 Orthographic and equidistant reconstructed hemispheric views versus a control fisheye image with corresponding SVF specified below each image. (a) Orthographic reconstructed projection, (b) equidistant reconstructed projection, and, (c) control fisheye image taken with the SLFE12 mini fisheye lens. Pictures were taken at the Dover Street canyon, University of Manchester.

### 4.3.2 Panorama Reconstruction from Google Street View Images

Figure 4-3 shows the process of panorama reconstruction with the Google Street View images. The process was very similar to that shown in Figure 4-1 for the Nokia set, but with a different set of input images. The images from Google Street View have a particular advantage when carrying out panorama reconstructions: namely that the field of view is larger and thus fewer images are required to cover the hemisphere. In turn this enables a more consistent reconstruction to be formed using the Hugin software and better estimate of the SVF.

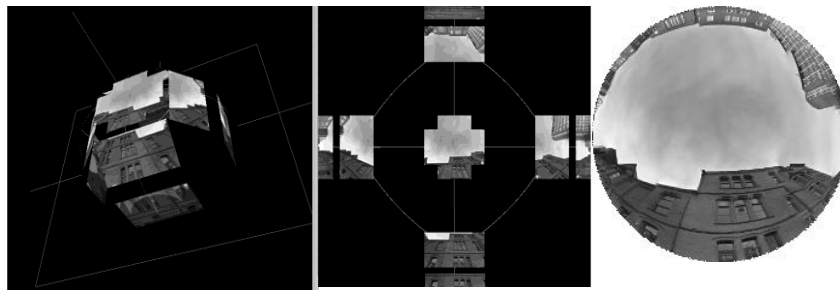


Figure 4-3 Reconstruction of Dover Street urban canyon from Google Street View database. Left and middle panels: Hugin interface screen showing the relative positioning of rectilinear images. Right panel: resulting orthographic projection.

### 4.3.3 Street-level Total-shortwave Irradiances

Figure 4-4a shows the projected sky view of the Dover Street canyon, overlaid with the calculated sun path for 3 April 2013 using the RayMan Software. The south-southeast section of the canyon is amplified in Figure 4-4b to better illustrate the solar track, relevant to the measured and modelled irradiances on this date, shown in Figures 4-5a and 4-6a. Notice from Figure 4-4b the path of the sun being obstructed at specific times of the day by the buildings in the canyon. In this figure (4-3) the projection of the canyon is shown with an equidistant projection in order to match the projection of the solar path that the RayMan software returns. When calculating the SVF, a cosine correction is applied to the obstructions. Notice that the



orientation of the canyon slightly differs from the projections shown in Figures 4-2 and 4-3. In the previous examples the orientation was not relevant. However, for irradiance calculations, which estimate the precise position of the sun at certain times of the day, the orientation of the canyon must be accurately represented.

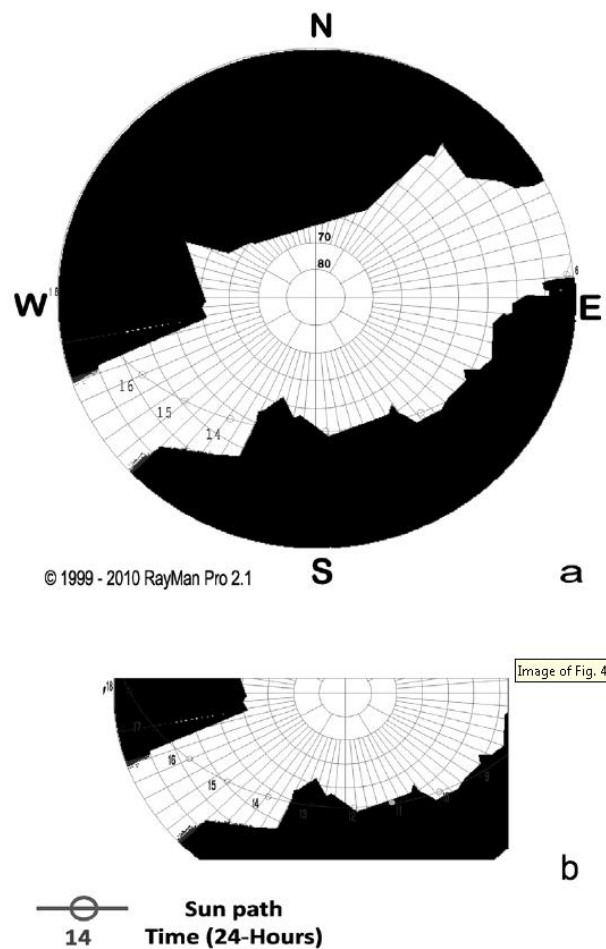


Figure 4-4 (a) Dover Street canyon equidistantly projected and oriented northwards with the corresponding solar path (times in UTC) for 3 April 2013. (b) Enlarged south-southeast section of the canyon showing the relevant parts of the sun path the sections where it is obstructed by buildings. This enlarged section includes the irradiance time series later shown in Figures 4-5a and 4-5b.

Figure 4-5 shows the results from modelling the total-shortwave global irradiance using the RayMan software combined with the reconstructed sky view at the Dover Street canyon. The black line corresponds to the modelled full-sky irradiance where the direct sunlight is visible at all times and, therefore it follows a monotonically increasing curve towards midday (4-5a) and similarly but decreasing after midday (4-5b). In contrast the grey broken line corresponds to the modelled canyon irradiance where the direct sunlight is blocked during different parts of the day by the specific geometry of the Dover Street canyon and it thus exhibits distinct steps as the sun's path transitions behind an obstruction.

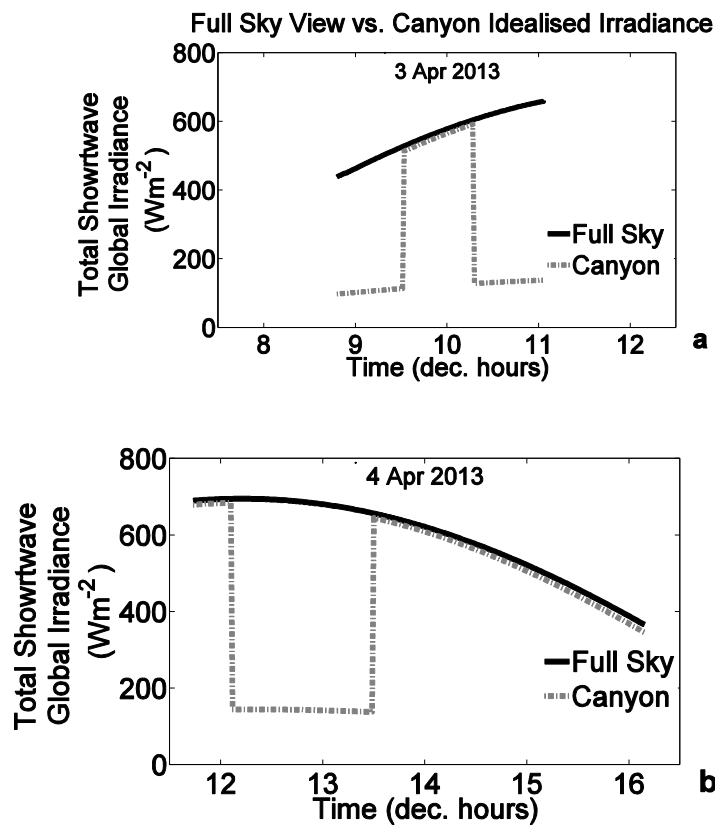


Figure 4-5 Showing the clear-sky modelled differences between obstructed (Dover Street canyon) and full sky (Whitworth Observatory) views on 3 (a) and 4 (b) April 2013, notice how the times of building obstructions of direct sunlight correspond to those measured in Figure 4-6).

Notice that, when the sun is visible, the canyon irradiances nearly approximate the full-sky view irradiances, but not completely. This small difference between canyon and full sky irradiances is due to the blocking of diffuse light by all the buildings in the canyon. Although the model assumed clear sky conditions, the potential use of clear sky models even for broken skies are discussed after analysing the irradiance measurements conducted for the corresponding dates and times.

Figure 4-6 shows the total-shortwave global irradiance measurements taken for 3 and 4 April 2013 at the Dover Street canyon, in a combination of clear and cloudy sky conditions.

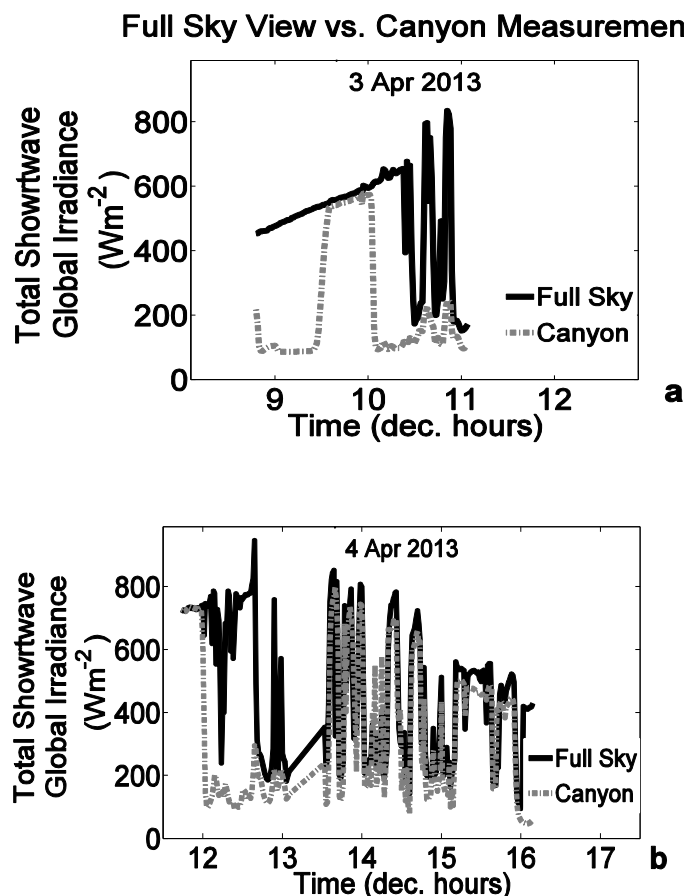


Figure 4-6 Showing the measurements and the observed differences between obstructed (Dover Street canyon) and full sky (Whitworth Observatory) views, on 3 April (a) and 4 April (b) 2013.

Paying attention to the differences between canyon and full sky measurements, notice how the general pattern predicted by the models (Figures 4-5a and 4-5b) is followed by the measurements, i.e. when the sun is visible from within the canyon, full-sky and canyon irradiances are approximately equal except for a small fraction explained by the blocking of the diffuse light component. On the other hand, when the sun was obstructed, the canyon irradiances dropped with respect to full sky (e.g. at time 10.1h in Fig 4-6a), Figures 4-5 to 4-7 show time specified in decimal hours referred to UTC. The effect of broken clouds is seen in Figures 6a and 6b as sudden increases and decreases of the full-sky view irradiances. However, the effect that broken clouds had on the canyon irradiances depended on the availability of direct sunlight: whenever the sun was visible in the canyon, the irradiance dynamics followed closely those of the full-sky view, with a small difference due to the obstruction of the diffuse irradiance (e.g. from 13.5h onwards in Fig 4-6b) On the other hand, when the sun was obstructed, canyon irradiances tend to remain at low values almost independently of the motion of clouds across the sky (e.g. from about 10.4h to 11.0h in Fig 4-6a). Since the relative relationship between canyon and full-sky view irradiances may be modelled under idealised cloudless conditions, it should then be possible to use a combination of actual full sky measurements with ideally modelled ratios between canyon and full-sky views, in order to construct more realistic approximations of canyon irradiances.

#### **4.3.4 Combined Model**

In order to create a more realistic model of a cloudy sky, a combined model for the canyon total-shortwave irradiances was built using the idealised ratio between obstructed to full-sky view, multiplied by the actual full sky irradiance as in equation 4.1.

$$E_C(t) = \frac{E_{IC}(t)}{E_{IF}(t)} \cdot E_F(t) \quad (4.1)$$

where:  $E_C(t)$  is the canyon irradiance ( $\text{Wm}^{-2}$ ) at time,  $t$ ;  $E_{IC}(t)$  is the idealised canyon irradiance inside a given canyon profile under cloudless conditions calculated from the RayMan model and SVF;  $E_{IF}(t)$  likewise is the idealised full-sky irradiance under a full-sky view and cloudless conditions; and,  $E_F(t)$  is the actual measured irradiance under a full-sky view (in our case from Whitworth Observatory measurements).

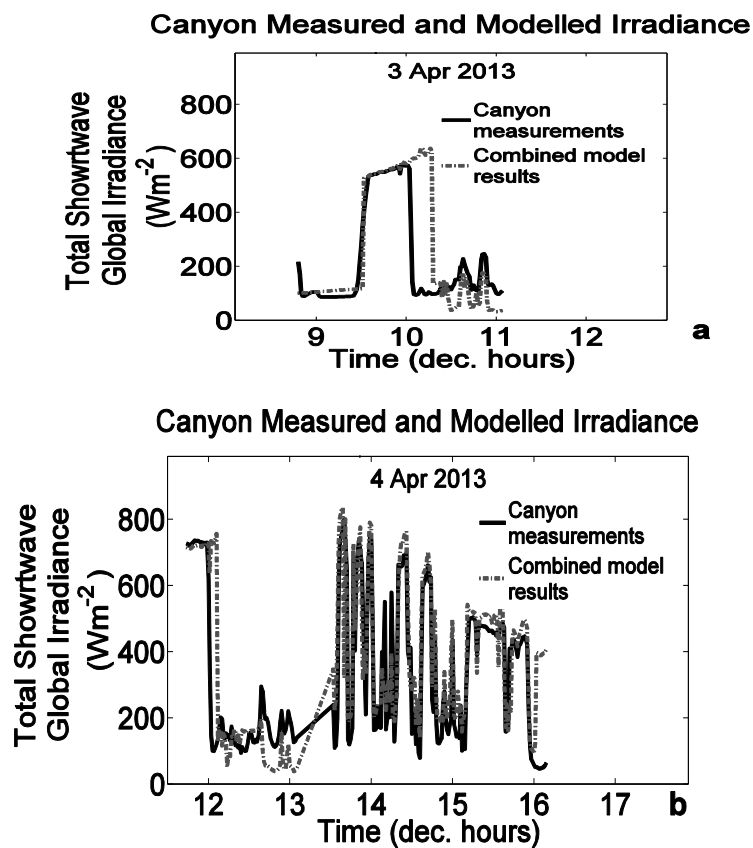


Figure 4-7 Comparison between modelled (dashed grey line) and measurements (black line) of global total-shortwave irradiances, conducted on 3 April (a) and 4 April (b) 2013, at the Dover Street Canyon, University of Manchester. The models have been constructed using Eq. 4.1 for a combined model which used full-sky view measurements and an idealised ratio of canyon to full sky irradiances.

The combined model shown in Figure 4-7 provides a better appreciation of the model's performance in respect to irradiance calculations and remaining sources of uncertainty. The time offset between measured and modelled direct beam incidence (e.g. 10.1h to 10.3h in Figure 4-7a) is directly related to the goodness of the reconstruction of urban geometries. For these times in Figure 4-7a as compared with Figures 4-2 and 4-4. It can be seen that at the corresponding azimuth angle the sun just grazes the canyon skyline; so any small inaccuracies in defining the building edges may lead to possible erroneous inclusion or exclusion of the solar disc in the calculations. Otherwise, there is a good correspondence between modelled and measured irradiance. Time offsets (i.e. horizontal differences between models and measurements in Figures 4-7a and b) are one way of describing discrepancies. Although it is not an accurate representation of the overall goodness of the projection, these observed time offsets between models and measurements evidence errors in the projection. For example, in Figure 4-7a an offset of approximately 15 minutes is observable after 10h. It should also be acknowledged that different positions in the canyon sometimes experience different irradiances (sunny and shady sides of the street) particularly when the sun is close to the building edge. In fact, separations of a few centimetres are enough to create large differences between different positions within a canyon, especially in regard to direct sunlight.

In general, the models and measurements of canyon irradiances are very similar. However the modelled canyon irradiance was often slightly underestimated when the sun was blocked by a building and slightly overestimated when the sun was visible in the canyon. This general pattern may indicate that the proportional contributions of direct and diffuse light are slightly biased, with the direct light having a larger weighting in the model than it takes in reality.

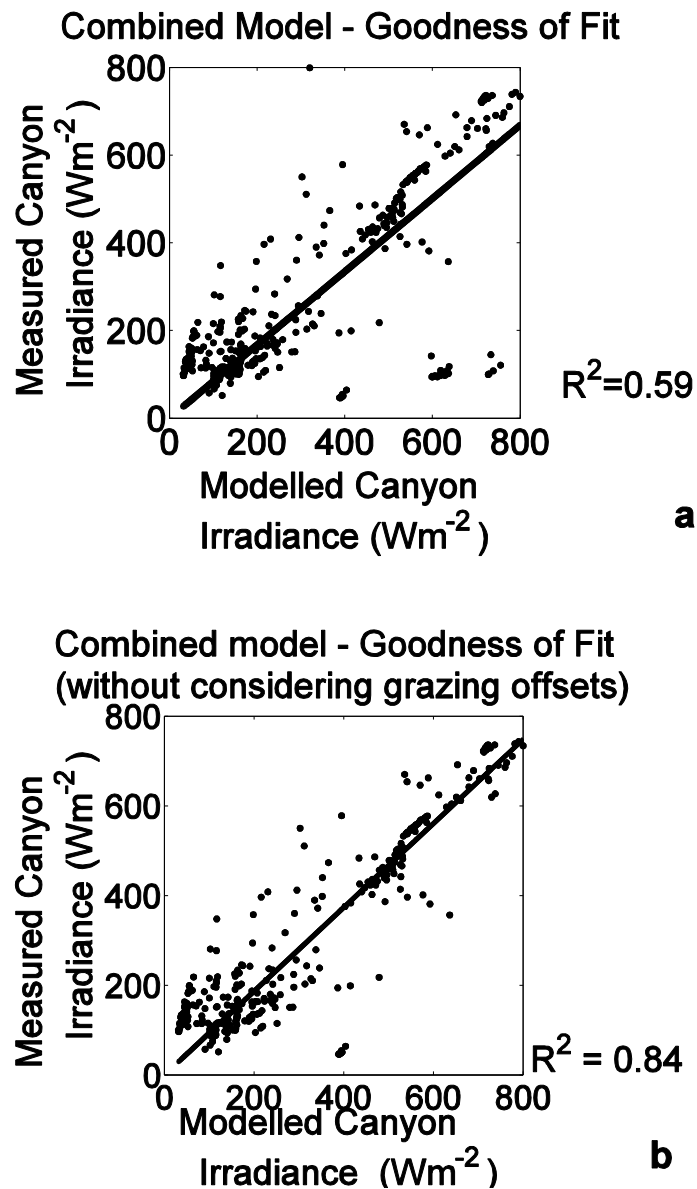


Figure 4-8 Goodness of fit of the model described by Eq.4.1 for the data from both 3 and 4 April 2013 together. (a) shows the scatter plot of measured against modelled data considering all points. (b) shows the scatterplot after removing the identified time offsets. Both panels include a linear fit and the corresponding  $R^2$  values.

According to Figure 4-8a the combined model explains 59% of the variation in the measured canyon irradiances. Note that the data in Figure 4-8a includes the errors resulting from the modelled building misplacements at the specific sky positions where the direct solar

beam transitions behind buildings. However, when excluding these few points (Figure 4-8b), the performance of the model increased to explain 84% of the variation in measurements.

## 4.4 Discussion

### 4.4.1 Reconstructed vs. Control Fisheye Hemispheric Images.

Hugin allowed both equidistant and orthographic projections to be reconstructed from the Google Street View images. In terms of radiation measurements on a horizontal surface, it is the orthographic image that is most useful. Flat-horizontal surfaces present a smaller response to radiation incident from high zenith angles as the response of many solarimeters and radiometers is proportional to the cosine of the zenith angle of the radiance from each region in the hemispheric view.

It is important to note that, although the fisheye lens used in this study has an orthographic projection, other fisheye lenses (commonly used in literature for describing urban canyons) have an equidistant projection instead. For equidistant images a cosine law must be applied *a-priori*; in order to calculate a geometrically correct SVF that matches the cosine response of a flat horizontal surface [39, 40]. This cosine law assigns a smaller weight to the area occupied by pixels towards the edge of the fisheye equidistant image (corresponding to the horizon line). In contrast, orthographic lenses compress objects towards the horizon line as a function of the sine of their zenith angles; this is equivalent to applying the same cosine law used to calculate the SVF from equidistant images. The use of the cosine law then becomes redundant when calculating the SVF from an orthographic image.

One advantage of the RayMan software is that it allows the user to choose whether or not to apply the cosine law when calculating SVFs [40], but the user must know the projection of the fisheye image, and the geometry of the reference surface. Users of magnetic mini-fisheye lenses (such as the one used in this study) must, therefore, be aware of the orthographic



projection of these lenses, and the need to choose the correct option in the RayMan software. The equidistant projection might still become very important when modelling irradiance upon non-flat surfaces, since, with an equidistant image one can match the sky views of either flat horizontal surfaces (cosine law applied) or spherical surfaces (cosine law not applied). Much of the information about walls and buildings contained in the equidistant projection is compressed towards the edges in an orthographic projection. However, this information can become highly relevant for vertical and spherical surfaces, for example when investigating human exposure to solar radiation. The human skin could be considered a complex combination of vertical and horizontal surfaces or a spherical surface for simplicity [27]. In any case, the radiative environment to which it is exposed differs a lot to that of the standard flat horizontal surfaces, used for general solar measurements. Different projections of reconstructed panoramas may allow researchers to infer SVFs for different purposes.

#### **4.4.2 Panorama reconstruction from Google snapshots**

The Google Street View images are taken from the carriageway rather than the pavement, and so are reasonably representative of the centre of the canyon. Yet, Figures 4-2 and 4-3 show images taken at different positions separated by only a few metres within the same canyon. Even with a relatively small separation it can be seen that the position of the camera — or similarly any surface receiving radiation — has a different perspective of the geometry of the canyon. In Figure 4-2 the southern wall dominates the upper-hemispheric view, whereas Figures 4-1 and 4-2 have the opposite walls as the main obstructing feature. Given that the Google Street View images must be specified by their coordinates in the Hugin model, one way to adjust the perspective of the viewer would be to rotate the relative hemispheric coordinates of the Google images in the hemispheric view. Figure 4-9 shows an example of the Google images tilted  $45^\circ$  in the hemispheric view and re-projected.

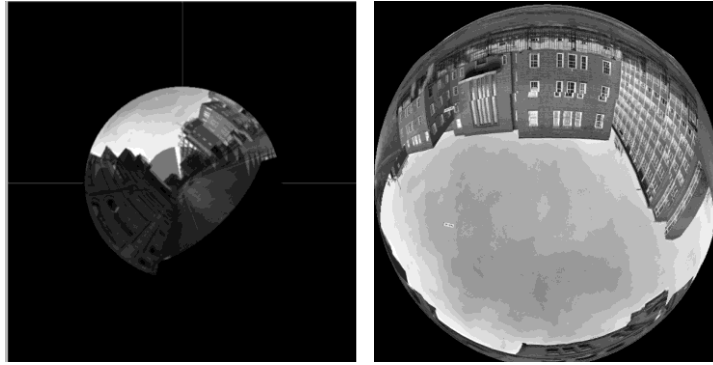


Figure 4-9 Hugin interface screen. Left-hand side: shows the overall 45° rotation made from Google snapshots. Right-hand side: The panorama was then orthographically re-projected in order to simulate the perspective of the Dover Street canyon from the opposite side of the road.

#### 4.4.3 Street-level total-shortwave irradiances

The general relationship between canyon and full sky irradiances was satisfactorily modelled ( $R^2 = 0.84$ , Figure 4-8b). The measurements conducted in this work generated a time series of canyon irradiances (Figures 4-6a and 4-6b), which illustrate the two main controls on canyon irradiances. These are the times of the day when the solar disc is blocked by buildings in the canyon, and times when clouds cover the solar disc. When the solar disc is not blocked by the buildings in a canyon, the irradiance patterns closely follow those received under an unobstructed view. Such patterns also include any intermittent drops due to cloud cover (e.g. around 14.0 h in Fig 6b). In such cases, clouds (instead of buildings) are the determining factor blocking direct solar radiation, but their effect is inherent in the signal from the unobstructed (full-sky) pyranometer.

At times when the solar disc is blocked by the canyon buildings, the canyon irradiance comes only from diffuse radiation and hence remains low irrespective of any cloud cover of the sun. In this case, the building obstruction becomes the controlling modification on the canyon irradiance. The small effect of diffuse irradiance blocking due to the reduced SVF

could also be seen in the model (e.g. 9.5 – 10.0 h in Fig 6a). It is important to mention that the original articles describing the RayMan model [27, 43] included validations of the calculated total-shortwave irradiances under an unobstructed clear sky and for mean radiant temperatures within an urban canyon. However, the performance of calculated irradiances within canyons had not been tested. Our results provide support for the usefulness of the RayMan model for calculating urban canyon total-shortwave irradiances.

It is also important to acknowledge that the models presented here depend on nearby observatory measurements. Any street canyon located far away from the full sky measurements will potentially present larger differences, particularly in broken-cloud conditions.

The proportional contributions of direct and diffuse light to global irradiance also need to be analysed. As was mentioned earlier, the model seems to have overestimated canyon irradiances when the sun is visible and underestimate them when the sun is blocked; this suggests that the proportional contribution of direct sunlight is outweighed. These kind of problems can be solved when complementing the models with further measurements of turbidity or aerosol and water vapour contents in the atmosphere. An atmosphere with increased turbidity (e.g. due to a higher concentration of aerosols or water vapour) will tend to absorb and scatter any passing beam of light (e.g. direct sunlight), thus reducing its intensity. At the same time, the increased amounts of scattered radiation, in turn, increases the proportion of diffuse radiation from the atmosphere. The RayMan software allows the modification of the atmospheric turbidity, which would need to be supported by observatory measurements.

Future work to improve these kinds of model is to consider the anisotropy of diffuse irradiance, since on a clear day the circumsolar region has a higher radiance than other areas

of the sky. The effects of blocking the circumsolar region can be observed in Figure 4-7a at about 9.5 decimal hours: while the modelled irradiance series predicted a sharp transition of the solar disc from behind an obstruction, the measurements showed a smooth curve. This smooth curve is explained by the partial blocking of the circumsolar radiation (brightest regions of diffuse light), which by definition cannot be modelled when assuming an isotropic diffuse component. A model of the anisotropy of diffuse light would allow us to assess the position, size, and intensity of the circumsolar region; therefore calculate more accurately the amounts of the estimate of the blocked diffuse irradiance in the canyon at different times of the day may become more accurate. The current models, however, consider diffuse light to be isotropic, which means that obstructions of similar size have the same effect on diffuse light, regardless of their azimuthal orientation in the canyon.

Additional improvements of these models may include a spectral partitioning of total-shortwave irradiances, considering that each wavelength is affected by the atmosphere and the horizon obstructions in a different manner. Spectral irradiance models are of great interest to the study of biological processes, e.g. human exposure to ultraviolet radiation because responses are often strongly wavelength dependent. Finally, the inclusion of complex building reflections of sunlight, along with automated material identification algorithms from colour images, may also increase the precision of the models; especially in extreme cases where metal coatings or glass walls are the dominant feature within the urban canyon. One of the major advantages of the Google Street View images is precisely the colour information they contain about the urban canyons, which can be related to the underlying materials and their reflective properties.

#### **4.5 Conclusions**

Urban geometries reconstructed with the Hugin software may be projected onto a plane using different geometrical algorithms (e.g. orthographic or equidistant projections, among

others). In this study we found that the orthographic projection of the reconstructed canyon approximately matched an orthographic camera image taken with a fisheye lens (SVFs of 0.503 and 0.550, respectively). This type of projection is useful to represent the sky view of flat-horizontal surfaces. On the other hand, an equidistant projection was needed because of the specific projections of the solar path across the sky used by the RayMan software. The options provided by Hugin are, therefore, highly useful for suiting different research needs (i.e. to match different optical devices or to match the exposure of different surface geometries).

The RayMan software was used to model the total-shortwave irradiances for the reconstructed urban canyon. These models combined with full-sky measurements represented a good approximation to the measured canyon irradiance in all sky conditions. This close correspondence ( $R^2=0.59$  to  $0.84$  depending on sky conditions) provides support for future use of reconstructed canyons with the method proposed here, in order to calculate irradiance within urban canyons.

The use of Google Street View in combination with free access software we demonstrates that it is possible to reconstruct fisheye images of urban canyons and their associated irradiance throughout the day, without the need of detailed and expensive 3D models. The method has been validated in Manchester, UK, but in principle it could be applied at any location where Google Street View images exist. The reconstructed urban geometries provide accurate descriptions that may be used for more general scientific purposes beyond the examples provided here. Other applications of this approach may be worth considering in the near future, e.g. SVF calculations for energy exchanges, daylighting or human exposure.

## Acknowledgements

This work was generously funded by the Mexican Council for Science and Technology (CONACyT) (grant reference: 214428). Google are acknowledged as the proprietors of all images extracted from the Google Street View database. Finally we thank the staff of the Whitworth Observatory, University of Manchester for providing the rooftop measurements dataset [<http://www.cas.manchester.ac.uk/restools/whitworth/>].

## References

1. A. McKinley, M. Janda, J. Auster, and M. Kimlin, "In Vitro Model of Vitamin D Synthesis by UV Radiation in an Australian Urban Environment," *Photochemistry and Photobiology* 87, 447-451 (2011).
2. E. Andreou, "The effect of urban layout, street geometry and orientation on shading conditions in urban canyons in the Mediterranean," *Renewable Energy* 63, 587-596 (2014).
3. Y. Kurazumi, T. Tsuchikawa, N. Matsubara, E. Kondo, and T. Horikoshi, "Evaluation of enhanced conduction-corrected modified effective temperature ETFe as the outdoor thermal environment evaluation index," *Energy and Buildings* 43, 2926-2938 (2011).
4. A. W. Schmalwieser, C. Enzi, S. Wallisch, F. Holawe, B. Maier, and P. Weihs, "UV Exposition During Typical Lifestyle Behavior in an Urban Environment," *Photochemistry and Photobiology* 86, 711-715 (2010).
5. A. R. Webb, "Who, what, where and when—influences on cutaneous vitamin D synthesis," *Progress in Biophysics and Molecular Biology* 92, 17-25 (2006).
6. C. S. B. Grimmond, S. K. Potter, H. N. Zutter, and C. Souch, "Rapid methods to estimate sky-view factors applied to urban areas," *International Journal of Climatology* 21, 903-913 (2001).
7. I. D. Watson, and G. T. Johnson, "Graphical estimation of sky view-factors in urban environments," *Journal of climatology* 7, 193-197 (1987).
8. T. Gal, F. Lindberg, and J. Unger, "Computing continuous sky view factors using 3D urban raster and vector databases: comparison and application to urban climate," *Theoretical and Applied Climatology* 95, 111-123 (2009).
9. S. Yamashita, K. Sekine, M. Shoda, K. Yamashita, and Y. Hara, "On relationships between heat island and sky view factor in the cities of Tama River basin, Japan," *Atmospheric Environment* (1967) 20, 681-686 (1986).
10. M. K. Svensson, "Sky view factor analysis – implications for urban air temperature differences," *Meteorological Applications* 11, 201-211 (2004).
11. B. Holmer, S. Thorsson, and I. Eliasson, "Cooling rates, sky view factors and the development of intra-urban air temperature differences," *Geografiska Annaler: Series A, Physical Geography* 89, 237-248 (2007).
12. Y. Nakamura, and T. R. Oke, "Wind, temperature and stability conditions in an east-west oriented urban canyon," *Atmospheric Environment* (1967) 22, 2691-2700 (1988).
13. M. Eeftens, J. Beekhuizen, R. Beelen, M. Wang, R. Vermeulen, B. Brunekreef, A. Huss, and G. Hoek, "Quantifying urban street configuration for improvements in air pollution models," *Atmospheric Environment* 72, 1-9 (2013).

14. J. Unger, "Connection between urban heat island and sky view factor approximated by a software tool on a 3D urban database," *International Journal of Environment and Pollution* 36, 59-80 (2009).
15. C. L. Tan, N. H. Wong, and S. K. Jusuf, "Outdoor mean radiant temperature estimation in the tropical urban environment," *Building and Environment* 64, 118-129 (2013).
16. S. Zhu, H. Guan, J. Bennett, R. Clay, C. Ewenz, S. Benger, A. Maghrabi, and A. C. Millington, "Influence of sky temperature distribution on sky view factor and its applications in urban heat island," *International Journal of Climatology* 33, 1837-1843 (2013).
17. P.-C. Lai, C.-T. Low, W.-S. C. Tse, C.-K. Tsui, H. Lee, and P.-K. Hui, "Risk of tuberculosis in high-rise and high density dwellings: An exploratory spatial analysis," *Environmental Pollution* (2013).
18. L. Chen, E. Ng, X. An, C. Ren, M. Lee, U. Wang, and Z. He, "Sky view factor analysis of street canyons and its implications for daytime intra-urban air temperature differentials in high-rise, high-density urban areas of Hong Kong: a GIS-based simulation approach," *International Journal of Climatology* 32, 121-136 (2012).
19. S. Park, and S. Tuller, "Advanced view factor analysis method for radiation exchange," *International Journal of Biometeorology*, 1-18 (2013).
20. J. Strømmand-Andersen, and P. A. Sattrup, "The urban canyon and building energy use: Urban density versus daylight and passive solar gains," *Energy and Buildings* 43 (2011).
21. M. Lu, and J. Du, "Assessing the daylight and sunlight availability in high-density residential areas: a case in North-east China," *Architectural Science Review* 56, 168-182 (2013).
22. J. Hofierka, and M. Zlocha, "A New 3-D Solar Radiation Model for 3-D City Models," *Transactions in GIS* 16, 681-690 (2012).
23. F. Lindberg, and C. Grimmond, "The influence of vegetation and building morphology on shadow patterns and mean radiant temperatures in urban areas: model development and evaluation," *Theoretical and Applied Climatology*, 1-13-13 (2011).
24. J. Turner, and A. V. Parisi, "Measuring the influence of UV reflection from vertical metal surfaces on humans," *Photochemical and Photobiological Sciences* 8, 62-69 (2009).
25. A. Tsangrassoulis, and M. Santamouris, "Numerical estimation of street canyon albedo consisting of vertical coated glazed facades," *Energy and Buildings* 35, 527-531 (2003).
26. N. L. Alchapar, E. N. Correa, and M. A. Cantón, "Classification of building materials used in the urban envelopes according to their capacity for mitigation of the urban heat island in semiarid zones," *Energy and Buildings* 69, 22-32 (2014).
27. A. Matzarakis, F. Rutz, and H. Mayer, "Modelling radiation fluxes in simple and complex environments: basics of the RayMan model," *International Journal of Biometeorology* 54, 131 (2010).
28. T. M. Smith, and V. Lakshmanan, "Utilizing Google Earth as a GIS platform for weather applications," in *22nd International Conference on Interactive Information Processing Systems for Meteorology, Oceanography, and Hydrology*(2006).
29. G. Dall'O', A. Galante, and M. Torri, "A methodology for the energy performance classification of residential building stock on an urban scale," *Energy and Buildings* 48, 211-219 (2012).
30. R. Patel, N. Warren, M. Williams, E. Chen, and X. Xu, "An investigation of urban agriculture on residential blocks in Vancouver," (2011).
31. A. Dragomir, "Google Street View: Capturing the World at Street Level," D. Carole, F. Daniel, F. Christian, L. Stephane, L. Richard, O. Abhijit, V. Luc, and W. Josh, eds. (2010), pp. 32-38.

32. A. R. Zamir, and M. Shah, "Accurate image localization based on google maps street view," in *Computer Vision–ECCV 2010*(Springer, 2010), pp. 255-268.
33. L. Vincent, "Taking online maps down to street level," *Computer* 40, 118-120 (2007).
34. A. Frome, G. Cheung, A. Abdulkader, M. Zennaro, B. Wu, A. Bissacco, H. Adam, H. Neven, and L. Vincent, "Large-scale privacy protection in google street view," in *Computer Vision, 2009 IEEE 12th International Conference on*(IEEE2009), pp. 2373-2380.
35. A. G. Rundle, M. D. M. Bader, C. A. Richards, K. M. Neckerman, and J. O. Teitler, "Using Google Street View to audit neighborhood environments," *American journal of preventive medicine* 40, 94-100 (2011).
36. P. d'Angelo, "Radiometric alignment and vignetting calibration," *Proc. Camera Calibration Methods for Computer Vision Systems* (2007).
37. D. M. German, P. d'Angelo, M. Gross, and B. Postle, "New methods to project panoramas for practical and aesthetic purposes," (*Eurographics Association*), pp. 15-22.
38. C. Reinhart, Christoph. "Daylight performance predictions." *Building performance simulation for design and operation* 235 (2011)..
39. D. G. Steyn, "The calculation of view factors from fisheye-lens photographs: Research note," *Atmosphere-Ocean* 18, 254-258 (1980).
40. M. Hämmerle, T. Gál, J. Unger, and A. Matzarakis, "Comparison of models calculating the sky view factor used for urban climate investigations," *Theoretical and Applied Climatology*, 1 (2011).



## Chapter 5

The previous chapter described a reconstruction of urban geometries where manual user input was required to delineate the profile of buildings in the canyon; this, by using a tool provided by the RayMan software. In this chapter the potential use of parametric and non-parametric image training algorithms will be described for the automatic classification of sky/building pixels in the reconstructed canyon images.

The methods presented here additionally illustrate the possibilities of automatizing the identification of pixels corresponding to different materials of the panoramic view (e.g. windows, bricks, trees). Although these algorithms show promise for future use in assessing reflections within urban canyons, they have not been included in the general methods of this thesis for calculating street canyon solar irradiance (which, for simplicity, assume that obstructions are non-reflecting). To incorporate real surface effects further research is needed regarding the reflective and/or transmissive properties of different materials and then their complex interactions with sunlight, due to the ever changing juxtaposition of source, surface and target. While this complexity is beyond the scope of this thesis, these preliminary investigations illustrate the promise of such techniques for future studies.

## Use of image-learning algorithms to facilitate the automatic reconstruction of the urban geometry reconstruction from Google Street View

### Abstract

Automatic material identification from panoramic components may be a useful aid for describing sky obstructions and, potentially, the radiation reflections within street canyons. The present chapter explores the outcomes of using different supervised image-learning algorithms for the classification of various urban panoramic components in an image. Firstly, a widely-used software package, MAXENT (Phillips et al., 2006) is used in order to illustrate the general suitability of supervised classification algorithms in the identification of urban materials (i.e. sky, building walls, road surfaces, trees and windows). Results are presented as a classified image, where each pixel is assigned to a different class. Finally, a simple classification algorithm written by the author is presented. The algorithm written in the *Octave* programming language allows the implementation of non-parametric analyses to generate more flexible classification rules.

### 5.1 Introduction

The geometry of sky obstructions at the street level is the main factor affecting the solar radiation that reaches any individual urban canyon (Matzarakis et al., 2010). A key step to describe sky obstructions is to differentiate sky sections from buildings in an urban panoramic view, for example, a fisheye or a rectilinear photograph of a specific urban canyon. Software packages like RayMan provide tools for the manual delineation of street canyon profiles in a “fisheye” projection of an urban canyon. However, the manual delimitation of horizon obstructions of each individual canyon in a large city may become a problematic task. Other partially automatic algorithms to identify sky/building pixels are generally based on user-determined threshold digital brightness value, for discriminating between both classes (e.g. Holmer et al., 2001). Computer-based image-learning algorithms

(e.g. MAXENT, Phillips et al., 2006) may reduce time and effort through the automatic identification of panoramic components.

The present work proposes the use of image-learning algorithms that remove the need for manually defining threshold values or manually delineating horizon obstructions. The algorithms still require some user input in the creation of a “training set” of pixels that belong to a desired class (e.g. sky pixels). However, once trained, these algorithms can be automatically applied for characterizing horizon obstructions on other images, potentially extending to the numerous individual street canyons across large cities. Firstly, the use of the MAXENT algorithm is proposed for parametric image classification from multi-band RGB images. Then, a non-parametric approach is proposed, based on the histograms of RGB values of sky-pixels. Finally, further strategies are discussed to improve classifications, through the use of convolution matrix operations for the analysis of the neighbourhood of “problematic” pixels (e.g. a reflecting window-pixel that appears as a sky-pixel). According to Chapman and Thornes (2004), the main disadvantage faced with this “threshold” method is that dark clouds (or bright building walls) can be erroneously assigned to the opposite class due to brightness alone. Neighbouring information may provide a means for distinguishing between bright sky and bright windows.

Considering that wall reflections of sunlight in an urban canyon may—at certain times—contribute to street-level irradiance, the MAXENT algorithm has also been used to distinguish between other urban panoramic components (i.e. windows, bricks, road surfaces, trees). The spectral albedo signatures of different materials have been reported previously (Feister and Grewe, 1995; Heisler and Grant, 2000) and this information may be of great importance at specific urban canyons dominated by highly reflective materials. Metal coatings or glass windows may become important reflectors that increase solar irradiances at certain times of the day (Turner and Parisi, 2009). Trees, on the other hand, may filter part of

incoming radiation (Lindberg and Grimmond, 2011). Thus, the correct identification of specific materials in the streets is also a potential aid for the creation of accurate micro-meteorological models at individual street canyons.

### **5.1.1 Identification of urban panoramic components**

For the purposes of this text, the concept of “urban panoramic component” is defined as any material present within the hemispherical panoramic view. Urban components can include construction materials such as brick walls, road surfaces, glass or metal, as well as vegetation materials like grass and trees. Sky sections of the images can be mathematically treated as another panoramic component.

The automatic identification of panoramic components falls within the general methods for image classification. One strategy, known as supervised classification, requires the user to select a specific set of pixels, known to belong to a certain class “A”. This set of selected pixels will be called a training set and the corresponding pixel values will be called training values. The core of the algorithms consists of obtaining descriptive statistics (i.e. mean and standard deviation) from the training values, then, the rest of the pixels in the image are evaluated in terms of their “similarities” to the training values. These “similarities” regard the position of each pixel value within the frequency distribution curve of the training values. Parametric supervised algorithms assume predetermined shapes of the frequency distribution curves (e.g. a normal distribution around the training mean). These methods are usually multivariate, having several layers of information in order to classify the pixels. For example, the digital brightness values of the Red, Green and Blue bands of any digital colour image (RGB bands) may be considered as different information layers. A frequency distribution of training values must be described for each different layer of information. In non-supervised classification, the class frequency distributions are unknown. Non-supervised algorithms are based on the iterative creation of random classes, with random centres of distribution. In such

cases, the user may determine the number of random classes to be created, and may also define a desired standard deviation for the classes. The present work focuses on supervised classification only; where the user provides a set of training points in order to classify the image.

The final result of a supervised classification process is a value assigned to every pixel in the image, which is proportional to its probability of belonging to the user-defined class “A”. Although the algorithms require some initial user input, materials may then be identified in several images on the basis of the first training image.

### **5.1.2 Parametric Classification**

A training set of pixels, known to belong to a certain class “A”, allows the calculation of statistical descriptors. Parametric classification consists of assuming that pixel values within the training set will distribute normally around the training average. Any pixel in the image has a probability of belonging to class “A” given the location of the pixel value with respect to the normal frequency distribution of training values. To exemplify this, Figure 5-1 shows the RGB signatures of digital values, at pixels identified by the author as sky in a colour photograph.

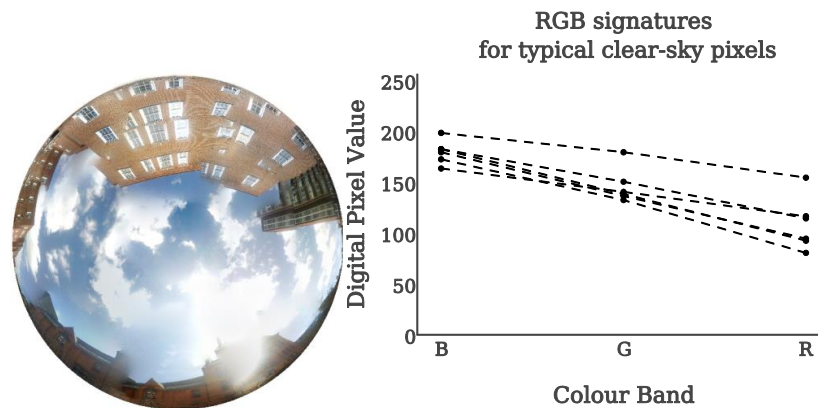


Figure 5-1 Left panel: RGB colour photograph of an urban canyon. Right panel: Scatter plot of digital pixel values in the RGB bands, for pixels identified as “clear-sky”. “Clear-sky” pixel values correspond to five arbitrarily chosen pixels, from the blue-sky sections in the left panel. RGB bands in the x-axis (right panel) have been put in inverse order (BGR) as proportional to the electromagnetic wavelength ranges they represent.

The canyon projection on Figure 5-1 was created using the open-source Hugin software (d’Angelo, 2007; German et al., 2007) for the construction of panoramic projection, on the basis of rectilinear images extracted from Google Street View (see Carrasco-Hernandez et al., 2015).

The scatter plot, Right panel in Figure 5-1, exemplifies typical signatures of clear-sky pixels. The scattered RGB (or BGR) training values of the “clear-sky” class will tend to distribute around average or centroid RGB values, which define the spectral signature of an average clear-sky pixel. Then, the RGB signature of any other pixel “*i*” in the image may fall close or far away from the centroid signature, depending on whether “*i*” belongs—or not—to the clear-sky class. Therefore, in parametric algorithms, a probability of belonging to the class “clear-sky” may be calculated for each pixel in the image, under the assumption that pixel values within the class have a normal probability distribution around the training average at each band.

It can be said that some layers of information (RGB bands) may be “more relevant” than others, due to the tightness of the scattering of pixel values in each band. The selected training pixels show narrowly scattered values in the blue band (B), with an average digital value of approximately 175 (Right panel, Fig. 5-1). However, the distribution of values in the red band (R) is seemingly more spread. Because the blue band training values are more restricted around the average, the blue band can be regarded as a better classifier for clear-sky pixels. Considering the small standard deviation of the training values in the blue band, any pixel not belonging to the clear-sky class will be probabilistically distant to the training centroid; this occurs because the calculations of probabilities of belonging to the class are weighted by the standard deviation at each band.

### **5.1.3 Non parametric image classification**

The normal distribution of training values around an average is usually true for homogeneous classes. However, certain user-defined classes are in reality comprised of two or more subclasses, which causes the distributions of pixel training values to depart from the expected normal distribution; in which case they tend to have a bimodal or a multi-modal distribution. The basic principle of non-parametric statistics is to avoid assuming any type of theoretical probability distributions. These methods mainly work on the basis of empirical frequency histograms, obtained directly from the sample training set. The sky, as an urban component, is a good example of a heterogeneous class as it usually comprises two subclasses (i.e. clear sky and clouds). Figure 5-2 shows the RGB signatures of pixels identified as clouds in the photograph previously shown in Figure 5-1.

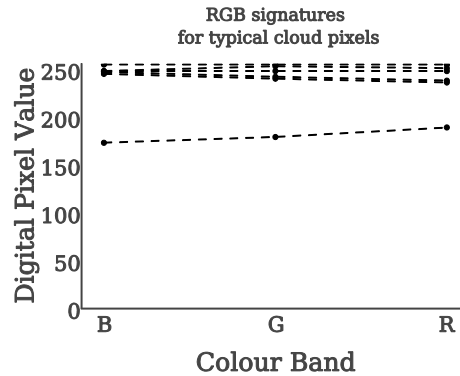


Figure 5-2 Digital pixel values in the RGB bands, for three arbitrarily chosen pixels identified as “cloud”. Cloud-pixels were manually chosen from the Left panel on Figure 5-1. RGB bands in the x-axis (right panel) have been put in inverse order (BGR) as proportional to the electromagnetic wavelength ranges they represent.

Notice how the signature of the “cloud” class in Figure 5-2 is different from that of the “clear-sky” class (Figure 5-1). If we combined both classes into one single “sky” class, the frequency distribution would be bimodal. Therefore, the assumption of a normal distribution around a hypothetical average would render any true “sky” pixel as unlikely to belong to the class, due to its distance from the assumed average.

The present chapter explores the outcomes of using different supervised learning algorithms for the classification of urban components in an image. Firstly, a widely-used classification software (MAXENT) is used in order to illustrate the general suitability of supervised classification algorithms to identify urban components. However, MAXENT is an example of a parametric algorithm that assumes a normal distribution of training values. Then, a simple classification algorithm written in the Octave language is presented. This second algorithm allows the implementation of a non-parametric analysis for classifying heterogeneous classes.



## 5.2 Methods

### 5.2.1 MAXENT image classification

MAXENT stands for Maximum Entropy in general information theory, which—in simple terms and for image classification applications—attempts to assign to all pixels in the image the most uniform probability of belonging to a class (i.e. the maximum entropy distribution). At the same time it must satisfy another restriction that for every layer of information (e.g. the RGB bands), the total sum of weighted pixel values (i.e. each pixel value multiplied by its assigned probability) should equal the training average (Phillips et al., 2010). For any image there is only one solution that satisfies both restrictions and it usually assigns higher probability to those pixels closer to the training average, without exaggerating the differences in probability with the rest of the pixels. Maximum entropy algorithms applied to image classification provide the advantage of requiring only-presence data, instead of requiring both presence and absence data, thus demanding less user input (Li and Guo, 2010). The MAXENT algorithm by Phillips et al. (2006) is generally used with maps in image formats (i.e. raster maps) to model geographic phenomena such as land-use or the distribution of biological species. Yet, the software can be used for general image classification problems, with any type of image in ESRI ASCII format (from the ArcGIS software).

In this work, a few urban panoramic components (or classes) have been identified using MAXENT. Firstly, a Google Street View photograph was imported to a \*.bmp file (Figure 5-3). The colour image was then separated into its Blue, Green and Red bands (Figure 5-4). This image will be used for training the classifying algorithm. Five different training sets were created comprising the urban components: Sky, Walls, Ground Concrete, Trees and Windows.



Figure 5-3 Original Image from Google Street View.



Figure 5-4 Blue, Green and Red Bands (in that order) extracted from the original image.

In Figure 5-4 notice, for example, how red bricks are brighter in the right hand side image which corresponds to red colours.

A point vector file was created in ArcGIS with training points (Figure 5-5) for five different classes (i.e. trees, road surfaces, sky walls, windows), corresponding to examples of common urban panoramic components. In ArcGIS, a vector file is associated to a spreadsheet data file containing, for each point, an identification number (ID number) (later associated to each class) and x-y coordinates of its relative position. This information will allow the extraction of training RGB values for each class.

The training points for each class were chosen visually. With the intention of covering the full range of RGB values for each class, the manual assignation of training points attempted to include the extremes of apparent brightness of each class, as well as covering the spatial extent of each class within the image. The resulting sample sizes for each class are arbitrary, but all the classes are represented by at least 20 points. A total of 185 training points including all the classes were associated in the ArcGIS vector file with ID numbers (1 – 185),

corresponding to the different classes as follows: ID numbers 1 – 27 for trees; ID numbers 28 – 77 for road surfaces; ID numbers 77 – 125 for sky; ID numbers 125 – 146 for walls. ID 146-185 for windows.



Figure 5-5 Training points assigned manually to represent each urban panoramic component: trees, road surfaces, sky, walls and windows. Each point was associated to its corresponding class in an ArcGIS spread sheet file.

In order to run MAXENT, all the information layers from ArcGIS must be exported as ASCII raster format. Additionally the training locations and identification strings (ID) must be submitted as a spread sheet file. With this input information the MAXENT algorithm will extract RGB training values and then calculate the probability of the rest of the pixels to belong to each class. Notice that each different class will behave as an independent training set, therefore, the final classification will return six different probabilities for each pixel. Each pixel may finally be assigned to the class of higher probability.

The MAXENT algorithm assumes a normal distribution of each band's training values within homogeneous classes. In the following section, the methods of a second algorithm will be described that allow the non-parametric classification of a heterogeneous "sky" class (i.e. all sky conditions).

### **5.2.2 A simple non-parametric supervised classification algorithm**

A non-parametric algorithm was written in the Octave language to classify sky pixels under a broken-cloud sky. As explained before, "sky" pixels under such conditions will

comprise at least two subclasses: “clear-sky” and “cloud”. Therefore the frequency distributions of training values, in each RGB band are expected to be—at least—bimodal.

The non-parametric algorithm requires two images as input data: i) a colour image to be classified (Figure 5-6, Left panel) and ii) a training image (Figure 5-6, Right panel), where individual pixels identified by the user as “sky” have a white colour (digital value  $\approx 255$ ); the rest of the pixels have a black colour (digital value of 0). Notice that, unlike the MAXENT software, this simple algorithm does not require a spread sheet file containing the locations and ID strings of the training points. The training image can be easily created on top of the original image, using common software such as Adobe Photoshop or MyPaint. Figure 5-6 shows the input images used in this example.

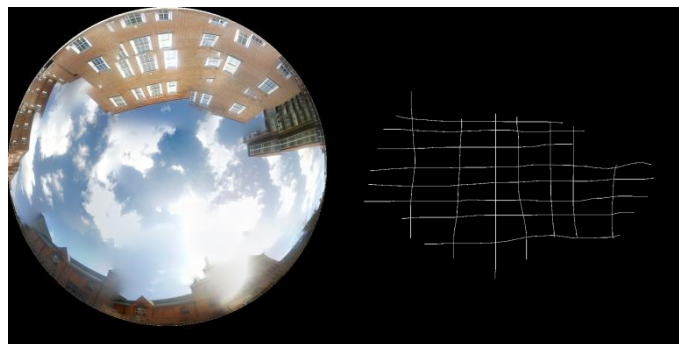


Figure 5-6 Left panel: RGB fisheye projection of an urban canyon to be classified. Right panel: Image layer where a sample of “sky” pixels have been assigned with a white colour (digital value of circa 255). The training set image was manually created, using the MyPaint software, as an independent layer drawn on top of the original image.

### 5.2.3 Description of the non-parametric algorithm

The algorithm presented here consists of the automatic analysis of frequency histograms from the training values of the three colour bands (RGB). From the histograms, three probability distributions ( $p_R$ ,  $p_G$  and  $p_B$ ) of pixel values can be created, expressed as:

$$pX_v = \frac{\text{Pixel count}_v}{N}, \quad (\text{Eq. 5.1})$$

where  $pX_v$  is defined here as the probability of the digital value  $v$  occurring within the “sky” class, in the band “ $X$ ”. “ $X$ ” may refer to any of the three bands (R,G or B). *Pixel count* <sub>$v$</sub>  refers to the count of pixels in the training set that hold the digital value  $v$ . Finally  $N$  is the number of training pixels.

Then, the values of each pixel in the image may be evaluated independently for the three colour bands. Given that each pixel value  $v$  at each band  $X$  is now associated to a probability of occurring within the “sky” class, each pixel can be assigned with a band probability of belonging to the class, which equals  $pX_v$ . The overall probability of each pixel belonging to the class “sky” is given as the combined probability at the three independent bands.

A final consideration must be made in case a band of information is *less relevant* to the classification of pixels. An example of a less relevant band was already given in Figure 5-1, which showed how the clear-sky pixels had more widely distributed values in the Red band. In such cases, the frequency distributions of the training values will tend to show low pixel counts at any given value; therefore, any pixel in the image will have a low probability of belonging to the “sky” class due to the Red band. This in turn, may affect the overall probability calculation. In order to avoid this issue, a weighted probability is proposed, given the “relevance” of each band. It is proposed that the band relevance can be measured as the maximum probability  $\max(pX_v)$ , from the non-parametric probability distribution calculated with Eq. 5.1. Then, the overall pixel probability  $p$  of belonging to the “sky” class (considering the pixel values at all three information layers) may therefore be calculated as:

$$p = [(1 + \max(pR_v)) \cdot pR_v] \cdot [(1 + \max(pG_v)) \cdot pG_v] \cdot [(1 + \max(pB_v)) \cdot pB_v]. \quad (\text{Eq. 5.2})$$

## 5.3 Results

### 5.3.1 Supervised classification of a street photograph to identify urban components.

MAXENT returned a set of images indicating the probability that each pixel has of belonging to each urban component. Images were imported back to ArcGIS to conduct a multivariate analysis to identify, for each pixel, which urban component has the highest membership probability, using the tool “Local Cell Statistics”. In Figure 5-7 each pixel is assigned to the class for which it obtained the highest membership probability.

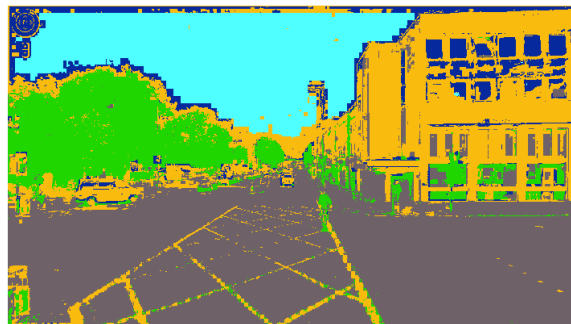


Figure 5-7 Showing the classification of image 5.3, pixels are classified according to their highest probability of membership to an urban component: Grey: road surfaces Green: tree. Light Blue: sky; Dark Blue: windows; Yellow: wall

As can be seen in the classified image (Figure 5-7), some errors do occur during the classification, e.g. some windows were classified as vegetation. However, the example still illustrates how image-learning algorithms provide acceptable coarse classifications for the automatic identification of different urban components. The possible reasons for misclassifications will be discussed later.

### 5.3.2 Results for the non-parametric classification of “sky” pixels

Sky pixels have been automatically identified for the canyon fisheye projection shown in Figure 5-6. Figures 5-8 A to C show the frequency distribution histograms of the training values for the RGB information layers.

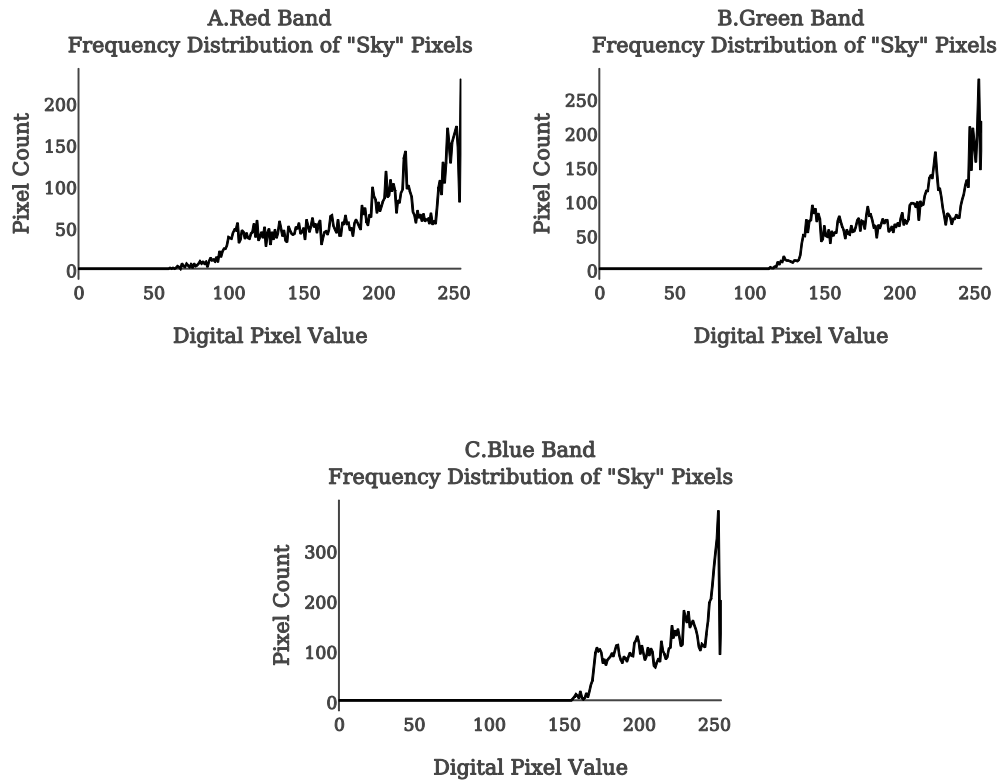


Figure 5-8 Frequency distribution histograms of the RGB bands obtained from the training set of “Sky” pixels shown in Figure 5-6. A. Red Band, B. Green Band, C. Blue Band.

Next, Figure 5-9 shows the probability assigned to each pixel of belonging to the heterogeneous “sky” class. Notice how this simple algorithm is not yet able to distinguish between the white clouds and the white window frames, nor between reflected and true sky. Strategies to improve the classification will be discussed below.

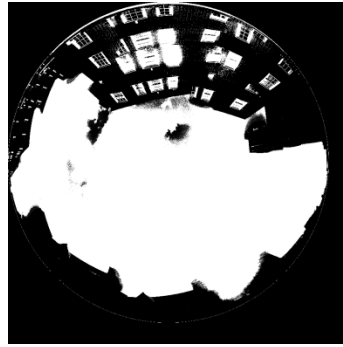


Figure 5-9 shows the classification of sky pixels in the image using the non-parametric algorithm presented in this text.

#### **5.4 Discussion**

The main issue behind classifying errors in Figure 5-7 is that misclassified pixels have a very small probability of belonging to any class. Despite this, a pixel that cannot be recognized as belonging to any class will still be classified, being assigned to the urban component to which it has the greatest similarities, however small the margin between probabilities. This could be a source of noise and bias in the model. To assess this problem the tool “Maximum” from cell statistics in Arc GIS was used to show the maximum probability value, among all classes.

The following image (Fig. 5-10) shows the maximum probability of each pixel of belonging to a class. Black coloured pixels are pixels which are simply too different from any of the classes defined during training to be reliably classified, i.e. they have a low probability of belonging to any class.





Figure 5-10 Showing for each pixel the highest probability of membership to any class. Black pixels show very low probabilities of belonging to any of these classes.

If Figures 5.7 and 5.10 are compared, it becomes clear that pixels with erroneous classifications are usually those with a low probability of belonging to any given class. One outstanding example is the case of people appearing in the image, since the RGB signatures of people would differ greatly from those of the other classes. For this reason, “people” and the rest of misclassified pixels appear as “black” regions in Picture 5.10. In Figure 5-10 the pixels with digital values  $< 30$  roughly correspond to the misclassified pixels of Figure 5-7. The number of pixels with a digital value  $< 30$  represented 11.6% of the pixels in the image. This can be interpreted as 11.6 % of misclassified pixels.

It is also important to mention the effect of having more than one training class in the classification. The MAXENT classification (Figure 5-7) showed remarkably good results. However, this is partially due to assigning each pixel to the class of highest probability of membership, regardless of their resemblance to other classes. On the other hand, Figure 5-9 (obtained with the non-parametric algorithm) shows the errors that may arise from having one single training class, i.e. If an additional “window” class existed for Figure 5-9, it is possible that window pixels would have been assigned to this class, despite their high resemblance to “sky” pixels. Nonetheless, if the window is reflecting sky as seen from the

position of the observer, then it is arguable whether or not, for that period of time, it should be correctly classified as sky when considering reflecting sources of radiation.

#### **5.4.1 Non-parametric classification**

The need for non-parametric classification algorithms becomes clear with the histograms shown in Figures 5.8 A to C. Notice in Figure 5.8 how the training frequency distributions in the three bands are, at least, bimodal. It is possible to say that the peaks correspond to the two known subclasses of “sky” (being clear sky and clouds). Therefore the assumption of a normal distribution would be erroneous. The average training values of the RGB bands were calculated as: 191, 204 and 205 respectively, if these values are compared against Figures 5.8 A to C respectively, the errors of parametric assumptions such as the normal distribution become clear. For example, from the histogram we know that a large proportion of true “sky” pixels have high values in the three bands (digital values *circa* 255), while a second large group of pixel values distributes slightly above 200. In this case, the brighter pixels correspond to clouds which, due to their pixel values, would be unlikely to belong to a normally distributed class with an average pixel value of 200

Finally, notice how an apparent third peak seems to appear in the lowest ranges of the green band training histogram (Figure 5-8 B). A third class may very well be comprised of “grey clouds”. However grey clouds are not well represented in the training image. Another shortcoming (of the specific example given here) is the lack of representation of all types of “sky” values in the training image. This issue may be dealt with if a second training image is concatenated, which represents grey clouds.

#### **5.4.2 Further strategies to improve the classification**

Some potential strategies to improve the results of pixel classification have already been identified, i.e. i) the inclusion of more than one training class and ii) the concatenation of

more than one training image, so that the whole amplitude of values is well represented for heterogeneous classes.

One further possible strategy is the analysis of the neighbourhood of pixels around each pixel in the image. In recent years, the surroundings of pixels have been suggested as useful additional information in artificial image-learning algorithms (Weiss and Freeman, 2007; Saxena et al., 2008; Luong et al., 2014). As shown in Figure 5-9, window pixels can be easily misclassified as sky, due to the reflective properties of windows. However, windows can be discriminated from sky, given the fact that the former are usually surrounded by a very heterogeneous neighbourhood of pixel values. In order to include the surroundings of a pixel into the described classification algorithms, each pixel should be assigned with a value that describes its neighbourhood; the convolution matrix operation allows this. Convolution matrix operations (a.k.a.: kernel, sliding window, filters, focal statistics, or neighbourhood analyses) consist of the element-by-element product of a small matrix (kernel) and a section of equal size of a larger target matrix (Figure 5-11). The total sum of the element-by-element products is then assigned to a single pixel in the resultant matrix (which has the same size as the target matrix).

$$\text{conv2} \left[ \begin{array}{|c|c|c|c|c|} \hline 20 & 20 & 20 & 20 & 20 \\ \hline 20 & 10 & 10 & 10 & 20 \\ \hline 20 & 10 & 0 & 10 & 20 \\ \hline 20 & 10 & 10 & 10 & 20 \\ \hline 20 & 20 & 20 & 20 & 20 \\ \hline \end{array} , \begin{array}{|c|c|c|} \hline 1 & 1 & 1 \\ \hline 1 & 1 & 1 \\ \hline 1 & 1 & 1 \\ \hline \end{array} \right] = \begin{array}{|c|c|c|c|c|} \hline 0 & 0 & 0 & 0 & 0 \\ \hline 0 & 0 & 0 & 0 & 0 \\ \hline 0 & 0 & 80 & 0 & 0 \\ \hline 0 & 0 & 0 & 0 & 0 \\ \hline 0 & 0 & 0 & 0 & 0 \\ \hline \end{array}$$

Figure 5-11 Graphically shows the convolution matrix operation. In the Octave language the “conv2” command will return a 2D convolution between two matrices. The second matrix of the comma-separated list is defined as the sliding kernel.

Next, the kernel “slides” throughout the entire target matrix repeating the same process on every element. Different transformations may be performed, either to the kernel or the target

matrices, in order to obtain different statistical descriptors of the surroundings of each pixel, e.g. average or standard deviation. In order to calculate an average value of the neighbourhood, each value in the kernel must equal the inverse of the total number of its elements.

A test was performed using convolution operations. If Figure 5-9 is analysed carefully, a very simple rule becomes clear: True “sky” pixels are usually surrounded by other “sky” pixel, whereas misclassified windows are mostly surrounded by non-sky-pixels.

However, this rule occurs at different spatial scales in the image, given that windows appear at different distances from the camera lens. Because of this, it is difficult to define a kernel size that would successfully describe the surroundings of all misclassified pixels. Yet, it may be expected that a series of nested convolution operators performed on the classified image (Figure 5-9) will eventually substitute the values of all window pixels, i.e. from being “likely members of the sky class” to unlikely members. The nested convolution operations can be understood as a series of consecutive neighbourhood analyses; which describe the surroundings, then the surroundings of the surroundings, and so on. Preliminary results of a series nested convolution operations is shown in Figure 5-12.

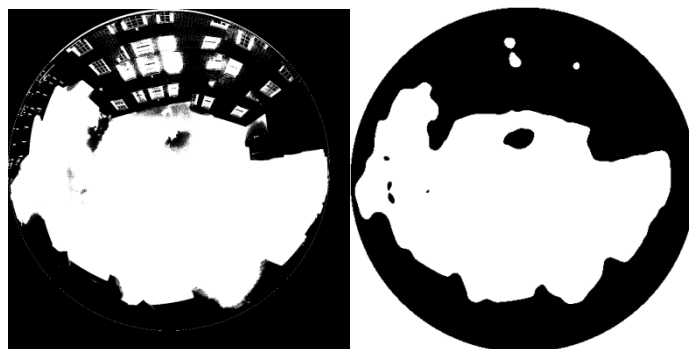


Figure 5-12 Left classified image as shown in Figure 5-9. Right: showing the results of a series of 20 nested convolution operations performed on the classified image (Figure 5-9), using a 5x5 kernel for calculating a neighbourhood average.

In Figure 5-12 most windows originally misclassified as “sky” are corrected after the nested convolution operations. The overall shape of the canyon profile becomes “blurred” due to the operations, especially at the borderlines between buildings and the sky. However notice how some architectural details like those found at the bottom of the images (south of the canyon) still remain outlined after the nested convolutions. The reconstruction shown on Figure 5-12 can be considered acceptable for large scale purposes.

Finally, other strategies may also be followed to improve the learning algorithms. One of them should comprise the analysis of correlation between the information values at different layers, within the training set. This can be done by obtaining the arithmetical differences between the RGB layers:

$$R - G; R - B; G - B,$$

where: R, G and B represent the RGB bands of a colour image to be classified. The subtraction operations represent an element-by-element matrix subtraction of the RGB image bands.

The resultant difference matrices may be added to the classification algorithms as additional layers of information, and undergo the same processes as the original RGB layers. Notice from Figures 5-1 and 5-2 how the arithmetical difference  $R - G$  (i.e. “Red” minus “Green” value in the digital RGB layers) will tend to be negative for most “clear-sky” pixels, and will tend to be zero for cloud pixels, regardless of the brightness of the cloud. Therefore, the training histogram at the information layer  $R-G$ , of an heterogeneous class “sky” (containing clear-sky, bright clouds and grey clouds), should be a bimodal curve with two peaks: at 0 and another at some negative value. This is then an example of a layer with relevant information; added to the classification algorithm.

Further research is needed to test the suitability of these and other strategies that may be followed in order to automatize the identification of sky pixels and other materials in the urban panoramic composition of individual street canyons. Analyses of omission and commission in the classification are also needed to quantitatively assess the outcomes

## **5.5 Conclusion**

Parametric classification allowed the automatic identification of five urban panoramic components (i.e. trees, road surfaces, bricks, windows, sky) for most pixels in the image (with approximately 11.6% of the total pixels being misclassified). Misclassifications were especially abundant in the borders between pixels from one class and the other and in pixels corresponding to unidentified classes (e.g. people and cars). It is possible that the multi-class classification performed aided in the correct classification of most pixels (by assigning each pixel to the class with the highest probability of belonging). The non-parametric classification algorithm allowed the classification of a heterogeneous sky (with broken cloud and clear patches) within one single class. However, reflecting windows were misclassified as sky, neighbourhood analyses through convolution operations may aid in distinguishing sky-pixels from window-pixels; further research is required in these regards. It can be concluded that, although the algorithms of image classification need further modification, testing and validation, these methods will provide a useful aid in the automatic identification of the different urban components. The strategies described here may serve as the basis for further research, to automatize the reconstruction of urban canyon geometries.

## **References**

- d'Angelo, P. (2007). Radiometric alignment and vignetting calibration. Proc. Camera Calibration Methods for Computer Vision Systems.
- Carrasco-Hernandez, R., Smedley, A. R., and Webb, A. R. (2015). Using urban canyon geometries obtained from Google Street View for atmospheric studies: Potential applications in the calculation of street level total shortwave irradiances. *Energy and Buildings*, 86, 340-348.

- Chapman, L., and Thornes, J. E. (2004). Real-time sky-view factor calculation and approximation. *Journal of Atmospheric and Oceanic Technology*, 21(5), 730-741.
- Feister, U., and Grewe, R. (1995). Spectral albedo measurements in the UV and visible region over different types of surfaces. *Photochemistry and Photobiology*, 62(4), 736-744.
- German, D. M., d'Angelo, P., Gross, M., and Postle, B. (2007, June). New methods to project panoramas for practical and aesthetic purposes. In *Proceedings of the Third Eurographics conference on Computational Aesthetics in Graphics, Visualization and Imaging* (pp. 15-22). Eurographics Association.
- Heisler, G. M., and Grant, R. H. (2000). Ultraviolet radiation in urban ecosystems with consideration of effects on human health. *Urban Ecosystems*, 4(3), 193-229.
- Holmer, B., Postgård, U., and Eriksson, M. (2001). Sky view factors in forest canopies calculated with IDRISI. *Theoretical and Applied Climatology*, 68(1-2), 33-40.
- Li, W., and Guo, Q. (2010). A maximum entropy approach to one-class classification of remote sensing imagery. *International Journal of Remote Sensing*, 31(8), 2227-2235.
- Lindberg, F., and Grimmond, C. S. B. (2011). The influence of vegetation and building morphology on shadow patterns and mean radiant temperatures in urban areas: model development and evaluation. *Theoretical and applied climatology*, 105(3-4), 311-323.
- Luong, T. X., Kim, B. K., and Lee, S. Y. (2014, July). Color image processing based on Nonnegative Matrix Factorization with Convolutional Neural Network. In *Neural Networks (IJCNN), 2014 International Joint Conference on* (pp. 2130-2135). IEEE.
- Matzarakis, A., Rutz, F., and Mayer, H. (2010). Modelling radiation fluxes in simple and complex environments: basics of the RayMan model. *International Journal of Biometeorology*, 54(2), 131-139.
- Phillips, S. J., Anderson, R. P., and Schapire, R. E. (2006). Maximum entropy modeling of species geographic distributions. *Ecological modelling*, 190(3), 231-259.
- Saxena, A., Chung, S. H., and Ng, A. Y. (2008). 3-d depth reconstruction from a single still image. *International journal of computer vision*, 76(1), 53-69.
- Weiss, Y., and Freeman, W. T. (2007, June). What makes a good model of natural images?. In *Computer Vision and Pattern Recognition, 2007. CVPR'07. IEEE Conference on* (pp. 1-8). IEEE.

## Chapter 6

This chapter is presented as the final version submitted for review to the journal *Theoretical and Applied Climatology*. The article is currently under peer-review.

The author of this thesis (Roberto Carrasco Hernandez) is also the first author of the article. The original concept, research methods, and outcomes were developed by the first author, under the close supervision of co-authors Andrew R.D. Smedley and Ann R. Webb. The article was written by Carrasco-Hernandez, with advice and assistance from the co-authors.

The radiometric data for this article was obtained from a spectrometer installed at the monitoring station of the Centre for Atmospheric Sciences of the University of Manchester. The monitoring station is jointly run by co-authors Andrew R.D. Smedley and Ann R. Webb, and by Dr Richard Kift who is acknowledged for his help.

Supplementary information appears at the end of this chapter, as it supplementary data submitted to the journal of *Theoretical and Applied Climatology*.

An appendix (Appendix II) shows the published version of this chapter as it appears in *Theoretical and Applied Climatology*.



## **Fast calculations of the spectral diffuse-to-global ratios for approximating spectral irradiance at the street canyon level**

*Roberto Carrasco-Hernandez<sup>\*1</sup>, Andrew R.D. Smedley<sup>1</sup>, Ann R. Webb<sup>1</sup>*

*<sup>1</sup>Centre for Atmospheric Sciences, School of Earth, Atmospheric and Environmental Sciences, University of Manchester, Manchester, M13 9PL, UK*

### **Corresponding Author**

Name : Roberto Carrasco-Hernandez  
Affiliation : University of Manchester  
Address : School of Earth, Atmospheric and Environmental Sciences, Simon Building, Oxford Road, Manchester M13 9PL  
Email : rcarrash@yahoo.com.mx

### **Abstract**

Two radiative transfer models are presented that simplify calculations of street canyon spectral irradiances with minimum data input requirements, allowing better assessment of urban exposures than can be provided by standard unobstructed radiation measurements alone. Fast calculations improve the computational performance of radiation models, when numerous repetitions are required in time and location. The core of the models is the calculation of the spectral diffuse-to-global ratios (DGR) from an unobstructed global spectral measurement. The models are based on, and have been tested against, outcomes of the SMARTS2 algorithm (i.e. Simple Model of the Atmospheric Radiative Transfer of Sunshine). The modelled DGRs can then be used to partition global spectral irradiance values into their direct and diffuse components, for different solar zenith angles. Finally, the effects of canyon obstructions can be evaluated independently on the direct and diffuse components, which are then recombined to give the total canyon irradiance. The first model allows ozone and aerosol inputs, while the second provides a further simplification, restricted to average ozone and aerosol contents, but specifically designed for faster calculations. To assess the

effect of obstructions and validate the calculations, a set of experiments with simulated obstructions (simulated canyons) were performed. The greatest source of uncertainty in the simplified calculations is in the treatment of diffuse radiation. The measurement-model agreement is therefore dependent on the region of the sky obscured and ranges from  $< 5\%$  at all wavelengths to 20-40% (wavelength dependent) when diffuse sky only is visible from the canyon.

## 6.1 Introduction

Ground-level measurements and models of solar radiation find applications in studies of human health (Webb, 2006; Ludema et al., 2014; Yam and Kwok, 2014), photosynthetically active radiation (Hu and Wang, 2013) and photovoltaic generation (Myers, 1997; Bengler et al., 2014; Myers and Gueymard, 2014; Nofuentes et al., 2014). The spectral composition of the solar radiation at ground level acquires further relevance due to the spectrally dependent effects of UV radiation on biological processes (Kaskaoutis et al., 2007; Serrano and Bosca, 2011; Malinovic-Milicevic et al., 2014). Measurements and models of global spectral radiation generally refer to that falling on an unobstructed horizontal plane (e.g. radiation received upon a flat rooftop). Such data fail to give a realistic assessment of the exposures that may be gained at street-level, where most biological (human) exposure occurs. In order to translate the rooftop unobstructed data to the street-level, the canyon horizon obstructions must be described. In each specific street canyon, the horizon obstructions will exert independent effects on the direct and diffuse components; for this reason, the global irradiance must be represented as the sum of its direct and diffuse components. This can be achieved by either measuring or modelling the direct and diffuse components of a global measurement. In recent literature, the importance of partitioning global broadband irradiance has been addressed for analysing the effects of horizon obstructions (Ruiz-Arias et al., 2011). Ruiz-Arias et al., affirm that “*in any event* (overcast,

cloudy, cloudless conditions), *knowledge of the solar irradiance components is fundamental to discern terrain effects on solar irradiance*". The present work addresses the problem of partitioning spectral irradiance values into their direct and diffuse components.

SMARTS (Myers and Gueymard, 2014) is a widely validated one-dimensional radiative transfer model (i.e. it considers the atmosphere as a series of homogenous planes stacked vertically), for the calculation of spectral global irradiance (in  $\text{Wm}^{-2}\text{nm}^{-1}$ ) for an unobstructed (full) sky-view, as well as its direct and diffuse spectral components. However, for high temporal resolution applications, the SMARTS calculations can still become computationally intensive. More complex algorithms, like MYSTIC (Mayer et al., 2010), allow Monte-Carlo tracking of independent photons, in a three dimensional complex atmosphere which can include mountains and buildings as topographic reflectors (Weihs et al., 2012; Krayenhoff et al., 2014; Kreuter et al., 2014; Petersen et al., 2014). Although reported to return more realistic radiation models (Wagner et al., 2011), Monte-Carlo ray tracing models are even more demanding of computational resources. The first goal of this work was to develop a fast method of partitioning the global radiation using an unobstructed measurement and a simple algorithm. Street canyon exposures can then be estimated from the independent direct and diffuse components provided the obstruction profiles are known.

A common technique for describing sky obstructions is by projecting the upper-hemispheric view of any individual location onto a two-dimensional polar plane. Such projections are usually obtained by using a *fisheye* photograph of the sky-view (Grimmond et al., 2001). Alternatively, fisheye projections may be reconstructed from the Google Street View image database (Carrasco-Hernandez et al., 2015). Other methods for describing horizon obstructions on a larger scale are also available through the use of digital elevation terrain models (de Carvalho Alves et al., 2013). The methods proposed in the present work

can be applied to any location where the visibility of the direct solar beam can be evaluated, along with a measurement of the fraction of visible sky (i.e. the sky view factor, SVF).

The SVF is a basic way of parameterizing sky obstructions and can be understood as the fraction of the sky that is visible from the perspective of a ground observer. It is a dimensionless quantity, and has been used in explaining urban atmospheric phenomena (Holmer et al., 2007; Unger, 2009; Lindberg and Grimmond, 2011; Matzarakis and Matuschek, 2011; Eeftens et al., 2013; Zhu et al., 2013). The RayMan model software (Matzarakis et al., 2010) can evaluate the visibility of the solar disc and the SVF from a fisheye polar projection of a specific canyon. The software also calculates a total shortwave irradiance (broadband irradiance), under the provided canyon sky-view. In this paper we elaborate on the RayMan model methods, towards the calculation of global spectral irradiance within urban canyons, for UV and visible wavelengths.

### **6.1.1 The diffuse-to-global spectral ratio (DGR)**

Ratios of the global spectral irradiance and either of its two components have been suggested as useful concepts in the atmospheric sciences (Badarinath et al., 2007; Kaskaoutis et al., 2007; Kaskaoutis et al., 2008). Measurements of the direct and diffuse components may be obtained by using an additional spectrometer equipped with a shadow band or by using a sun-tracking device with direct input optics. However, if the global irradiance is the only measurement available, the diffuse and direct components may still be modelled from a calculation of the ratio of diffuse-to-global irradiance (DGR). The DGR is dependent on wavelength and solar zenith angle (SZA). Fig. 6-1 shows the modelled changes in the spectral DGR for different wavelengths according to SMARTS.

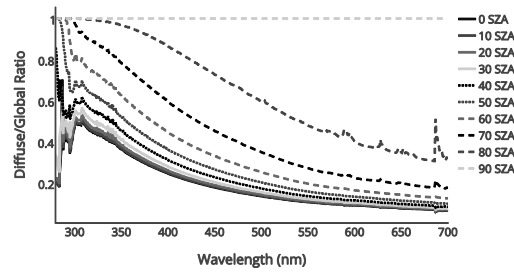


Figure 6-1 DGRs calculated for different solar zenith angles (SZA) for a standard mid-latitude urban atmosphere using the SMARTS radiative transfer algorithm. Ozone (0.31 atm-cm) and aerosol (0.1 AOT<sub>500nm</sub>) atmospheric contents corresponded to those measured on 7 June 2013

Note that the DGR decreases towards the red end of the spectrum, since Rayleigh scattering is a function of the fourth power of wavelength. Interactions with ozone produce the patterns observed at ultraviolet wavelengths. Both models presented in this work intend to reconstruct Fig. 6-1 through simplified calculations.

## 6.2 Methods

### 6.2.1 Global spectral irradiance in urban canyons

For practicality, the spectral irradiances reaching any urban canyon can be considered to be a fraction of those measured under an unobstructed view. Such assumption is not always true since the irradiance reflected by urban materials (e.g. ground, building walls) may become a significant part of the total irradiance. However, the modelling of such contributions would require complex 3D Monte-Carlo simulations that are not within the scope of this article. For large temporal scale purposes, and for the sake of simple and fast calculations, the effect of reflections may be neglected as their effects usually occur over a limited range of solar positions. To calculate the fraction corresponding to the canyon irradiance, it is first necessary to split the global irradiance into its direct and diffuse components. The effects of obstructions on these components are evaluated independently,

and then summed (Eq. 6.1). For cloudless skies, direct irradiance in the canyon depends on whether the solar disc is blocked by a building, while diffuse irradiance is proportional to the SVF.

$$E_{C,\lambda} = (E_{b,F,\lambda})S_{bin} + (E_{d,F,\lambda})SVF, \quad (\text{Eq. 6.1})$$

where  $E_{C,\lambda}$  is the global spectral irradiance within a specific urban canyon  $C$ , at wavelength  $\lambda$ ;  $E_{b,F,\lambda}$  is the direct beam spectral irradiance under a full sky-view  $F$ , at wavelength  $\lambda$ ;  $S_{bin}$  is a binary digit (1 or 0) representing the visibility of the direct solar beam;  $E_{d,F,\lambda}$  is the diffuse irradiance under full sky-view  $F$ , at wavelength  $\lambda$ ;  $SVF$  is the sky view factor

However, if the only parameter available is the full sky-view global irradiance ( $E_{F,\lambda}$ ), the canyon global irradiance  $E_{C,\lambda}$  may still be calculated, by knowing the proportional ratio of diffuse-to-global irradiance ( $DGR$ ):

$$E_{C,\lambda} = [(E_{F,\lambda}) \cdot (1 - DGR) \cdot S_{bin}] + [(E_{F,\lambda}) \cdot DGR \cdot svf] \quad (\text{Eq. 6.2})$$

Once the pre-requisites are satisfied (i.e. a *fisheye* projection of the obstructions and a measurement of unobstructed global solar radiation), the radiation at street-level in a canyon can be estimated from the DGR only (equation 2). Our goal is to calculate the DGR in a simple manner.

The assumptions made in these models are similar to those found in the RayMan model for total shortwave irradiance (Matzarakis et al., 2010). Reflections from walls are neglected and the diffuse component is considered as isotropic. Although allowing simple and fast calculations, errors can be introduced into the models by these assumptions. At certain moments, for some building surfaces, the reflections from walls can substantially increase canyon irradiance. In addition, for cloudless skies, the anisotropy of the diffuse component

implies that obstructions of similar size may have different shading effects, depending on their proximity to the circumsolar region. One objective of this work was to measure the magnitude of the errors arising from such assumptions.

## 6.2.2 Modelling the spectral DGR

The first model presented is a mathematical simplification of a well validated radiative transfer model (SMARTS) to calculate the DGR. The second model is a semi-empirical fit, which represents a further simplification of the DGR calculations, but is limited by the conditions under which it was derived. Either can later be used, in combination with fisheye projections of canyon profiles and equation (2), to approximate relative global spectral irradiances within simulated canyons.

### 6.2.2.1 DGR - Model 1

Our first theoretical approach attempts to reduce the number of atmospheric parameters required by SMARTS. The following section shows that the DGR is only affected by Rayleigh scattering, ozone absorption, and aerosol scattering:

In simplified calculations found in literature (Bird and Riordan, 1986), the spectral diffuse component  $E_{d,F,\lambda}$ , under a full sky-view  $F$ , is approximated as the sum of three sub-components: i.e. the Rayleigh scattering diffuse component ( $E_{d,F,R\lambda}$ ), the aerosol scattering diffuse component ( $E_{d,F,as,\lambda}$ ) and the ground reflectance backscattering ( $B_s$ ) component ( $E_{d,F,Bs,\lambda}$ ). It then follows that the diffuse component of global spectral irradiance may be expressed as:

$$E_{d,F,\lambda} = E_{d,F,R\lambda} + E_{d,F,as,\lambda} + E_{d,F,Bs,\lambda} \quad (\text{Eq. 6.3})$$

For simplicity, the backscattered component will be implemented later via the *backscattering amplification factor (BAF)* proposed in the SMARTS algorithm (Gueymard, 1995). For now, the *sky-only* diffuse component is:

$$E_{d,F,\lambda} = E_{d,F,R\lambda} + E_{d,F,as,\lambda} \quad (\text{Eq. 6.3.1})$$

The calculations found in the works of Bird and Riordan, later modified by Gueymard (1995), calculate each sub-component of diffuse light, according to the following set of equations:

Consider the direct beam irradiance  $E_{b,F,\lambda}$  upon a horizontal, unobstructed plane ( $F$ ) as:

$$E_{b,F,\lambda} = E_{0n\lambda} T_{R\lambda} T_{o\lambda} T_{n\lambda} T_{g\lambda} T_{w\lambda} T_{a\lambda} \cos Z \quad (\text{Eq. 6.3.2})$$

Where  $E_{0n\lambda}$  is the extra-terrestrial spectral irradiance;  $T_{R\lambda}$  is the Rayleigh scattering transmittance;  $T_{o\lambda}$  is the ozone transmittance;  $T_{n\lambda}$  is the nitrogen transmittance;  $T_{g\lambda}$  is the mixed gases transmittance;  $T_{w\lambda}$  is water vapour transmittance;  $T_{a\lambda}$  is aerosol transmittance and  $Z$  is the solar zenith angle.

Following Gueymard (1995), the aerosol and Rayleigh sub-components of diffuse irradiance (equation 3.1) are approximated as:

$$E_{d,F,R\lambda} = F_R E_{0n\lambda} (1 - T_{R\lambda}^{0.9}) \Gamma_{o\lambda} T_{n\lambda} T_{g\lambda} T_{w\lambda} T_{aa\lambda} \cos Z, \quad (\text{Eq. 6.3.3})$$

$$E_{d,F,as,\lambda} = F_a E_{0n\lambda} (1 - T_{as\lambda}) T_{R\lambda} \Gamma_{o\lambda} T_{n\lambda} T_{g\lambda} T_{w\lambda} T_{aa\lambda} \cos Z, \quad (\text{Eq. 6.3.4})$$

where  $F_R$  corresponds to the fraction of Rayleigh scattered radiation that is directed towards the ground,  $F_a$  is the fraction of aerosol scattered light directed toward the ground, and  $\Gamma_{o\lambda}$  is the effective ozone transmittance for diffuse radiation;  $T_{aa\lambda}$  is the transmittance if the only attenuator were aerosol absorption; and  $T_{as\lambda}$  is the equivalent for aerosol scattering alone.



Notice that, as in the SMARTS algorithm, an effective ozone transmittance ( $\Gamma_{o\lambda}$ ) is used for calculating the diffuse irradiance, instead of the standard ozone transmittance ( $T_{o\lambda}$ ). Previous models, that did not consider this modification (Leckner 1978; Bird and Riordan 1986), reportedly returned underestimations of the diffuse irradiance reaching “*several orders of magnitude, especially for large SZAs*” (Gueymard, 1995). In this work, we also incorporate the effective ozone transmittance as the ratio of effective-to-standard ozone transmittance.

Since our objective is to calculate the DGR, the number of atmospheric input parameters required can be reduced as follows:

$$DGR \text{ or } \frac{Diffuse}{Global} = \frac{E_{d,F,\lambda}}{E_{d,F,\lambda} + E_{b,F,\lambda}} = \frac{1}{\frac{E_{d,F,\lambda} + E_{b,F,\lambda}}{E_{d,F,\lambda}}} = \frac{1}{1 + \frac{E_{b,F,\lambda}}{E_{d,F,\lambda}}} = \frac{1}{1 + \left[\frac{E_{d,F,\lambda}}{E_{b,F,\lambda}}\right]^{-1}}.$$

Then, using equation (3.1)

$$DGR = \frac{1}{1 + \left[\frac{E_{d,F,R\lambda} + E_{d,F,as,\lambda}}{E_{b,F,\lambda}}\right]^{-1}}, \quad (\text{Eq. 6.3.5})$$

also, by using equations (6.3.2) and (6.3.3),

$$\frac{E_{d,F,R\lambda}}{E_{b,F,\lambda}} = \frac{F_R E_{0n\lambda} (1 - T_{R\lambda}^{0.9}) \Gamma_{o\lambda} T_{n\lambda} T_{g\lambda} T_{w\lambda} T_{aa\lambda} \cos Z}{E_{0n\lambda} T_{R\lambda} T_{o\lambda} T_{n\lambda} T_{g\lambda} T_{w\lambda} T_{a\lambda} \cos Z} = \frac{F_R (1 - T_{R\lambda}^{0.9}) T_{aa\lambda} \Gamma_{o\lambda}}{T_{R\lambda} T_{a\lambda} T_{o\lambda}}, \quad (\text{Eq. 6.3.6})$$

additionally, using equations (6.3.2) and (6.3.4)

$$\frac{E_{d,F,as,\lambda}}{E_{b,F,\lambda}} = \frac{F_a E_{0n\lambda} (1 - T_{as\lambda}) T_{R\lambda} \Gamma_{o\lambda} T_{n\lambda} T_{g\lambda} T_{w\lambda} T_{aa\lambda} \cos Z}{E_{0n\lambda} T_{R\lambda} T_{o\lambda} T_{n\lambda} T_{g\lambda} T_{w\lambda} T_{a\lambda} \cos Z} = F_a (1 - T_{as\lambda}) \frac{T_{aa\lambda} \Gamma_{o\lambda}}{T_{a\lambda} T_{o\lambda}}. \quad (\text{Eq. 6.3.7})$$

By substituting equations (6.3.6) and (6.3.7) into equation (6.3.5), we have:

$$DGR = \frac{1}{1 + \left[ \frac{T_{aa\lambda} \Gamma_{o\lambda}}{T_{a\lambda} T_{o\lambda}} \left( \frac{F_R(1-T_{R\lambda}^{0.9})}{T_{R\lambda}} + F_a(1-T_{as\lambda}) \right) \right]}^{-1}. \quad (\text{Eq. 6.3.8})$$

Since  $T_{as\lambda} = T_{a\lambda} / T_{aa\lambda}$ , according to its definition (Gueymard, 1995), then

$$T_{aa\lambda} / T_{a\lambda} = 1 / T_{as\lambda}.$$

Therefore,

$$DGR = \frac{1}{1 + \left[ \frac{1}{T_{as\lambda} T_{o\lambda}} \left( \frac{F_R(1-T_{R\lambda}^{0.9})}{T_{R\lambda}} + F_a(1-T_{as\lambda}) \right) \right]}^{-1}. \quad (\text{Eq. 6.3.9})$$

Finally, the equation for calculating the DGR, including the backscattering amplification factor (*BAF*), is

$$DGR = \frac{1}{1 + \left[ BAF * \frac{1}{T_{as\lambda} T_{o\lambda}} \left( \frac{F_R(1-T_{R\lambda}^{0.9})}{T_{R\lambda}} + F_a(1-T_{as\lambda}) \right) \right]}^{-1}. \quad (\text{Eq. 6.3.10})$$

The *BAF* (Gueymard, 1995 p.32) is a dimensionless quantity with values  $> 1$ , that represents the increase of downwelling radiation due to radiation reflected from the ground, and then further backscattered (towards the ground) by the atmosphere. The *BAF* is a function of the sky reflectance, the ground reflectance (urban concrete in this case) and the direct-to-diffuse irradiance ratio (see Table 6-1).

The model then requires only three variables: solar zenith angle (SZA), columnar ozone (in atm-cm) and aerosol (expressed as aerosol optical thickness at 500 nm or  $AOT_{500\text{nm}}$ ). Current and historic ozone and aerosol contents in the atmosphere are available globally from satellite sources (Remer et al., 2005) or at limited locations from ground-based measurements.

The individual equations required for the terms in equation (6.3.10) are summarised in Table 6-1.

**Table 6-1. Equations for the terms expressed in Equation (3.10)**

Each individual term is either a standard equation (e.g. atmospheric air mass), or comes from Gueymard (1995), or in the case of those marked \*, are parameterizations to fit the data from the indicated author: † (Molina and Molina, 1986) ‡ (Gueymard, 1995)

Term	Expression	Notes
Atmospheric air mass	$M = \sqrt{\left(\left(\frac{r}{\cos Z}\right)^2 + 2r + 1\right)} - \frac{r}{\cos Z}$	$r = \frac{\text{Radius of the Earth}}{\text{Height of the Atmosphere}}$ Z= Solar Zenith Angle (SZA). $\lambda$ = wavelength in (nm)
Rayleigh scattering transmittance *	$T_{R\lambda} = \sqrt{\exp\left(-\frac{((360^4) * (M))}{\lambda^4}\right)}$	
Ozone spectral absorption * ( $A_{O\lambda}$ )	$A_{O\lambda\text{Hartley}} = 1140 \exp(-1.5E - 3 * (\lambda - 253.65)^2)$ $A_{O\lambda\text{Huggins}} = A_{O\lambda\text{Hartley}} \cdot \frac{1}{2} \exp((2.7E - 4) \cdot (\lambda - 253.65)^2)$ $A_{O\lambda} = \max(A_{O\lambda\text{Hartley}}, A_{O\lambda\text{Huggins}})$	$A_{O\lambda\text{Hartley}}$ = Empirical fit to the Hartley absorption band $A_{O\lambda\text{Huggins}}$ = Empirical fit to the Huggins band absorption From†
Ozone optical thickness	$\tau_{O\lambda} = u_{O\lambda} A_{O\lambda}$	$u_{O\lambda}$ = atmospheric ozone column (atm-cm)
Ratio of effective-to-standard ozone transmittance *.	$\frac{\Gamma_{O\lambda}}{T_{O\lambda}} \approx 10^{\tau_{O\lambda} \left(\frac{1}{\cos(Z)} - \frac{1}{\cos(35)}\right)^3}$	From‡
Aerosol optical thickness	$\tau_{A\lambda} = \beta \lambda^{-\alpha}$	$\alpha = 1.02$ $\beta = \frac{A_{ot0.5}}{\ln(10)}$
Aerosol scattering transmittance	$T_{as\lambda} = \exp(-W_0 * \tau_A * M)$	$W_0$ = single scattering albedo. $\tau_A$ = aerosol optical thickness
Average ground reflectance (concrete)	$\rho g \lambda = a \lambda^6 + b \lambda^5 + c \lambda^4 + d \lambda^3 + e \lambda^2 + f \lambda + g$	$a = -3.54e-15$ ; $b = 1.05e-11$ ; $c = -1.272e-08$ ; $d = 8.08e-06$ ; $e = -2.79e-03$ ; $f = 5.02e-01$ ; $g = -3.6e+01$ Empirically fit from averaged local ground reflectance SMARTS outputs at different SZAs
Sky reflectance	$(\rho s \lambda) = \text{Equation (3.9)}$	See equations (3.1) to (3.9) (Sky-only DGR)
Direct-to-diffuse ratio	$\frac{E_{b,F,\lambda}}{E_{d,F,R\lambda}} = \frac{1}{\frac{1}{T_{as\lambda}} \frac{\Gamma_{O\lambda}}{T_{O\lambda}} \left[ \left( \frac{F_R(1 - T_{R\lambda}^{0.9})}{T_{R\lambda}} \right) + (F_a(1 - T_{as\lambda})) \right]}$	Deduced using a rationale similar to that used in Eqns.3.5 - 3.10
Backscattering amplification factor	$BAF = 1 + \left[ \rho g \lambda \cdot \rho s \lambda \cdot \frac{\text{Direct}}{\text{Diffuse}} \right]$	$\rho g \lambda$ =ground reflectance $\rho s \lambda$ = sky reflectance

### 6.2.2.2 DGR - Model 2

Models with fewer mathematical computations are advantageous in studies where repetitive calculations are required, as here for multiple times of day and year. Although simpler than full radiative transfer models, the previously presented approach can still be numerically intensive when used multiple times. As an alternative method, equation (4) is proposed which was obtained empirically to resemble the DGR modelled with SMARTS for

the in-situ conditions shown in Fig. 6-1. Although this empirical fit may be limited to ozone and aerosol values for local conditions, its simple form makes it computationally fast.

$$DGR = 1 - \exp \left[ \left( \frac{280}{\lambda} \right)^{4 \cdot 0.79} \cdot \left( 1 - \left( \frac{255}{\lambda} \right)^{10} \right)^{1 - \tan(Z)} \cdot \frac{1}{\cos Z} \right], \quad (\text{Eq. 6.4})$$

where  $\lambda$  is the wavelength and  $Z$  is the SZA.

Equation (6.4) includes terms that approximate the effects of Rayleigh scattering, the effective ozone transmittance, and the air mass of the direct beam path. This model is restricted to the specific atmospheric contents of ozone (0.31 atm-cm) and aerosol ( $AOT_{500\text{nm}} = 0.1$ ) which were used to model Fig. 6-1 with SMARTS. An  $AOT_{500\text{nm}}$  of 0.1 represents a rather clean atmosphere not easily found in many urban locations world-wide. However, in-situ conditions had to be modelled in order to conduct the comparisons against spectral measurements that will be shown in section 2.3.3.

## 6.2.3 Model Validations

### 6.2.3.1 Comparisons against SMARTS

The intention for both proposed approaches was to reproduce the spectral DGRs found at different SZAs under a full sky-view, as modelled by SMARTS (Fig. 6-1) before applying the DGRs to modelled canyon irradiances. Most input parameters in the SMARTS model corresponded to default library parameters for the selected atmosphere (MLS: Mid-Latitude Summer). Ozone and aerosol input contents were measured on 7 June 2013, at the Pariser Building, University of Manchester, UK: ozone measurements were taken with a Brewer spectrophotometer (Smedley et al., 2010) with readings of 310 DU or 0.31 atm-cm.  $AOT_{500\text{nm}}$  of 0.1 was obtained from a MODIS satellite image, corresponding to the same day (NASA LAADS, 2013). Global and diffuse spectral irradiances were calculated using SMARTS at ten different SZAs from  $0^\circ$  to  $90^\circ$  and from these the DGR was obtained. The same inputs

were used for equation (3.10). Equation (4) was also solved for the 10 SZAs. Proportional errors in the outputs from equations (3.10) and (4) with respect to those from the SMARTS model are presented in the results section.

### **6.2.3.2 Sensitivity Analyses for changing ozone and aerosol conditions**

The theoretical sensitivity to changes in aerosol and ozone atmospheric contents was modelled with SMARTS at a constant SZA of  $32.2^\circ$ , corresponding to 1125 UTC on 7 June 2013, Manchester  $53.47^\circ$  N and  $2.23^\circ$  W. The first approach (Equation 3.10) allows parameterization of ozone and aerosol loading. We therefore compared the modelled DGR with SMARTS and equation (3.10), with five different ozone columns (from 0.2 to 0.4 atm-cm) and aerosol loadings ( $AOT_{500nm}$  0.05 to 2.5). Equation (4) was also compared against the SMARTS outputs under the same sets of atmospheric constituents. Because equation (4) remained unchanged, results illustrate the restrictions of this second approach.

### **6.2.3.3 Empirical Validations of Canyon Irradiance Calculations**

The outcomes of either DGR equation (3.10 or 4) can be substituted into equation (2) to calculate relative street canyon irradiances. In order to validate the proposed canyon irradiances, a series of experiments were conducted with simulated horizon obstructions. To measure global horizontal spectral irradiance (in  $Wm^{-2}nm^{-1}$ ), a METCON single-grating diode array spectroradiometer, with a 280 to 700 nm wavelength range was used. The instrument was temperature stabilized and calibrated with a NIST 1000W FEL lamp at 0.5 m distance (Bais et al., 2005). Stray light corrections were applied following (Kreuter and Blumthaler, 2009). In order to simulate horizon obstructions, a 20cm thick polyurethane foam block was manually positioned above the entrance optics for a period of 10 seconds, during which a series of spectra were taken and then averaged. Fisheye digital photographs of the

obstructions were taken during the same period using an orthographic mini-fisheye lens (Sumlung, model: SL-FE12) attached to a Nokia E5 mobile phone camera.

Three simulated canyons were tested, labelled here as C1, C2 and C3 (Fig. 6-2). In C1 a part of the circumsolar region was obstructed but left the solar disc visible to the input optics. In C2 the anti-solar region was blocked and in C3 direct irradiance along with the circumsolar region was obstructed. Between each simulated obstruction, a full sky-view measurement was obtained. This sequence of measurements was repeated 25 times between 1100 UTC and 1230 UTC 7 June 2013, at the Manchester surface radiation site (Pariser Building, University of Manchester). The nearly cloudless conditions and the proximity to solar noon resulted in consistent measurements during the experimental period, for example measurements of canyon C1 exhibit a standard deviation of 1.8% (spectrally integrated irradiance across the wavelength range 305 nm to 700 nm). In contrast measurements with the C1 obstruction were 10.1% lower than the corresponding full-sky view measurement.

Since replicas were consistent, a representative measurement set is analysed in the results section, corresponding to 1125 UTC. The SVFs were calculated using the RayMan software (Matzarakis et al., 2010), without the cosine-law, since the fisheye lens had an orthographic projection. Fig. 6-2 shows the acquired images and their corresponding SVFs.



Figure 6-2 Orthographic fisheye images of four sky-views: Full,  $SVF = 0.99$ ,  $S_{bin} = 1$ : Full sky-view with no simulated obstructions. C1,  $SVF = 0.54$ ,  $S_{bin} = 1$ : Simulated Canyon obstructing the circum-solar region. C2,  $SVF = 0.41$ ,  $S_{bin} = 1$ : Simulated Canyon obstructing the sky opposite to the sun. C3,  $SVF = 0.42$ ,  $S_{bin} = 0$ : Simulated Canyon obstructing the solar disc and the circum-solar region. The sky view factor (SVF) was calculated using the RayMan software.

Fig. 6-2 shows that the SVF of canyon C1 is larger than that of canyon C2, but part of the bright circum-solar region is blocked in canyon C1. Also part of the circum-solar region is visible in canyon C3. After the SVFs were obtained, spectral global irradiances were calculated for the four sky-views shown in Fig. 6-2. In order to calculate spectral irradiance values for each canyon, the DGR was solved using equations (6.3.10) and (6.4) and then these values were substituted in equation (6.2) to obtain canyon global irradiance on the basis of full-sky global measurements.

## 6.3 Results

### 6.3.1 Modelling the DGR under a full sky-view

Figs. 3a and 3b show the solutions from equations (6.3.10) and (6.4) respectively under a full sky-view, for wavelengths from 280 to 700 nm, at ten different SZAs (0 to 90 °). Notice their similarities to the output from SMARTS in Fig. 6-1.

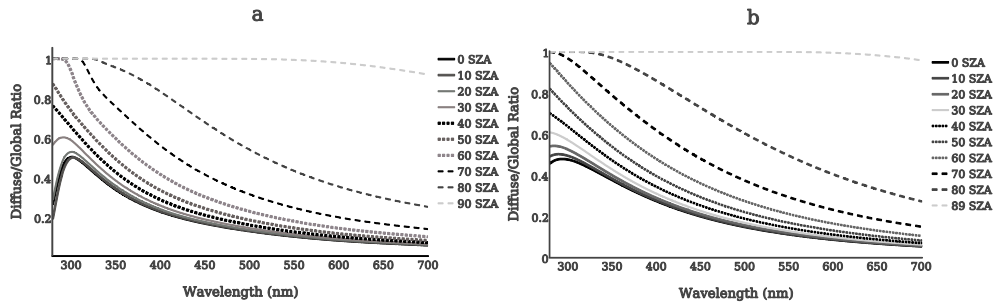


Figure 6-3 Modelled curves of spectral DGRs for different SZAs, using Equations (6.3.10) (Panel a) and (6.4) (Panel b). Note that Panel B has a limit of solar zenith angles of  $< 90^\circ$ ; this is because the use of a tangent function (see Eq. 6.4).

Figs. 3a and 3b closely resemble the effects of Rayleigh scattering assigning lower diffuse proportions to larger wavelengths. They also simulate the effects of ozone absorption on the diffuse component at the shorter ultraviolet wavelengths. Additionally, the effects of aerosol scattering and changing SZA are also simulated which strongly increase the diffuse components of longer wavelengths (600 to 700 nm) at higher solar zenith angles.

### 6.3.2 Comparisons against SMARTS

The differences between Fig. 6-1 and Figs. 6-3a and 6-3b were quantified by their proportional error, that is:

$$\text{Proportional Error} = \frac{DGR_{Eq3.10 \text{ or } 4} - DGR_{SMARTS}}{DGR_{SMARTS}}$$

These proportional errors are shown in Figs. 6-4a and 6-4b respectively for equations 3.10 and 4.



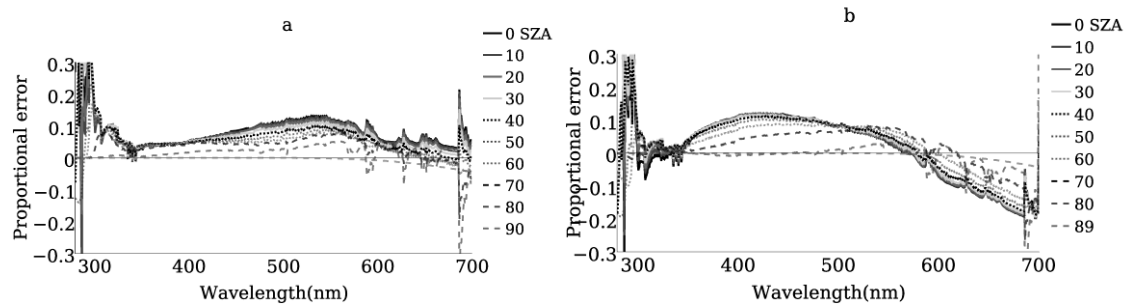


Figure 6-4 Proportional errors at different SZAs of spectral DGRs using equations (3.10) (Panel a) and (4) (Panel b), when compared against the SMARTS outputs for the same local atmospheric conditions (ozone 0.31 atm-cm and 0.1  $AOT_{500nm}$ ).

In Figs. 6-4a and 6-4b positive errors imply an overestimation in comparison to the SMARTS modelled values, and negative errors imply an underestimation. The proportional errors for wavelengths between 300 nm and 600 nm are generally below 0.15, increasing towards 0.2 for wavelengths  $> 600$  nm. For ultraviolet wavelengths below 300 nm, errors increase dramatically although there is very little solar radiation at these wavelengths. It must be noted that these tests were performed using constant values of atmospheric ozone (0.3 atm-cm) and aerosol ( $AOT_{500nm}$  0.1). The suitability of the models for different environments is assessed next.

### 6.3.3 Sensitivity analyses for changing ozone and aerosol conditions at a constant SZA

Sensitivity analyses against SMARTS models under varying aerosol and ozone conditions were performed for both proposed models and results, expressed using the proportional error defined earlier, are shown in Figs. 6-5 a to d.

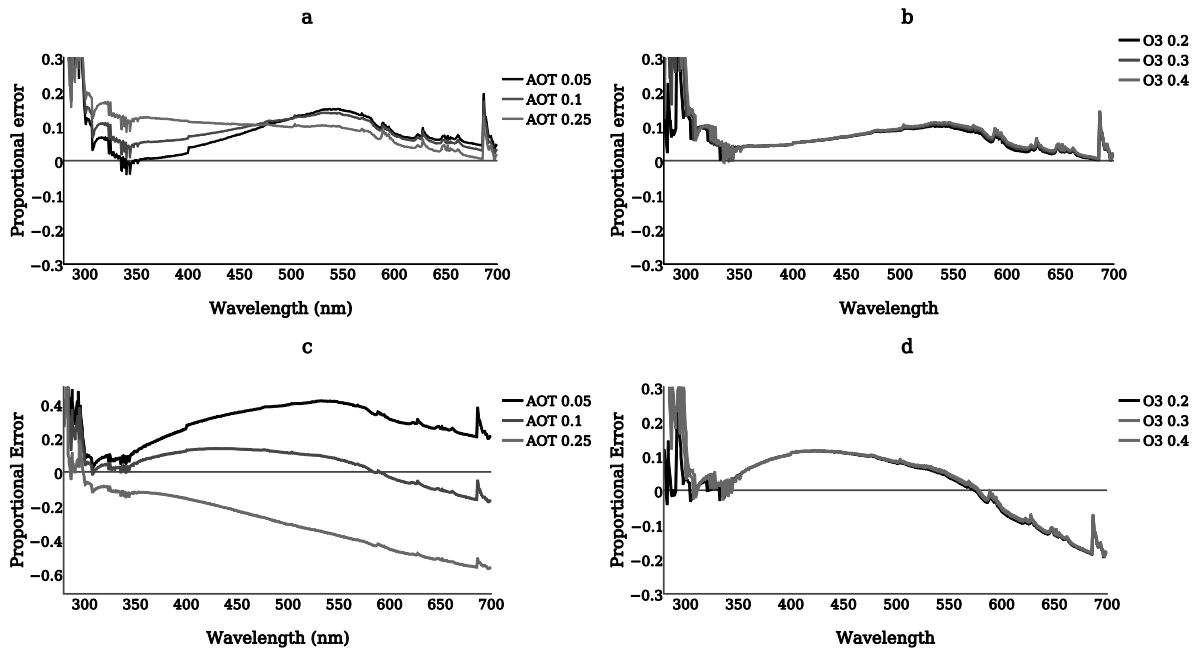


Figure 6-5 Results of the sensitivity analyses show errors found when comparing the SMARTS-calculated DGR ratios against equation (3.10) (Panels a and b) and equation (4) (Panels c and d). Panels a and c show the proportional errors found at different aerosol levels (AOT<sub>500nm</sub>), with constant ozone of 0.3 atm-cm. Panels b and d show the proportional error found at different ozone levels (O<sub>3</sub>) with constant AOT<sub>500nm</sub> at 0.1. All variations were modelled with a constant SZA of 32°.

Note how equation (6.3.10) returned proportional errors smaller than  $\pm 0.2$  with changing aerosol and ozone conditions (Figs. 6-5a and 6-5b). This is made possible because equation (3.10) accepts ozone and aerosol values as input parameters. Nonetheless, equation (6.3.10) apparently shows a trend of increasing error with increasing atmospheric aerosol loading. On the other hand, equation (6.4) has a fixed form (suitable for average atmospheric conditions) but that will return larger errors for extreme conditions (Figs. 6-5c and 6-5d). Despite this, except for turbid conditions and long wavelengths, the uncertainties are within 20% of the SMARTS modelled data.

### 6.3.4 Irradiance Measurements in Simulated Canyons

The effects of horizon obstructions are illustrated in Fig. 6-6, which shows the relative canyon irradiance as the ratio of canyon to full-sky measurements for each canyon. Relative canyon irradiance is shown for three simulated canyons (C1 to C3, see Fig. 6-2). Canyons C1 and C2 had a visible direct solar beam and simulated obstructions blocked different sections of the diffuse irradiance. In canyon C1 the circumsolar section was obstructed, whereas in canyon C2 the anti-solar region was obscured (leaving the circumsolar completely visible). Note that irradiance received at C2 is slightly larger than that of C1. In turn, in canyon C3 the direct solar beam was blocked along with the circumsolar region. The spectral pattern of relative canyon irradiance for canyon C3 is the inverse of C1 and C2 due to the blocking of the direct solar beam.

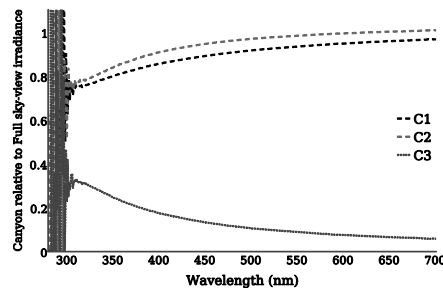


Figure 6-6 Measurements of relative canyon spectral irradiances. Relative canyon irradiances are the ratio of canyon/full sky measured irradiances, for the three simulated canyons (C1, C2 and C3).

### 6.3.5 Validation of canyon irradiance models

Figure 6-7 shows a comparison between modelled and measured relative canyon irradiances for canyons C1 to C3. The models for canyons C1 and C2 predicted an inverse relationship regarding the brighter of these two canyons. i.e. C1 was assigned a larger irradiance than C2 due to their respective sky view factors. However, measurements showed

the opposite pattern (see Figs. 6-6 and 6-7). Nonetheless, Fig.6- 8 shows that the differences between models and measurements are generally  $< 20\%$ , with canyon 3 presenting the greatest challenge to the models.

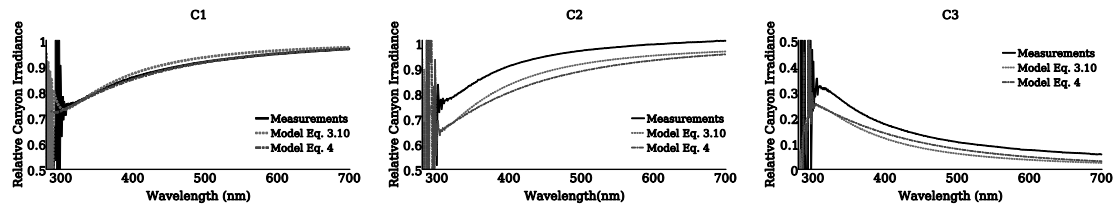


Figure 6-7 Model validations for the three simulated canyons (C1 to C3). Relative irradiances calculated with equations (6.3.10) and (6.4) irradiances (black lines), all relative to full sky-view. Panel C1: Canyon 1 (blocking circumsolar region). Panel C2: Canyon 2 (blocking the sky opposite to the sun), Panel C3: Canyon 3 (blocking the solar disc and circumsolar region).

Proportional errors of both models against measurements are shown in Figs.8 C1 to C3.

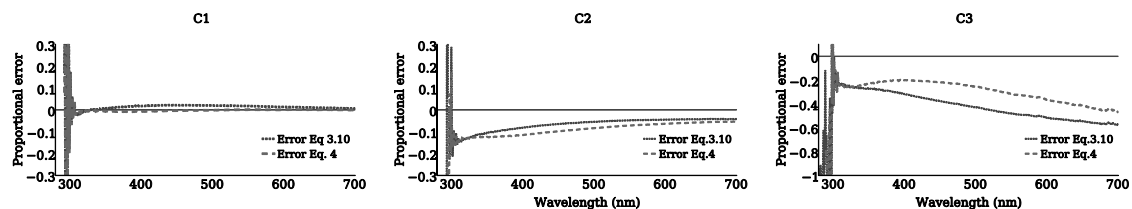


Figure 6-8 Proportional errors of both proposed models, when comparing measured versus modelled relative canyon irradiance values. Panel C1: Canyon C1 (blocking circumsolar region). Panel C2: Canyon C2 (blocking the sky opposite to the sun). Panel C3: Canyon C3 (blocking the solar disc and circumsolar region).

Figure 6-8 shows that errors are significantly higher for canyon C3 where the direct solar beam is blocked (proportional errors values of 0.2 to 0.5). Since global irradiance in canyon C3 was entirely comprised of scattered radiation (i.e. diffuse irradiance), the relative errors in

the calculations of diffuse irradiance become more apparent (up to 0.6 in the red wavelength range) due to the small quantities of global irradiance.

The errors in the models proposed here are potentially due to the assumptions and simplifications made in relation to the diffuse component. In particular, it is hypothesized that neglecting the anisotropy of diffuse irradiance may account for the underestimation of irradiance in canyon C2 (which blocked the less bright anti-solar region). Additionally simplifications for the calculations of Rayleigh scattering, ground albedo and the ozone and aerosol transmittances will also affect the diffuse component. In canyons C1 and C2, the errors in the diffuse irradiance calculations are less noticeable, due to the major contribution to global irradiance of the direct beam.

## **6.4 Discussion**

Equations (6.3.10) and (6.4) take a measured full sky global irradiance as their main input parameter, and their only purpose is to estimate the fraction of irradiance that would correspond to the diffuse component. This is in order to partition global irradiance for its analysis within a street canyon projected profile.

### **6.4.1 DGRs for a full sky-view**

When models were compared against SMARTS, under typical aerosol and ozone conditions, proportional errors of both proposed models are below absolute values of 0.2 for all solar zenith angles (Figs. 4a and b). These values of proportional error (or 20% in percentage terms) have been considered by other authors a good estimation in studies of human exposure (Vernez et al., 2014). It was observed that errors in the model outputs have a tendency to increase towards both extremes of the spectral region considered (280 – 700 nm); this is potentially due to simplifications in parameterising atmospheric effects. For example, in equation (3.10) the ozone absorption empirical tables, used by SMARTS, were substituted

by a polynomial fit to the ozone absorption reported by Molina and Molina (1986). Errors below 300 nm may also be due to our proposed fit for the ratio between effective and standard ozone transmittance (see Table 6-1). We found that our proposed equation for the ratio of effective-to-standard ozone transmittance is extremely sensitive to small variations in its parameters, and in turn has strong effects on the shorter wavelength irradiance (below 300nm). It was also found that the backscattering amplification factor (*BAF*) calculated underestimates the *BAF* proposed by Gueymard (1995 p32.) for shorter wavelengths. For applications where the small amounts of radiation at UV wavelengths are important, corrections to this particular equation may result in better estimation of the DGR below 300 nm.

On the other hand, errors found in longer wavelengths (towards 700 nm) may be better explained by the simplifications made to the aerosol transmittances. One of the parameters for calculating aerosol scattering transmittance is the single scattering albedo. The single scattering albedo ( $W_0$ ) is a complex function of wavelength and relative humidity of the atmosphere (Gueymard, 1995; Redemann et al., 2001; Collaud Coen et al., 2004). However for simplicity, a single value of 0.85 was used. Additionally, the SMARTS algorithm for aerosol transmittances considers two values for the “ $\alpha$ ” Ångström parameter (in Equation 3.14.1) assigned to two different sections of the spectrum (i.e.  $\lambda < 500$  nm and  $\lambda \geq 500$  nm). In this work, however, the use of two different alpha values resulted in mismatching curves for the two spectral regions. In recent studies (Jaus et al., 2012) a single  $\alpha$  value is also used for the calculations. According Jaus et al.,  $\alpha$  values circa 1.5 are the most frequent from 612 sites in the AERONET database. Thus, a single  $\alpha$  value of 1.5 has been used in this work.

#### **6.4.2 Sensitivity analyses for changing ozone and aerosol conditions**

Both approaches bring advantages and disadvantages for modelling DGRs. Our first approach (equation 3.10) provided means for including values of ozone and aerosol

atmospheric contents. For this reason, the errors modelled remained below 0.2 (Figs. 5a and 5b) when compared to SMARTS under different atmospheric conditions. On the other hand, the second approach (equation 4) provides an extremely simple calculation of the spectral DGRs. However, as shown in Figs.5c and 5d, it may only be suitable for ozone columns and aerosol loadings close to those under which it was derived (as is usual for empirically derived applications) since errors tend to increase with extreme atmospheric contents. This limitation may still prove to be an advantageous trade-off for a simple calculation that requires no further knowledge of the state the atmosphere.

One application of this work would be to create models of human exposure to erythemally-weighted UV radiation in the streets, in which case it would be advantageous to reduce errors in the UV as much as possible. However, the peak of the erythema solar spectrum is at approximately 310 nm, and the action spectrum extends well into the UV-A where model results have smaller uncertainties. Therefore, the models presented here should still be suitable for fast and simple calculations in realistic studies of human exposure to erythema radiation. The following section uses the calculated DGRs in order to approximate spectral irradiances under obstructed views. This type of model will be more representative of human exposure than the unobstructed sky-view data that is frequently available.

#### **6.4.3 Irradiance measurements in simulated canyons**

Obstructions of diffuse radiation have a greater effect on the shorter wavelengths, due to Rayleigh and aerosol scattering. Irradiance received at C2 is slightly larger than that of C1 (Figure 6-6) despite C2 having a smaller SVF (SVF = 0.41 in C2 vs 0.54 in C1, see Figure 6-2). This is explained by the fact that the brighter circumsolar region was completely visible in C2 whereas in C1 it was partially blocked. Further, due to the spectrally-dependent radiative transfer of the direct solar beam, blocking the direct beam has a smaller effect on global irradiance at short wavelengths than it has at longer wavelengths. The spectral pattern of

relative canyon irradiance is inversely proportional to wavelength in canyon C3, due to the blocking of the direct solar beam.

#### **6.4.4 Spectral irradiance calculations in simulated canyons**

Figure 6-7 C1 – C3 show how the modelled canyon irradiance values closely resemble the observed measurements. Also notice how the spectral dependence of the effects of obstructions is shown by the simulated canyons measurements, i.e. in canyons C1 and C2, the short-wavelength end of the spectrum has a lower relative canyon irradiance when only diffuse radiation is blocked due to the large proportions of such wavelengths found in the diffuse component. The third canyon (C3) where only diffuse radiation is available illustrates the spectral effects of Rayleigh and aerosol scattering, i.e. shorter wavelengths exhibit relatively higher intensities (nearly 40% of the irradiance under full sky-view).

In the canyon models, the SVF was the governing aspect affecting diffuse irradiance, whereas the visibility of the solar disc was determined by the geometric position of buildings with respect to the sun's position. The diffuse irradiance was considered isotropic, and was not affected by the orientation of the canyon. Although the absolute uncertainties are relatively small, the results show that this assumption (an isotropic diffuse component) gave larger proportional errors for canyons C2 and especially C3. For these simple models, the larger SVF should have the largest estimated irradiance. However, measurements showed that, when the SVFs are very similar, the irradiance is greater when the circumsolar region is fully visible (C2) than when it is partially blocked (C1), even when the SVF was slightly smaller in C2. The circumsolar radiation illustrates the greatest anisotropy in the diffuse radiation and reveals the weakness in the isotropic assumption. Similarly, canyon C3 – with the direct irradiance blocked – still showed a bright circumsolar region that may have contributed to the larger-than-expected observed irradiances.



A further factor, not considered by the current models, is the reflectivity of horizon obstructions. Reflections may be particularly important when a horizon obstruction is located opposite to the direct solar beam and it is irradiated by it, therefore it will potentially reflect radiation towards the observer in the canyon. Notice in Fig. 6-7 (middle panel) that for wavelengths  $>620$  nm the relative canyon irradiance is larger than 1, meaning that canyon irradiance is larger than the full sky irradiance. The present models do not consider any reflections from wall surfaces. In principle, given the requirement for a fisheye view of the canyon as pre-requisite, wall reflections could be added where indicated by the architecture. Methods for assessing wall reflections include Monte-Carlo ray-tracing and radiosity finite-element applications (Robinson and Stone, 2005). However, these methods add a complexity to the models that is at odds with the goal of fast calculations.

State-of-the-art techniques for fast calculations of spectral irradiance have been developed for the SMARTS algorithm (Jaus et al., 2012), but they require a multi-core architecture for the parallel computation of the algorithm. These techniques have been designed for parallel calculations of large sets of solar cells, similar to what would be required for modelling the spatial and temporal variation of ground solar irradiance within large regions. If multi-core hardware facilities are available, these parallelized versions of SMARTS represent a suitable option for fast calculations while retaining the high accuracy of the SMARTS model. The present approach may, in turn, represent an acceptable trade-off between accuracy and computational performance with low hardware requirements for our purpose, that is calculating the diffuse-to-global ratio (DGR) as an aid to partition global irradiance into its direct and diffuse components. Our simplifications consist, firstly, of the exclusion of certain variables from the calculations (see Eqns. 6.3.6 and 6.3.7). Additionally, compressed empirical equations are included for ozone absorption and the backscattered component of the diffuse radiation (see Table 6-1). Such simplifications certainly limit the

scope of the model and, more importantly, introduce discrepancies when compared against the full SMARTS model. Discrepancies (measured as proportional errors) are shown to illustrate the trade-off between reducing computational demand at the expense of model accuracy. Further modifications can be made to the equations that may increase accuracy, but can potentially increase computational demand. The choice of model might also depend upon the accuracy required of the output. One application we have mentioned is that of human exposure where the infinite vagaries of human behaviour far exceed the uncertainties in the radiation model, yet for which even a simplified canyon model is far more realistic for the radiation environment than a flat horizontal plane.

## 6.5 Conclusions

The proposed models generated acceptable approximations of the spectral DGRs when compared against a well-validated model (SMARTS), for the specific atmospheric conditions studied here. Overall discrepancies (proportional errors) between SMARTS and both compressed models (under cloudless conditions and a full horizon) were below absolute values of 0.2 (or 20%) for a modelled atmosphere with a total ozone column of 0.31 atm-cm and 0.1 AOT<sub>500nm</sub>. The first compressed model accepted aerosol and ozone readings as input parameters, therefore it returned smaller discrepancies against SMARTS (proportional errors below 0.2), even in the sensitivity analyses with changing ozone and aerosol contents. However, a general tendency was observed of increasing discrepancies with increasing aerosol contents (proportional errors changing from < 0.1 at 0.1 AOT<sub>500nm</sub> to > 0.1 at 0.25 AOT<sub>500nm</sub>). Such discrepancies may arise from the empirical fits and simplifications used to represent aerosol transmittances. Larger wavelength ranges (> 500 nm) were more affected by such simplifications, showing the larger discrepancies (absolute proportional errors circa 0.2). The second model had empirically fitted constants which did not accept variations in ozone and aerosol; this model showed even larger discrepancies with changing ozone and

aerosol conditions (proportional errors as large as -0.6), thus illustrating the limitation of empirical fits to specific local atmospheric conditions. Further improvements of these issues may include better representations of ozone and aerosol atmospheric contents in the equations, but they should be accompanied by a cost-benefit analysis for the computational efficiency of the algorithms. The canyon irradiance models were compared against measurements under simulated canyons and returned good approximations when the sun was visible within the obstructed views (with absolute proportional errors approximately below 15% in canyons C1 and C2). However, when the sun was blocked by an obstruction (canyon C3) relative canyon irradiances were underestimated by nearly 40%. This is partially explained by the relative measurement of discrepancies as proportional errors, which tend to increase for small absolute quantities. However, the effect of the anisotropic diffuse irradiance remains to be studied when bright parts of the circumsolar region are visible, even when the direct solar beam is blocked.

In addition to sources of errors in the models, those arising from the assumption of an isotropic diffuse component were made evident when testing the effect of blocking the circumsolar (C1) or the anti-solar (C2) regions. In this case the anisotropy of diffuse irradiance has an effect that was ignored by the models, but could be measured with the instruments. For this reason canyon C2 underestimates the measured spectral irradiance (proportional errors circa -0.1). Unfortunately, so far the anisotropy of diffuse irradiance is complex to model and is computationally intensive. Consequently, it is likely that including such parameters in the models would not currently be cost-effective. In addition the anisotropy of diffuse light is relevant for cloudless skies, but becomes far more complex with broken clouds, and can tend more towards isotropy in dense overcast conditions. As a general conclusion, it can be said that the computationally efficient methods proposed here allow reasonable approximations of street canyon global spectral irradiances, with minimum input

data. The approximations generated by these models will be of most utility for large scale studies, for example when trying to assess human exposure to UV in street canyons for large populated cities.

### **Acknowledgements**

This work was generously funded by the Mexican Council for Science and Technology (CONACyT) (grant reference: 214428). We thank Dr Richard Kift from the Centre for Atmospheric Sciences, University of Manchester for his help in obtaining the global spectral measurements.

### **References**

- Badarinath KVS, Kharol SK, Kaskaoutis DG, Kambezidis HD (2007) Influence of atmospheric aerosols on solar spectral irradiance in an urban area. *J Atmos Solar-Terrestrial Phys* 69:589–599. doi: <http://dx.doi.org/10.1016/j.jastp.2006.10.010>
- Bais A, Blumthaler M, Webb A, et al (2005) Intercomparison of solar UV direct irradiance spectral measurements at Izana in June 2005. *Optics and Photonics 2005*. International Society for Optics and Photonics, p 588609
- Benger SN, Zhou S, Guan H (2014) A dynamic solar irradiance model for assessing solar PV power generation potential in urban areas. *Green Energy for Sustainable Development (ICUE), 2014 International Conference and Utility Exhibition on*. IEEE, pp 1–4
- Bird RE, Riordan C (1986) Simple solar spectral model for direct and diffuse irradiance on horizontal and tilted planes at the earth's surface for cloudless atmospheres. *J Clim Appl Meteorol* 25:87–97.
- Carrasco-Hernandez, R., Smedley, A. R., and Webb, A. R. (2015). Using urban canyon geometries obtained from Google Street View for atmospheric studies: Potential applications in the calculation of street level total shortwave irradiances. *Energy Build*, 86, 340-348.
- Collaud Coen M, Weingartner E, Schaub D, et al (2004) Saharan dust events at the Jungfraujoch: detection by wavelength dependence of the single scattering albedo and first climatology analysis. *Atmos Chem Phys* 4:2465–2480.
- De Carvalho Alves M, Sanches L, de Souza Nogueira J, Silva VAM (2013) Effects of Sky Conditions Measured by the Clearness Index on the Estimation of Solar Radiation Using a Digital Elevation Model. *Atmos Clim Sci* 3:618–626
- Eeftens M, Beekhuizen J, Beelen R, et al (2013) Quantifying urban street configuration for improvements in air pollution models. *Atmos Environ* 72:1–9. doi: <http://dx.doi.org/10.1016/j.atmosenv.2013.02.007>
- Grimmond CSB, Potter SK, Zutter HN, Souch C (2001) Rapid methods to estimate sky-view factors applied to urban areas. *Int J Climatol* 21:903–913.
- Gueymard C (1995) SMARTS2, simple model of the atmospheric radiative transfer of sunshine: algorithms and performance assessment. Florida Solar Energy Center, Florida Solar Energy Center, Cocoa, FL

- Holmer B, Thorsson S, Eliasson I (2007) Cooling rates, sky view factors and the development of intra-urban air temperature differences. *Geogr Ann Ser A, Phys Geogr* 89:237–248. doi: 10.1111/j.1468-0459.2007.00323.x
- Hu B, Wang Y (2013) Comparison of multi-empirical estimation models of photosynthetically active radiation under all sky conditions in Northeast China. *Theor Appl Climatol* 1–11.
- Jaus J, Gueymard CA, Dimroth F, et al (2012) Generalized spectral performance evaluation of multijunction solar cells using a multicore, parallelized version of SMARTS. *AIP Conference Proceedings-American Institute of Physics*. p 122
- Kaskaoutis DG, Kambezidis HD, Kumar Kharol S, Badarinath KVS (2008) The diffuse-to-global spectral irradiance ratio as a cloud-screening technique for radiometric data. *J Atmos Solar-Terrestrial Phys* 70:1597–1606. doi: <http://dx.doi.org/10.1016/j.jastp.2008.04.013>
- Kaskaoutis DG, Kambezidis HD, Tóth Z (2007) Investigation about the dependence of spectral diffuse-to-direct-beam irradiance ratio on atmospheric turbidity and solar zenith angle. *Theor Appl Climatol* 89:245–256.
- Krayenhoff ES, Christen A, Martilli A, Oke TR (2014) A multi-layer radiation model for urban neighbourhoods with trees. *Boundary-Layer Meteorol* 151:139–178.
- Kreuter A, Blumthaler M (2009) Stray light correction for solar measurements using array spectrometers. *Rev Sci Instrum* 80:96108.
- Kreuter A, Buras R, Mayer B, et al (2014) Solar irradiance in the heterogeneous albedo environment of the Arctic coast: measurements and a 3-D-model study. *Atmos Chem Phys Discuss* 14:3499–3536.
- Leckner B (1978) The spectral distribution of solar radiation at the earth's surface—elements of a model. *Sol energy* 20:143–150.
- Lindberg F, Grimmond C (2011) The influence of vegetation and building morphology on shadow patterns and mean radiant temperatures in urban areas: model development and evaluation. *Theor Appl Climatol* 105:311–323. doi: 10.1007/s00704-010-0382-8
- Ludema C, Cole SR, Poole C, et al (2014) Association Between Unprotected Ultraviolet Radiation Exposure and Recurrence of Ocular Herpes Simplex Virus. *Am J Epidemiol* 179:208–215.
- Malinovic-Milicevic S, Mihailovic DT, Radovanovic MM (2014) Reconstruction of the erythemal UV radiation data in Novi Sad (Serbia) using the NEOPLANTA parametric model. *Theor Appl Climatol* 1–8.
- Matzarakis, Andreas, and Olaf Matuschek. "Sky View Factor as a parameter in applied climatology—Rapid estimation by the SkyHelios Model." *Meteorologische Zeitschrift* 20, no. 1 (2011): 39-45.
- Matzarakis A, Rutz F, Mayer H (2010) Modelling radiation fluxes in simple and complex environments: basics of the RayMan model. *Int J Biometeorol* 54:131. doi: 10.1007/s00484-009-0261-0
- Mayer B, Hoch SW, Whiteman CD (2010) Validating the MYSTIC three-dimensional radiative transfer model with observations from the complex topography of Arizona's Meteor Crater. *Atmos Chem Phys* 10:8685–8696.
- Molina LT, Molina MJ (1986) Absolute absorption cross sections of ozone in the 185- to 350-nm wavelength range. *J Geophys Res Atmos* 91:14501–14508. doi: 10.1029/JD091iD13p14501
- Myers D (1997) Radiometric instrumentation and measurements guide for photovoltaic performance testing. National Renewable Energy Laboratory, Golden, Colorado 80401-3393, USA

- Myers, D. R., and Gueymard, C. A. (2004, November). Description and availability of the SMARTS spectral model for photovoltaic applications. In *Optical Science and Technology, the SPIE 49th Annual Meeting*. International Society for Optics and Photonics. pp. 56-67
- NASA LAADS (2013) MOD04\_L2 - Level Aerosol. MOD04\_L2.A2013158.1105.051.2013158202400.hdf. In: 51 - MODIS Collect. 5.1 - Sel. Atmos L. Prod. <http://ladsweb.nascom.nasa.gov/data/search.html>. Accessed 29 Jul 2014
- Nofuentes G, García-Domingo B, Muñoz J V, Chenlo F (2014) Analysis of the dependence of the spectral factor of some PV technologies on the solar spectrum distribution. *Appl Energy* 113:302–309.
- Petersen S, Momme AJ, Hviid CA (2014) A simple tool to evaluate the effect of the urban canyon on daylight level and energy demand in the early stages of building design. *Sol Energy* 108:61–68.
- Redemann J, Russell PB, Hamill P (2001) Dependence of aerosol light absorption and single scattering albedo on ambient relative humidity for sulfate aerosols with black carbon cores. *J Geophys Res Atmos* 106:27485–27495.
- Remer LA, Kaufman YJ, Tanré D, et al (2005) The MODIS Aerosol Algorithm, Products, and Validation. *J Atmos Sci* 62:947–973. doi: 10.1175/JAS3385.1
- Robinson D, Stone A (2005) A simplified radiosity algorithm for general urban radiation exchange. *Build Serv Eng Res Technol* 26:271–284.
- Ruiz-Arias JA, Pozo-Vázquez D, Lara-Fanego V, et al (2011) A high-resolution topographic correction method for clear-sky solar irradiance derived with a numerical weather prediction model. *J Appl Meteorol Climatol* 50:2460–2472.
- Serrano M-A, Boscà J V (2011) Validation of a method to estimate direct normal irradiance of UVA and PAR bands from global horizontal measurements for cloudless sky conditions in Valencia, Spain, by a measurement campaign. *Theor Appl Climatol* 103:95–101.
- Smedley A, Webb A, Rimmer J (2010) Baseline measurement and analysis of UK ozone and UV. *Weather* 65:254.
- Unger J (2009) Connection between urban heat island and sky view factor approximated by a software tool on a 3D urban database. *Int J Environ Pollut* 36:59–80. doi: 10.1504/IJEP.2009.021817
- Vernez, D., Milon, A., Vuilleumier, L., Bulliard, J. L., Koechlin, A., Boniol, M., and Doré, J. F. (2015). A general model to predict individual exposure to solar UV by using ambient irradiance data. *J. Expo. Sci. Environ. Epidemiol.*, 25(1), 113-118.
- Wagner JE, Angelini F, Blumthaler M, et al (2011) Investigation of the 3-D actinic flux field in mountainous terrain. *Atmos Res* 102:300–310.
- Webb AR (2006) Who, what, where and when—influences on cutaneous vitamin D synthesis. *Prog Biophys Mol Biol* 92:17–25.
- Weihls P, Wagner JE, Schreier SF, et al (2012) The influence of the spatial resolution of topographic input data on the accuracy of 3-D UV actinic flux and irradiance calculations. *Atmos Chem Phys* 12:2297–2312.
- Yam JCS, Kwok AKH (2014) Ultraviolet light and ocular diseases. *Int Ophthalmol* 34:383–400.
- Zhu S, Guan H, Bennett J, et al (2013) Influence of sky temperature distribution on sky view factor and its applications in urban heat island. *Int J Climatol* 33:1837–1843. doi: 10.1002/joc.3660.

## Supplementary information for the article

### Fast calculations of the spectral diffuse-to-global ratios for approximating spectral irradiance at the street canyon level

*Roberto Carrasco-Hernandez<sup>\*1</sup>, Andrew R.D. Smedley<sup>1</sup>, Ann R. Webb<sup>1</sup>*

*<sup>1</sup>Centre for Atmospheric Sciences, School of Earth, Atmospheric and Environmental Sciences, University of Manchester, Manchester, M13 9PL, UK*

*Corresponding Author:*

Name : Roberto Carrasco-Hernandez  
Affiliation : University of Manchester  
Address : Room 2.11, Simon Building, Oxford Road, Manchester M139PL  
Phone : +44 7412852056  
Email : [roberto.carrascohernandez@postgrad.manchester.ac.uk](mailto:roberto.carrascohernandez@postgrad.manchester.ac.uk);  
rcarrash@yahoo.com.mx

#### Abstract

Two radiative transfer models are presented that simplify calculations of street canyon spectral irradiances with minimum data input requirements, allowing better assessment of urban exposures than can be provided by standard unobstructed radiation measurements alone. Fast calculations improve the computational performance of radiation models, when numerous repetitions are required in time and location. The core of the models is the calculation of the spectral diffuse-to-global ratios (DGR) from an unobstructed global spectral measurement. The models are based on, and have been tested against, outcomes of the SMARTS2 algorithm (i.e. Simple Model of the Atmospheric Radiative Transfer of Sunshine). The modelled DGRs can then be used to partition global spectral irradiance values into their direct and diffuse components, for different solar zenith angles. Finally, the effects of canyon obstructions can be evaluated independently on the direct and diffuse components, which are then recombined to give the total canyon irradiance. The first model allows ozone and aerosol inputs, while the second provides a further simplification, restricted to average

ozone and aerosol contents, but specifically designed for faster calculations. To assess the effect of obstructions and validate the calculations, a set of experiments with simulated obstructions (simulated canyons) were performed. The greatest source of uncertainty in the simplified calculations is in the treatment of diffuse radiation. The measurement-model agreement is therefore dependent on the region of the sky obscured and ranges from < 5% at all wavelengths to 20-40% (wavelength dependent) when diffuse sky only is visible from the canyon.

## **Introduction**

Table 6-1 in the article contains expressions for individual transmittances required for the calculation of the DGR. Some of these expressions are further simplifications of more complex tables and algorithms used by the SMARTS software; created for the specific purposes of the authors' work. The present supplementary information document shows comparisons of the proposed simplified expressions against SMARTS outputs and data. Note that the supplementary sections, figures and equations presented in this supplementary material are numbered with the prefix **S** before the figure or equation number.

### **S1. Simplification of the Rayleigh scattering transmittance equation**

For the purposes of this work, a simplified approximation to Rayleigh scattering as calculated by SMARTS is provided in the following equation:

$$T_{R\lambda} = \sqrt{\exp\left(-\frac{((360^4)*(M))}{\lambda^4}\right)}. \quad (S1)$$

The following figures show the Rayleigh transmittance for different SZAs, as calculated by Eq. S1 (Figure S1) and a comparison against the calculations of SMARTS for an atmospheric pressure of 1atm (Figure S2).



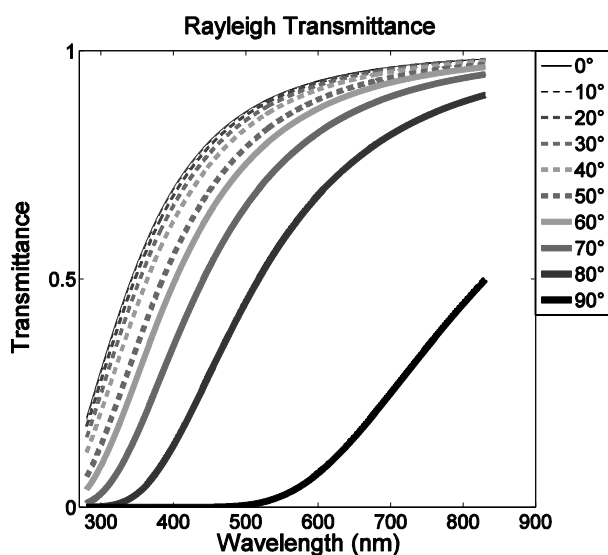


Figure S1 shows the solution of Eq. 1 for different SZA (0 to 90°). This simplified approximation closely matches the calculations proposed by Gueymard, as shown in Figure S2.

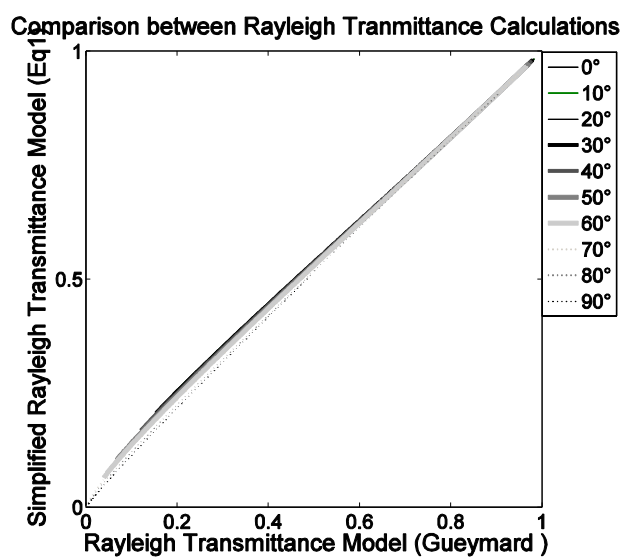


Figure S2 The relationship between Gueymard's approach to calculate Rayleigh transmittance and the approach proposed in the present work.

## S2. Ozone absorption and the effective ozone absorption of the diffuse radiation

For the specific purposes of this work, simple empirical fits are also proposed to the ozone absorption coefficients provided by Molina and Molina (1986). Two fits were needed to better approximate the Hartley and Huggins absorption bands. Equations S3 and S4 show the empirical fits for ozone absorption cross sections at the Hartley ( $A_{O\lambda Hartley}$ ) and Huggins ( $A_{O\lambda Huggins}$ ) bands of ozone absorption, based on the original laboratory data from (Molina and Molina, 1986).

$$A_{O\lambda Hartley} = 1140 \exp(-1.5E - 3 \cdot (\lambda - 253.65)^2), \quad (S3)$$

$$A_{O\lambda Huggins} = A_{O\lambda Hartley} \cdot \frac{1}{2} \exp((2.7E - 4) \cdot (\lambda - 253.65)^2). \quad (S4)$$

Note that the constants 1140 and 253.65 in Eq. S3 correspond to the wavelength with maximum absorption (253.65) and its absorption coefficient according to the reported values of Molina and Molina (1986).

Equation S4 returned good estimates of the spectral ozone absorption cross sections at wavelengths near 253.65 nm (Hartley band) (see Figure S3). However, as shown in Figure S4, the Huggins absorption band ( $\lambda > 320$  nm) was strongly underestimated.

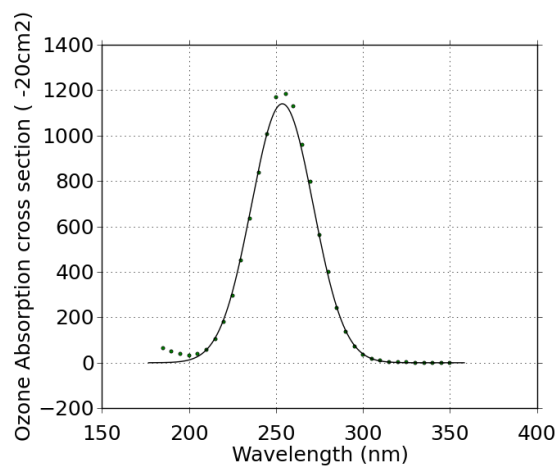


Figure S3 The fit (Eq S3) for the Hartley band ozone absorption data of Molina and Molina.

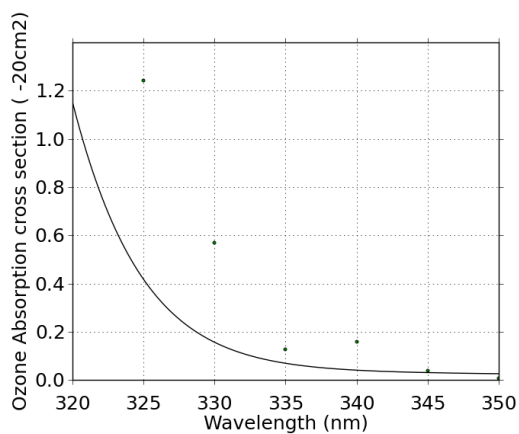


Figure S4 A detailed section of larger wavelengths that illustrate the associated error of Equation S3.

In Figure S4 the fit to the Huggins band (Eq. S4) was used to better approximate absorption cross sections at larger wavelengths in the ultraviolet range:

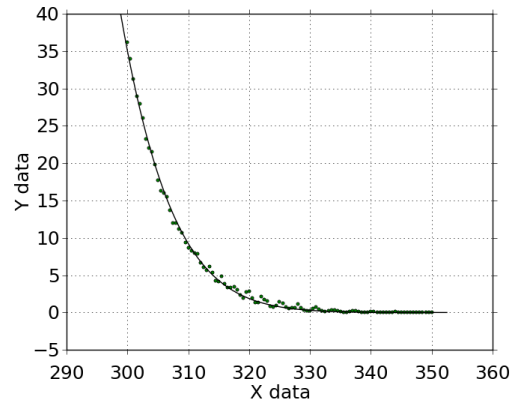


Figure S5 The Huggins band fit (Eq S4) to the ozone absorption cross section of Molina and Molina.

Equation S3 better approximated absorptions at wavelengths below 320nm and underestimated them above this limit; Equation S4 showed the inverse pattern. For this reason, a final function for the ozone absorption coefficients  $A_{O\lambda}$  is set to be as follows:

$$A_{O\lambda} = \max(A_{O\lambda\text{Hartley}}, A_{O\lambda\text{Huggins}}). \quad (\text{S5})$$

Finally,  $A_{O\lambda}$  can then substituted into Eq. S2.

### S3 Effective to standard ozone transmittance

Gueymard (1995 p 28) presents a figure showing that the ratio of effective-to-standard ozone transmittance  $\frac{\Gamma_{O\lambda}}{T_{O\lambda}}$  is approximately a logarithmic linear function of the ozone optical thickness and air mass. Equation S6 represents an approximation to Gueymard's figure for the ratio of effective-to-standard ozone transmittance.

$$\frac{\Gamma_{O\lambda}}{T_{O\lambda}} \approx 10^{0.3_{ot} \left( \frac{1}{\cos(Z)} - \frac{1}{\cos(35)} \right)^3}. \quad (\text{S6})$$

Figure S6 shows the solution of equation S6 for five different air masses:

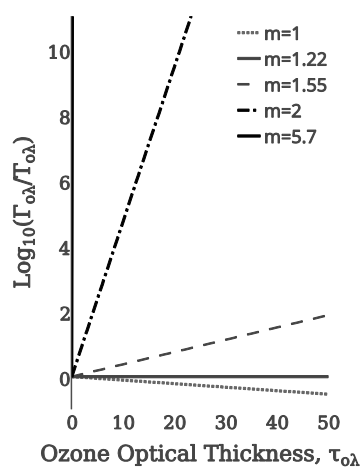


Figure S6 The solution of Eq. S6 for values of ozone optical thickness of 0 to 50 and 5 different air masses (i.e. 1, 1.22, 1.55, 2 and 5.7), corresponding respectively to SZAs of  $0^\circ, 35^\circ, 50^\circ, 60^\circ, 80^\circ$ . The selected SZAs roughly correspond to the air masses in Figure S1.

## Chapter 7

This chapter paper is planned to be submitted to *Theoretical and Applied Climatology*.

The author of this thesis (Roberto Carrasco Hernandez) is also the first author of the article. The original concept, research methods, and outcomes were developed by the first author, under the close supervision of co-authors Andrew R.D. Smedley and Ann R. Webb. The article was written by Carrasco-Hernandez, with advice and assistance from the co-authors.

The radiometric data for this article was obtained from a spectrometer installed at the monitoring station of the Centre for Atmospheric Sciences of the University of Manchester. The monitoring station is jointly run by co-authors Andrew R.D. Smedley and Ann R. Webb, and by Dr Richard Kift who is acknowledged for his help.

## Using RGB images to approximate the angular sky distribution of ultraviolet and visible wavelengths as affected by street-canyon obstructions

Roberto Carrasco-Hernandez<sup>\*1</sup>, Andrew R.D. Smedley<sup>1</sup>, Ann R. Webb<sup>1</sup>

<sup>1</sup>Centre for Atmospheric Sciences, School of Earth, Atmospheric and Environmental Sciences, University of Manchester, Manchester, M13 9PL, UK

### Abstract

A low-cost method is proposed for approximating street-canyon global spectral irradiances for ultraviolet and visible wavelengths, while considering the anisotropic distribution of sky irradiance under a cloudless sky. A digital mobile phone camera, equipped with a commercial mini-fisheye lens was used to obtain whole-sky RGB images. RGB images were digitally processed in order to approximate the anisotropy of sky irradiance for three visible wavelengths (460, 530, 600 nm, respectively assumed to correspond to the effective wavelengths represented by each RGB channel). Afterwards, the RGB signatures of each pixel in the images were extrapolated to approximate the relative pixel brightness in three ultraviolet wavelengths (310, 355 and 400 nm). Finally, each RGB+UV sky distribution was combined with a projection of a simulated horizon obstruction to obtain “weighted” sky view factors ( $SVF_w$ ), which included information on the brightness of blocked/visible pixels.  $SVF_w$  were evaluated for simulated obstructions in two different orientations, blocking the anti-solar and the circumsolar region respectively. The  $SVF_w$  were then introduced in a simple spectral model to calculate street-canyon (i.e. obstructed view) irradiance as a fraction of a full sky-view irradiance measurement. The present model improves on previous assessments of canyon irradiance that assumed diffuse irradiance to be isotropic.

### 7.1. Introduction

The angular distribution of sky radiation may be defined as the anisotropic incoming radiation from the upper-hemispheric view of a ground observer. Under cloudless conditions,

the main source of anisotropy is the relative position of the direct solar beam in the sky, rendering increased radiances for solid angles located in the vicinity of the solar disc (Rosen et al., 1989). Additionally, because of Rayleigh scattering, the gradient of radiances across the sky is wavelength dependent, with shorter wavelengths (e.g. the ultraviolet) showing a more isotropic distribution across the sky. The angular distribution of diffuse spectral irradiance becomes relevant when considering horizon obstructions in different orientations, for example, those exerted by buildings inside street canyons, which affect human exposure.

For simplicity, some approximations to street canyon irradiances have assumed an isotropic distribution of diffuse irradiance across the sky (Matzarakis et al., 2010, Carrasco-Hernandez et al., 2015). However, according to Grant et al. (1997), such assumption may be a poor description even for the ultraviolet bands. Sky obstructions may have a larger effect on street-level irradiance when blocking brighter parts of the sky (i.e. the circumsolar region) than blocking the duller parts (i.e. the anti-solar region). In order to account for anisotropy, the sky distribution of spectral irradiance may be theoretically modelled, for cloudless conditions, by using radiative transfer models like LibRadTran (Rezaei-Ghaleh, 2003) or even for all-weather conditions (Darula and Kittler, 2002; Igawa et al., 2004). Unfortunately, these algorithms are usually time consuming and generally not suitable for real-time applications.

Whole-sky cameras are a suitable alternative for instantaneously describing the true angular distribution of sky radiation. Whole-sky images represent a polar (fisheye) 2D projection of the 3D hemispheric sky-view. If combined with a corresponding polar projection of horizon obstructions (e.g. from a fisheye photograph taken inside a street canyon), whole-sky images can be used to assess the effects of blocking different sections of the anisotropic sky (Hess and Koepke, 2008). Fisheye projections of horizon obstructions may either be obtained by using a camera equipped with 180° fisheye lenses, or they can be



reconstructed from rectilinear images (Carrasco-Hernandez et al., 2015b). In turn, whole-sky fisheye images (i.e. of the unobstructed sky) may be obtained from a convenient location (e.g. a rooftop with a full sky-view).

In previous work (Carrasco-Hernandez et al., 2015), we have verified the relevance of blocking different sky sections when validating models that neglected anisotropy. Models assuming an isotropic diffuse component would always calculate larger irradiances for canyons with a larger SVF, regardless of the blocking of brighter sections of the sky (i.e. the circumsolar region). In contrast, empirical validations of the models showed that a canyon with a blocked circumsolar region would receive lower irradiances than a canyon with a fully visible circumsolar region, despite the former having a slightly larger SVF.

The present article attempts to include the anisotropy of diffuse sky radiation into the calculations of street-canyon global spectral irradiances. It is also an objective to provide a method using low-cost commercial instruments (i.e. mobile phone cameras with detachable mini-fisheye lens). The proposed algorithms may return acceptable approximations of angular irradiance distributions, without the need of specialised instruments and laboratory characterisations.

This article is divided in three blocks: Block I (Section 7.2) describes a polar representation (i.e. sky-maps) of the angular sky distribution in three visible wavelengths (460, 530, 600 nm). Sky-maps in the visible range are obtained from RGB fisheye photographs of a full sky-view. Block II (Section 7.3) describes the methods for extrapolating the sky-maps towards ultraviolet wavelengths (310, 355, 400 nm). Finally, in Block III (Section 7.4), the methods for calculating canyon spectral irradiance are described, which require as input parameters: i) a full-sky view measurement of global spectral irradiance, ii) “fisheye” projected canyon profiles, and iii) a weighted sky view factor ( $SVF_w$ ) containing

information on the obstruction of the anisotropic diffuse component. This  $SVF_w$  is obtained (for each UV-visible wavelength) from the sky-maps masked with the projected obstructions. Methods and results are presented independently within each section and a comparison against our previous modelling techniques (which assumed isotropic diffuse irradiance) is presented in the Discussions section.

## **7.2 Block I. Digital processing of whole-sky RGB maps**

This section describes the digital processing techniques used to approximate sky-maps in three visible wavelengths (470, 530 600 nm). All digital image processing was done using Octave 3.2.4.

Whole-sky RGB images were taken with a Nokia E5 mobile phone equipped with a magnetic mini-fisheye lens (Sumlung, model: SL-FE12). The projection of the SL-FE12 fisheye lens was determined to be orthographic. The spectral sensitivity of the Nokia E5 camera was assumed to be equivalent to that of a Nokia N900 reported by (Jiang et al., 2013), with peak sensitivities for the Blue, Green and Red channels at 460, 530 and 600 nm respectively. It was also assumed that peak sensitivity wavelengths correspond to the effective wavelength represented by each channel (Kholopov, 1975). This assumption was made based on the reports of Román et al. (2012), in which the calculated effective wavelengths resulted slightly below peak channel sensitivities (with small differences of 5nm approximately). Fig. 7-1 shows the three RGB images obtained.

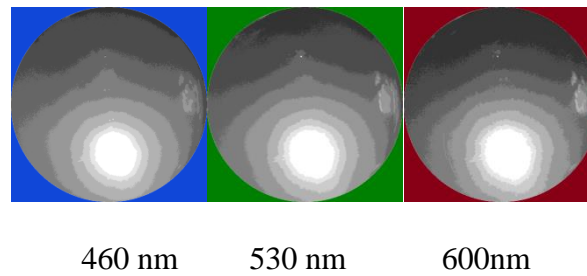


Figure 7-1 Original RGB images obtained with a Nokia E5 digital camera, equipped with a Sumlung SL-FE12 magnetic mini-fisheye lens. Each channel approximately represents the angular distribution of peak sensitivity wavelengths: 460, 530 and 600 nm, as indicated. Digital pixel values, ranging from 0 to 255, have been reclassified in ten classes, at equal intervals across the range (This reclassification will not be used in any of the calculations, and it is only intended for illustrative purposes).

Fig. 7-1 illustrates the spectral differences in angular distribution. For example, the darker pixels (i.e. digital values < 25) on the “Blue” channel (460 nm) occupy only a thin line on top of the image; while the same range of “dark” values occupies a thicker area on the “Red” image. In general, as expected from atmospheric scattering, brighter pixel values tend to be more spread on the images representing shorter wavelengths.

RGB sky images were then digitally processed into representations of the angular sky irradiance distributions of three visible wavelengths (460, 530 and 600nm). Digital processing was necessary since certain intrinsic characteristics of digital cameras and fisheye lenses differ from those of global irradiance radiometers. The digital processing considered: i) the nonlinearity of the sensors’ response to radiance intensity, and ii) saturation and the misrepresentation of the direct beam. Saturated pixels were removed (zeroed) from the images, under the assumption that—without these values—the direct beam and the circumsolar radiation would be removed from the images. The consequence of such assumption is that the total sum of pixel values is proportional to the diffuse irradiance minus

the circumsolar radiation. These issues will be further described in Subsection 7.2.2 and included into the models in Blocks II and III. The following section (7.2.1) describes the corrections to the non-linear response of the camera. For the purpose of this study, we will refer as “sky-maps”, to the single-wavelength distributions that result from the digital processing of the original fisheye camera images.

### 7.2.1 Non-linear response to light intensity.

The radiometric response of digital cameras is not linear with respect to the received irradiance. Figure 7-2 shows an average normalized radiometric response; extracted from the EMoR database (Grossberg and Nayar, 2003). The EMoR database contains data from 171 devices, including CCDs, as well as video, and digital cameras of common commercial brands.

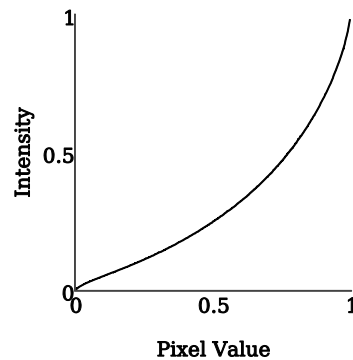


Figure 7-2 Inverse average response of 171 cameras obtained from the EMoR database (Grossberg and Nayar, 2003).

A fourth order polynomial (Eq. 7.1) was fitted to the original average values from Grossberg and Nayar (2003) ( $R^2 = 0.9994$ ).

$$\rho_{ri} = 0.9855\rho_i^4 - 0.8791\rho_i^3 + 0.6401\rho_i^2 + 0.2552\rho_i - 0.0038, \quad (\text{Eq. 7.1})$$

where  $\rho_i$  is the normalized response pixel value, and  $\rho_{ri}$  is the response-corrected pixel value.

Applying Equation 7.1 to each individual pixel in the images would correct the camera's response to intensity. Fig. 7-3 shows a comparison between the original "Red" image (Left panel) against the corresponding response corrected image (Right panel).

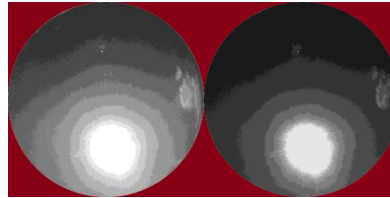


Figure 7-3 Example comparison between the original "Red" channel image (Left panel) against the corresponding response corrected image, after applying Eq. 7.1 to all pixels (Right panel). The same process was repeated for the "Green" and "Blue" images.

### **7.2.2 Saturation and the misrepresentation of the direct beam (removal of saturated pixels)**

For any fisheye lens, internal diffraction of the direct beam may occur, as well as the internal dispersion of the beam as stray light. Additionally, the intensity of the direct beam could overpass the saturation capacity of individual pixels in the camera and therefore fail to be fully represented by pixel digital intensity values. Thus, in the image, each saturated pixel in the vicinity of the direct beam contains the corresponding proportion of circumsolar radiation, plus an unknown fraction of the dispersed direct solar beam. Under this assumption, by removing the saturated pixels from the images, the direct beam and the circumsolar radiation are removed from the image. In order to do this, saturated pixels (i.e. pixels with values equal to the maximum) were reclassified as zero. Fig. 7-4 shows an example where the saturated pixels have been removed from the "Red" image.

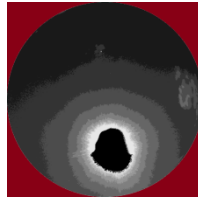


Figure 7-4 Showing the response-corrected Red image after the saturated pixels have been reclassified as “zero”. The same process was repeated for the “Green” and “Blue” images.

### 7.2.3 The spectral Diffuse-minus-Circumsolar irradiance ( $D - C_\lambda$ )

After the saturated pixels have been removed (Fig. 7-4), it can now be assumed the total sum of the remaining pixel values is proportional to the diffuse irradiance minus the circumsolar ( $D - C_\lambda$ ). These assumptions will be of great relevance in the extrapolation towards UV bands (Block II), because the extrapolation will require an estimation of global irradiance from the total sum of pixels.

The total sum of pixel values in the sky maps will be referred to as the *Digital Diffuse-minus-Circumsolar Irradiance* ( $d.D - C_\lambda$ )

$$d.D - C_\lambda = \sum \alpha_{f,\lambda},$$

where  $d$  stands for “digital value”;  $D$  is the spectral diffuse component;  $C$  is the spectral circumsolar component;  $\sum \alpha_{f,\lambda}$  denotes the total sum of pixels from each processed full-sky-view sky map at wavelength  $\lambda$ .

In Blocks II and III (Sections 7.3 and 7.4, respectively), digital values of global irradiance ( $d.G_\lambda$ ) will also be needed. The following rationale was used to infer a  $d.G_\lambda$  value from the  $d.D - C_\lambda$

In order to approximate the  $d. G_{\lambda}$ , a quotient must be known, defined as the ratio of the diffuse-minus-circumsolar to global irradiance  $((D - C_{\lambda}):G_{(\lambda)})$ .

$$(D - C_{\lambda}):G_{(\lambda)} \equiv \frac{E_{d,F,\lambda} - E_{Cs,F,\lambda}}{E_{F,\lambda}}, \quad (\text{Eq. 7.2})$$

where  $E_{d,F,\lambda}$  is the diffuse component of global irradiance;  $E_{Cs,F,\lambda}$  is the circumsolar component,  $E_{F,\lambda}$  is the global irradiance. All of them under a full sky-view F, for wavelength  $\lambda$ . Note that these are irradiance instead of digital values.

The  $(D - C_{\lambda}):G_{(\lambda)}$  ratio is a function of wavelength, solar zenith angle and other atmospheric parameters (e.g. ozone, aerosol contents). For a cloudless sky, this ratio can be modelled using radiative transfer software, such as SMARTS (Myers and Gueymard, 2004). SMARTS allows the calculation of circumsolar irradiance normal to the direct beam, as received by simulated input optics with a user-specified field of view. In SMARTS, the simulated field of view can be expressed as half of the aperture angle of the input optics' collimator (Gueymard, 2005). Once calculated, the circumsolar must be projected unto a flat horizontal surface (i.e. multiplying it by the cosine of the solar zenith angle). Finally, the projected circumsolar can be substituted into Eq. 7.2, along with the corresponding diffuse and global irradiances to obtain a  $(D - C_{\lambda}):G_{(\lambda)}$  ratio.

Table 7-1 shows the  $(D - C_{\lambda}):G_{(\lambda)}$  ratios, calculated using SMARTS for each of the three visible wavelengths (460, 530 and 600 nm). They were calculated for a standard mid-latitude urban summer atmosphere at a SZA of 32.03 °; corresponding to 11:25:00, 7<sup>th</sup> June 2013 at the Pariser Building University of Manchester (53.46° N, 2.23°W). These parameters also correspond to the conditions of a set of experiments, described in Block III.

**Table 7-1**  
 **$(D - C_\lambda): G_{(\lambda)}$  ratios for three visible**  
**wavelengths, as calculated using SMARTS**

$\lambda$ (nm)	$(D - C_\lambda): G_{(\lambda)}$
<b>460</b>	0.17
<b>530</b>	0.12
<b>600</b>	0.09

The circumsolar irradiance was calculated considering that the amount of removed (saturated) pixels in the images was approximately 4% of the total number of pixels. In order to cover 4% of the upper-hemispheric sky-view, a half aperture angle ( $\theta$ ) of  $16^\circ$  was calculated for the simulated collimator. However, SMARTS would only allow the calculation of circumsolar irradiances up to  $10^\circ$ . Therefore, a test was run to determine the change of the  $(D - C): G_{(\lambda)}$  ratio, with changing  $\theta$ . When changing  $\theta$  from  $4^\circ$  to  $10^\circ$ , the  $(D - C): G_{(\lambda)}$  ratio is reduced by 5.2% on average throughout the spectrum (310 to 700 nm). It can be assumed that the reduction when changing  $\theta$  from  $10^\circ$  to  $16^\circ$  will be approximately or even lower than 5.2%. For this reason the change was neglected, and modelled circumsolar irradiances correspond to those calculated with a  $\theta$  of  $10^\circ$ . Finally the circumsolar irradiance must be projected onto a flat horizontal surface, by multiplying it by the cosine of the solar zenith angle.

The  $(D - C): G_{(\lambda)}$  ratio will then allow the approximation of the digital global irradiance from a known  $d \cdot D - C_\lambda$ , as follows:



$$d. G_{f,\lambda} = \frac{d.D - C_\lambda}{(D-C):G(\lambda)}, \quad (\text{Eq. 7.3})$$

where  $d. G_{f,\lambda}$  is the digital global irradiance at wavelength  $\lambda$ , under a full-sky view  $f$ ;  $d.D - C_\lambda$  is the digital diffuse-minus-circumsolar irradiance at wavelength  $\lambda$ ; and  $(d - c):G(\lambda)$  is the spectral ratio defined in Eq. 7.2 at wavelength  $\lambda$ , and calculated using SMARTS.

Then, it is possible to calculate an approximation to the digital global irradiance ( $d. G_\lambda$ ), by assuming that the total sum of pixel values ( $\alpha$ ) (i.e. without saturated pixels) is only proportional to the  $d. D - C_\lambda$ .

$$d. G_\lambda = \frac{\sum \alpha_{f,\lambda}}{(D-C):G(\lambda)}. \quad (\text{Eq. 7.4})$$

In Block II, the estimated  $d. G_\lambda$  will be used to normalize pixel RGB signatures, so that the post-processed sky-maps (exemplified in Fig 7-4) can be extrapolated towards three ultraviolet wavelengths (400, 350, 310 nm). In Block III global digital irradiances, in combination with the generated RGB+UV sky-maps, will be used to approximate street canyon irradiances in the corresponding visible and UV wavelengths. The removal of saturated pixels will, however, add complexity to the modelling process of street canyon irradiances (as will be explained in Block III), since the global irradiance must be partitioned into direct, diffuse and circumsolar irradiance, in order to assess the independent effect of horizon obstructions on these components.

### **7.3 Block II. Extrapolated UV whole-sky maps**

#### **7.3.1 Extrapolation of a hypothetical UV sky distribution**

The raw spectral radiance signature from any solid angle in the sky has a characteristic shape (Figure 7-5, Left panel), as a result of radiative transfer in the atmosphere. However, if

the spectral signature of a single solid angle is normalized with respect to the corresponding global irradiance, a smooth curve is obtained (Figure 7-5, Right panel), in which UV wavelengths are easier to extrapolate from visible (e.g. RGB) information.

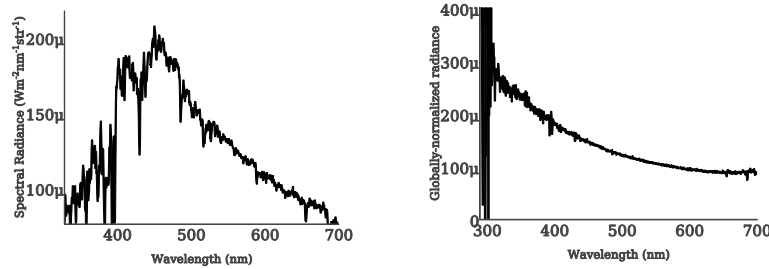


Figure 7-5 Left panel: Raw spectral signature of small solid angle pointing at a clear sky). Right panel: Globally-normalized radiance i.e. the quotient between sky radiance projected onto a flat horizontal surface and the corresponding global irradiance. Sky radiance was measured from a  $2^\circ$  field-of-view input optics, with angular position:  $180^\circ$  azimuth and  $30^\circ$  zenith. Measurements were taken with a calibrated 2-channel Ocean Optics S2000 spectrophotometer, under clear sky conditions.

In order to obtain globally-normalized RGB pixel values, equation 7.4 was used to approximate a digital global irradiance ( $d.G_\lambda$ ). Then, the following equation (Eq. 7.5) was used to normalize digital pixel values in each of the RGB bands with respect to the calculated global irradiance.

$$n\alpha_{if\lambda} = \alpha_{if\lambda}/d.G_\lambda, \quad (\text{Eq. 7.5})$$

where  $n\alpha_{i,f,\lambda}$  is the globally-normalized digital value  $\alpha$  of pixel  $i$  under the full-sky view  $f$ , at wavelength  $\lambda$ ;  $\alpha_{i,f,\lambda}$  is the digital value of pixel  $i$ ;  $d.G_\lambda$  is the digital global irradiance at wavelength (obtained with Eq. 7.4).

### 7.3.2 Extrapolation of globally-normalized RGB signatures towards the ultraviolet

A linear extrapolation is proposed for each pixel in the image, from globally-normalized RGB towards the UV i.e. by using the average slope between the three RGB data points (E. 7.6.1)

$$\frac{UV_i - B_i}{\Delta\lambda_{UV-B}} = \frac{\left[ \frac{B_i - G_i}{\Delta\lambda_{B-G}} + \frac{G_i - R_i}{\Delta\lambda_{G-R}} \right]}{2}, \quad (\text{Eq. 7.6.1})$$

where  $UV_i$  represents an ultraviolet digital globally-normalized value extrapolated from the Blue ( $B_i$ ), Green ( $G_i$ ) and Red ( $R_i$ ), also globally-normalized, all at pixel  $i$ . Each one of the **RGB** values represents the wavelengths 430, 560 and 700 nm respectively. The symbols  $\Delta\lambda_{x1-x2}$  represent the wavelength step within which a linear slope is being assumed (e.g.  $\Delta\lambda_{B-G}$  is the linear step between the blue and green bands).

Rearranging Eq. 7.6.1:

$$UV_i = \left[ \frac{\Delta\lambda_{UV-B}}{2\Delta\lambda_{B-G}} (B_i - G_i) + \frac{\Delta\lambda_{UV-B}}{2\Delta\lambda_{G-R}} (G_i - R_i) \right] - B_i. \quad (\text{Eq. 7.6.2})$$

Equation 7.6.2 can be applied to every pixel on the sky-maps, under the assumption that the globally-normalized spectral curve exhibits a linear trend, regardless of the pixel's angular position in the hemispheric view.

To test the suitability of the linear extrapolation, radiance values were modelled for points in the sky vault using LibRadTran, and afterwards were globally-normalized. Spectral diffuse radiances were calculated for a standard mid-latitude summer atmosphere with a 25° solar zenith angle. Nine different spectral radiances were obtained at different zenith angles (0 to 80°) for 6 wavelengths at: 310, 355, 400, 460, 530 and 700 nm. LibRadTran-modelled radiance values were then projected onto a flat horizontal surface. Finally, the projected diffuse radiances were normalized to a corresponding modelled global calculation. A

comparison of the LibRadTran-modelled ultraviolet spectral irradiances versus the linearly extrapolated values (according to Eq. 7.6.2) is shown in Figure 7-6. In this case, Equation 7.6.2 was applied to RGB radiances modelled with LibRadTran at 460, 530 and 600 nm.

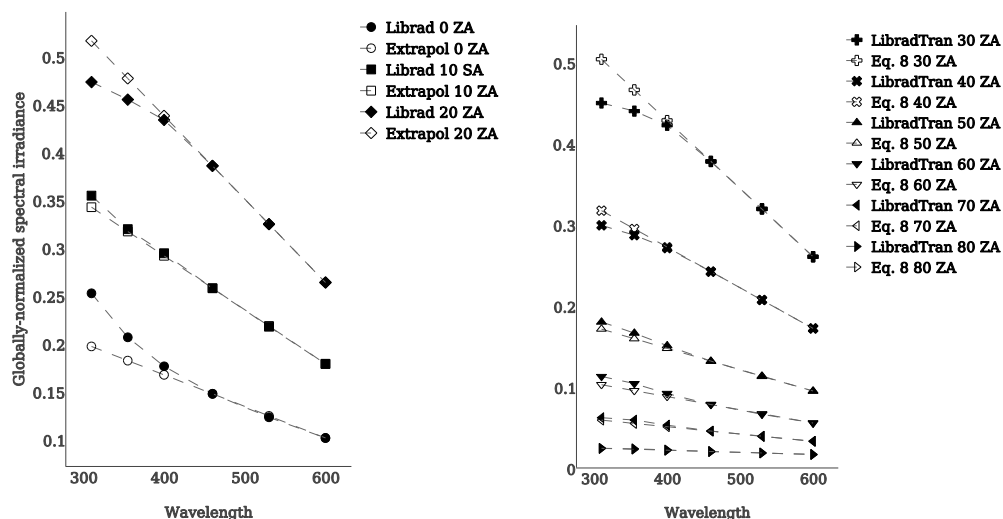


Figure 7-6 Globally-normalized spectral signature of different angular positions in the hemispheric sky view, modelled with LibRadTran (black filled ticks) for 6 UV and visible wavelengths (310, 355, 400, 460, 530 and 700 nm); compared against a linear extrapolation towards the UV (Eq. 7.6.2) from the LibRadTran-modelled visible wavelengths (white outlined ticks). Left panel shows radiances from angular positions towards the solar azimuth at zenith angles ranging from 0 to 20°. Right panel shows angular positions at zenith angles ranging from 30 to 80 ° towards the solar azimuth.

According to Fig 7-6, the globally-normalized diffuse radiance tends to increase towards the solar zenith angle (in this case 25°) for all wavelengths. Additionally, the normalized diffuse radiance is relatively higher for the ultraviolet than the visible, at any specific angular position. However, the slope of increase towards the UV, estimated by SMARTS, is reduced towards the UV (see, for example, the SMARTS calculations at 20 and 30 ZAs in Fig 7-6). This phenomenon is possibly due to strong ozone absorption of the diffuse radiation. For this

reason, the linear extrapolation tends to overestimate the SMARTS-calculations in the UV at certain zenith angles (see comparisons from ZAs 20° to 40° in Fig. 7-6). On the other hand, towards the horizon, RGB diffuse radiances tend to homogenize and the resulting extrapolation does not overestimate the SMARTS-modelled results at higher zenith angles (ZA >50 °, Figure 7-4 Right panel). Measured percentage errors from data in Fig. 7-6 were, mostly, below 5%, yet with a maximum error of 21% for the 310nm extrapolation at zenith (0 ° ZA).

The linear extrapolation from visible information represents a simple approximation to globally normalized radiance values in the UV. To reconstruct sky-maps in the UV wavelengths, Equation 7-6 was applied to individual pixel in the images, using the RGB signatures.

### **7.3.3 Extrapolated UV sky-map from RGB information.**

Three representative wavelengths in the UV were extrapolated, namely 310, 355 and 400 nm: The 310nm wavelength is of interest because it represents the peak of the erythemally-weighted ultraviolet radiation. The 355 nm wavelength represents the central position of the UVA range. Finally, the 400 nm represents the end of the UV range. UV sky-maps were extrapolated from RGB sky-maps. A pixel-by-pixel linear extrapolation was performed using Equation 6. Figure 7-5 shows the three extrapolated sky-maps.

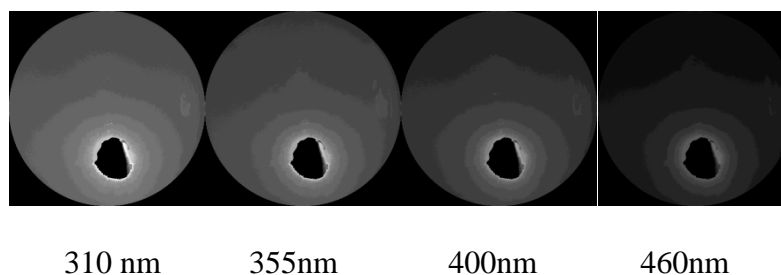


Figure 7-7 Globally-normalized sky-maps for three UV wavelengths (310, 355 and 400nm), compared against the globally-normalized values in the blue channel (460nm). (For illustrative purposes, all pixel values have been reclassified into twenty classes, and rescaled with respect to the maximum pixel value at the 310 nm sky-map).

The sky-maps presented in Figure 7-7 are globally-normalized values; therefore, sky-maps towards the UV appear “brighter” than visible wavelengths (as expected by the linear extrapolations of Equation 6). A consequence of such “global normalization” is that the digital global irradiance from normalized values should equal 1. Under the assumption that only the  $D - C$  irradiance is represented in the image, the total sum of globally-normalized pixel values should approximately correspond to the expected  $(D - C):G_{(\lambda)}$  ratio at each wavelength. Comparisons of the total pixel sum of images in Figure 7-7 (i.e. the extrapolated  $(D - C):G_{(\lambda)}$  for UV wavelengths) against the same expected ratios, as calculated using SMARTS, are presented in Table 7-2 for the UV.

<b>Table 7-2. Comparisons between extrapolated and expected (SMARTS) <math>(D - C):G_{(\lambda)}</math> ratios, in ultraviolet wavelengths</b>		
$\lambda$ (nm)	<b>Extrapolated</b> $(D - C):G_{(\lambda)}$	<b>Modelled</b> $(D - C):G_{(\lambda)}$ <b>(SMARTS)</b>
310	0.587	0.521
355	0.461	0.373
400	0.334	0.264

Discrepancies at shorter wavelengths were expected from Figure 7-6, where the linear extrapolation shows a tendency to either overestimate or underestimate the modelled values at different angular positions for shorter wavelengths. Note in Table 7-2 that the extrapolated  $(D - C): G_{(\lambda)}$  ratio, obtained from the total sum of pixel values, overestimates the same ratio, as calculated using SMARTS. The average proportional error between the extrapolated and SMARTS-modelled ratios in Table 7-2 is 0.20 (i.e. 20%).

Block III will describe the general methods for calculating the proportion of visible sky (i.e. SVF) under simulated canyons, while including information on the obstruction of sky sections with different brightness. These weighted SVFs ( $SVF_w$ ) will be calculated as the quotient between total pixel sum of the sky maps under the obstructed and the total pixel sum under a full-sky view. In Block III, the globally-normalized UV sky-maps (Figure 7-7) will be used as substitutes for the absolute sky-maps (originally obtained for the RGB images, Figure 7-4). This substitution is justified by the fact that the quotient between obstructed and full-sky views is arithmetically identical, regardless if it is obtained from absolute distributions or globally-normalized distributions.

## **7.4 Block III. Calculations of street canyon spectral irradiance using $SVF_w$**

### **7.4.1 General methods for the calculation of street canyon spectral irradiance**

A simple approach to calculate street-canyon global irradiance is by assuming that canyon irradiance is a fraction of a full-sky global irradiance measurement. Such fraction is a function of the visibility of the solar disc and the SVF. Equation 7.7 describes the general form of these models.

$$E_{u,\lambda} = (E_{s,f,\lambda})S_{bin} + (E_{d,f,\lambda})SVF, \quad (\text{Eq. 7.7})$$

where  $E_{u,\lambda}$  is the global irradiance in an urban canyon at wavelength  $\lambda$ ;  $E_{s,f,\lambda}$  is the direct irradiance under full-sky view at wavelength  $\lambda$ ;  $S_{bin}$  is a binary digit representing the visibility of the direct solar beam;  $E_{d,f,\lambda}$  is the diffuse irradiance under full-sky view at wavelength  $\lambda$ ;  $SVF$  is the sky view factor within the canyon.

The effects of sky obstructions on the direct and diffuse components are analysed independently and then summed together by Eq. 7.7. Direct irradiance in the canyon depends on whether the solar disc is visible, while diffuse irradiance is proportional to the SVF. Equation 7.7 serves as a basis for the model proposed in the present work, as it considers irradiance in any urban canyon as a fraction of the irradiance measured under a full-sky view, and a function of  $S_{bin}$  and the SVF. However, the “raw” SVF of Eq. 7.7 will be substituted by a weighted SVF ( $SVF_w$ )—specific for each wavelength—containing information on the obstructions of the anisotropic sky.

In the original Eq. 7.7, the diffuse radiation is assumed to be isotropic. Unfortunately, the effects of building orientation on the diffuse cannot be calculated using such type of models. Our previous models, under the isotropy assumption (Carrasco-Hernandez et al., 2015), showed evident errors when validating the calculated spectral irradiance in simulated canyons with different orientations, against empirical data. The measurements obtained from our previous simulations have been used again in the present work, but the present models use the approximated RGB+UV sky-maps (Blocks I and II) to calculate  $SVF_w$  and account for the anisotropy of the diffuse component.

The input parameters required to model street canyon spectral irradiance are, according to Eq. 7.7: i) a measurement of global spectral irradiance under a full (unobstructed) view, partitioned into its direct and diffuse components (Eq. 7.7); ii) full-view sky maps for the



angular distribution of selected wavelengths (see Block II); finally, iii) a profile of specific horizon obstructions within an urban canyon (to calculate a weighted sky view factor containing information on obstructions of the anisotropic diffuse radiation). These parameters will be used with a modified version of Eq. 7.7 to model global spectral irradiance within simulated canyon obstructions. Modifications to Eq. 7.7 will consider the removal of saturated pixels (and the circumsolar radiation) by partitioning global irradiance into its direct, diffuse and circumsolar components (see Section 7.4.5).

The following subsections (7.4.2 to 7.4.4) describe the experiments with simulated canyons, as well as the methods for calculating weighted sky view factors  $SVF_w$ . Finally, Subsection 7.4.5 describes the calculations of relative canyon spectral irradiances on the basis of unobstructed global spectral measurements.

#### **7.4.2 Simulated canyons**

Our model validations consisted of comparing two simulated obstructions, one blocking the circumsolar and the other, the anti-solar regions from the sky view of a global spectrometer. Projected fisheye images of canyon obstructions were obtained (Fig. 7-8), from which the “raw” SVF (i.e. considering the dimensions of the obstructions only) was calculated using the RayMan software (Matzarakis et. al., 2010). The canyon simulations were obtained by alternatively blocking the sky view of the global spectrometer, using a block of dark foam padding.

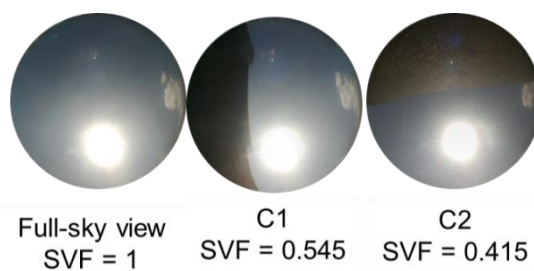


Figure 7-8 Orthographic fisheye photographs for three sky views. Full-sky view: image of the upper-hemispheric sky view with no simulated obstructions. C1: Simulated Canyon obstructing a section of the circumsolar region. C2: Simulated Canyon obstructing the anti-solar region. The “raw” sky view factor (SVF) was calculated using the RayMan software.

These experiments were conducted under nearly cloudless conditions on the 7<sup>th</sup> of July 2013 at the Pariser rooftop in the University of Manchester, UK. Each simulated obstruction was linked to a corresponding global spectral measurement under the obstructed view, and a fisheye camera image that described the horizon obstructions. Also, unobstructed measurements were taken after each obstruction with an offset of 20 seconds. Given the stability of sky conditions during the experiment, it can be said that any differences between measurements were mainly explained by the simulated obstructions. The experiment consisted of 25 repetitions for each simulated canyon, between 1100 and 1230 UTC. Since results from all repetitions were approximately equal, and for the sake of simplicity, a typical example outcome has been chosen to illustrate our results. The example corresponds to the experiment replica between 11:25:00 and 11:26:00 am.

The simulated canyons blocked different parts of the sky as shown in Figure 7-8. Canyon C1 obstructed a section of the circumsolar region; while the anti-solar region was obstructed in canyon C2. The SVFs and relative canyon spectral irradiances were then obtained for each canyon as the ratio of obstructed to full-view irradiances. Both simulated canyons allowed the

direct sunlight component to be visible; therefore, differences between these two simulated canyons were due to blockings of diffuse irradiance.

### 7.4.3 Weighted SVF ( $SVF_w$ )

In order to calculate a  $SVF_w$ , the horizon profiles were digitally overlaid onto the full-view sky-maps (Fig. 7-9). The obstructions were manually delineated using the RayMan software tool and pixel values of 0 were assigned to obstructions, while visible sky pixels were assigned values of 1. Finally, sky-maps were multiplied (element-by-element matrix multiplication) by the obstruction masks using Octave.



Figure 7-9 Example showing the overlapping of simulated canyon C1. The same process was repeated for each RGB+UV sky-map. As well as for each simulated canyon

The total sum of pixel values from the masked sky-maps was divided by the total sum of pixel values in the original sky-maps. Because of the orthographic projection returned by the lens, this quotient is equivalent to a weighed sky view factor ( $SVF_w$ ) containing information about the obstruction of pixels with different brightness values. Table 7-3 shows the calculated  $SVF_w$  for the selected wavelengths (i.e. 310, 355, 400, 460, 530, 600 nm), for both simulated canyons (C1 and C2).

**Table 7-3**  
**Weighted Sky View factors (SVF<sub>w</sub>) for six**  
**different wavelengths, under two simulated**  
**canyons (C1 and C2)**

Wavelength (nm)	C1	C2
<b>310</b>	0.621	0.624
<b>355</b>	0.623	0.636
<b>400</b>	0.627	0.656
<b>460</b>	0.641	0.730
<b>530</b>	0.647	0.751
<b>600</b>	0.656	0.776

Weighted sky view factors shown in Table 7-3 agree with the expected tendencies, regarding differences between simulated canyons and the effects of obstructions at different wavelengths. Since shorter wavelengths are more easily scattered and distributed across the sky, UV wavelengths were expected to be more affected by blocking the diffuse component of sky radiation (in Table 7-3 the calculated SVF<sub>w</sub> is smaller for shorter wavelengths). Also, since simulated canyon C1 blocked the brighter circumsolar region, canyon C1 was expected to have a smaller SVF<sub>w</sub> than C2 at all wavelengths (as shown in Table 7-3).

#### **7.4.4 Circumsolar SVF (SVF<sub>C</sub>)**

Finally, the proportion of saturated pixels blocked by a canyon obstruction must also be taken into consideration. This may be defined as the “circumsolar sky view factor” (SVF<sub>C</sub>). The SVF<sub>C</sub> for canyons C1 and C2 is 1.

#### **7.4.5 Modelling relative canyon irradiance**

Models for the relative obstructed irradiance were created by modifying Equation 7.7 (for calculating canyon irradiance), at including each weighted SVF. However, the weighted SVFs are defined for the diffuse-minus-circumsolar component only (due to the digital processing of images described on Block I). Eq. 7.7 must be modified according to Eq. 7.8.

$$E_{u,\lambda} = \left( (E_{f,\lambda}) \left( \frac{E_{s,f,\lambda}}{E_{f,\lambda}} \right) S_{bin} \right) + \left( (E_{f,\lambda}) ((D - C):G_{(\lambda)}) SVF_w \right) + \left( (E_{f,\lambda}) \left( \frac{E_{Cs,F,\lambda}}{E_{f,\lambda}} \right) SVF_c \right), \quad (\text{Eq. 7.8})$$

where  $E_{u,\lambda}$  is the urban canyon global spectral irradiance under the sky-view  $u$ , at wavelength  $\lambda$ .  $E_{f,\lambda}$  is the reference full-sky-view global spectral irradiance. The three terms on the right hand side of the equation represent the partitioning of full-sky-view global irradiance into its direct, diffuse-minus-circumsolar and circumsolar components. The direct is affected by  $S_{bin}$ . The diffuse-minus-circumsolar ( $D - C$ ) is affected by the  $SVF_w$  calculated from the processed sky-maps. Finally, the circumsolar is affected by  $SVF_c$ .

Equation 7.8 was used to model relative canyon irradiance of canyons C1 and C2. Notice that, for both canyons,  $S_{bin}$  and  $SVF_c$  were both equal to 1. Figure 7-10 shows a comparison between measured and modelled relative canyon irradiances for canyons C1 and C2:

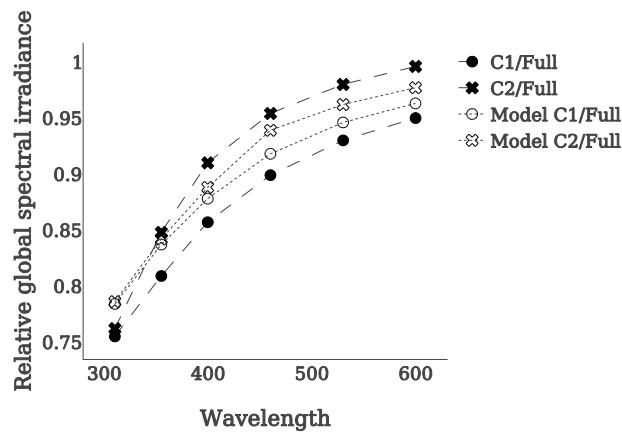


Figure 7-10 Modelled vs. Measured relative global spectral canyon irradiances, for six different wavelengths (310, 355, 400, 460, 530 and 600nm) within two simulated canyons C1 and C2. Relative irradiance values were obtained as the quotient between obstructed and full views.

Figure 7-10 shows that modelled and measured irradiance was higher for canyon C2 than it was for canyon C1. This was expected due to the blocking of the brighter circumsolar

radiation in canyon C1; in spite of the fact that Canyon C1 had a slightly larger (un-weighted) SVF factor (see Figure 7-8).

Table 7-4 shows the proportional error at each wavelength obtained from the difference between models and measurement. Maximum errors were observed at 310nm, of 0.067 (i.e. a percentage error lower than of 6.7%).

<b>Wavelength</b>	<b>C1</b>	<b>C2</b>
<b>310</b>	0.053	0.067
<b>355</b>	0.046	0.015
<b>400</b>	0.032	-0.014
<b>460</b>	0.024	-0.025
<b>530</b>	0.019	-0.024
<b>600</b>	0.015	-0.024

## **7.5 Discussions**

The first aim of the present work was to develop a cost-effective method to represent the irradiance sky-distribution in the visible ranges from RGB information, then, to extrapolate the visible (RGB) information towards three hypothetical UV irradiance sky-distributions (i.e. 310, 355, 400 nm). In the literature, the use of digital RGB cameras is generally restricted to describing luminance angular distributions (Robinson and Stone, 2004; Rossini and Krenzinger, 2007), or the distribution of specific wavelengths in the visible ranges (Román et al., 2012). Unfortunately, these methods still fail to address the sky distribution of UV radiation. Efforts to measure the distribution of sky radiance in the UV include the MUDIS spectrometer (Seckmeyer et al., 2014). However, as pointed out by (Sabburg and Long, 2004), the increasing progress made in the field of automated whole sky imagers comes with a considerable cost to users, with reported of costs of up to \$18,000 USD for UV

sensitive cameras (Bluth et al., 2007). In this work, the use of images from a commercial mobile phone camera (with a detachable mini-fisheye lens) returned acceptable approximations of the angular distributions of diffuse radiation in UV and visible wavelengths.

In order to approximate irradiance values from the camera output, a digital process was first necessary to account for non-linearity of the sensors' response and for saturation and the misrepresentation of the direct solar beam. The polynomial response correction also improved the extrapolation towards the ultraviolet. The increased contrast between bright and dark pixels outside the circumsolar region allowed for a better approximation of the inter-wavelength contrasts, i.e. the differences in pixel intensity expected across the spectrum: Larger contrasts between the channels result in sharper slopes, which result in sharper linear extrapolations. Still, results in Table 7-2 suggest that the overall "brightness" of the ultraviolet extrapolations underestimated the expected relative amounts of diffuse radiation.

Sky distributions of irradiance were finally used to validate the modelled effects of horizon obstructions on anisotropic irradiance, simulated obstructions were performed by blocking the circumsolar and anti-solar sky regions of a global spectrometer. Figure 7-10 showed that the obstructions of the diffuse radiation alone have larger effects on the ultraviolet radiation than on the visible wavelengths (blocking nearly 25% of the shorter UV global irradiances in the canyon). These differences between the UV and visible ranges occur because the diffuse component represents a larger proportion of global radiation for shorter wavelengths (Navntoft et al., 2012). In our models, one of the effects of the extrapolations is that the relative brightness of all pixels is homogenized in the UV sky-maps. The models therefore approximate the observed trends of the effects of sky obstructions with proportional errors of 0.05 and 0.06 approx. for canyons C1 and C2 respectively.

When comparing these results under simulated canyons against previous models, which assumed an isotropic diffuse (Carrasco-Hernandez et al., 2015), the present methods returns better predictions of relative canyon irradiance. Below (Fig. 7-11) is a comparison of the present methods against our previous models. Canyon C2 showed larger measured irradiances even when it had a smaller SVF (un-weighted) (see Figure 7-8). Thus, in our previous models (with isotropic diffuse irradiance) the C2 canyon was assigned lower global spectral irradiances (Figure 7-11 Left panel), due to a smaller raw SVF. Although the differences are small, the empirical data showed that the conventional SVF may fail to predict canyon irradiances even in the UV ranges and may return inversed relationships of brightness between different canyons. The correct assignation of “the brighter canyon” was achieved with the proposed inclusion of the anisotropic distribution when calculating the SVFs (results in Figure 7-11, Right panel).

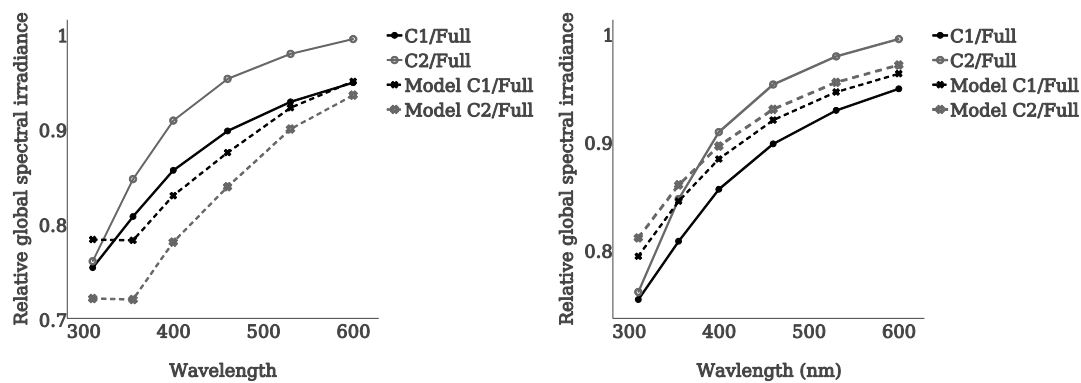


Figure 7-11. Left panel: Measured canyon relative global spectral irradiance compared to models assuming isotropic distributions of the diffuse component. Right panel: Proposed corrections by including the anisotropy of diffuse radiation obtained from RGB whole-sky images (same as Figure 7-10).



The overall proportional errors increase when assuming an isotropic diffuse irradiance (shown below in Table 7-5), with a maximum proportional error of 0.15 at 355 (C2), in contrast with the maximum error of 0.067 at 310 nm (C2), shown previously in Table 7-4

Below, Table 7-4 is presented again for ease of comparison.

<b>Wavelength</b>	<b>C1</b>	<b>C2</b>
<b>310</b>	0.039	-0.051
<b>355</b>	-0.031	-0.150
<b>400</b>	-0.031	-0.141
<b>460</b>	-0.025	0.119
<b>530</b>	-0.006	-0.081
<b>600</b>	0.001	-0.059

<b>Wavelength</b>	<b>C1</b>	<b>C2</b>
<b>310</b>	0.053	0.067
<b>355</b>	0.046	0.015
<b>400</b>	0.032	-0.014
<b>460</b>	0.024	-0.025
<b>530</b>	0.019	-0.024
<b>600</b>	0.015	-0.024

In other models found in the literature, canyon irradiance calculations are made under the assumption of diffuse isotropy (Matzarakis et al., 2010). Hess and Koepke (2008) presented an interesting approach which included modelled sky-maps of the UV radiation, as affected by specific horizon profiles. In their work, plane-projected sky radiance distribution maps were overlaid with fisheye images of a canyon's horizon profile, allowing a graphical assessment of obstructions. However, according to Navntoft et al. (2012), this model remains to be thoroughly tested.

The cost-effective method proposed here may provide useful information for more accurate representations of street-canyon spectral irradiance. For long term studies and model validations whole-sky cameras may be installed, to continuously monitor the sky under all conditions; and thus have a record of the complex dynamics of radiance distributions during

the day. Even though the scope of this work is limited to analysing the usefulness of RGB images under a clear sky, our approach may be generalized (with the appropriate modifications) to be used under all-sky conditions.

## **7.6 Conclusion**

In previous models, the assumed isotropic diffuse component could not account for the effects of blocking the brighter sections of the sky in the circumsolar region. A simple approximation to the anisotropic distribution of sky radiation, presented in this paper, allowed for the correction of such inadequacies. The approximations were based on unobstructed RGB whole-sky images, additionally extrapolated towards the ultraviolet. Each sky-map represents the sky-distribution of a specific wavelength (i.e. 310, 355, 400, 460, 530, 600 nm). To create the UV-*RGB* sky-maps, digital processing was required on the original images to include corrections for non-linear radiometric response to light sources and saturation of the digital camera. The post-processed sky-maps represent the globally-normalized distribution of the diffuse radiation, excluding a small section of the circumsolar (4% of the whole sky view) and the direct component of global irradiance. The extrapolated sky-maps in the UV wavelengths were compared against an expected corresponding globally-normalized diffuse-minus-circumsolar component (modelled using SMARTS). Average discrepancies between the UV extrapolated vs. the UV expected ratios were of the order 0.20 (or 20%). Calculated canyon spectral irradiances for specific wavelengths, combined with the sky-maps, improved calculations respective to the previous models; this by assigning a lower canyon irradiance to the obstructed view that blocked the circumsolar region (despite having a slightly larger SVF) in comparison to a different view where the anti-solar region was blocked. Whereas in previous models (not including the anisotropic sky-maps) the brighter canyon was always the one with a larger SVF, regardless its orientation. Overall discrepancies between canyon measurements and calculations with the present method were below 0.067 (or 6.7%). These

sky-maps may represent a cost-effective solution for including the anisotropic distribution of diffuse radiation in models of urban canyon spectral irradiances.

## References

- Bluth, G. J. S., Shannon, J. M., Watson, I. M., Prata, A. J., and Realmuto, V. J. (2007). Development of an ultra-violet digital camera for volcanic SO<sub>2</sub> imaging. *Journal of Volcanology and Geothermal Research*, 161(1), 47-56.
- Carrasco-Hernandez, R., Smedley, A. R., & Webb, A. R. (2015). Fast calculations of the spectral diffuse-to-global ratios for approximating spectral irradiance at the street canyon level. *Theoretical and Applied Climatology*, 1-13.
- Carrasco-Hernandez, R., Smedley, A. R., and Webb, A. R. (2015b). Using urban canyon geometries obtained from Google Street View for atmospheric studies: Potential applications in the calculation of street level total-shortwave irradiances. *Energy and Buildings*, 86, 340-348.
- Darula, S., and Kittler, R. (2002). CIE general sky standard defining luminance distributions. *Proceedings eSim*, 11-13.
- Grant, R. H., Heisler, G. M., and Gao, W. (1997). Ultraviolet sky radiance distributions of translucent overcast skies. *Theoretical and Applied climatology*, 58(3-4), 129-139.
- Grossberg, M. D., and Nayar, S. K. (2003). What is the space of camera response functions?. In *Computer Vision and Pattern Recognition, 2003. Proceedings. 2003 IEEE Computer Society Conference on (Vol. 2, pp. II-602)*. IEEE.
- Gueymard, C. A. (2005). SMARTS Code, Version 2.9. 5 User's Manual. Solar Consulting Services. Available from [http://www.solarconsultingservices.com/SMARTS295\\_manual.pdf](http://www.solarconsultingservices.com/SMARTS295_manual.pdf).
- Hess, M., and Koepke, P. (2008). Modelling UV irradiances on arbitrarily oriented surfaces: effects of sky obstructions. *Atmospheric Chemistry and Physics*, 8(13), 3583-3591.
- Igawa N, Koga Y, Matsuzawa T, Nakamura H (2004) Models of sky radiance distribution and sky luminance distribution. *Sol Energy* 77:137–157.
- Jiang, J., Liu, D., Gu, J., and Susstrunk, S. (2013, January). What is the space of spectral sensitivity functions for digital color cameras?. In *Applications of Computer Vision (WACV), 2013 IEEE Workshop on (pp. 168-179)*. IEEE.
- Kholopov, G. K. (1975). Calculation of the effective wavelength of a measuring system. *Journal of Applied Spectroscopy*, 23(2), 1146-1147.
- Matzarakis A, Rutz F, Mayer H (2010) Modelling radiation fluxes in simple and complex environments: basics of the RayMan model. *Int J Biometeorol* 54:131. doi: 10.1007/s00484-009-0261-0
- Myers, D. R., and Gueymard, C. A. (2004, November). Description and availability of the SMARTS spectral model for photovoltaic applications. In *Optical Science and Technology, the SPIE 49th Annual Meeting (pp. 56-67)*. International Society for Optics and Photonics.
- Navntoft, L. C., Fernandez-Ibañez, P., and Garreta, F. (2012). UV solar radiation on a tilted and horizontal plane: Analysis and comparison of 4years of measurements. *Solar Energy*, 86(1), 307-318.
- Rezaei-Ghaleh A (2003) Ultraviolet Spectral Radiance Distribution under Cloudy Skies (Doctoral dissertation). University of Manchester, UK.
- Robinson, D., and Stone, A. (2004). Solar radiation modelling in the urban context. *Solar Energy*, 77(3), 295-309.

- Román, R., Antón, M., Cazorla Cabrera, A., Miguel, A. D., Olmo Reyes, F. J., Bilbao, J., and Alados-Arboledas, L. (2012). Calibration of an all-sky camera for obtaining sky radiance at three wavelengths..
- Rosen, M. A., Hooper, F. C., and Brunger, A. P. (1989). The characterization and modelling of the diffuse radiance distribution under partly cloudy skies. *Solar Energy*, 43(5), 281-290.
- Rossini, E. G., and Krenzinger, A. (2007). Maps of sky relative radiance and luminance distributions acquired with a monochromatic CCD camera. *Solar Energy*, 81(11), 1323-1332.
- Sabburg, J. M., and Long, C. N. (2004). Improved sky imaging for studies of enhanced UV irradiance. *Atmospheric Chemistry and Physics*, 4(11/12), 2543-2552.
- Seckmeyer, G., Schrempf, M., Riechelmann, S., and Stührmann, A. (2014). 2 UV research by simultaneous spectral radiance measurements. *Thematic Network for Ultraviolet Measurements*, 4.

## **Chapter 8**

### **General Discussion and Main conclusion**

In this closing chapter a general discussion will be provided that summarizes findings, provides an overall view of the main highlights and defines potential future developments of this research.

## 8.1 Introduction

The measurement and modelling of solar radiation reaching urban canyons is of relevance for urban atmospheric studies, as well as for studies in human photobiology (Heisler and Grant, 2000). The creation of street-level models of solar irradiance will allow better approximations to, for example, the biologically active radiation reaching the human skin or to the potential for photovoltaic generation at street level. However, most current indices of solar exposure (e.g. the UV index) are obtained from observatory full-sky-view measurements, reconstructed from satellite observations (Fioletov et al., 2010; Feister et al., 2011; Damiani et al., 2014; Sharma, 2014) or calculated with one-dimensional radiation models; thus failing to consider the horizon obstructions exerted by buildings at the street level.

The aim of the present work was to provide a method for estimating model urban canyon exposures to solar radiation using readily available data and with minimum computational requirements. The most rigorous method for modelling solar radiation within urban canyons would be to use 3-D Monte-Carlo algorithms (Mayer et al., 2010), which can track each individual photon within a complex environment, but such methods can be computationally demanding. Less demanding solutions are provided by one-dimensional radiative transfer packages such as LibRadTran (Mayer and Kylling, 2005) or SMARTS (Myers and Gueymard, 2014), but these are not specifically designed for including horizon obstructions. Other software packages, such as RayMan (Matzarakis et al., 2010) designed for the calculation of solar irradiance within urban canyons, can only calculate total-shortwave global irradiance but not spectral irradiance. Within the reviewed literature, only Koepke (Hess and Koepke, 2008) proposed a one-dimensional spectral model for the calculation of ground-level irradiance with horizon obstructions included. Unfortunately, personal communication with Koepke indicated that the group developing these tools in Germany is

no longer operational. Hence, state-of-the-art tools in the field of solar radiation modelling are not routinely available for calculations at the street level.

The first complication for modelling street-level solar irradiances is the description of urban geometries. To tackle this problem, this thesis proposed a method that uses the free access image database Google Street View. The Google Street View database represents an enormous source of information readily available for its analysis and for general use in the field of urban atmospheric studies. In practice, the Hugin software (d'Angelo, 2007; German et al., 2007) was an exceptionally useful tool for the geometric positioning and merging of independent rectilinear photographs, which may be obtained from Google Street View on a standard PC computer. Rectilinear images were projected onto a polar fisheye panorama of the hemispheric sky-view.

The combination of tools described here will allow the calculations of SVFs and the visibility of the solar disc, hence, solar irradiance at any geographical location with Google Street View coverage. The Street View coverage includes cities of North America, Brazil, Europe and Australia. Google Street View also possesses a world-wide fleet of vehicles equipped with standard cameras at a standard height. These standard features make the database a source of easily comparable information. It must also be acknowledged that the current coverage of the database surpasses that of 3D city models, in addition to which, high resolution GIS data is not always freely available. The Google Street View database therefore allows researchers to conduct comparative analyses at many geographical locations.

Chapter 4 (published as: Carrasco-Hernandez et al., 2015b) described how the SVF can be defined for any location with Google Street View images. This provides vital input to any model that calculates the radiation situation at street level. This first step could equally well be used to provide input to Monte-Carlo or other radiation models for multi-reflection processes; although these are not the focus of the current work.

Another advantage of using Google Street View images is that they allow the identification of materials within the urban panorama (i.e. buildings, trees, windows). While these are easily identified by the human observer, categorising the surface materials automatically is a more complex task. Material identification is relevant to the amounts of solar radiation received at the street level, due to the reflected radiation that each material contributes to the street environment. The intensity and spectral composition of reflections within canyons may vary a lot from one canyon to the other, creating complex geographical patterns. The simple modelling techniques of this thesis did not consider such variables and, for simplicity, assumed canyon surfaces as non-reflecting. Nevertheless, the use of Google Street View images with an automated system for identifying surface properties has been explored in Chapter 5, and success in basic categorisation illustrated. Thus, techniques now exist first to represent the geometry and then to include the nature of reflecting materials in urban canyons; although the latter technique remains to be further developed. Future research is needed to include reflections in the irradiance calculations. For the present work, non-reflective surfaces remained an assumption of all models.

## **8.2 Total-shortwave irradiance in urban canyons**

Having determined the canyon's SVF, the next step was to assess the impact of the horizon obstructions on solar radiation reaching the street. Total-shortwave irradiance is a useful parameter for modelling urban microclimates and energy budgets (Gros et al., 2011), as well as for modelling human comfort in the outdoors environment (Huang et al., 2014). The RayMan software (Matzarakis et al., 2010) was used to model total-shortwave irradiance in urban canyons. RayMan also allows assessment of the sky view factor (SVF) and the visibility of the solar disc at any specific urban canyon, by using a polar fisheye projection of the upper-hemispheric view of the sky, derived from the Google Street View images. Verified fisheye projections of building horizon obstructions were used to calculate: the SVF,



the visibility of the solar disc and the total-shortwave irradiance, at specific moments of the day. To validate the proposed methods, urban canyon geometries and solar irradiance were measured and modelled within the campus of the University of Manchester (Dover street canyon). The canyon's solar irradiance was measured with a CM5 Kipp & Zonen pyranometer and compared to a similar pyranometer at the (unobstructed) Whitworth Observatory, University of Manchester. Modelled results of canyon irradiance represented satisfactory approximations to the empirical data. Through the combined use of Hugin and RayMan software, it was demonstrated that it is possible to reconstruct urban geometries and model total-shortwave solar irradiance from Google Street View images, as detailed in Chapter 4 (Carrasco-Hernandez et al., 2015b)

A potential limitation of the proposed methods is their dependence on local observatory measurements. The combined use of reconstructed canyon geometries and observatory measurements provided the advantage of modelling real-sky conditions for the specific canyon (i.e. including the effects of clouds on the overall solar radiation). However, any local observatory measurement will only be valid for representing local radiation within a limited geographical extent. Street canyons too far from the reference measurement will tend to diverge from those at close proximity, at least for high time resolution and variable cloud conditions. The extent to which a wider area can be represented by a local ground measurement may be a complex function of topography, cloud cover and even land use. For example, in a study of ultraviolet radiation in Mexico City, UV-B levels were reported to be 20% lower at the city centre than those measured at a suburban station (Acosta and Evans, 2000). The authors found that different pollution levels were the main reason for this pattern, Also, the complex topography of Mexico City may have accounted for the observed differences. For variable landscapes, observatory networks may be needed to create real-time realistic models. Nevertheless, if canyon irradiances cannot be represented by a local ground

measurement, satellite measurements can still be used to reconstruct the reference ground level unobstructed irradiances for all sky conditions (Sun and Liu, 2013; Sun et al., 2014), albeit at the resolution of a pixel size.

Although the examples given throughout this thesis describe radiation received at individual urban canyons, the same algorithms can be automatically repeated for other neighbouring sites and extended to describe the variation of sky views along streets and avenues. To give an example of this possibility, urban geometries were obtained for 15 sequential sites from Google Street View, covering a transect of 118.24 m in northwest direction along Oxford Road, Manchester, UK. Figure 8-1 shows the location and size of the transect on Oxford Road, Manchester UK.

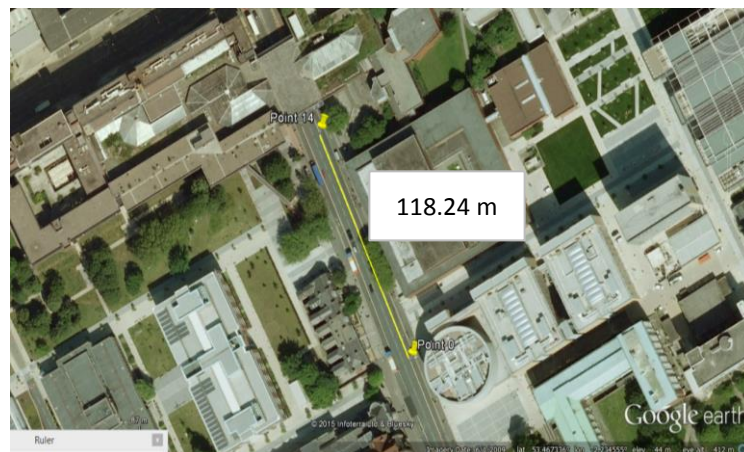









Figure 8-1 Sampling transect along Oxford Road, Manchester, UK. The transect is comprised of 15 sequential Google Street View locations covering 118.24 m along Oxford Road. Panoramas of the upper-hemispheric sky-view were obtained for each location.

For each of the 15 sites within the transect, an upper-hemispheric fisheye panorama was obtained using the methods described in Chapter 4. For each site, rectilinear images were obtained covering the full upper-hemispheric view at ground level. These images were then processed using Hugin to create equidistant fisheye projections. Then, the non-parametric algorithm for pixel classification (Chapter 5) was used to distinguish between sky and

building pixels. Additionally, the SVF with the cosine law (given the equidistant projection of images) and daily canyon irradiance (as total daily sum) was obtained for each site using RayMan. The total daily sum of global shortwave irradiance (in  $\text{Wm}^{-2}$ ) was calculated using RayMan for a mid-summer day (Julian day 182 in Manchester, UK).









To automatically repeat the same processing algorithms for every site, a macro script was written with the AutoHotkey language. This routine requires further optimization, since the full process for these 15 sites took approximately 1 hour. Results are shown in Table 8-1, which has been split in two parts (Table 8-1 Part1 and Part 2) for a better display.

**Table 8-1 Part 1. Sites 1 to 7 of 15. SVF and canyon irradiance models. The 15 sites are sequential locations of Google Street View along a transect of 118.24 m in northwest direction along Oxford Road, Manchester, UK.**

Site Number ID	SVF	$E\text{-sum}$ ( $\text{Wm}^{-2}$ )	Fisheye
1	0.832	7235.2	
2	0.845	7774.6	
3	0.871	7979.1	
4	0.869	8245.5	
5	0.858	8043.8	
6	0.74	6990.2	
7	0.719	6544.2	

**Columns show for each canyon: the Sky View Factor (SVF); the accumulated total-shortwave-global-irradiance ( $E\text{-sum}$ ) for Julian day 182; and the projected and classified fisheye image.**

**Table 8-1 Part 2. Sites 8 to 15 of 15. SVF and canyon irradiance models. The 15 sites are sequential locations of Google Street View along a transect of 118.24 m in northwest direction along Oxford Road, Manchester, UK.**

<b>Site Number ID</b>	<b><i>SVF</i></b>	<b><i>E-sum</i> (Wm<sup>-2</sup>)</b>	<b>Fisheye</b>
8	0.767	7059.7	
9	0.708	5581.2	
10	0.75	6611.1	
11	0.711	4920.1	
12	0.751	5469.4	
13	0.845	7882.3	
14	0.849	7639.3	
15	0.86	8131.8	

**Columns show for each canyon: the Sky View Factor (*SVF*); the accumulated total-shortwave-global-irradiance (*E-sum*) for Julian day 182; and the projected and classified fisheye image.**

To better appreciate these results, Figure 8-2 graphically shows the data in Table 8-1. Note how the variations of SVF and accumulated radiation (total daily sum) follow similar tendencies. However, at some sites, irradiance seems to decrease more than the SVF (e.g. sites 9, 11, 12, Fig. 8-2). This can be explained by the effect of obstructing the direct beam for larger periods of time in certain urban canyons. In this case, the orientation and azimuthal position of obstructions plays an important role. For example, at sites 11 and 12 (which receive lower amounts of daily irradiance), the obstructions are positioned towards the south (see Table 8-1. Part 2), thus, blocking the solar path for longer periods of time.

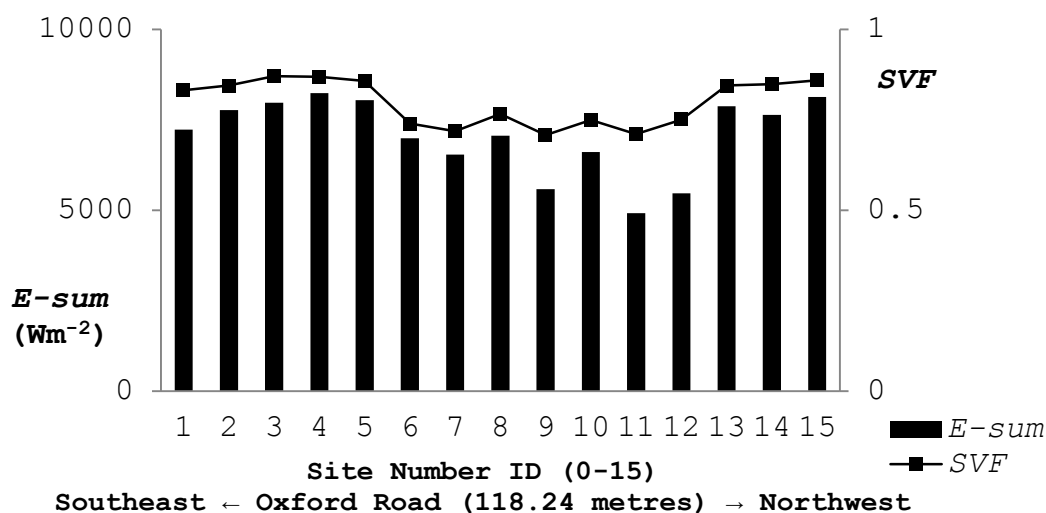


Figure 8-2 Variations of SVF and accumulated irradiance ( $E\text{-sum}$ ), for 15 (Site Number ID 0-15) sites, along a transect of 118.24 metres on Oxford Road, Manchester UK.

These results illustrate how it is possible to model the variation of urban geometries and canyon energy budgets at a fine level of detail, not easily achieved by digital elevation models. Additionally, these methods rely upon free-access data and can be extended to any city with Google Street View coverage from a standard PC computer.

The associated sources of uncertainty of these irradiance calculations (and of their potential applications) still need to be addressed. For example, the position of the Google

Street View perspectives (at approximately 2.5 metres from the ground) may not represent the sky-view of relevant surfaces such as the ground. In this regard, Svensson (2004) reported how the correlation between local air temperature and SVF is also affected by the height of the fisheye photograph used to describe the SVF. Fisheye photographs taken at different heights in the same point location will return different perspectives of the same urban canyon and therefore different SVFs. According to Svensson, fisheye photographs taken near the ground describe a SVF that is better correlated to night-time air temperature, while fisheye photographs taken 2 metres above the ground were less correlated to air temperature. This was explained by the fact that the main heat source for air temperature is the ground. In the present work, Google Street View images have been used to describe SVF, these images were taken at 2.5 metres above the ground level. Although the present methods may become useful for modelling urban micrometeorological conditions, it will be important to address the potential uncertainties introduced by the local position of the photographs.

The next step was to extend the modelling towards spectral calculations of global irradiance in urban canyons. Unfortunately, the RayMan model does not allow the assessment of spectral irradiance; therefore, the use of spectral radiative transfer software was required.

### **8.3 Spectral irradiance in urban canyons**

The SMARTS algorithm for radiative transfer modelling (Myers and Gueymard, 2004), was explored during the course of this work, to allow calculations of spectral irradiance. Nonetheless, the RayMan software was still used to include the effects of horizon obstructions, by evaluating the visibility of the direct beam and calculating the SVF. The combined use of these tools will permit a better assessment of spectral radiation, and its behaviour within the urban canyon.

The assessment of single wavelengths or specific wavebands can be important for a range of applications, especially those related to human health. Given that the human skin reacts to radiation as a function of wavelength, weighted irradiance values at each wavelength become crucial when studying such interactions. The term “biologically active radiation” refers to spectral radiation intensities weighted by the spectral response for specific biological effects (i.e. the specific action spectrum). Particularly, the erythema action spectrum is extensively used in assessing the effects of UV radiation on the human skin. Although the erythema action spectrum was created on the basis of the sunburn effect, it is often used as a substitute for quantifying other effects of UV (in particular, it is used as a proxy for skin cancer, and also as a rough guide for vitamin D synthesis) (Webb et al., 2011). The erythema action spectrum forms the basis of the UV index (CIE, 2003) which is used globally to inform the public about ultraviolet exposure levels.

These action spectra can also be understood as weighting factors which can be multiplied by a measured irradiance spectrum. Although the scope of this study did not include the analysis of action spectra or the biologically active radiation, the models of spectral irradiance proposed here can be used for these kinds of study. Radiant exposures and biologically active radiation can be derived from integrated irradiance measurements over time and weighted by specific action spectra (Moan et al., 2008). The methods proposed here will allow evaluating the effects of horizon obstructions on the biologically active radiation.

In the specific case of UV radiation within street canyons, somewhat different behaviour to longer (visible) wavelengths might be expected because of strong scattering. For example, if the sun is blocked by a building, we can expect a great reduction in total-shortwave measurements which are dominated by visible and infra-red radiation; which, in turn, are mainly retained in the direct beam radiation. Ultraviolet radiation will be less affected by such obstructions because less UV is in the direct beam, and the diffuse component



represents a comparatively greater proportion. On the other hand, blocking significant parts of the sky view—not the solar disc—may have a greater effect on the ultraviolet than on the rest of the spectrum. This occurs because UV irradiance has a large diffuse component and a smaller component in the direct beam, in comparison to the rest of the solar spectrum.

The first approach to calculating spectral irradiance in Chapter 6 (Carrasco-Hernandez et al., 2015) followed the same general guidelines of the RayMan model to calculate total-shortwave irradiance (i.e. to use the SVF to determine the losses in diffuse radiation and to calculate whether the solar disc is blocked by a building). The models of canyon spectral irradiance were created on the basis of full-sky-view spectral measurements taken at the Pariser Building measuring site of the Centre for Atmospheric Sciences, University of Manchester. Then, it was necessary to partition global irradiance into its direct and diffuse components for their analysis within the canyon geometry. Such partitioning was achieved through the calculation of the diffuse-to-global irradiance ratio (DGR) and it was a function of wavelength, Rayleigh scattering, aerosol, and ozone in the atmosphere. Two equations were presented to calculate the DGR under standard clear sky atmospheric conditions. The first equation was theoretical, using simplifications to the SMARTS algorithms, and the second was a semi-empirical approximation to SMARTS DGR output results. The full-sky diffuse and direct components were then modified by the visibility of the solar disc and the SVF calculated with the RayMan tools and the projected canyon geometry. The models were validated with simulated canyons to assess different canyon orientations without having to move to different locations in the city (Chapter 6).

The models of spectral irradiance in simulated canyons returned good approximations to empirical data, but an error due to one of the assumptions of the model became apparent. An assumption, “inherited” from the RayMan model, considered the diffuse irradiance to be isotropic (i.e. having the same intensity regardless its position in the upper-hemispheric

view). Under cloudless sky conditions this assumption is not true. Because of the higher relative brightness of diffuse irradiance in the circumsolar region, specific urban geometries might obstruct a brighter or less bright part of the sky depending on the canyon's orientation. Therefore, under a clear sky, the diffuse component is not only affected by the SVF but also by the canyon's orientation. To neglect the anisotropy of the diffuse component may lead to errors in the calculations when comparing canyons with different orientations. One of the simulated canyons in the experiments blocked a section of the circumsolar region, without blocking the solar disc, whereas a different simulated canyon blocked the anti-solar region. Under clear sky conditions, measured data showed that the canyon with the anti-solar region blocked had higher relative irradiance values for all wavelengths than the canyon with the circumsolar region blocked, even though its SVF was slightly smaller. This occurred because the model would only consider the SVF for calculating diffuse irradiance, disregarding the anisotropic brightness of the blocked radiation. The errors due to the assumption of isotropic diffuse irradiance were, however, small. In general it can be said that the models of canyon spectral irradiances returned good approximations to the measured data. The proposed models are therefore suitable for approximating urban canyon spectral irradiances, if a fisheye projection of the canyon obstruction profile is available (or can be reconstructed).

#### **8.4 Corrections for global measurements under cloudy skies**

Although the models proposed here were designed for cloudless skies, simple adjustments to the DGR ratios may suffice for estimating canyon irradiances under cloudy conditions. The use of real-time measurements provides an advantage that standard one-dimensional models cannot provide. That is, the possibility of including the dynamic effects of clouds in global irradiance. Although the models presented here were created for cloudless-sky conditions, they use a reference real-time measurement of global spectral irradiance under a full-sky

view and calculate the canyon irradiance relative to this. In real-life conditions, the strongest effect of clouds is the obstruction of the direct solar beam; which in turn reduces global irradiance to only the diffuse component. Algorithms can be created to automatically identify moments of the day when a cloud blocks the solar beam in a series of measurements. At those specific moments we would know that full-sky diffuse irradiance is approximately equal to the measured full-sky global irradiance, and therefore the DGR equals 1. Within the canyon,  $S_{bin}$  equals zero regardless of buildings orientation and geometry. Equation 6.1 (from Chapter 6, but shown below for comparison) could take a different form (Eq. 8.1) to approximate irradiance within a canyon when the direct beam is blocked by a cloud.

$$E_{C,\lambda} = [E_{b,F,\lambda} \cdot S_{bin}] + [E_{d,F,\lambda} \cdot SVF], \quad (\text{Eq.6.1})$$

where  $E_{C,\lambda}$  is the approximated global spectral irradiance within a specific urban canyon  $C$ , at wavelength  $\lambda$ ;  $E_{s,f,\lambda}$  is the direct spectral irradiance measured under a full sky-view  $F$ , at wavelength  $\lambda$ ;  $S_{bin}$  is a binary digit (1 or 0) representing the visibility of the direct solar beam;  $D_{f,\lambda}$  is the measured diffuse irradiance under a full sky-view ( $F$ ), at wavelength  $\lambda$ ;  $SVF$  is sky view factor.

$$E_{C,\lambda} = [E_{F,\lambda} \cdot SVF], \quad (\text{Eq.8.1})$$

where  $E_{F,\lambda}$  is the global spectral irradiance when the direct beam is blocked by a cloud, measured under  $F$ .

Unlike Eq.6.1, in Eq. 8.1 global irradiance is not partitioned into its direct and diffuse components because, when the direct beam is blocked by a cloud, the unobstructed global irradiance is equal to the diffuse. In such a case, according to Eq. 8.1, canyon irradiance simply equals the measured global multiplied by the canyon's SVF.

In order to automatically identify clouds on records of global irradiance, it may be possible to apply low-pass and high-pass data filters. Another possibility is to compare actual global measurements against expected cloudless-sky models. Ultimately, it is conceivable to set rules for automatically switching between Equations 6.1 and 8.1 for calculating canyon irradiance, whenever a cloud blocking of the direct beam is identified in the data. The associated uncertainties to such approximations would include momentarily enhancements of global irradiance by multi-reflection processes in clouds.

### **8.5 Including the anisotropy of the diffuse component**

Whole-sky digital cameras are a simple way of describing real-time changes in the angular distribution of sky radiation. Historically, the radiation group at University of Manchester has had digital RGB sky cameras installed as part of their routine monitoring devices; these cameras were programmed to automatically return minute-by-minute all-sky images. The present thesis provided a method for analysing this kind of information, for its use in the reconstruction of street-level irradiance.

In Chapter 7 a solution for including the anisotropy of the diffuse component into canyon irradiance calculations was proposed by using a whole-sky digital camera. Firstly, whole-sky digital photographs were taken under an unobstructed view, using a mobile phone camera equipped with a magnetic mini-fisheye lens. RGB digital images were processed to better represent irradiance values for the three wavebands (Red, Green, Blue). Digital processing included a correction for the non-linear radiometric response of digital cameras and removal of saturated pixels of the direct sun light. Finally the pixel RGB signature was extrapolated to create sky-maps of the relative angular distribution in three UV wavelengths. The final outcome of this process was a set of six sky-maps representing the instantaneous distribution of diffuse irradiance at specific visible and UV wavelengths. Each sky-map was then masked with the projected canyon obstructions in order to calculate weighted sky view factors

( $SVF_w$ ), as the total sum of the “visible” pixel values.  $SVF_w$  therefore included information on the obstruction of the anisotropic diffuse component.  $SVF_w$  were then included into models of relative canyon spectral irradiance as a fraction of a full-sky global spectral irradiance measurement (similar to those in Chapter 6).

The calculations of relative canyon irradiances with  $SVF_w$  were better than those of models that assumed an isotropic distribution of the diffuse component (Chapter 6). Both approaches returned similarly satisfactory approximations (with 10 to 20% error in the calculated relative canyon irradiance). However, a rather qualitative improvement was achieved when including the anisotropy of the diffuse component. That is, when including anisotropy, the “brighter” irradiances were correctly assigned to the canyon where the circumsolar was completely visible (i.e. simulated canyon C2), in spite of having a  $SVF$  slightly smaller than that of a canyon that blocked part of the circumsolar (canyon C1).

The methods proposed here for the description of diffuse irradiance distributions can be further improved in future work. For example, laboratory analyses may be performed for characterising the optical properties of fisheye lenses (e.g. internal light diffraction). The main problem of commercial cameras is still their low dynamic range that does not allow a correct representation of the direct solar beam. The solution proposed here (i.e. removing saturated pixels) returned acceptable approximations but it required adding complexity to the modelling process (i.e. it required the calculation of the circumsolar irradiance with SMARTS and the assumption that the latter was represented by saturated pixels in the images). A solution that may reduce model complexity is a technique called “Real-Time High Dynamic Range Texture Mapping” (Cohen et al., 2001). This technique consists on digitally merging a sequential set of low dynamic range sky-images with different exposition times, allowing an approximation of any high dynamic range scene.

Finally, the experiments conducted with simulated obstructions illustrate the usefulness of the proposed methods to calculate spectral irradiances under an obstructed view. They show the relevance of the orientation of obstructions as affecting both the direct and the anisotropic diffuse irradiance. Although further large scale validations would be beneficial, the experiments allowed the identification of error sources in the models. Large scale validations of these methods would require street canyon measurements synchronized with rooftop measurements; as for those obtained for total-shortwave irradiance in chapter 4. In the future, the proposed methods for the reconstruction of urban geometries, combined with standard full sky-view measurements, could be applied to calculate canyon spectral irradiances in real-time.

### **Main Conclusion**

The methods proposed here allow the modelling of street-level total-shortwave and spectral global irradiance, requiring only Google Street View, a standard (free horizon) measurement and minimal computational facilities. The main advantage of the methods is the vast geographic extent of the Google Street View database, which virtually covers the entire territories of North America and Europe and includes some important cities of South America, South Africa and Australia. If a local measurement is not available then satellite data might also be used as the unobstructed solar input, at least in cloud-free conditions. Calculations of solar irradiance in urban canyons have been validated against measured data and returned acceptable approximations (i.e. with proportional errors generally below 0.1 or 0.2). For realistic approximations of all-sky conditions a similar system can be used but is much improved by the addition of RGB sky camera data that identifies the diffuse anisotropy and the location of clouds and further anisotropy that they may invoke.

Measuring the radiation directly for every urban situation would be impossible, as would full Monte-Carlo modelling at high temporal and spatial resolution. The general outcome of

this thesis is a computationally simple approximation requiring easily available inputs, which in turn, can be developed with minimum equipment and computer power.

The primary models described here may be further developed to create more realistic approximations of the human exposure to solar radiation. Firstly, the modelled spectral irradiances can be weighted through biological action spectra such as the standard CIE erythema action spectrum (CIE, 2003). Another improvement that can be made is the projection of canyon geometries and spectral irradiances onto a spherical surface or a set of vertical plane surfaces, instead of the standard flat horizontal surface used in this work. This adjustment would also be necessary for other applications, e.g. that of daylight into building where the radiation falling on a vertical window is that which will enter the building. Additionally, as was mentioned in chapter 6, the colour information in the Google Street View images provides another unique advantage which may be used to reconstruct reflection patterns within urban canyons. This would allow researchers to identify hot spots where window walls may significantly increase irradiance levels, or places where vegetation may filter incoming radiation.

The methods developed within this thesis have a range of potential applications in several fields, such as the creation of models of photovoltaic generation, human exposure or microclimate models within urban canyons. All these disciplines need a way to convert the standard radiation measure (radiation on a flat, horizontal, unobstructed plane) into the more common and realistic state found in urban areas.

## **References**

- Acosta, L. R., and Evans, W. F. J. (2000). Design of the Mexico City UV monitoring network: UV-B measurements at ground level in the urban environment. *Journal of Geophysical Research: Atmospheres* (1984–2012), 105(D4), 5017-5026.
- Carrasco-Hernandez, R., Smedley, A. R., and Webb, A. R. (2015). Fast calculations of the spectral diffuse-to-global ratios for approximating spectral irradiance at the street canyon level. *Theoretical and Applied Climatology*, 1-13.

- Carrasco-Hernandez, R., Smedley, A. R., and Webb, A. R. (2015b). Using urban canyon geometries obtained from Google Street View for atmospheric studies: Potential applications in the calculation of street level total-shortwave irradiances. *Energy and Buildings*, 86, 340-348.
- CIE. (2003). International Standard Global Solar UV Index. CIE Standard S013/E:2003. CIE, Vienna.
- Cohen, J., Tchou, C., Hawkins, T., and Debevec, P. (2001). Real-Time high dynamic range texture mapping (pp. 313-320). Springer Vienna.
- d'Angelo, P. (2007). Radiometric alignment and vignetting calibration. *Proc. Camera Calibration Methods for Computer Vision Systems*.
- Damiani, A., Cordero, R. R., Cabrera, S., Laurenza, M., and Rafanelli, C. (2014). Cloud cover and UV index estimates in Chile from satellite-derived and ground-based data. *Atmospheric Research*, 138, 139-151.
- Feister, U., Laschewski, G., and Grewe, R. D. (2011). UV index forecasts and measurements of health-effective radiation. *Journal of Photochemistry and Photobiology B: Biology*, 102(1), 55-68.
- Fioletov, V. E., Kerr, J. B., and Fergusson, A. (2010). The UV index: definition, distribution and factors affecting it. *Canadian Journal of Public Health*, 101(4), I5-I9.
- German, D. M., d'Angelo, P., Gross, M., and Postle, B. (2007, June). New methods to project panoramas for practical and aesthetic purposes. In *Proceedings of the 3rd Eurographics Conference on Computational Aesthetics in Graphics, Visualization and Imaging* (pp. 15-22). Eurographics Association.
- Gros, A., Bozonnet, E., and Inard, C. (2011). Modelling the radiative exchanges in urban areas: A review. *Advances in Building Energy Research*, 5(1), 163-206.
- Heisler, G. M., and Grant, R. H. (2000). Ultraviolet radiation in urban ecosystems with consideration of effects on human health. *Urban Ecosystems*, 4(3), 193-229.
- Hess, M., and Koepke, P. (2008). Modelling UV irradiances on arbitrarily oriented surfaces: effects of sky obstructions. *Atmospheric Chemistry and Physics*, 8(13), 3583-3591.
- Huang, J., Cedeño-Laurent, J. G., and Spengler, J. D. (2014). CityComfort+: A simulation-based method for predicting mean radiant temperature in dense urban areas. *Building and Environment*, 80, 84-95.
- Matzarakis, A., Rutz, F., and Mayer, H. (2010). Modelling radiation fluxes in simple and complex environments: basics of the RayMan model. *International Journal of Biometeorology*, 54(2), 131-139.
- Mayer, B., Hoch, S. W., and Whiteman, C. D. (2010). Validating the MYSTIC three-dimensional radiative transfer model with observations from the complex topography of Arizona's Meteor Crater. *Atmospheric Chemistry and Physics*, 10(18), 8685-8696.
- Mayer, B. A., and Kylling, A. (2005). Technical note: The LibRadTran software package for radiative transfer calculations-description and examples of use. *Atmospheric Chemistry and Physics*, 5(7), 1855-1877.
- Moan, J., Porojnicu, A. C., Dahlback, A., and Setlow, R. B. (2008). Addressing the health benefits and risks, involving vitamin D or skin cancer, of increased sun exposure. *Proceedings of the National Academy of Sciences*, 105(2), 668-673.
- Myers, D. R., and Gueymard, C. A. (2004, November). Description and availability of the SMARTS spectral model for photovoltaic applications. In *Optical Science and Technology, the SPIE 49th Annual Meeting* (pp. 56-67). International Society for Optics and Photonics.
- Sharma, N. P. (2014). Satellite Estimation and Ground Based Measurements of Solar UV Index in Kathmandu. *Journal of the Institute of Engineering*, 9(1), 18-26.



- Sun, Z., and Liu, A. (2013). Fast scheme for estimation of instantaneous direct solar irradiance at the Earth's surface. *Solar Energy*, 98, 125-137.
- Sun, Z., Zeng, X., Liu, J., Liang, H., and Li, J. (2014). Parameterization of instantaneous global horizontal irradiance: clear-sky component. *Quarterly Journal of the Royal Meteorological Society*, 140(678), 267-280.
- Svensson, M. K. (2004). Sky view factor analysis—implications for urban air temperature differences. *Meteorological applications*, 11(03), 201-211.
- Turner, J., and Parisi, A. V. (2009). Measuring the influence of UV reflection from vertical metal surfaces on humans. *Photochemical and Photobiological Sciences*, 8(1), 62-69.
- Webb, A. R. (2006). Who, what, where and when—influences on cutaneous vitamin D synthesis. *Progress in biophysics and molecular biology*, 92(1), 17-25.
- Webb, A. R., and Engelsen, O. (2006). Calculated ultraviolet exposure levels for a healthy vitamin D status. *Photochemistry and Photobiology*, 82(6), 1697-1703.
- Webb, A. R., Slaper, H., Koepke, P., and Schmalwieser, A. W. (2011). Know your standard: clarifying the CIE erythema action spectrum. *Photochemistry and photobiology*, 87(2), 483-486.
- Wolpowitz, D., and Gilchrist, B. A. (2006). The vitamin D questions: how much do you need and how should you get it?. *Journal of the American Academy of Dermatology*, 54(2), 301-317.

**Appendix I**  
**Published Version of Chapter 4**

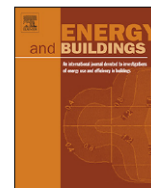
The following pages correspond to the published version of Chapter 4 as it appears in the

*Energy and Buildings Journal*



Contents lists available at ScienceDirect

## Energy and Buildings

journal homepage: [www.elsevier.com/locate/enbuild](http://www.elsevier.com/locate/enbuild)

# Using urban canyon geometries obtained from Google Street View for atmospheric studies: Potential applications in the calculation of street level total shortwave irradiances

Roberto Carrasco-Hernandez\*, Andrew R.D. Smedley, Ann R. Webb

Centre for Atmospheric Sciences, School of Earth, Atmospheric and Environmental Sciences, University of Manchester, Simon Building, Oxford Road, Manchester M13 9PL, UK

## ARTICLE INFO

### Article history:

Received 24 February 2014

Received in revised form

30 September 2014

Accepted 4 October 2014

### Keywords:

Google Street View

Street canyon irradiances

Canyon fisheye images

## ABSTRACT

This paper presents an implementation of digital image processing tools, in order to reconstruct building geometries and urban sky view factors for individual street canyons around the world. By using the Google Street View image database, it is possible to reconstruct canyon fisheye images at any point where a Google panorama is available. The Hugin software allows the geometrically correct merging of independent images in order to create a fisheye projection, covering the upper hemispheric view of the sky. Sky view factor calculations may then be performed by specialised software on the reconstructed fisheye image. In order to analyse the fitness of reconstructed panoramas, control images taken with a fisheye lens camera were used for comparison. The Rayman model was then used to calculate total shortwave global irradiances from the restricted canyon view and from a full hemispheric view. Finally, total shortwave global irradiances were measured for the same position in the street canyon and compared against observational measurements under a full sky view, this in order to evaluate the performance and usefulness of idealised calculations. The reconstructed urban geometries returned acceptable fine-scale descriptions, and their potential utility for scientific purposes in the atmospheric sciences was demonstrated with the examples provided.

© 2014 Elsevier B.V. All rights reserved.

## 1. Introduction

A growing proportion of the global population lives within urban canyons, i.e. city streets surrounded by buildings [1], in which the restricted sky view reduces solar energy access. Because of the unique microclimate conditions created by the specific geometry of each canyon, urban geometries affect the energy performance of buildings and, since main outdoor activities occur at these spaces, they also play a crucial role in human thermal comfort in streets [2,3]. Human exposure to sunlight within urban canyons is also a relevant health issue due to the diverse biological effects of ultraviolet light [4,5]. Some of the future aims of our study will include spectral irradiance calculations within urban canyons in order to determine urban solar UV patterns, as an aid for health studies. This paper presents the initial stages of reconstructing urban geometries for the calculation of total shortwave irradiances.

The geometry of urban canyons, defined by the variations in height, length and spacing between buildings, has a significant effect on the energy budgets of urban areas [6]. Since the 1980s many urban meteorologists and climatologists have been using geometrical indices for describing urban canyons, particularly the Sky View Factor (SVF). According to the definition of [7] in [8], the Sky View Factor is “the ratio of the radiation received (or emitted) by a planar surface to the radiation emitted (or received) by the entire hemispheric environment”. However a more common way of understanding it is as the proportion of unobscured sky from the perspective of an observer. The SVF index has proven to be useful, not only for describing canyons, but also for modelling and predicting atmospheric conditions on urban micro-scales, affecting energy exchanges, temperature variations, and air movement phenomena [9–16]. The SVF has also been used to explain public health issues and create geographic models of disease risks, for example tuberculosis [17]. It also has potential applications in building and city planning e.g. daylight in buildings, heat loading and energy conservation. In addition, it can provide with the exposure to sunlight of individuals within the canyons, for realistic assessment of people's exposure to ultraviolet radiation, for example. Given its importance, current and future research needs to focus on creating ways

\* Corresponding author. Present address: Simon Building, Oxford Road, Manchester M13 9PL, UK. Tel.: +44 7412852056.

E-mail address: [roberto.carrascoherandez@postgrad.manchester.ac.uk](mailto:roberto.carrascoherandez@postgrad.manchester.ac.uk) (R. Carrasco-Hernandez).

### Abbreviations and nomenclature

SVF	Sky View Factor
$E_C(t)$	canyon irradiance ( $Wm^{-2}$ ) at time $t$
$E_F(t)$	actual measured irradiance ( $Wm^{-2}$ ) under a full-sky view (in our case from the Whitworth observatory measurements, University of Manchester)
$E_{IC}(t)$	idealised canyon irradiance ( $Wm^{-2}$ ) inside a given canyon profile under cloudless conditions calculated using the Rayman model and the canyon's SVF
$E_{IF}(t)$	idealised full-sky irradiance ( $Wm^{-2}$ ) under a full-sky view and cloudless conditions.

to model the SVF factors for large cities, without compromising the level of detail and resolution required.

In general, methods for determining SVF and solar access calculations can be divided into four groups: Geometrical Methods, Fisheye image analyses, inferences from GPS signals, and 3D models of terrain and buildings. For a short review of these methods see: [18], also [19] gave a comprehensive up-to-date list of associated literature. Hitherto, three dimensional modelling techniques have been most widely used to generate SVF maps and solar radiation models for cities [20–22]. However the geographic coverage of 3D models is restricted since it may compromise computational performance. Most digital models of cities will also oversimplify the complex shapes of urban canyons. Additionally, these models contain information about buildings' heights and widths, but not details about materials comprising the urban canopy. Certain features and materials like glass windows, trees or walls exert different effects on the incoming radiation (i.e. reflection, filtering and absorption) [4,23–26]. Although it is not within the scope of this article to analyse these particular effects, the proposed methods will allow researchers to map SVFs for large cities at a very high resolution, while maintaining detailed descriptions of urban canopy shapes and colours, which in turn could be related to the underlying materials.

In this work it is proposed to use the Google Street View image database, to reconstruct fisheye images and SVFs for an individual urban canyon, at a location where a Google panorama is available. For this purpose, we used the open-source software Hugin for image merging and projection, and the Rayman software tool – originally developed for modelling mean radiant temperatures and thermal comfort [27] –. The combination of these tools enables us to calculate detailed SVFs for an urban canyon, without the need to physically taking fisheye images. Furthermore, street level total shortwave irradiances can be modelled using the Rayman software, as a tool for the assessment of urban energy budgets and microclimate patterns.

## 2. Materials and methods

### 2.1. Software tools

Google Street View has not often been used for scientific purposes in the atmospheric sciences. Other Google products have been proposed as platforms for sharing atmospheric data, e.g. Smith and Lakshmanan [28] proposed the usage of Google Earth, for the integration of weather data with GIS information. Dall'O [29] addresses the potential usefulness of using Google Earth satellite imagery for the assessment of energy performance of buildings. Patel et al. [30] used Google Street View to estimate the heights of buildings in a study block by comparing them with objects of known dimensions; they used building height information to create a digital elevation model and calculate shading patterns using

ArcGIS. However, it seems that the usefulness of Google Street View for urban atmospheric studies has been overlooked. Within the reviewed literature, most academic articles either discuss technical and computational issues [31–33], or focus on potential social implications and uses of Google Street View, like privacy protection [34] or neighbourhood assessment [35]. Google Street View possesses an immense collection of images, comprising 360 degree (spherical) panoramas of individual locations at street level in many countries around the world. This opens up the possibility of describing the SVF wherever Google Street View is available.

Hugin is an open source software originally created by d'Angelo [36,37]. This software allows the assemblage of independent rectilinear images into a single panorama. It also allows the user to collocate different images according to their central positions on a three dimensional hemisphere. Such hemisphere represents the upper hemispheric view of the camera which is very useful for sunlight and skylight calculations.

The freely available Rayman Model 2.1 software was released in the year 2010 [27]; it calculates total shortwave global irradiance and mean radiant temperature for any minute of the day. Calculations can be performed at any geographical location, including urban canyons, for which the building geometry can be described using a fisheye image. The Rayman software has a graphical user interface to manually draw polygons covering the area of buildings in the projected “fisheye” hemispheric view of the canyon, simply by delimiting the boundary between sky and buildings. The result is basically a binary classification of the pixels in the fisheye image, where white pixels are considered to be sky and therefore contribute to radiation; while black “building” pixels represent obstructions to the background light, which may be direct or diffuse radiation. The proportion of white pixels is proportional to the SVF. However, note that the exact proportion of sky that each pixel represents also depends on its elevation angle, which in turn depends on the planar projection used for the hemispheric view. Additionally, the Rayman software allows the generation of sun path diagrams for the analysis of sunlight duration and irradiance intensity within a canyon. Other commercial software packages like ECOTECT provide similar tools [38].

### 2.2. Study site and image details

The Dover Street urban canyon is located in the University of Manchester city campus, UK. The canyon has a northeast–southwest orientation, with medium size (5 to 7 storey) buildings at both sides. Two sets of rectilinear images were taken from different directions that cover the full upper hemispheric view of the canyon. These sets were projected into a reconstructed fisheye view; the reconstruction was compared against a control fisheye image taken at the same location with an orthographic fisheye lens that closely represents a cosine response, i.e. that of radiation incident on a horizontal plane.

Twenty-five independent rectilinear images were taken with an E5 Nokia mobile phone camera, with a 50 degree horizontal field of view (HFV). The set of images covered the full hemispheric view of the Dover Street canyon and were each associated with the 3D hemispheric coordinates of the image centre. This set is referred to as the Nokia set in the following sections.

A set of 10 Google Street View images, with a 90 degree HVF, were taken at the closest possible point to that used in the Google database. The set covered the entire hemispheric view of the Dover Street canyon. The images were also labelled according to their 3D hemispheric coordinates.

The centre of the hemispheric view of these two sets differed in horizontal position by a few metres. It also differed in vertical position by approximately 2 m, since Google images are taken at approximately 2.5 m above street level in the centre of the

carriageway [31], whereas the Nokia set were taken at 0.5 m above ground to match the radiation measurements used for validation.

In order to record a control orthographic hemispheric image, a mini fisheye lens (Sumlung, model: SL-FE12) was fitted to the same E5 Nokia phone camera as used to record the rectilinear images. The mini lens consists of a detachable fisheye lens, with a small magnet to align it in front of the optics of a mobile or digital camera. The orthographic projection of the mini-fisheye lens was confirmed in the laboratory against objects of known heights with respect to the edge of the lens. Canyon control images were taken to describe the upper hemispheric view within the canyon: the lens was positioned facing towards the zenith, and the vertical axis of the camera was oriented with the north–south axis. However, the internal CCD array of the camera is not able to capture the full upper hemispheric view in one single take, being cropped on the north and south edges in this orientation. Therefore, a second image was taken with a 90 degree azimuthal rotation to cover the missing parts of the hemispheric view. Finally the two images were overlaid.

Two panorama reconstructions were made for the Dover Street canyon: the first one was made from the twenty five rectilinear images set taken at the canyon. The second reconstruction was made from the Google Street View images by using the Hugin software: images were positioned and projected according to their hemispheric coordinates. The fisheye projections (equidistant and orthographic) were constructed with the Hugin software for comparison with the directly measured fisheye image.

The reconstructed projections and the control image were imported into the Rayman software, in order to calculate their corresponding sky view factors using the method described by Steyn [39]. SVFs of the two reconstructions and the control images were compared.

### 2.3. Street level total shortwave irradiance measurements

Total shortwave irradiances were measured in a city canyon and compared against measurements under a full sky view. On 3–4 April 2013 total shortwave global irradiances were measured at the Dover Street urban canyon using a Kipp and Zonen CM5 pyranometer with a verified cosine response and compared against measurements of another CM5 pyranometer installed at the rooftop of the Whitworth Observatory of the University of Manchester. The Whitworth Observatory has an almost unobstructed view of the sky with an estimated SVF > 0.999. Previously, the Dover Street pyranometer had been cross-calibrated under a full sky view with the instrument at the Whitworth Observatory, the calibration of the Whitworth pyranometer being traceable to the World Radiation Centre in Davos, Switzerland. The data logging systems for both devices were synchronised and set to Universal Coordinated Time. The distance between the measuring sites was approximately 230 m, and this can be considered a sufficiently small distance such that both sites are subject to the same meteorological and cloud conditions.

### 2.4. Street level modelling

The measured irradiances for both pyranometer positions were modelled using the Rayman software which allows the calculation of the path of the sun across the sky for a particular date, time and geographical location. The software evaluates the visibility of the solar disc throughout the day, given the specific horizon obstructions of the canyon; and additionally it calculates the observable fraction of diffuse irradiance by using the calculated SVF.

The objective of this core part of the study is to evaluate the accuracy of the canyon reconstruction by comparing modelled and

measured irradiances in the canyon both in terms of their absolute and relative values, and any temporal offsets.

Notice that, although the Rayman model allows the introduction of clouds in the sky, it does not assess the complex interactions of moving clouds blocking and unblocking the solar disc from the observer's perspective, for this reason the models were run assuming cloudless skies. Still, the relative patterns of canyon irradiances throughout the day are expected to be well described by idealised models, because of the dominance of direct sunlight in global irradiance: i.e. whenever the sun is visible in the canyon, irradiance values should be very similar between full sky and canyon irradiances. If intermittent decreases due to the passage of clouds occur, we anticipate both full sky and canyon irradiances to be affected in a similar manner. On the other hand, when the sun is obstructed by the canyon buildings, then the difference between canyon and full sky irradiances should be larger; in this case the effect of clouds blocking direct sunlight are not anticipated to be observable in the canyon assuming the diffuse component to be isotropic.

## 3. Results

### 3.1. Panorama reconstructions from the Nokia E5 set of rectilinear images

The Hugin software tool allowed the relative 3D positioning of the Nokia set of independent images to be specified, shown in Fig. 1a as a hemispheric view and in Fig. 1b as a plan view. These images are subsequently deformed to create a continuous hemispheric image (Fig. 1c) which is then finally projected onto a plane (Fig. 1d). All deformations produced as well as any overlapping between images are automatically calculated by Hugin, the only input information required is the relative position of each image and its horizontal field of view. Lastly the Hugin tool handles merging of the overlapping images from Fig. 1d by edge softening; the first two images in Fig. 2 are the result of this complete process, showing both an equidistant projection for comparison (Fig. 2a) and an orthographic projection in Fig. 2b. The latter projection is most relevant for instruments such as pyranometers which have a cosine response. In this case the pixel distance from the centre of the image is related to the sine of the zenith angle for the corresponding point of the sky. The orthographic projection of the SLFE12 fisheye is also confirmed by the much better agreement in the calculated SVF for the Hugin orthographic projection to that for the fisheye image.

### 3.2. Panorama reconstruction from Google Street View images

Fig. 3 shows the process of panorama reconstruction with the Google Street View images. The process was very similar to that shown in Fig. 1 for the Nokia set, but with a different set of input images. The images from Google Street View have a particular advantage when carrying out panorama reconstructions: namely that the field of view is larger and thus fewer images are required to cover the hemisphere. In turn this enables a more consistent reconstruction to be formed using the Hugin software and better estimate of the SVF.

### 3.3. Street level total shortwave irradiances

Fig. 4a shows the projected sky view of the Dover Street canyon, overlaid with the calculated sun path for 3 April 2013 using the Rayman software. The south–southeast section of the canyon is amplified in Fig. 4b to better illustrate the solar track, relevant to the measured and modelled irradiances on this date, shown in Figs. 5a and 6a. Notice from Fig. 4b the path of the sun being obstructed at specific times of the day by the buildings in the canyon. It is important to note that in this figure the projection of the canyon is shown

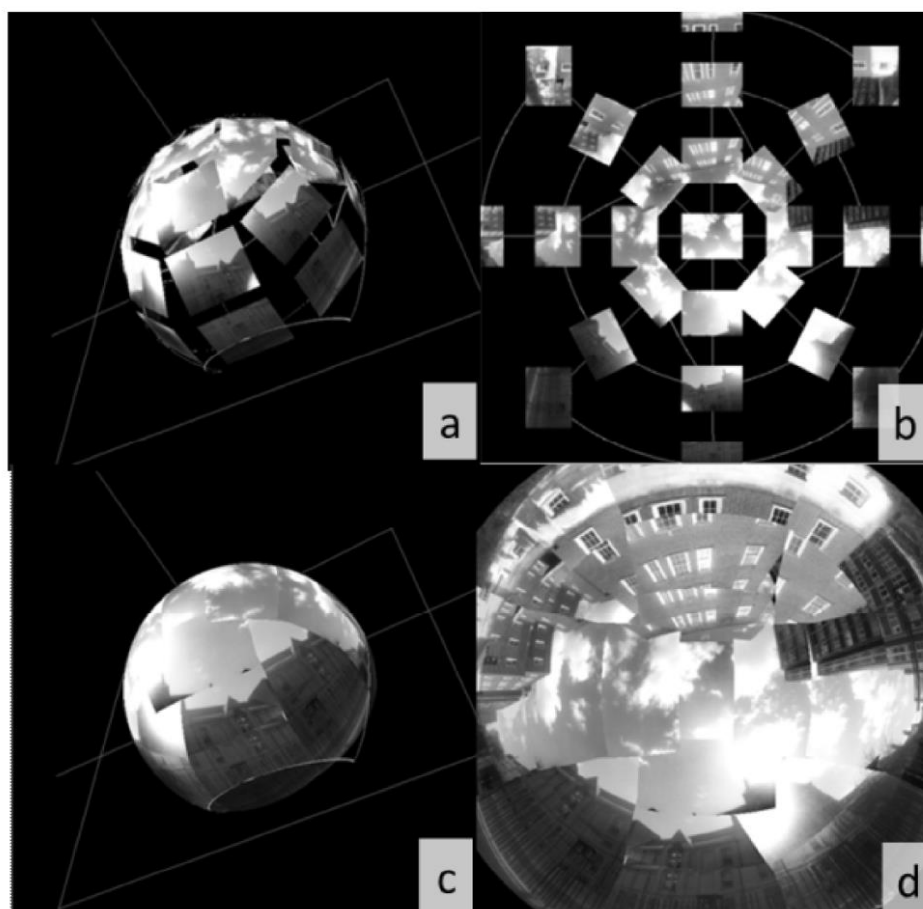
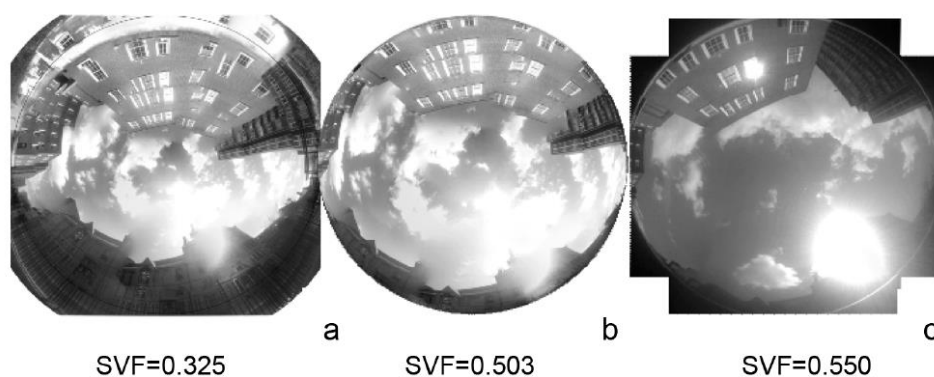


**Fig. 1.** Screenshots of the Hugin interface. Twenty-five independent images covering the full view from the Dover Street canyon in a hemispheric view (a) and plan view (b). (c) Shows the continuous hemispheric image of the view from the canyon, also projected onto a plane (d).

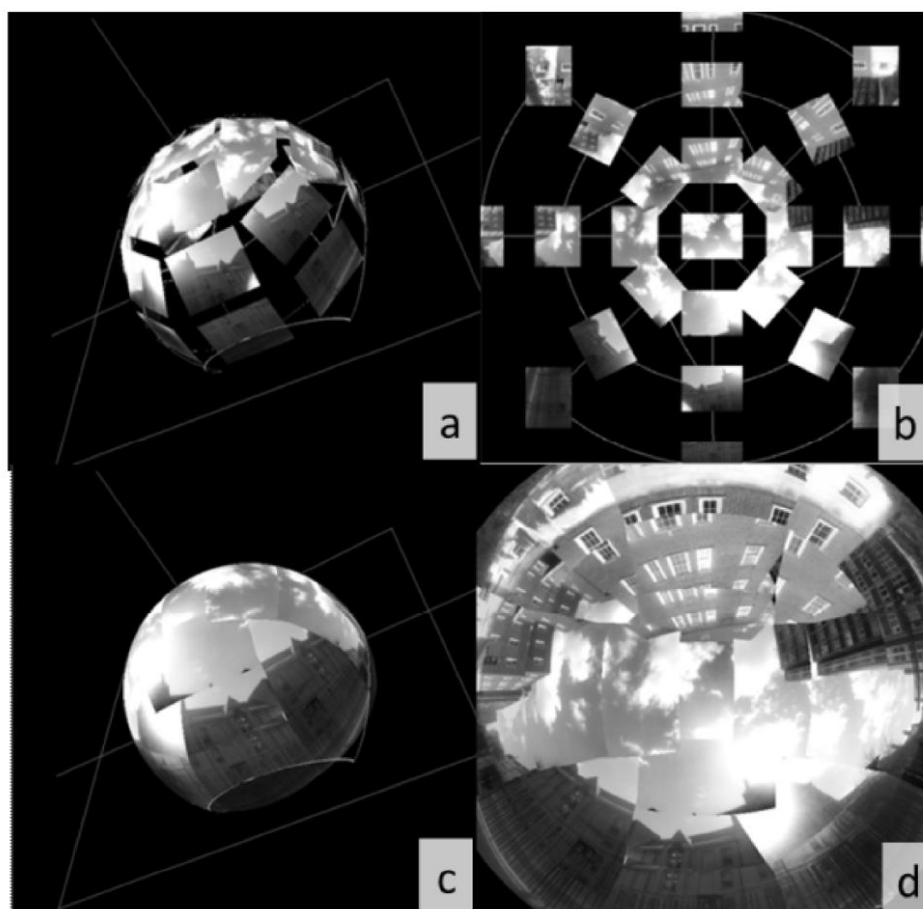
with an equidistant projection in order to match the projection of the solar path that the Rayman software returns. When calculating the SVF, however, a cosine weighting is applied to the obstructions. Notice that the orientation of the canyon slightly differs from the projections shown in Figs. 2 and 3. In the previous examples the orientation was not relevant. However, for irradiance calculations, which estimate the precise position of the sun at certain times of the day, the orientation of the canyon must be accurately represented.

Fig. 5 shows the results from modelling the total shortwave global irradiance using the Rayman software combined with the

reconstructed sky view at the Dover Street canyon. The black line corresponds to the modelled full-sky irradiance where the direct sunlight is visible at all times and, therefore it follows a monotonically increasing curve towards midday (Fig. 5a) and similarly but decreasing after midday (Fig. 5b). In contrast the grey broken line corresponds to the modelled canyon irradiance where the direct sunlight is blocked during different parts of the day by the specific geometry of the Dover Street canyon and it thus exhibits distinct steps as the sun's path transitions behind an obstruction.



**Fig. 2.** Orthographic and equidistant reconstructed hemispheric views versus a control fisheye image with corresponding SVF specified below each image. (a) Orthographic reconstructed projection, (b) equidistant reconstructed projection, and, (c) control fisheye image taken with the SLFE12 mini fisheye lens. Pictures were taken at the Dover Street canyon, University of Manchester.

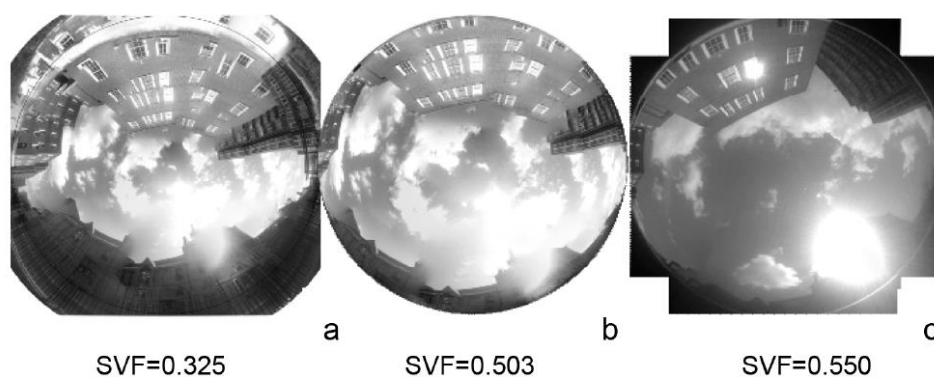


**Fig. 1.** Screenshots of the Hugin interface. Twenty-five independent images covering the full view from the Dover Street canyon in a hemispheric view (a) and plan view (b). (c) Shows the continuous hemispheric image of the view from the canyon, also projected onto a plane (d).

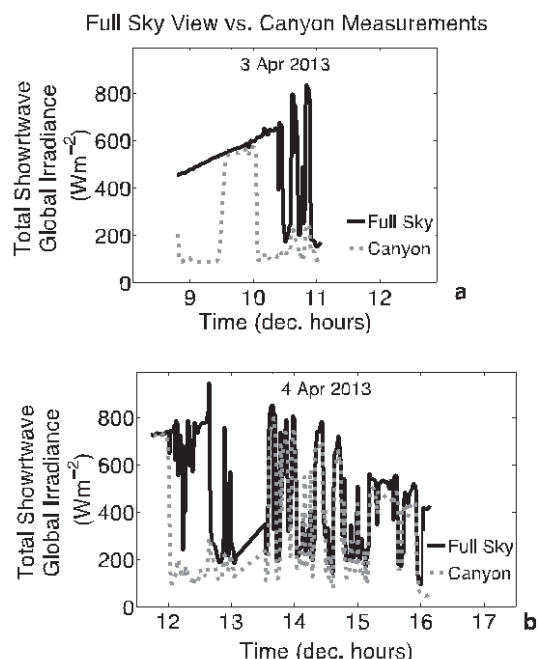
with an equidistant projection in order to match the projection of the solar path that the Rayman software returns. When calculating the SVF, however, a cosine weighting is applied to the obstructions. Notice that the orientation of the canyon slightly differs from the projections shown in Figs. 2 and 3. In the previous examples the orientation was not relevant. However, for irradiance calculations, which estimate the precise position of the sun at certain times of the day, the orientation of the canyon must be accurately represented.

Fig. 5 shows the results from modelling the total shortwave global irradiance using the Rayman software combined with the

reconstructed sky view at the Dover Street canyon. The black line corresponds to the modelled full-sky irradiance where the direct sunlight is visible at all times and, therefore it follows a monotonically increasing curve towards midday (Fig. 5a) and similarly but decreasing after midday (Fig. 5b). In contrast the grey broken line corresponds to the modelled canyon irradiance where the direct sunlight is blocked during different parts of the day by the specific geometry of the Dover Street canyon and it thus exhibits distinct steps as the sun's path transitions behind an obstruction.



**Fig. 2.** Orthographic and equidistant reconstructed hemispheric views versus a control fisheye image with corresponding SVF specified below each image. (a) Orthographic reconstructed projection, (b) equidistant reconstructed projection, and, (c) control fisheye image taken with the SLFE12 mini fisheye lens. Pictures were taken at the Dover Street canyon, University of Manchester.



**Fig. 6.** Showing the measurements and the observed differences between obstructed (Dover Street canyon) and full sky (Whitworth Observatory) views, on 3 (a) and 4 (b) April 2013.

Since the relative relationship between canyon and full sky view irradiances may be modelled under idealised cloudless conditions, it should then be possible to use a combination of actual full sky measurements with ideally modelled ratios between canyon and full sky views, in order to construct more realistic approximations of canyon irradiances.

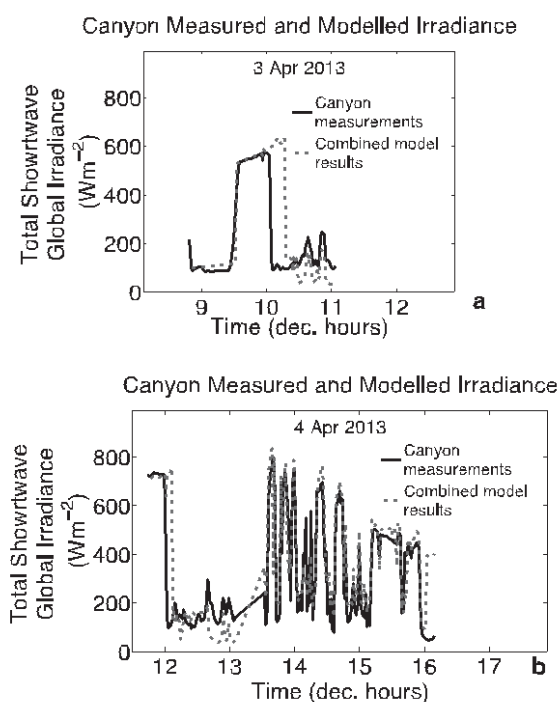


**Fig. 7.** Comparison between modelled (dashed grey line) and measurements (black line) of global total shortwave irradiances, conducted on 3 (a) and 4 (b) April 2013, at the Dover Street Canyon, University of Manchester. The models have been constructed using Eq. (1) for a combined model which used full-sky view measurements and an idealised ratio of canyon to full sky irradiances.

### 3.4. Combined model

In order to create a more realistic model of a cloudy sky, a combined model for the canyon total shortwave irradiances was built using the idealised ratio between obstructed to full sky view, multiplied by the actual full sky irradiance as in the following equation:

$$E_C(t) = \frac{E_{IC}(t)}{E_{IF}(t)} \times E_F(t) \quad (1)$$

where:  $E_C(t)$  is the canyon irradiance ( $\text{W m}^{-2}$ ) at time,  $t$ ;  $E_{IC}(t)$  is the idealised canyon irradiance inside a given canyon profile under cloudless conditions calculated from the Rayman model and SVF;  $E_{IF}(t)$  likewise is the idealised full-sky irradiance under a full-sky view and cloudless conditions; and,  $E_F(t)$  is the actual measured irradiance under a full-sky view (in our case from Whitworth Observatory measurements).

The combined model shown in Fig. 7 provides a better appreciation of the model's performance in respect to irradiance calculations and remaining sources of uncertainty. The time offset between measured and modelled direct beam incidence (e.g. 10.1 h to 10.3 h in Fig. 7a) is directly related to the goodness of the reconstruction of urban geometries. For these times in Fig. 7a as compared with Figs. 2 and 4. It can be seen that at the corresponding azimuth angle the sun just grazes the canyon skyline; so any small inaccuracies in defining the building edges may lead to possible erroneous inclusion or exclusion of the solar disc in the calculations. Otherwise, there is a good correspondence between modelled and measured irradiance. Time offsets (i.e.: horizontal differences between models and measurements in Fig. 7a and b) are one way of describing discrepancies. Although it is not an accurate representation of the overall goodness of the projection, these observed time offsets between models and measurements evidence errors in the projection. For example, in Fig. 7a an offset of approximately 15 min is observable after 10 h. It should also be acknowledged that different positions in the canyon sometimes experience different irradiances (sunny and shady sides of the street) particularly when the sun is close to the building edge. In fact, separations of a few centimetres are enough to create large differences between different positions within a canyon, especially in regard to direct sunlight.

In general, the models and measurements of canyon irradiances are very similar. However the modelled canyon irradiance was often slightly underestimated when the sun was blocked by a building and slightly overestimated when the sun was visible in the canyon. This general pattern may indicate that the proportional contributions of direct and diffuse light are slightly biased, with the direct light having a larger weighting in the model than it takes in reality.

According to Fig. 8a the combined model explains 59% of the variation in the measured canyon irradiances. Note that the data in Fig. 8a includes the errors resulting from the modelled building misplacements at the specific sky positions where the direct solar beam transitions behind buildings. However, when excluding these few points (Fig. 8b), the performance of the model increased to explain 84% of the variation in measurements.

## 4. Discussion

### 4.1. Reconstructed vs. control fisheye hemispheric images

Hugin allowed both equidistant and orthographic projections to be reconstructed from the Google Street View images. In terms of radiation measurements on a horizontal surface, it is the orthographic image that is most useful. Flat-horizontal surfaces present a smaller response to radiation incident from high zenith angles as the response of many solarimeters and radiometers is proportional



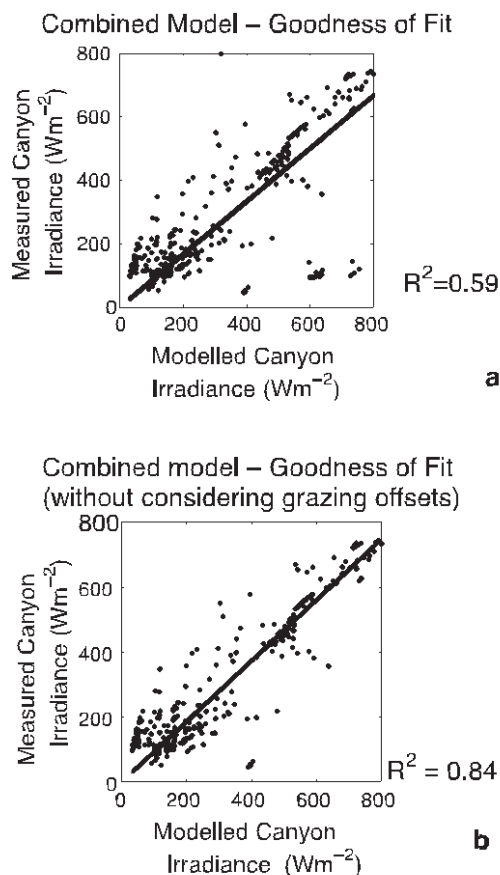


**Fig. 8.** Goodness of fit of the model described by Eq. (1) for the data from both 3 and 4 April 2013 together. (a) shows the scatter plot of measured against modelled data considering all points. (b) shows the scatterplot after removing the identified time offsets. Both panels include a linear fit and the corresponding  $R^2$  values.

to the cosine of the zenith angle of the radiance from each region in the hemispheric view.

It is important to note that, although the fisheye lens used in this study has an orthographic projection, other fisheye lenses – commonly used in literature for describing urban canyons – have an equidistant projection instead. For equidistant images a cosine law must be applied *a-priori*; in order to calculate a geometrically correct SVF that matches the cosine response of a flat horizontal surface [39,40]. This cosine law assigns a smaller weight to the area occupied by pixels towards the edge of the fisheye equidistant image (corresponding to the horizon line). In contrast, orthographic lenses compress objects towards the horizon line as a function of the sine of their zenith angles; this is equivalent to applying the same cosine law used to calculate the SVF from equidistant images. The use of the cosine law then becomes redundant when calculating the SVF from an orthographic image.

One advantage of the Rayman software is that it allows the user to choose whether or not to apply the cosine law when calculating SVFs [40], but the user must know the projection of the fisheye image, and the geometry of the reference surface. Users of magnetic mini-fisheye lenses (such as the one used in this study) must, therefore, be aware of the orthographic projection of these lenses, and the need to choose the correct option in the Rayman software. The equidistant projection might still become very important when modelling irradiance upon non-flat surfaces, since, with an equidistant image one can match the sky views of either flat horizontal surfaces (cosine law applied) or spherical surfaces (cosine law not applied). Much of the information about walls and buildings

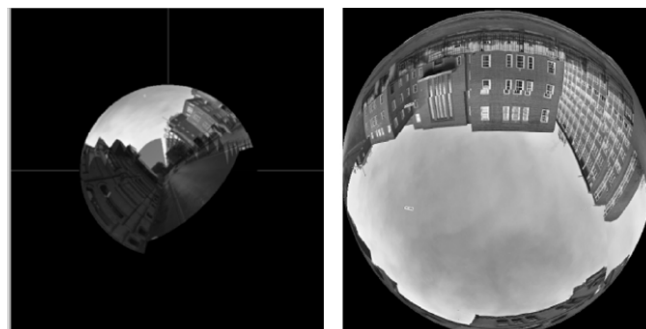


**Fig. 9.** Hugin interface screen. Left-hand side: shows the overall 45 degree rotation made from Google snapshots. Right-hand side: The panorama was then orthographically re-projected in order to simulate the perspective of the Dover Street canyon from the opposite side of the road.

contained in the equidistant projection is compressed towards the edges in an orthographic projection. However, this information can become highly relevant for vertical and spherical surfaces, for example when investigating human exposure to solar radiation. The human skin could be considered a complex combination of vertical and horizontal surfaces or a spherical surface for simplicity [27]. In any case, the radiative environment to which it is exposed differs a lot to that of the standard flat horizontal surfaces, used for general solar measurements. In other words, the SVF perceived by flat-horizontal radiometers does not necessarily match the SVF perceived by other surfaces such as the human skin; having different projections may allow us to infer SVFs for different purposes.

#### 4.2. Panorama reconstruction from Google snapshots

The Google Street View images are taken from the carriageway rather than the pavement, and so are reasonably representative of the centre of the canyon. Yet, Figs. 2 and 3 show images taken at different positions separated by only a few metres within the same canyon. Even with a relatively small separation it can be seen that the position of the camera – or similarly any surface receiving radiation – has a different perspective of the geometry of the canyon. In Fig. 3 the southern wall dominates the upper hemispheric view, whereas Figs. 1 and 2 have the opposite walls as the main obstructing feature. Given that the Google Street View images must be specified by their coordinates in the Hugin model, one way to adjust the perspective of the viewer would be to rotate the relative hemispheric coordinates of the Google images in the hemispheric view. Fig. 9 shows an example of the Google images tilted 45 degree in the hemispheric view and re-projected.

#### 4.3. Street level total shortwave irradiances

The general relationship between canyon and full sky irradiances was satisfactorily modelled ( $R^2 = 0.84$ , Fig. 8b). The measurements conducted in this work generated a time series of canyon irradiances (Fig. 6a and b), which illustrate the two main controls on canyon irradiances. These are the times of the day when the solar disc is blocked by buildings in the canyon, and times when clouds cover the solar disc. When the solar disc is not blocked by the buildings in a canyon, the irradiance patterns closely follow those received under an unobstructed view. Such patterns also include any intermittent drops due to cloud cover (e.g. around 14.0h in Fig. 6b). In such cases, clouds – instead of buildings – are the determining factor blocking direct solar radiation, but their effect is inherent in the signal from the unobstructed (full-sky) pyranometer.

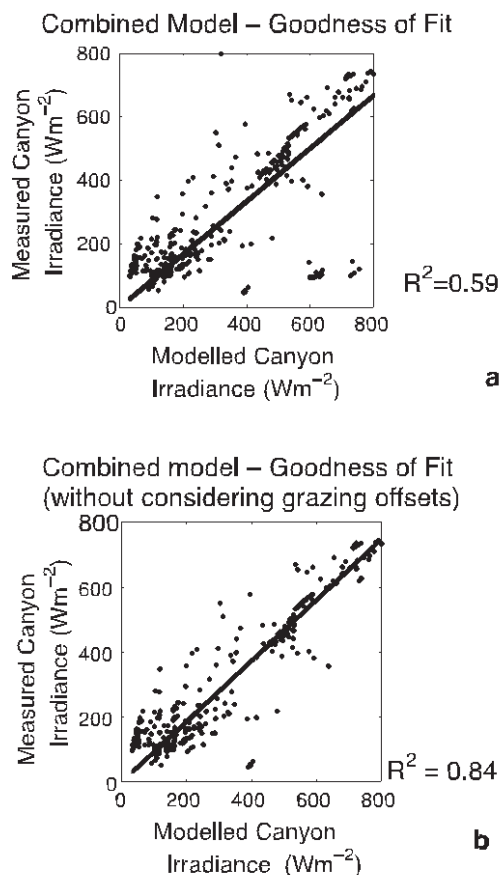


**Fig. 8.** Goodness of fit of the model described by Eq. (1) for the data from both 3 and 4 April 2013 together. (a) shows the scatter plot of measured against modelled data considering all points. (b) shows the scatterplot after removing the identified time offsets. Both panels include a linear fit and the corresponding  $R^2$  values.

to the cosine of the zenith angle of the radiance from each region in the hemispheric view.

It is important to note that, although the fisheye lens used in this study has an orthographic projection, other fisheye lenses – commonly used in literature for describing urban canyons – have an equidistant projection instead. For equidistant images a cosine law must be applied *a-priori*; in order to calculate a geometrically correct SVF that matches the cosine response of a flat horizontal surface [39,40]. This cosine law assigns a smaller weight to the area occupied by pixels towards the edge of the fisheye equidistant image (corresponding to the horizon line). In contrast, orthographic lenses compress objects towards the horizon line as a function of the sine of their zenith angles; this is equivalent to applying the same cosine law used to calculate the SVF from equidistant images. The use of the cosine law then becomes redundant when calculating the SVF from an orthographic image.

One advantage of the Rayman software is that it allows the user to choose whether or not to apply the cosine law when calculating SVFs [40], but the user must know the projection of the fisheye image, and the geometry of the reference surface. Users of magnetic mini-fisheye lenses (such as the one used in this study) must, therefore, be aware of the orthographic projection of these lenses, and the need to choose the correct option in the Rayman software. The equidistant projection might still become very important when modelling irradiance upon non-flat surfaces, since, with an equidistant image one can match the sky views of either flat horizontal surfaces (cosine law applied) or spherical surfaces (cosine law not applied). Much of the information about walls and buildings

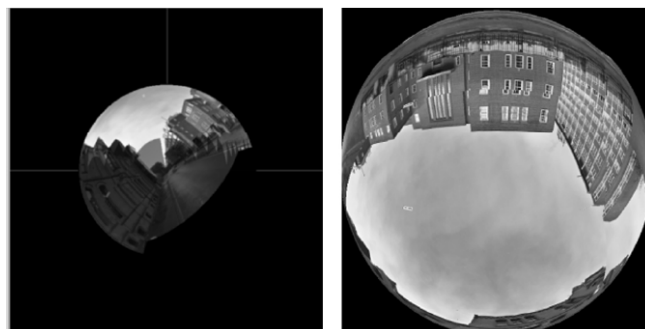


**Fig. 9.** Hugin interface screen. Left-hand side: shows the overall 45 degree rotation made from Google snapshots. Right-hand side: The panorama was then orthographically re-projected in order to simulate the perspective of the Dover Street canyon from the opposite side of the road.

contained in the equidistant projection is compressed towards the edges in an orthographic projection. However, this information can become highly relevant for vertical and spherical surfaces, for example when investigating human exposure to solar radiation. The human skin could be considered a complex combination of vertical and horizontal surfaces or a spherical surface for simplicity [27]. In any case, the radiative environment to which it is exposed differs a lot to that of the standard flat horizontal surfaces, used for general solar measurements. In other words, the SVF perceived by flat-horizontal radiometers does not necessarily match the SVF perceived by other surfaces such as the human skin; having different projections may allow us to infer SVFs for different purposes.

#### 4.2. Panorama reconstruction from Google snapshots

The Google Street View images are taken from the carriageway rather than the pavement, and so are reasonably representative of the centre of the canyon. Yet, Figs. 2 and 3 show images taken at different positions separated by only a few metres within the same canyon. Even with a relatively small separation it can be seen that the position of the camera – or similarly any surface receiving radiation – has a different perspective of the geometry of the canyon. In Fig. 3 the southern wall dominates the upper hemispheric view, whereas Figs. 1 and 2 have the opposite walls as the main obstructing feature. Given that the Google Street View images must be specified by their coordinates in the Hugin model, one way to adjust the perspective of the viewer would be to rotate the relative hemispheric coordinates of the Google images in the hemispheric view. Fig. 9 shows an example of the Google images tilted 45 degree in the hemispheric view and re-projected.

#### 4.3. Street level total shortwave irradiances

The general relationship between canyon and full sky irradiances was satisfactorily modelled ( $R^2 = 0.84$ , Fig. 8b). The measurements conducted in this work generated a time series of canyon irradiances (Fig. 6a and b), which illustrate the two main controls on canyon irradiances. These are the times of the day when the solar disc is blocked by buildings in the canyon, and times when clouds cover the solar disc. When the solar disc is not blocked by the buildings in a canyon, the irradiance patterns closely follow those received under an unobstructed view. Such patterns also include any intermittent drops due to cloud cover (e.g. around 14.0h in Fig. 6b). In such cases, clouds – instead of buildings – are the determining factor blocking direct solar radiation, but their effect is inherent in the signal from the unobstructed (full-sky) pyranometer.

- [8] T. Gal, F. Lindberg, J. Unger, Computing continuous sky view factors using 3D urban raster and vector databases: comparison and application to urban climate, *Theoretical and Applied Climatology* 95 (2009) 111–123.
- [9] S. Yamashita, K. Sekine, M. Shoda, K. Yamashita, Y. Hara, On relationships between heat island and sky view factor in the cities of Tama River basin, Japan, *Atmospheric Environment* 20 (1986) 681–686 (1967).
- [10] M.K. Svensson, Sky view factor analysis—implications for urban air temperature differences, *Meteorological Applications* 11 (2004) 201–211.
- [11] B. Holmer, S. Thorsson, I. Eliasson, Cooling rates, sky view factors and the development of intra-urban air temperature differences, *Geografiska Annaler: Series A, Physical Geography* 89 (2007) 237–248.
- [12] Y. Nakamura, T.R. Oke, Wind, temperature and stability conditions in an east-west oriented urban canyon, *Atmospheric Environment* 22 (1988) 2691–2700 (1967).
- [13] M. Eeftens, J. Beekhuizen, R. Beelen, M. Wang, R. Vermeulen, B. Brunekreef, A. Huss, G. Hoek, Quantifying urban street configuration for improvements in air pollution models, *Atmospheric Environment* 72 (2013) 1–9.
- [14] J. Unger, Connection between urban heat island and sky view factor approximated by a software tool on a 3D urban database, *International Journal of Environment and Pollution* 36 (2009) 59–80.
- [15] C.L. Tan, N.H. Wong, S.K. Jusuf, Outdoor mean radiant temperature estimation in the tropical urban environment, *Building and Environment* 64 (2013) 118–129.
- [16] S. Zhu, H. Guan, J. Bennett, R. Clay, C. Ewenz, S. Bengler, A. Maghrabi, A.C. Millington, Influence of sky temperature distribution on sky view factor and its applications in urban heat island, *International Journal of Climatology* 33 (2013) 1837–1843.
- [17] P.-C. Lai, C.-T. Low, W.-S.C. Tse, C.-K. Tsui, H. Lee, P.-K. Hui, Risk of tuberculosis in high-rise and high density dwellings: an exploratory spatial analysis, *Environmental Pollution* 183 (2013) 40–45.
- [18] L. Chen, E. Ng, X. An, C. Ren, M. Lee, U. Wang, Z. He, Sky view factor analysis of street canyons and its implications for daytime intra-urban air temperature differentials in high-rise, high-density urban areas of Hong Kong: a GIS-based simulation approach, *International Journal of Climatology* 32 (2012) 121–136.
- [19] S. Park, S. Tuller, Advanced view factor analysis method for radiation exchange, *International Journal of Biometeorology* 1–18 (2013) 161–178.
- [20] J. Strömman-Andersen, P.A. Sattrup, The urban canyon and building energy use: urban density versus daylight and passive solar gains, *Energy and Buildings* 43 (8) (2011) 2011–2020.
- [21] M. Lu, J. Du, Assessing the daylight and sunlight availability in high-density residential areas: a case in North-east China, *Architectural Science Review* 56 (2013) 168–182.
- [22] J. Hofierka, M. Zlocha, A new 3-D solar radiation model for 3-D city models, *Transactions in GIS* 16 (2012) 681–690.
- [23] F. Lindberg, C. Grimmond, The influence of vegetation and building morphology on shadow patterns and mean radiant temperatures in urban areas: model development and evaluation, *Theoretical and Applied Climatology* 105 (3–4) (2011) 311–323, 1–13–13.
- [24] J. Turner, A.V. Parisi, Measuring the influence of UV reflection from vertical metal surfaces on humans, *Photochemical & Photobiological Sciences* 8 (2009) 62–69.
- [25] A. Tsangrassoulis, M. Santamouris, Numerical estimation of street canyon albedo consisting of vertical coated glazed facades, *Energy and Buildings* 35 (2003) 527–531.
- [26] N.L. Alchapar, E.N. Correa, M.A. Cantón, Classification of building materials used in the urban envelopes according to their capacity for mitigation of the urban heat island in semi-arid zones, *Energy and Buildings* 69 (2014) 22–32.
- [27] A. Matzarakis, F. Rutz, H. Mayer, Modelling radiation fluxes in simple and complex environments: basics of the RayMan model, *International Journal of Biometeorology* 54 (2010) 131.
- [28] T.M. Smith, V. Lakshmanan, Utilizing Google Earth as a GIS platform for weather applications, in: 22nd International Conference on Interactive Information Processing Systems for Meteorology, Oceanography, and Hydrology, 2006.
- [29] G. Dall’O, A. Galante, M. Torri, A methodology for the energy performance classification of residential building stock on an urban scale, *Energy and Buildings* 48 (2012) 211–219.
- [30] R. Patel, N. Warren, M. Williams, E. Chen, X. Xu, An Investigation of Urban Agriculture on Residential Blocks in Vancouver, EOSC 448E/ENVR 400 Undergraduate Essay, Environmental Science Undergraduate Research Papers and Reports, University of British Columbia, Vancouver, 2011, <https://circle.ubc.ca/handle/2429/38881>.
- [31] A. Dragomir, Google Street View: Capturing the World at Street Level, in: D. Carole, F. Daniel, F. Christian, L. Stephane, L. Richard, O. Abhijit, V. Luc, W. Josh (Eds.), *Compter* 43, no. 6 (2010): 32–38.
- [32] A.R. Zamir, M. Shah, Accurate image localization based on Google Maps Street View, in: *Computer Vision—ECCV 2010*, Springer, Berlin Heidelberg, 2010, pp. 255–268.
- [33] L. Vincent, Taking online maps down to street level, *Computer* 40 (2007) 118–120.
- [34] A. Frome, G. Cheung, A. Abdulkader, M. Zennaro, B. Wu, A. Bissacco, H. Adam, H. Neven, L. Vincent, Large-scale privacy protection in Google Street View, in: *Computer Vision, 2009 IEEE 12th International Conference on IEEE*, 2009, pp. 2373–2380.
- [35] A.G. Rundle, M.D.M. Bader, C.A. Richards, K.M. Neckerman, J.O. Teitler, Using Google Street View to audit neighborhood environments, *American Journal of Preventive Medicine* 40 (2011) 94–100.
- [36] P. d’Angelo, Radiometric alignment and vignetting calibration, in: *Proc. Camera Calibration Methods for Computer Vision Systems*, 2007.
- [37] D.M. German, P. d’Angelo, M. Gross, B. Postle, New methods to project panoramas for practical and aesthetic purposes. In *Proceedings of the Third Eurographics conference on Computational Aesthetics in Graphics, Visualization and Imaging*, pp. 15–22. Eurographics Association, 2007.
- [38] C. Reinhart, Daylight performance predictions, in: Jan L.M. Hensen, R. Lamberts (Eds.), in: *Building performance simulation for design and operation*, Routledge, 2011, pp. 235–274.
- [39] D.G. Steyn, The calculation of view factors from fisheye-lens photographs: research note, *Atmosphere-Ocean* 18 (1980) 254–258.
- [40] M. Hämmerle, T. Gál, J. Unger, A. Matzarakis, Comparison of models calculating the sky view factor used for urban climate investigations, *Theoretical and Applied Climatology* 1 (2011) 521–527.

## **Appendix II**

### **Published Version of Chapter 6**

The following pages correspond to the published version of Chapter 6 as it appears in *Theoretical and Applied Climatology*. The supplementary information for this article has been made public in its original .docx format, as already presented at the end of Chapter 6.

*Fast calculations of the spectral diffuse-to-global ratios for approximating spectral irradiance at the street canyon level*

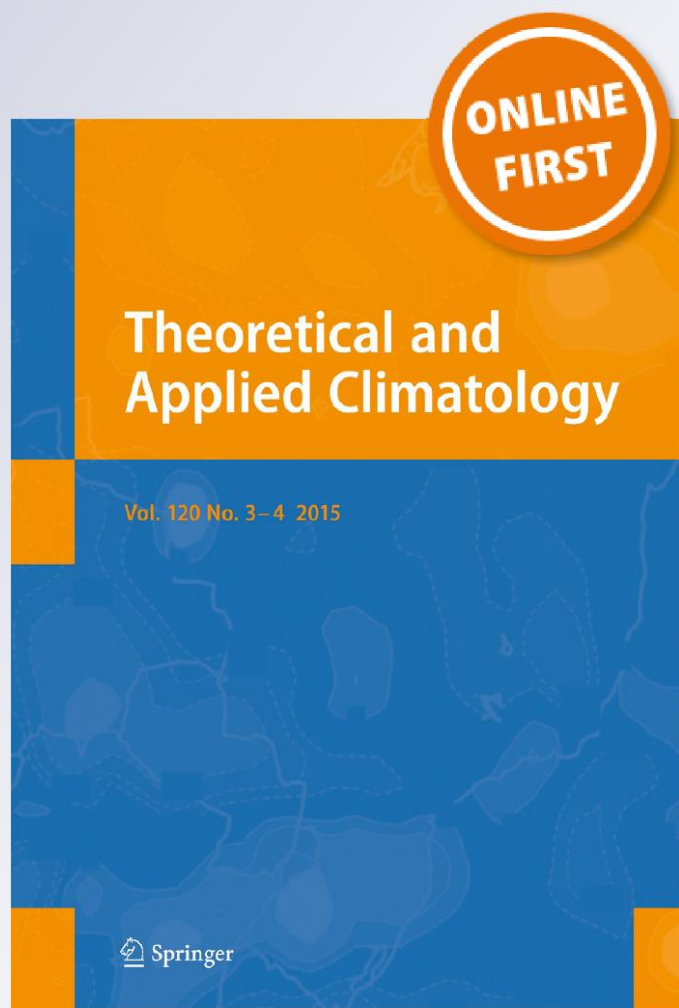
**Roberto Carrasco-Hernandez, Andrew R. D. Smedley & Ann R. Webb**

**Theoretical and Applied Climatology**

ISSN 0177-798X

Theor Appl Climatol

DOI 10.1007/s00704-015-1473-3



**Your article is protected by copyright and all rights are held exclusively by Springer-Verlag Wien. This e-offprint is for personal use only and shall not be self-archived in electronic repositories. If you wish to self-archive your article, please use the accepted manuscript version for posting on your own website. You may further deposit the accepted manuscript version in any repository, provided it is only made publicly available 12 months after official publication or later and provided acknowledgement is given to the original source of publication and a link is inserted to the published article on Springer's website. The link must be accompanied by the following text: "The final publication is available at [link.springer.com](http://link.springer.com)".**

# Fast calculations of the spectral diffuse-to-global ratios for approximating spectral irradiance at the street canyon level

Roberto Carrasco-Hernandez<sup>1</sup> · Andrew R. D. Smedley<sup>1</sup> · Ann R. Webb<sup>1</sup>

Received: 17 November 2014 / Accepted: 12 April 2015

© Springer-Verlag Wien 2015

**Abstract** Two radiative transfer models are presented that simplify calculations of street canyon spectral irradiances with minimum data input requirements, allowing better assessment of urban exposures than can be provided by standard unobstructed radiation measurements alone. Fast calculations improve the computational performance of radiation models, when numerous repetitions are required in time and location. The core of the models is the calculation of the spectral diffuse-to-global ratios (DGR) from an unobstructed global spectral measurement. The models are based on, and have been tested against, outcomes of the SMARTS2 algorithm (i.e. Simple Model of the Atmospheric Radiative Transfer of Sunshine). The modelled DGRs can then be used to partition global spectral irradiance values into their direct and diffuse components for different solar zenith angles. Finally, the effects of canyon obstructions can be evaluated independently on the direct and diffuse components, which are then recombined to give the total canyon irradiance. The first model allows ozone and aerosol inputs, while the second provides a further simplification, restricted to average ozone and aerosol contents but specifically designed for faster calculations. To assess the effect of obstructions and validate the calculations, a set of experiments with simulated obstructions (simulated canyons) were performed. The greatest source

of uncertainty in the simplified calculations is in the treatment of diffuse radiation. The measurement-model agreement is therefore dependent on the region of the sky obscured and ranges from <5 % at all wavelengths to 20–40 % (wavelength dependent) when diffuse sky only is visible from the canyon.

## 1 Introduction

Ground-level measurements and models of solar radiation find applications in studies of human health (Webb 2006; Ludema et al. 2014; Yam and Kwok 2014), photosynthetically active radiation (Hu and Wang 2013), and photovoltaic generation (Myers 1997; Bengert et al. 2014; Myers and Gueymard 2004; Nofuentes et al. 2014). The spectral composition of the solar radiation at ground level acquires further relevance due to the spectrally dependent effects of UV radiation on biological processes (Kaskaoutis et al. 2007; Serrano and Bosca 2011; Malinovic-Milicevic et al. 2014). Measurements and models of global spectral radiation generally refer to that falling on an unobstructed horizontal plane (e.g. radiation received upon a flat rooftop). Such data fail to give a realistic assessment of the exposures that may be gained at street level, where most biological (human) exposure occurs. In order to translate the rooftop unobstructed data to the street level, the canyon horizon obstructions must be described. In each specific street canyon, the horizon obstructions will exert independent effects on the direct and diffuse components; for this reason, the global irradiance must be represented as the sum of its direct and diffuse components. This can be achieved by either measuring or modelling the direct and diffuse components of a global measurement. In recent literature, the importance of partitioning global broadband irradiance has been addressed for analysing the effects of horizon obstructions (Ruiz-Arias et al. 2011).

**Electronic supplementary material** The online version of this article (doi:10.1007/s00704-015-1473-3) contains supplementary material, which is available to authorized users.

✉ Roberto Carrasco-Hernandez  
rcarrash@yahoo.com.mx

<sup>1</sup> Centre for Atmospheric Sciences, School of Earth, Atmospheric and Environmental Sciences, University of Manchester, Simon Building, Oxford Road, Manchester M139PL, UK

Ruiz-Arias et al. affirm that “in any event [overcast, cloudy or cloudless conditions], knowledge of the solar irradiance components is fundamental to discern terrain effects on solar irradiance”. The present work addresses the problem of partitioning spectral irradiance values into their direct and diffuse components.

SMARTS (Myers and Gueymard 2004) is a widely validated one-dimensional radiative transfer model (i.e., it considers the atmosphere as a series of homogenous planes stacked vertically) for the calculation of spectral global irradiances (in  $\text{Wm}^{-2}\text{nm}^{-1}$ ) for an unobstructed (full) sky view, as well as its direct and diffuse spectral components. However, for high temporal resolution applications, the SMARTS calculations can still become computationally intensive. More complex algorithms, like MYSTIC (Mayer et al. 2010), allow Monte-Carlo tracking of independent photons in a three-dimensional complex atmosphere which can include mountains and buildings as topographic reflectors (Weihs et al. 2012; Krayenhoff et al. 2014; Kreuter et al. 2014; Petersen et al. 2014). Although reported to return more realistic radiation models (Wagner et al. 2011), Monte-Carlo ray tracing models are even more demanding of computational resources. The first goal of this work was to develop a fast method of partitioning the global radiation using an unobstructed measurement and a simple algorithm. Street canyon exposures can then be estimated from the independent direct and diffuse components provided the obstruction profiles are known.

A common technique for describing sky obstructions is by projecting the upper hemispheric view of any individual location onto a two-dimensional polar plane. Such projections are usually obtained by using a *fisheye* photograph of the sky view (Grimmond et al. 2001). Alternatively, fisheye projections may be reconstructed from the Google Street View image database (Carrasco-Hernandez et al. 2015). Other methods for describing horizon obstructions on a larger scale are also available through the use of digital elevation terrain models (De Carvalho et al. 2013). The methods proposed in the present work can be applied to any location where the visibility of the direct solar beam can be evaluated along with a measurement of the fraction of visible sky (i.e. the sky view factor, SVF).

The SVF is a basic way of parameterizing sky obstructions and can be understood as the fraction of the sky that is visible from the perspective of a ground observer. It is a dimensionless quantity and has been used in explaining urban atmospheric phenomena (Holmer et al. 2007; Unger 2009; Lindberg and Grimmond 2011; Matzarakis and Matuschek 2011; Eeftens et al. 2013; Zhu et al. 2013). The RayMan model software (Matzarakis et al. 2010) can evaluate the visibility of the solar disk and the SVF from a fisheye polar projection of a specific canyon. The software also calculates a total shortwave irradiance (broadband irradiance) under the provided canyon sky view. In this paper, we elaborate on the RayMan model methods towards the calculation of global

spectral irradiance within urban canyons for UV and visible wavelengths.

### 1.1 The diffuse-to-global spectral ratio

Ratios of the global spectral irradiance and either of its two components have been suggested as useful concepts in the atmospheric sciences (Kaskaoutis et al. 2007; Badarinarth et al. 2007; Kaskaoutis et al. 2008). Measurements of the direct and diffuse components may be obtained by using an additional spectroradiometer equipped with a shadow band or by using a sun-tracking device with direct input optics. However, if the global irradiance is the only measurement available, the diffuse and direct components may still be modelled from a calculation of the ratio of diffuse-to-global irradiance (DGR). The DGR is dependent on wavelength and solar zenith angle (SZA). Figure 1 shows the modelled changes in the spectral DGR for different wavelengths according to SMARTS.

Note that the DGR decreases towards the red end of the spectrum, since Rayleigh scattering is a function of the fourth power of wavelength. Interactions with ozone produce the patterns observed at ultraviolet wavelengths. Both models presented in this work intend to reconstruct Fig. 1 through simplified calculations.

## 2 Methods

### 2.1 Global spectral irradiance in urban canyons

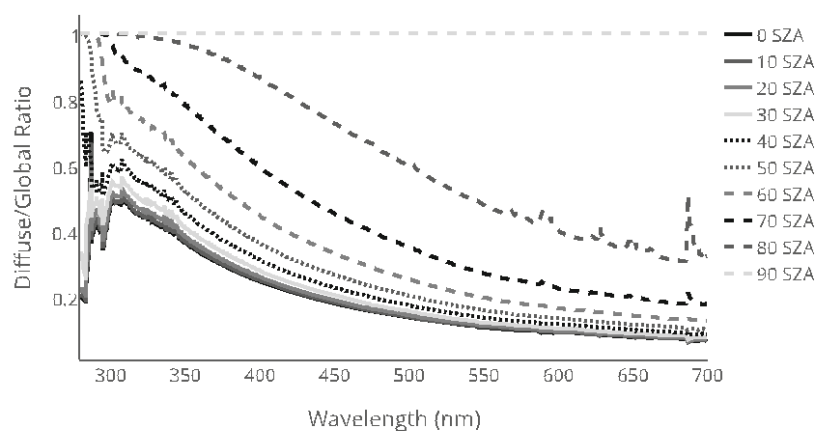
For practicality, the spectral irradiances reaching any urban canyon can be considered to be a fraction of those measured under an unobstructed view. Such assumption is not always true since the irradiance reflected by urban materials (e.g. ground, building walls) may become a significant part of the total irradiance. However, the modelling of such contributions would require complex 3D Monte-Carlo simulations that are not within the scope of this article. For large temporal scale purposes and for the sake of simple and fast calculations, the effect of reflections may be neglected as their effects usually occur over a limited range of solar positions. To calculate the fraction corresponding to the canyon irradiance, it is first necessary to split the global irradiance into its direct and diffuse components. The effects of obstructions on these components are evaluated independently and then summed (Eq. 1). For cloudless skies, direct irradiance in the canyon depends on whether the solar disk is blocked by a building, while diffuse irradiance is proportional to the SVF.

$$E_{C,\lambda} = (E_{b,F,\lambda})S_{\text{bin}} + (E_{d,F,\lambda})\text{SVF}, \quad (1)$$

where  $E_{C,\lambda}$  is the global spectral irradiance within a specific urban canyon C, at wavelength  $\lambda$ ;  $E_{b,F,\lambda}$  is the direct beam



**Fig. 1** DGRs calculated for different solar zenith angles (SZA) for a standard mid-latitude urban atmosphere using the SMARTS radiative transfer algorithm. Ozone (0.31 atm-cm) and aerosol (0.1 AOT<sub>500nm</sub>) atmospheric contents corresponded to those measured on 7 June 2013



spectral irradiance under a full sky view  $F$  at wavelength  $\lambda$ ;  $S_{bin}$  is a binary digit (1 or 0) representing the visibility of the direct solar beam;  $E_{d,F,\lambda}$  is the diffuse irradiance under full sky view  $F$  at wavelength  $\lambda$ ;  $SVF$  is the sky view factor

However, if the only parameter available is the full sky view global irradiance:  $E_{F,\lambda}$ , the canyon global irradiance  $E_{C,\lambda}$  may still be calculated, by knowing the proportional ratio of diffuse-to-global irradiance (DGR):

$$E_{C,\lambda} = [(E_{F,\lambda}) \times (1 - \text{DGR}) \times S_{bin}] + [(E_{F,\lambda}) \times \text{DGR} \times svf] \quad (2)$$

Once the prerequisites are satisfied (i.e. a *fish-eye* projection of the obstructions and a measurement of unobstructed global solar radiation), the radiation at street level in a canyon can be estimated from the DGR only (Eq. 2). Our goal is to calculate the DGR in a simple manner.

The assumptions made in these models are similar to those found in the RayMan model for total shortwave irradiance (Matzarakis et al. 2010). Reflections from walls are neglected, and the diffuse component is considered as isotropic. Although allowing simple and fast calculations, errors can be introduced into the models by these assumptions. At certain moments, for some building surfaces, the reflections from walls can substantially increase canyon irradiance. In addition, for cloudless skies, the anisotropy of the diffuse component implies that obstructions of similar size may have different shading effects, depending on their proximity to the circumsolar region. One objective of this work was to measure the magnitude of the errors arising from such assumptions.

## 2.2 Modelling the spectral DGR

The first model presented is a mathematical simplification of a well-validated radiative transfer model (SMARTS) to calculate the DGR. The second model is a semi-empirical fit, which represents a further simplification of the DGR calculations, but is limited by the conditions under which it was derived.

Either can later be used in combination with fish-eye projections of canyon profiles and Eq. (2) to approximate relative global spectral irradiances within simulated canyons.

### 2.2.1 DGR—Model 1

Our first theoretical approach attempts to reduce the number of atmospheric parameters required by SMARTS. The following section shows that the DGR is only affected by Rayleigh scattering, ozone absorption and aerosol scattering:

In simplified calculations found in literature (Bird and Riordan 1986), the spectral diffuse component  $E_{d,F,\lambda}$  under a full sky view  $F$  is approximated as the sum of three subcomponents: i.e. the Rayleigh scattering diffuse component ( $E_{d,F,R,\lambda}$ ), the aerosol scattering diffuse component ( $E_{d,F,as,\lambda}$ ) and the ground reflectance backscattering ( $B_s$ ) component ( $E_{d,F,Bs,\lambda}$ ). It then follows that the diffuse component of global spectral irradiance may be expressed as:

$$E_{d,F,\lambda} = E_{d,F,R,\lambda} + E_{d,F,as,\lambda} + E_{d,F,Bs,\lambda} \quad (3.0)$$

For simplicity, the backscattered component will be implemented later via the *backscattering amplification factor* (BAF) proposed in the SMARTS algorithm (Gueymard 1995). For now, the *sky-only* diffuse component is:

$$E_{d,F,\lambda} = E_{d,F,R,\lambda} + E_{d,F,as,\lambda} \quad (3.1)$$

The calculations found in the works of Bird and Riordan, later modified by Gueymard (1995), calculate each subcomponent of diffuse light, according to the following set of equations:

Consider the direct beam irradiance  $E_{b,F,\lambda}$  upon a horizontal, unobstructed plane ( $F$ ) as:

$$E_{b,F,\lambda} = E_{0n\lambda} T_{R\lambda} T_{o\lambda} T_{n\lambda} T_{g\lambda} T_{w\lambda} T_{a\lambda} \cos Z \quad (3.2)$$

where  $E_{0n\lambda}$  is the extraterrestrial spectral irradiance;  $T_{R\lambda}$  is the Rayleigh scattering transmittance;  $T_{o\lambda}$  is the ozone transmittance;  $T_{n\lambda}$  is the nitrogen transmittance;  $T_{g\lambda}$  is the mixed gases

transmittance;  $T_{w\lambda}$  is water vapour transmittance;  $T_{a\lambda}$  is aerosol transmittance; and  $Z$  is the solar zenith angle.

Following Gueymard (1995), the aerosol and Rayleigh sub-components of diffuse irradiance (Eq. 3.1) are approximated as:

$$E_{d,F,R\lambda} = F_R E_{0n\lambda} (1 - T_{R\lambda}^{0.9}) G_{o\lambda} T_{n\lambda} T_{g\lambda} T_{w\lambda} T_{aa\lambda} \cos Z \quad (3.3)$$

$$E_{d,F,as,\lambda} = F_a E_{0n\lambda} (1 - T_{as\lambda}) T_{R\lambda} G_{o\lambda} T_{n\lambda} T_{g\lambda} T_{w\lambda} T_{aa\lambda} \cos Z \quad (3.4)$$

where  $F_R$  corresponds to the fraction of Rayleigh scattered radiation that is directed towards the ground,  $F_a$  is the fraction of aerosol scattered light directed towards the ground, and  $G_{o\lambda}$  is the effective ozone transmittance for diffuse radiation.  $T_{aa\lambda}$  is the aerosol transmittance due to aerosol absorption, and  $T_{as\lambda}$  is due to aerosol scattering.

Notice that, as in the SMARTS algorithm, an effective ozone transmittance ( $G_{o\lambda}$ ) is used for calculating the diffuse irradiance, instead of the standard ozone transmittance ( $T_{o\lambda}$ ). Previous models that did not consider this modification (Leckner 1978; Bird and Riordan 1986) reportedly returned underestimations of the diffuse irradiance reaching "several orders of magnitude, especially for large SZAs" (Gueymard 1995). In this work, we also incorporate the effective ozone transmittance as the ratio of effective-to-standard ozone transmittance.

Since our objective is to calculate the DGR, the number of atmospheric input parameters required can be reduced as follows:

$$\begin{aligned} \text{DGR or } \frac{\text{Diffuse}}{\text{Global}} &= \frac{E_{d,F,\lambda}}{E_{d,F,\lambda} + E_{b,F,\lambda}} = \frac{1}{\frac{E_{d,F,\lambda}}{E_{d,F,\lambda}} + \frac{E_{b,F,\lambda}}{E_{d,F,\lambda}}} \\ &= \frac{1}{1 + \frac{E_{b,F,\lambda}}{E_{d,F,\lambda}}} = \frac{1}{1 + \left[ \frac{E_{b,F,\lambda}}{E_{d,F,\lambda}} \right]} \end{aligned}$$

using Eq. (3.1):

$$= \frac{1}{\left[ \frac{E_{d,F,R\lambda}}{E_{b,F,\lambda}} + \frac{E_{d,F,as,\lambda}}{E_{b,F,\lambda}} \right]} \quad (3.5)$$

then using Eqs. (3.2) and (3.3):

$$\begin{aligned} \frac{E_{d,F,R\lambda}}{E_{b,F,\lambda}} &= \frac{F_R E_{0n\lambda} (1 - T_{R\lambda}^{0.9}) G_{o\lambda} T_{n\lambda} T_{g\lambda} T_{w\lambda} T_{aa\lambda} \cos Z}{E_{0n\lambda} T_{R\lambda} T_{o\lambda} T_{n\lambda} T_{g\lambda} T_{w\lambda} T_{a\lambda} \cos Z} \\ &= \frac{F_R (1 - T_{R\lambda}^{0.9})}{T_{R\lambda}} \frac{T_{aa\lambda}}{T_{a\lambda}} \frac{G_{o\lambda}}{T_{o\lambda}} \end{aligned} \quad (3.6)$$

also, using Eqs. (3.2) and (3.4):

$$\begin{aligned} \frac{E_{d,F,as,\lambda}}{E_{b,F,\lambda}} &= \frac{F_a E_{0n\lambda} (1 - T_{as\lambda}) T_{R\lambda} G_{o\lambda} T_{n\lambda} T_{g\lambda} T_{w\lambda} T_{aa\lambda} \cos Z}{E_{0n\lambda} T_{R\lambda} T_{o\lambda} T_{n\lambda} T_{g\lambda} T_{w\lambda} T_{a\lambda} \cos Z} \\ &= F_a (1 - T_{as\lambda}) \frac{T_{aa\lambda}}{T_{a\lambda}} \frac{G_{o\lambda}}{T_{o\lambda}} \end{aligned} \quad (3.7)$$

By substituting Eqs. (3.6) and (3.7) into Eq. (3.5), we have:

$$\text{DGR} = \frac{1}{1 + \left[ \frac{T_{aa\lambda} G_{o\lambda}}{T_{a\lambda} T_{o\lambda}} \left( \frac{F_R (1 - T_{R\lambda}^{0.9})}{T_{R\lambda}} + F_a (1 - T_{as\lambda}) \right) \right]} \quad (3.8)$$

Since  $T_{as\lambda} = T_{a\lambda} / T_{aa\lambda}$ , according to its definition (Gueymard 1995),

then  $T_{aa\lambda} / T_{a\lambda} = 1 / T_{as\lambda}$ :

$$\text{DGR} = \frac{1}{1 + \left[ \frac{1}{T_{as\lambda}} \frac{G_{o\lambda}}{T_{o\lambda}} \left( \frac{F_R (1 - T_{R\lambda}^{0.9})}{T_{R\lambda}} + F_a (1 - T_{as\lambda}) \right) \right]} \quad (3.9)$$

Finally, the equation for calculating the DGR, including the backscattering amplification factor (BAF), is:

$$\text{DGR} = \frac{1}{1 + \left[ \text{BAF} \times \frac{1}{T_{as\lambda}} \frac{G_{o\lambda}}{T_{o\lambda}} \left( \frac{F_R (1 - T_{R\lambda}^{0.9})}{T_{R\lambda}} + F_a (1 - T_{as\lambda}) \right) \right]} \quad (3.10)$$

The BAF (Gueymard 1995 p.32) is a dimensionless quantity with values  $>1$  that represents the increase of downwelling radiation due to radiation reflected from the ground and then further backscattered (towards the ground) by the atmosphere. The BAF is a function of the sky reflectance, the ground reflectance (urban concrete in this case) and the direct-to-diffuse irradiance ratio (see Table 1).

The model then requires only three variables: solar zenith angle (SZA), columnar ozone (in atm-cm) and aerosol (expressed as aerosol optical thickness at 500 nm or  $\text{AOT}_{500\text{nm}}$ ). Current and historic ozone and aerosol contents in the atmosphere are available globally from satellite sources (Remer et al. 2005) or at limited locations from ground-based measurements.

The individual equations required for the terms in Eq. (3.10) are summarised in Table 1.

## 2.2.2 DGR—Model 2

Models with fewer mathematical computations are advantageous in studies where repetitive calculations are required, as here for multiple times of day and year. Although simpler than full radiative transfer models, the previously presented approach can still be numerically intensive when used multiple times. As an alternative method, Eq. (4) is proposed which was obtained empirically to resemble the DGR modelled with SMARTS for the in situ conditions

Fast calculations of the spectral diffuse-to-global ratios

**Table 1** Equations for the terms expressed in Eq. (3.10)

Term	Expression	Notes
Atmospheric air mass	$M = \sqrt{\left(\frac{r}{\cos Z}\right)^2 + 2r + 1} - \frac{r}{\cos Z}$	$r = \frac{\text{Radius of the Earth}}{\text{Height of the atmosphere}}$ $Z = \text{solar zenith angle (SZA)}$
Rayleigh scattering transmittance*	$T_{R\lambda} = \sqrt{\exp\left(-\frac{((360^\circ) \times (M))}{\lambda}\right)}$	$\lambda = \text{wavelength in (nm)}$
Ozone spectral absorption* ( $A_{O\lambda}$ )	$A_{O\lambda \text{Hartley}} = 1140 \exp(-1.5E-3 \times (\lambda - 253.65)^2)$ $A_{O\lambda \text{Huggins}} = A_{O\lambda \text{Hartley}} \times \frac{1}{2} \exp\left((2.7E-4) \times (\lambda - 253.65)^2\right)$ $A_{O\lambda} = \max(A_{O\lambda \text{Hartley}}, A_{O\lambda \text{Huggins}})$	$A_{O\lambda \text{Hartley}} = \text{empirical fit to the Hartley absorption band}$ $A_{O\lambda \text{Huggins}} = \text{empirical fit to the Huggins band absorption}$ From Molina and Molina (1986)
Ozone optical thickness	$\tau_{O\lambda} = u_{O\lambda} A_{O\lambda}$	$u_{O\lambda} = \text{atmospheric ozone column (atm-cm)}$
Ratio of effective-to-standard ozone transmittance*	$\frac{T_{\text{eff}}}{T_{\text{std}}} \approx 10^{\tau_{O\lambda} \left(\frac{1}{\cos Z} - \frac{1}{\cos 0^\circ}\right)}$	From Gueymard (1995)
Aerosol optical thickness	$\tau_{A\lambda} = \beta \lambda^{-\alpha}$	$\alpha = 1.02 \beta - \frac{A_{\text{max}}}{\ln(10)}$
Aerosol scattering transmittance	$T_{\text{as}\lambda} = \exp(-W_0 \times \tau_A \times M)$	$W_0 = \text{single scattering albedo}$ $\tau_A = \text{aerosol optical thickness}$
Average ground reflectance (concrete)	$\rho g \lambda = a\lambda^6 + b\lambda^5 + c\lambda^4 + d\lambda^3 + e\lambda^2 + f\lambda + g$	$a = -3.54E-15; b = 1.05E-11; c = -1.272E-08;$ $d = 8.08E-06; e = -2.79E-03; f = 5.02E-01;$ $g = -3.6E+01$ Empirically fit from averaged local ground reflectance SMARTS outputs at different SZAs
Sky reflectance	$(\rho s \lambda) = \text{Eq. (3.9)}$	See Eqs. (3.1) to (3.9) (sky-only DGR)
direct-to-diffuse ratio	$\frac{E_{b, \tau, \lambda}}{E_{d, \tau, \lambda}} = \frac{1}{\frac{1}{\tau_{\text{as}\lambda}} \tau_{O\lambda} \left[ \left( \frac{F_R(1 - \tau_{R\lambda}^{0.99})}{\tau_{R\lambda}} \right) + (F_d(1 - T_{\text{as}\lambda})) \right]}$	Deduced using a rationale similar to that used in Eqs. 3.5–3.10
Backscattering amplification factor	$\text{BAF} = 1 + \left[ \rho g \lambda \times \rho s \lambda \times \frac{\text{Direct}}{\text{Diffuse}} \right]$	$\rho g \lambda = \text{ground reflectance}$ $\rho s \lambda = \text{sky reflectance}$

Each individual term either is a standard equation (e.g. atmospheric air mass), or comes from Gueymard (1995), or is, in the case of those marked with \*, a parameterisation to fit the data from the indicated author: Molina and Molina (1986) and Gueymard (1995)

shown in Fig. 1. Although this empirical fit may be limited to ozone and aerosol values for local conditions, its simple form makes it computationally fast.

$$\text{DGR} = 1 - \exp \left[ \left( \frac{280}{\lambda} \right)^{4 \times 0.79} \times \left( 1 - \left( \frac{255}{\lambda} \right)^{10} \right)^{1 - \tan(Z)} \times \frac{1}{\cos Z} \right] \quad (4)$$

where  $\lambda$  is the wavelength, and  $Z$  is the SZA.

Equation (4) includes terms that approximate the effects of Rayleigh scattering, the effective ozone transmittance and the air mass of the direct beam path. Note that this model is restricted to the specific atmospheric contents of ozone (0.31 atm-cm) and aerosol ( $\text{AOT}_{500\text{nm}} = 0.1$ ) which were used to model Fig. 1 with SMARTS. An  $\text{AOT}_{500\text{nm}}$  of 0.1 represents a rather clean atmosphere not easily found in many urban locations worldwide. However, in situ conditions had to be modelled in order to conduct the comparisons against spectral measurements that will be shown in section 2.3.3.

## 2.3 Model validations

### 2.3.1 Comparisons against SMARTS

The intention for both proposed approaches was to reproduce the spectral DGRs found at different SZAs under a full sky view, as modelled by SMARTS (Fig. 1) before applying the DGRs to modelled canyon irradiances. Most input parameters in the SMARTS model corresponded to default library parameters for the selected atmosphere (MLS: Mid-Latitude Summer). Ozone and aerosol input contents were measured on 7 June 2013 at the Pariser Building, University of Manchester, UK: ozone measurements were taken with a Brewer spectrophotometer (Smedley et al. 2010) with readings of 310.7DU or 0.31 atm-cm.  $\text{AOT}_{500\text{nm}}$  of 0.1 was obtained from a MODIS satellite image, corresponding to the same day (NASA LAADS 2013). Global and diffuse spectral irradiances were calculated using SMARTS at ten different SZAs from  $0^\circ$  to  $90^\circ$  and from these, the DGR was obtained. The same inputs were used for Eq. (3.10). Equation (4) was also solved for the 10 SZAs. Proportional errors in the outputs

from Eqs. (3.10) and (4) with respect to those from the SMARTS model are presented in section 3.

### 2.3.2 Sensitivity analyses for changing ozone and aerosol conditions

The theoretical sensitivity to changes in aerosol and ozone atmospheric contents was modelled with SMARTS at a constant SZA of  $32.2^\circ$ , corresponding to 1125 UTC on 7 June 2013, Manchester  $53.47^\circ\text{N}$ ,  $2.23^\circ\text{W}$ . The first approach (Eq. 3.10) allows parameterization of ozone and aerosol loading. We therefore compared the modelled DGR with SMARTS and Eq. (3.10), with five different ozone columns (from 0.2 to 0.4 atm-cm) and aerosol loadings ( $\text{AOT}_{500\text{nm}}$  0.05 to 2.5). Equation (4) was also compared against the SMARTS outputs under the same sets of atmospheric constituents. Because Eq. (4) remained unchanged, results illustrate the restrictions of this second approach.

### 2.3.3 Empirical validations of canyon irradiance calculations

The outcomes of either DGR Eqs. (3.10 or 4) can be substituted into Eq. (2) to calculate relative street canyon irradiances. In order to validate the proposed canyon irradiances, a series of experiments were conducted with simulated horizon obstructions. To measure global horizontal spectral irradiance (in  $\text{W m}^{-2} \text{ nm}^{-1}$ ), a Metcon single-grating diode array spectroradiometer, with a 280 to 700 nm wavelength range was used. The instrument was temperature stabilized and calibrated with a NIST 1000 W FEL lamp at 0.5 m distance (Bais et al. 2005). Stray light corrections were applied following (Kreuter and Blumthaler 2009). In order to simulate horizon obstructions, a 20-cm-thick polyurethane foam block was manually positioned above the entrance optics for a period of 10 s, during which a series of spectra were taken and then averaged. Fisheye digital photographs of the obstructions were taken during the same period using an orthographic mini fisheye lens (Sumlung, model: SL-FE12) attached to a Nokia E5 mobile phone camera.

Three simulated canyons were tested, labelled here as C1, C2 and C3 (Fig. 2). In C1, a part of the circumsolar region was obstructed but left the solar disk visible to the input optics. In C2, the anti-solar region was blocked, and in C3 direct irradiance along with the circumsolar region was obstructed. Between each simulated obstruction, a full sky view measurement was obtained. This sequence of measurements was repeated 25 times between 1100 UTC and 1230 UTC 7 June 2013 at the Manchester surface radiation site (Pariser Building, University of Manchester). The nearly cloudless conditions and the proximity to solar noon resulted in consistent measurements during the experimental period, for example, measurements of canyon C1 exhibit a standard deviation of 1.8 % (spectrally integrated

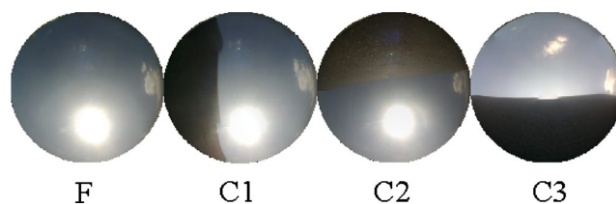


**Fig. 2** Orthographic fisheye images of four sky views: Full,  $\text{SVF}=0.99$ ,  $S_{\text{bin}}=1$ : Full sky view with no simulated obstructions. C1,  $\text{SVF}=0.54$ ,  $S_{\text{bin}}=1$ : Simulated canyon obstructing the circumsolar region. C2,  $\text{SVF}=0.41$ ,  $S_{\text{bin}}=1$ : Simulated canyon obstructing the sky opposite to the sun. C3,  $\text{SVF}=0.42$ ,  $S_{\text{bin}}=0$ : Simulated canyon obstructing the solar disk and the circumsolar region. The sky view factor (SVF) was calculated using the RayMan software

irradiance across the wavelength range 305 to 700 nm). In contrast measurements with the C1 obstruction were 10.1 % lower than the corresponding full sky view measurement.

Since replicas were consistent, a representative measurement set is analysed in section 3, corresponding to 1125 UTC. The SVFs were calculated using the RayMan software (Matzarakis et al. 2010), without the cosine law, since the fisheye lens had an orthographic projection. Figure 2 shows the acquired images and their corresponding SVFs.

Notice in Fig. 2 that the SVF of canyon C1 is larger than that of canyon C2; however, part of the bright circumsolar region is blocked in canyon C1. Also part of the circumsolar region is visible in canyon C3. After the SVFs were obtained, spectral global irradiances were calculated for the four sky views shown in Fig. 2. In order to calculate spectral irradiance values for each canyon, the DGR was solved using Eqs. (3.10) and (6.4), and then these values were substituted in Eq. (2) to obtain canyon global irradiance on the basis of full sky global measurements.

## 3 Results

### 3.1 Modelling the DGR under a full sky view

Figure 3a, b shows the solutions from Eqs. (3.10) and (4), respectively, under a full sky view for wavelengths from 280 to 700 nm at ten different SZAs ( $0$  to  $90^\circ$ ). Notice their similarities to the output from SMARTS in Fig. 1.

Figure 3a, b closely resembles the effects of Rayleigh scattering assigning lower diffuse proportions to larger wavelengths. They also simulate the effects of ozone absorption on the diffuse component at the shorter ultraviolet wavelengths. Additionally, the effects of aerosol scattering and changing SZA are also simulated which strongly increase the diffuse components of longer wavelengths (600 to 700 nm) at higher solar zenith angles.

Fast calculations of the spectral diffuse-to-global ratios

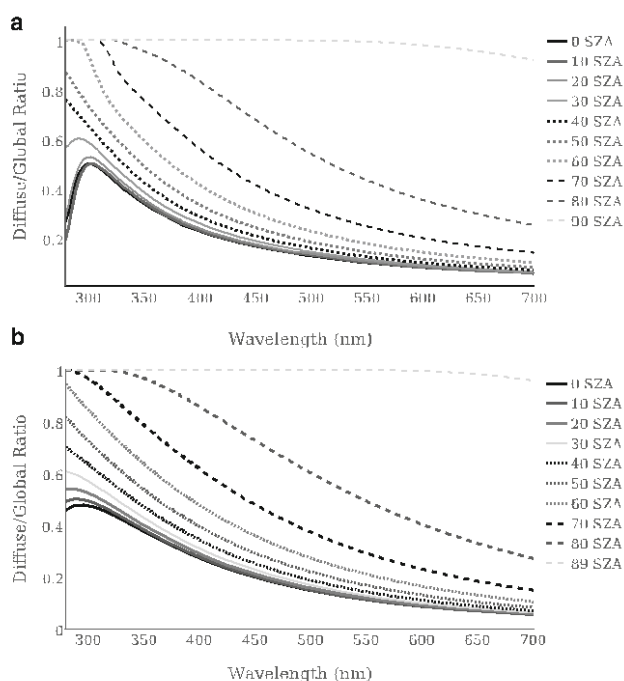


**Fig. 3** Modelled curves of spectral DGRs for different SZAs, using Eqs. (3.10) (Panel a) and (4) (Panel b). Note that Panel b has a limit of solar zenith angles of  $<90^\circ$ ; this is because of the use of a tangent function (see Eq. 4)

### 3.2 Comparisons against SMARTS

The differences between Figs. 1 and 3a, b were quantified by their proportional error, that is:

$$\text{Proportional Error} = \frac{\text{DGR}_{\text{Eq. 3.10 or 4}} - \text{DGR}_{\text{SMARTS}}}{\text{DGR}_{\text{SMARTS}}}$$

These proportional errors are shown in Fig. 4a, b, respectively, for Eqs. 3.10 and 4:

In Fig. 4a, b, positive errors imply an overestimation in comparison to the SMARTS modelled values, and negative errors imply an underestimation. The proportional errors for wavelengths between 300 and 600 nm are generally below 0.15, increasing towards 0.2 for wavelengths  $>600$  nm. For ultraviolet wavelengths below 300 nm, errors increase dramatically although there is very little solar radiation at these wavelengths. It must be noted that these tests were performed using constant values of atmospheric ozone (0.3 atm-cm) and aerosol ( $\text{AOT}_{500\text{nm}}$  0.1). The suitability of the models for different environments is assessed next.

### 3.3 Sensitivity analyses for changing ozone and aerosol conditions at a constant SZA

Sensitivity analyses against SMARTS models under varying aerosol and ozone conditions were performed for both proposed

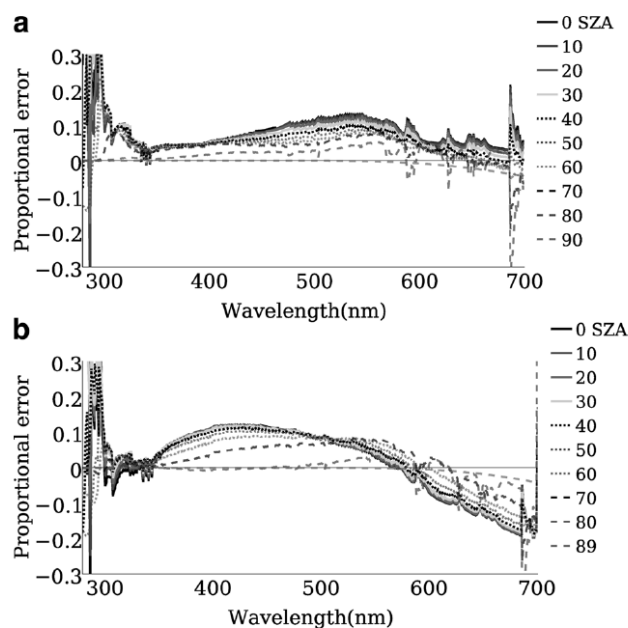


**Fig. 4** Proportional errors at different SZAs of spectral DGRs using Eqs. (3.10) (Panel a) and (4) (Panel b), when compared against the SMARTS outputs for the same local atmospheric conditions (ozone 0.31 atm-cm and 0.1  $\text{AOT}_{500\text{nm}}$ )

models, and results, expressed using the proportional error defined earlier, are shown in Fig. 5a–d.

Note how Eq. (3.10) returned proportional errors smaller than  $\pm 0.2$  with changing aerosol and ozone conditions (Fig. 5a, b). This is made possible because Eq. (3.10) accepts ozone and aerosol values as input parameters. Nonetheless, Eq. (3.10) apparently shows a trend of increasing error with increasing atmospheric aerosol loading. On the other hand, Eq. (4) has a fixed form (suitable for average atmospheric conditions) but that will return larger errors for extreme conditions (Fig. 5c, d). Despite this, except for turbid conditions and long wavelengths, the uncertainties are within 20 % of the SMARTS modelled data.

### 3.4 Irradiance measurements in simulated canyons

The effects of horizon obstructions are illustrated in Fig. 6, which show the relative canyon irradiance as the ratio of canyon to full sky measurements for each canyon. Relative canyon irradiance is shown for three simulated canyons (C1 to C3, see Fig. 2). Canyons C1 and C2 had a visible direct solar beam, and simulated obstructions blocked different sections of the diffuse irradiance. In canyon C1, the circumsolar section was obstructed, whereas in canyon C2, the anti-solar region was obscured (leaving the circumsolar completely visible). Note that irradiance received at C2 is slightly larger than that of C1. In turn, in canyon C3, the direct solar beam was blocked along with the circumsolar region. The spectral

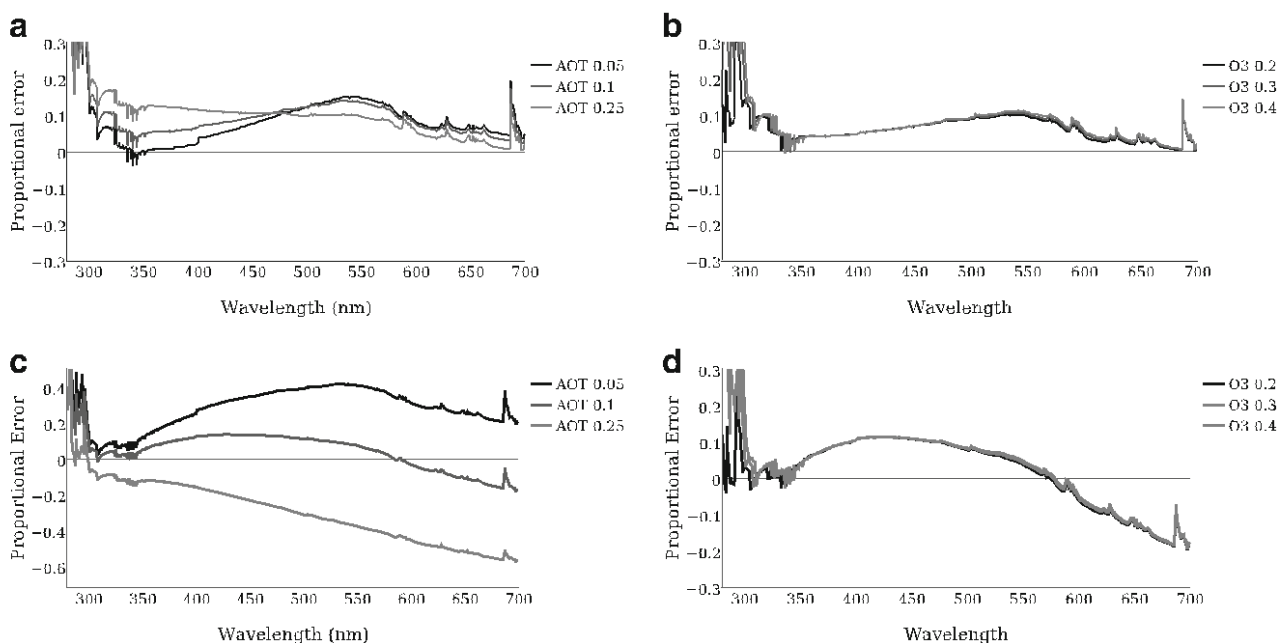


**Fig. 5** Results of the sensitivity analyses show errors found when comparing the SMARTS-calculated DGR ratios against Eq. (3.10) (Panels a and b) and Eq. (4) (Panels c and d). Panels a and c show the proportional errors found at different aerosol levels ( $AOT_{500nm}$ ), with

constant ozone of 0.3 atm-cm. Panels b and d show the proportional error found at different ozone levels ( $O_3$ ) with constant  $AOT_{500nm}$  at 0.1. All variations were modelled with a constant SZA of  $32^\circ$

pattern of relative canyon irradiance for canyon C3 is the inverse of C1 and C2 due to the blocking of the direct solar beam.

### 3.5 Validation of canyon irradiance models

Figure 7 shows a comparison between modelled and measured relative canyon irradiances for canyons C1 to C3. The models for canyons C1 and C2 predicted an inverse relationship regarding the brighter of these two canyons, i.e. C1 was assigned a larger irradiance than C2 due to their respective sky view factors. However, measurements showed the opposite

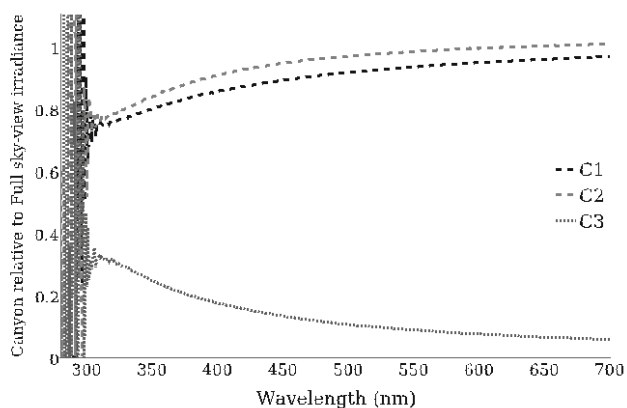


**Fig. 6** Measurements of relative canyon spectral irradiances. Relative canyon irradiances are the ratio of canyon/full sky measured irradiances, for the three simulated canyons (C1, C2 and C3)

pattern (see Figs. 6 and 7). Nonetheless, Fig. 8 shows that the differences between models and measurements are generally  $<20\%$ , with canyon 3 presenting the greatest challenge to the models.

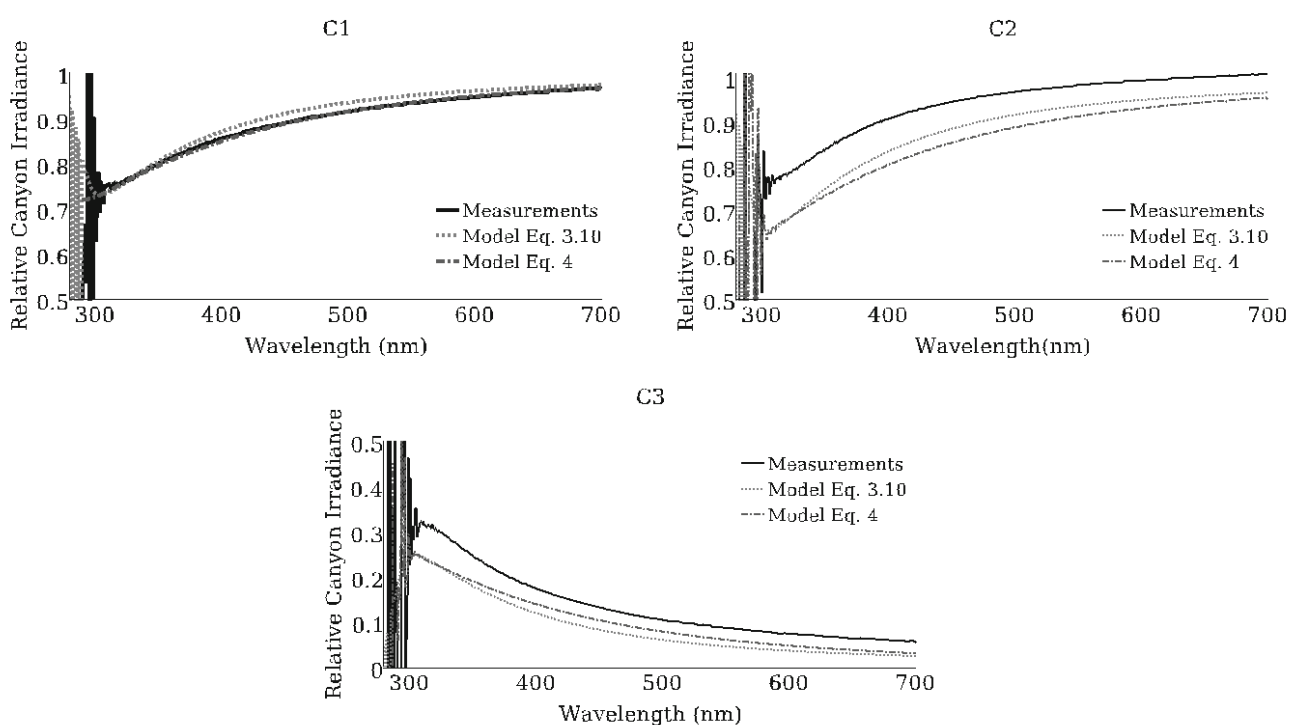
Proportional errors of both models against measurements are shown in Fig. 8a–c.

Figure 8 shows that errors are significantly higher for canyon C3 where the direct solar beam is blocked (proportional errors values of 0.2 to 0.5). Since global irradiance in canyon C3 was entirely comprised of scattered radiation (i.e. diffuse irradiance), the errors in the calculations of diffuse irradiance are more obvious. The errors in the models proposed here are mainly due to the assumptions and simplifications made in relation to the diffuse component, in particular neglecting the anisotropy of diffuse irradiance. Additionally, simplifications for the calculations of Rayleigh scattering, ground albedo and the ozone and aerosol transmittances will also affect the diffuse component. In canyons C1 and C2, however, the small errors in the diffuse irradiance calculations are less noticeable due to the major contribution to global irradiance of the direct beam.

## 4 Discussion

Equations (3.10) and (4) take a measured full sky global irradiance as their main input parameter, and their only purpose is to estimate the fraction of irradiance that would correspond to

Fast calculations of the spectral diffuse-to-global ratios



**Fig. 7** Model validations for the three simulated canyons (C1 to C3). Relative irradiances calculated with Eqs. (3.10) and (4) irradiances (*black lines*), all relative to full sky view. Panel C1: Canyon 1 (blocking circumsolar region). Panel C2: Canyon 2 (blocking the sky opposite to the sun), Panel C3: Canyon 3 (blocking the solar disk and circumsolar region)

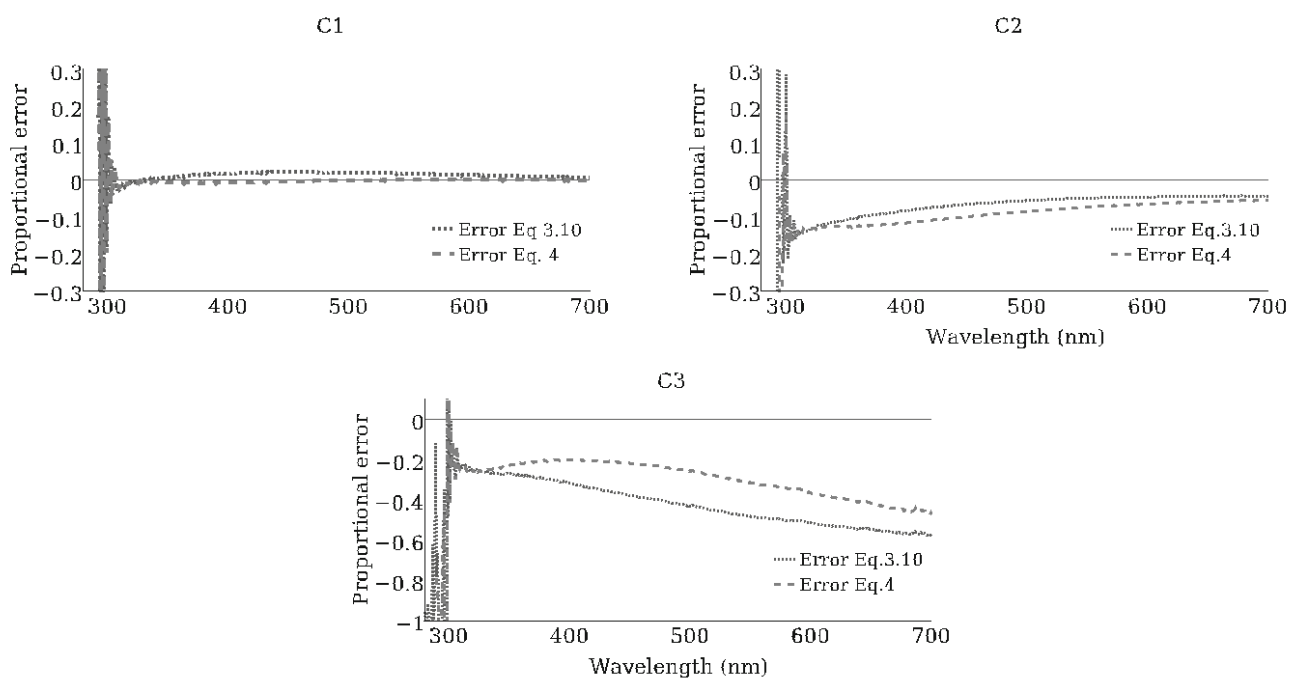


**Fig. 8** Proportional errors of both proposed models, when comparing measured versus modelled relative canyon irradiance values. Panel C1: Canyon C1 (blocking circumsolar region). Panel C2: Canyon C2 (blocking the sky opposite to the sun). Panel C3: Canyon C3 (blocking the solar disk and circumsolar region)

the diffuse component. This is in order to partition global irradiance for its analysis within a street canyon projected profile.

#### 4.1 DGRs for a full sky view

When models were compared against SMARTS, under typical aerosol and ozone conditions, proportional errors of both proposed models are below absolute values of 0.2 for all solar zenith angles (Fig. 4a, b). These values of proportional error (or 20 % in percentage terms) have been considered by other authors a good estimation in studies of human exposure (Vernez et al. 2015). It was observed, however, that errors in the model outputs have a tendency to increase towards both extremes of the spectral region considered (280–700 nm); this is potentially due to simplifications in parameterising atmospheric effects. For example, in Eq. (3.10), the ozone absorption empirical tables, used by SMARTS, were substituted by a polynomial fit to the ozone absorption reported by Molina and Molina (1986). Errors below 300 nm may also be due to our proposed fit for the ratio between effective and standard ozone transmittance (see Table 1). We found that our proposed equation for the ratio of effective-to-standard ozone transmittance is extremely sensitive to small variations in its parameters and in turn has strong effects on the shorter wavelength irradiance (below 300 nm). It was also found that the backscattering amplification factor (BAF) calculated underestimates the BAF proposed by Gueymard (1995 p32.) for shorter wavelengths. For applications where the small amounts of radiation at UV wavelengths are important, corrections to this particular equation may result in better estimation of the DGR below 300 nm.

On the other hand, errors found in longer wavelengths (towards 700 nm) may be better explained by the simplifications made to the aerosol transmittances. One of the parameters for calculating aerosol scattering transmittance is the single scattering albedo. The single scattering albedo ( $W_0$ ) is a complex function of wavelength and relative humidity of the atmosphere (Gueymard 1995; Redemann et al. 2001; Collaud Coen et al. 2004). However, for simplicity, a single value of 0.85 was used. Additionally, the SMARTS algorithm for aerosol transmittances considers two values for the  $\alpha$  Ångström parameter (see Eq. for aerosol optical thickness in Table 1) assigned to two different sections of the spectrum (i.e.  $\lambda < 500$  nm and  $\lambda \geq 500$  nm). In this work, however, the use of two different alpha values resulted in mismatching curves for the two spectral regions. In recent studies (Jaus et al. 2012), a single  $\alpha$  value is also used for the calculations. According to Jaus et al.,  $\alpha$  values circa 1.5 are the most frequent from 612 sites in the AERONET database. Thus, a single  $\alpha$  value of 1.5 has been used in this work.

#### 4.2 Sensitivity analyses for changing ozone and aerosol conditions

Both approaches bring advantages and disadvantages for modelling DGRs. Our first approach (Eq. 3.10) provided means for including values of ozone and aerosol atmospheric contents. For this reason, the errors modelled remained below 0.2 (Fig. 5a, b) when compared to SMARTS under different atmospheric conditions. On the other hand, the second approach (Eq. 4) provides an extremely simple calculation of the spectral DGRs. However, as shown in Fig. 5c, d, it may only be suitable for ozone columns and aerosol loadings close to those under which it was derived (as is usual for empirically derived applications) since errors tend to increase with extreme atmospheric contents. This limitation may still prove to be an advantageous trade-off for a simple calculation that requires no further knowledge of the state the atmosphere.

One application of this work would be to create models of human exposure to erythemally weighted UV radiation in the streets, in which case it would be advantageous to reduce errors in the UV as much as possible. However, the peak of the erythemal solar spectrum is at approximately 310 nm, and the action spectrum extends well into the UV-A where model results have smaller uncertainties. Therefore, the models presented here should still be suitable for fast and simple calculations in realistic studies of human exposure to erythemal radiation. The following section uses the calculated DGRs in order to approximate spectral irradiances under obstructed views. This type of model will be more representative of human exposure than the unobstructed sky view data that is frequently available.

#### 4.3 Irradiance measurements in simulated canyons

Obstructions of diffuse radiation have a greater effect on the shorter wavelengths due to Rayleigh and aerosol scattering. Irradiance received at C2 is slightly larger than that of C1 (Fig. 6) despite C2 having a smaller SVF (SVF=0.41 in C2 vs 0.54 in C1, see Fig. 2). This is explained by the fact that the brighter circumsolar region was completely visible in C2, whereas in C1, it was partially blocked. Further, due to the spectrally dependent radiative transfer of the direct solar beam, blocking the direct beam has a smaller effect on global irradiance at short wavelengths than it has at longer wavelengths. The spectral pattern of relative canyon irradiance is inversely proportional to wavelength in canyon C3 due to the blocking of the direct solar beam.

#### 4.4 Spectral irradiance calculations in simulated canyons

Figure 7a–c shows how the modelled canyon irradiance values closely resemble the observed measurements. Also notice how the spectral dependence of the effects of obstructions



is shown by the simulated canyons measurements, i.e. in canyons C1 and C2, the short wavelength end of the spectrum has a lower relative canyon irradiance when only diffuse radiation is blocked due to the large proportions of such wavelengths found in the diffuse component. The third canyon (C3) where only diffuse radiation is available illustrates the spectral effects of Rayleigh and aerosol scattering, i.e. shorter wavelengths exhibit relatively higher intensities (nearly 40 % of the irradiance under full sky view).

In the canyon models, the SVF was the governing aspect affecting diffuse irradiance, whereas the visibility of the solar disk was determined by the geometric position of buildings with respect to the sun's position. The diffuse irradiance was considered isotropic and was not affected by the orientation of the canyon. Although the absolute uncertainties are relatively small, the results show that this assumption (an isotropic diffuse component) gave larger proportional errors for canyons C2 and especially C3. For these simple models, the larger SVF should have the largest estimated irradiance. However, measurements showed that when the SVFs are very similar, the irradiance is greater when the circumsolar region is fully visible (C2) than when it is partially blocked (C1)—even when the SVF was slightly smaller in C2. The circumsolar radiation illustrates the greatest anisotropy in the diffuse radiation and reveals the weakness in the isotropic assumption. Similarly, canyon C3—with the direct irradiance blocked—still showed a bright circumsolar region that may have contributed to the larger-than-expected observed irradiances.

A further factor, not considered by the current models, is the reflectivity of horizon obstructions. Reflections may be particularly important when a horizon obstruction is located opposite to the direct solar beam, and it is irradiated by it; therefore, it will potentially reflect radiation towards the observer in the canyon. Notice in Fig. 7 (middle panel) that for wavelengths  $>620$  nm, the relative canyon irradiance is larger than 1, meaning that canyon irradiance is larger than the full sky irradiance. The present models do not consider any reflections from wall surfaces. In principle, given the requirement for a fisheye view of the canyon as prerequisite, wall reflections could be added where indicated by the architecture. Methods for assessing wall reflections include Monte-Carlo ray tracing and radiosity finite-element applications (Robinson and Stone 2005). However, these methods add a complexity to the models that is at odds with the goal of fast calculations.

State-of-the-art techniques for fast calculations of spectral irradiance have been developed for the SMARTS algorithm (Jaus et al. 2012); however, they require a multi-core architecture for the parallel computation of the algorithm. These techniques have been designed for parallel calculations of large sets of solar cells, similar to what would be required for modelling the spatial and temporal variation of ground solar irradiance within large regions. If multi-core hardware facilities are available, these

parallelized versions of SMARTS represent a suitable option for fast calculations while retaining the high accuracy of the SMARTS model. The present approach may, in turn, represent an acceptable trade-off between accuracy and computational performance with low hardware requirements for our purpose that is calculating the diffuse-to-global ratio (DGR) as an aid to partition global irradiance into its direct and diffuse components. Our simplifications consist firstly of the exclusion of certain variables from the calculations (see Eqs. 3.6 and 3.7). Additionally, compressed empirical equations are included for ozone absorption and the backscattered component of the diffuse radiation (see Table 1). Such simplifications certainly limit the scope of the model and, more importantly, introduce discrepancies when compared against the full SMARTS model. Discrepancies (measured as proportional errors) are shown to illustrate the trade-off between reducing computational demand at the expense of model accuracy. Further modifications can be made to the equations that may increase accuracy but can potentially increase computational demand. The choice of model might also depend upon the accuracy required of the output. One application we have mentioned is that of human exposure where the infinite vagaries of human behaviour far exceed the uncertainties in the radiation model, yet for which even a simplified canyon model is far more realistic for the radiation environment than a flat horizontal plane.

## 5 Conclusions

The proposed models generated acceptable approximations of the spectral DGRs when compared against a well-validated model (SMARTS) for the specific atmospheric conditions studied here. Overall discrepancies (proportional errors) between SMARTS and both compressed models (under cloudless conditions and a full horizon) were below absolute values of 0.2 (or 20 %) for a modelled atmosphere with a total ozone column of 0.31 atm-cm and 0.1 AOT<sub>500nm</sub>. The first compressed model accepted aerosol and ozone readings as input parameters, therefore it returned smaller discrepancies against SMARTS (proportional errors below 0.2), even in the sensitivity analyses with changing ozone and aerosol contents. However, a general tendency was observed of increasing discrepancies with increasing aerosol contents (proportional errors changing from  $<0.1$  at 0.1 AOT<sub>500nm</sub> to  $>0.1$  at 0.25 AOT<sub>500nm</sub>). Such discrepancies may arise from the empirical fits and simplifications used to represent aerosol transmittances. Larger wavelength ranges ( $>500$  nm) were more affected by such simplifications, showing the larger discrepancies (absolute proportional errors circa 0.2). The second model had empirically fitted constants which did not accept variations in ozone and aerosol; this model showed even larger discrepancies with changing ozone and aerosol conditions (proportional errors

as large as  $-0.6$ ), thus illustrating the limitation of empirical fits to specific local atmospheric conditions. Further improvements of these issues may include better representations of ozone and aerosol atmospheric contents in the equations, but they should be accompanied by a cost-benefit analysis for the computational efficiency of the algorithms. The canyon irradiance models were compared against measurements under simulated canyons and returned good approximations when the sun was visible within the obstructed views (with absolute proportional errors approximately below 15 % in canyons C1 and C2). However, when the sun was blocked by an obstruction (canyon C3), relative canyon irradiances were underestimated by nearly 40 %. This is partially explained by the relative measurement of discrepancies as proportional errors, which tend to increase for small absolute quantities. However, the effect of the anisotropic diffuse irradiance remains to be studied when bright parts of the circumsolar region are visible, even when the direct solar beam is blocked.

In addition to sources of errors in the models, those arising from the assumption of an isotropic diffuse component were made evident when testing the effect of blocking the circumsolar (C1) or the anti-solar (C2) regions. In this case, the anisotropy of diffuse irradiance has an effect that was ignored by the models but could be measured with the instruments. For this reason, canyon C2 underestimates the measured spectral irradiance (proportional errors circa  $-0.1$ ). Unfortunately, so far the anisotropy of diffuse irradiance is complex to model and is computationally intensive. Consequently, it is likely that including such parameters in the models would not currently be cost-effective. In addition, the anisotropy of diffuse light is relevant for cloudless skies but becomes far more complex with broken clouds and can tend more towards isotropy in dense overcast conditions. As a general conclusion, it can be said that the computationally efficient methods proposed here allow reasonable approximations of street canyon global spectral irradiances, with minimum input data. The approximations generated by these models will be of most utility for largescale studies, for example, when trying to assess human exposure to UV in street canyons for large populated cities.

**Acknowledgments** This work was generously funded by the Mexican Council for Science and Technology (CONACyT) (grant reference: 214428). We thank Dr Richard Kift from the Centre for Atmospheric Sciences, University of Manchester for his help in obtaining the global spectral measurements.

## References

- Badarinath KVS, Kharol SK, Kaskaoutis DG, Kambezidis HD (2007) Influence of atmospheric aerosols on solar spectral irradiance in an urban area. *J Atmos Solar-Terrestrial Phys* 69:589–599. doi:10.1016/j.jastp.2006.10.010
- Bais A, Blumthaler M, Webb A, et al. (2005) Intercomparison of solar UV direct irradiance spectral measurements at Izana in June 2005. *Optics & Photonics 2005*. Int Soc Opt Photon. p 588609
- Benger SN, Zhou S, Guan H (2014) A dynamic solar irradiance model for assessing solar PV power generation potential in urban areas. *Green Energy for Sustainable Development (ICUE), 2014 International Conference and Utility Exhibition on*. IEEE, pp 1–4
- Bird RE, Riordan C (1986) Simple solar spectral model for direct and diffuse irradiance on horizontal and tilted planes at the earth's surface for cloudless atmospheres. *J Clim Appl Meteorol* 25: 87–97
- Carrasco-Hernandez R, Smedley AR, Webb AR (2015) Using urban canyon geometries obtained from Google Street View for atmospheric studies: potential applications in the calculation of street level total shortwave irradiances. *Energy Build* 86:340–348
- Collaud Coen M, Weingartner E, Schaub D et al (2004) Saharan dust events at the Jungfraujoch: detection by wavelength dependence of the single scattering albedo and first climatology analysis. *Atmos Chem Phys* 4:2465–2480
- De Carvalho AM, Sanches L, de Souza NJ, Silva VAM (2013) Effects of sky conditions measured by the clearness index on the estimation of solar radiation using a digital elevation model. *Atmos Clim Sci* 3: 618–626
- Eeftens M, Beekhuizen J, Beelen R et al (2013) Quantifying urban street configuration for improvements in air pollution models. *Atmos Environ* 72:1–9. doi:10.1016/j.atmosenv.2013.02.007
- Grimmond CSB, Potter SK, Zutter HN, Souch C (2001) Rapid methods to estimate sky-view factors applied to urban areas. *Int J Climatol* 21:903–913
- Gueymard C (1995) SMARTS2, simple model of the atmospheric radiative transfer of sunshine: algorithms and performance assessment. Florida Solar Energy Center. Florida Solar Energy Center, Cocoa
- Holmer B, Thorsson S, Eliasson I (2007) Cooling rates, sky view factors and the development of intra-urban air temperature differences. *Geogr Ann Ser A, Phys Geogr* 89:237–248. doi:10.1111/j.1468-0459.2007.00323.x
- Hu B, Wang Y (2013) Comparison of multi-empirical estimation models of photosynthetically active radiation under all sky conditions in Northeast China. *Theor Appl Climatol* 1–11
- Jaus J, Gueymard CA, Dimroth F, et al. (2012) Generalized spectral performance evaluation of multijunction solar cells using a multicore, parallelized version of SMARTS. *AIP Conf Proc-Am Inst Phys*. p 122
- Kaskaoutis DG, Kambezidis HD, Tóth Z (2007) Investigation about the dependence of spectral diffuse-to-direct-beam irradiance ratio on atmospheric turbidity and solar zenith angle. *Theor Appl Climatol* 89:245–256
- Kaskaoutis DG, Kambezidis HD, Kumar Kharol S, Badarinath KVS (2008) The diffuse-to-global spectral irradiance ratio as a cloud-screening technique for radiometric data. *J Atmos Solar-Terrestrial Phys* 70:1597–1606. doi:10.1016/j.jastp.2008.04.013
- Krayenhoff ES, Christen A, Martilli A, Oke TR (2014) A multi-layer radiation model for urban neighbourhoods with trees. *Boundary-Layer Meteorol* 151:139–178
- Kreuter A, Blumthaler M (2009) Stray light correction for solar measurements using array spectrometers. *Rev Sci Instrum* 80:96108
- Kreuter A, Buras R, Mayer B et al (2014) Solar irradiance in the heterogeneous albedo environment of the Arctic coast: measurements and a 3-D-model study. *Atmos Chem Phys Discuss* 14:3499–3536
- Leckner B (1978) The spectral distribution of solar radiation at the earth's surface—elements of a model. *Sol Energy* 20:143–150
- Lindberg F, Grimmond C (2011) The influence of vegetation and building morphology on shadow patterns and mean radiant temperatures in urban areas: model development and evaluation. *Theor Appl Climatol* 105:311–323. doi:10.1007/s00704-010-0382-8

- Ludema C, Cole SR, Poole C et al (2014) Association between unprotected ultraviolet radiation exposure and recurrence of ocular herpes simplex virus. *Am J Epidemiol* 179:208–215
- Malinovic-Milicevic S, Mihailovic DT, Radovanovic MM (2014) Reconstruction of the erythema UV radiation data in Novi Sad (Serbia) using the NEOPLANTA parametric model. *Theor Appl Climatol* 1–8
- Matzarakis A, Matuschek O (2011) Sky view factor as a parameter in applied climatology—rapid estimation by the SkyHelios model. *Meteorol Z* 20(1):39–45
- Matzarakis A, Rutz F, Mayer H (2010) Modelling radiation fluxes in simple and complex environments: basics of the RayMan model. *Int J Biometeorol* 54:131. doi:10.1007/s00484-009-0261-0
- Mayer B, Hoch SW, Whiteman CD (2010) Validating the MYSTIC three-dimensional radiative transfer model with observations from the complex topography of Arizona's Meteor Crater. *Atmos Chem Phys* 10:8685–8696
- Molina LT, Molina MJ (1986) Absolute absorption cross sections of ozone in the 185- to 350-nm wavelength range. *J Geophys Res Atmos* 91:14501–14508. doi:10.1029/JD091iD13p14501
- Myers D (1997) Radiometric instrumentation and measurements guide for photovoltaic performance testing. National Renewable Energy Laboratory, Golden, Colorado 80401–3393, USA
- Myers DR, Gueymard CA (2004) Description and availability of the SMARTS spectral model for photovoltaic applications. In *Optical Science and Technology, the SPIE 49th Annual Meeting*. International Society for Optics and Photonics. pp. 56–67
- NASA LAADS (2013) MOD04\_L2 - Level Aerosol. MOD04\_L2. A2013158.1105.051.2013158202400.hdf. In: 51 - MODIS Collect. 5.1 - Sel. Atmos L. Prod. <http://ladsweb.nascom.nasa.gov/data/search.html>. Accessed 29 Jul 2014
- Nofuentes G, García-Domingo B, Muñoz JV, Chenlo F (2014) Analysis of the dependence of the spectral factor of some PV technologies on the solar spectrum distribution. *Appl Energy* 113:302–309
- Petersen S, Momme AJ, Hviid CA (2014) A simple tool to evaluate the effect of the urban canyon on daylight level and energy demand in the early stages of building design. *Sol Energy* 108:61–68
- Redemann J, Russell PB, Hamill P (2001) Dependence of aerosol light absorption and single scattering albedo on ambient relative humidity for sulfate aerosols with black carbon cores. *J Geophys Res Atmos* 106:27485–27495
- Remer LA, Kaufman YJ, Tanré D et al (2005) The MODIS aerosol algorithm, products, and validation. *J Atmos Sci* 62:947–973. doi:10.1175/JAS3385.1
- Robinson D, Stone A (2005) A simplified radiosity algorithm for general urban radiation exchange. *Build Serv Eng Res Technol* 26:271–284
- Ruiz-Arias JA, Pozo-Vázquez D, Lara-Fanego V et al (2011) A high-resolution topographic correction method for clear-sky solar irradiance derived with a numerical weather prediction model. *J Appl Meteorol Climatol* 50:2460–2472
- Serrano M-A, Bosca JV (2011) Validation of a method to estimate direct normal irradiance of UVA and PAR bands from global horizontal measurements for cloudless sky conditions in Valencia, Spain, by a measurement campaign. *Theor Appl Climatol* 103:95–101
- Smedley A, Webb A, Rimmer J (2010) Baseline measurement and analysis of UK ozone and UV. *Weather* 65:254
- Unger J (2009) Connection between urban heat island and sky view factor approximated by a software tool on a 3D urban database. *Int J Environ Pollut* 36:59–80. doi:10.1504/IJEP.2009.021817
- Vemez D, Milon A, Vuilleumier L, Bulliard JL, Koechlin A, Boniol M, Doré JF (2015) A general model to predict individual exposure to solar UV by using ambient irradiance data. *J Expo Sci Environ Epidemiol* 25(1):113–118
- Wagner JE, Angelini F, Blumthaler M et al (2011) Investigation of the 3-D actinic flux field in mountainous terrain. *Atmos Res* 102:300–310
- Webb AR (2006) Who, what, where and when—influences on cutaneous vitamin D synthesis. *Prog Biophys Mol Biol* 92:17–25
- Weihls P, Wagner JE, Schreier SF et al (2012) The influence of the spatial resolution of topographic input data on the accuracy of 3-D UV actinic flux and irradiance calculations. *Atmos Chem Phys* 12:2297–2312
- Yam JCS, Kwok AKH (2014) Ultraviolet light and ocular diseases. *Int Ophthalmol* 34:383–400
- Zhu S, Guan H, Bennett J et al (2013) Influence of sky temperature distribution on sky view factor and its applications in urban heat island. *Int J Climatol* 33:1837–1843. doi:10.1002/joc.3660